

# **STUDIES OF ASTRONOMICAL SEEING**

A Thesis

Submitted for the Degree of

**Doctor of Philosophy**

in the Faculty of Science

By

**VENKATESH S. L.**

**Indian Institute of Astrophysics**

**BANGALORE**

*Dedicated to my*

*dear parents*

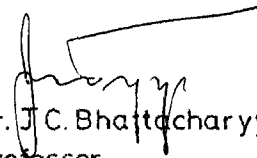
**Smt. MALATHI**

**and**

**Dr. S. L. RAO**

## CERTIFICATE

The thesis submitted is a record of research work done by Sri VENKATESH, S.L. during the period of study under us and it has not previously formed the basis for the award to him of any Degree, Diploma, Associateship, Fellowship or other similar titles. This thesis represents independent work on the part of Sri. VENKATESH, S.L.



Dr. J.C. Bhattacharyya,  
Professor,  
Indian Institute of Astrophysics,  
Bangalore.



Dr. K.S. Raghavendra Rao,  
Reader in Physics,  
Bangalore university,  
Bangalore.

Bangalore

D E C L A R A T I O N

The work forming the subject matter of this thesis was entirely done by me under the guidance of Dr. J. C. Bhattacharyya and Dr. K. S. Raghavendra Rao. This work has not been submitted earlier to any Institute or University for the award of any degree or diploma.

Bangalore

  
Venkatesh S.L.

### ACKNOWLEDGMENTS

This research work on "STUDIES OF ASTRONOMICAL SEEING" was undertaken and completed at the Kavalur Observatory and the main laboratory at Bangalore of the Indian Institute of Astrophysics. The same was facilitated by late Dr. M.K V. Bappu, who as our Institute Director was a great source of inspiration and encouragement for carrying out scientific work in a systematic manner.

I am very thankful to Dr. J.C.Bhattacharyya, Professor and Dy. Director, Indian Institute of Astrophysics and to Dr K.S.Raghavendra Rao, Reader in Physics, Bangalore University, who guided my research work.

Prof.P.R.Pisharoty of PRL, Ahmedabad, Dr. J.C.Kaimal of NOAA, USA., Dr. Vincent Lally of NCAR, USA., and Mr. Daniel Mazzarella of Scientific Associates Inc, USA, provided very useful and timely information about the use of micrometeorological instruments in this work.

Prof.R.Narasimha and Dr. A.Prabhu of the Department of Aeronautical Engineering, Indian Institute of Science, Bangalore, advised me in the use of the hot-wire anemometer. Sri.Syed Ameenullah and Sri.Venkatesh of the Department helped me in building the hot-wire anemometer sensors and calibrating them.

Dr. G.P.Srivatsava of India Meteorological Department provided  $100\ \Omega$  type thermistors used in this work.

Dr. K.S.Yajnik, Sri.A.K.Gurjale, Sri.S.V.Ramakrishna and Sri.S.Sundaram of the Boundary Layer Laboratory, National Aeronautical Laboratory, Bangalore, have helped in the planning and installation of an array of micrometeorological sensors in recording of atmospheric turbulence data.

Sri.S.Venugopal of the Electronics Laboratory of our Institute and Sri.T.V.Babu of Laktham Electronics, Bangalore contributed to the design, fabrication, testing and maintenance of thermocouple and thermistor amplifier electronics respectively.

Dr. K.Balakrishnan, Department of Mechanical Engineering and Sri.B.Gangaraju of the School of Automation, Indian Institute of Science, cooperated in digitizing the analog data and storing the same onto magnetic tapes.

Sri.S.Namperumal and Sri.H.R.Sreedhara Raju of the Computer Centre, Indian Institute of Science, gave valuable suggestions in writing computer programs for retrieval of data, evaluating power spectral and coherence values and plotting the same.

Computer program listings provided by Dr.C.Padha-  
krishna Rao of the Indian Institute of Geomagnetism,  
Colaba, Bombay and Dr.K.R.Sivaraman of our Institute,  
served as useful guidelines in my computation work.

Prof.J.W.Tukey, Bell Telephone Laboratories, New  
York, Prof.V.Krishnan, Department of Electrical Engi-  
neering, Indian Institute of Science and Dr.P.K.Dash,  
National Aeronautical Laboratory, gave many useful sugges-  
tions on the method of power spectral and coherence  
analyses as applied in the present work.

Sri.A.Charles, Sri.F.Gabriel and Sri.K.Kuppuswamy  
of our Institute came to my aid on several occasions  
during the course of the observational work and in main-  
taining and using the 1-m optical telescope with its  
accessories at Kavalur.

The drawings and manuscripts are provided by Sri.J.  
Raghunathan, Regional Instrumentation Centre, Indian  
Institute of Science. Sri.C.V.M.Bhanu Murthy spent many  
hours in very carefully typing the thesis matter. Sri.T.V.  
Balajee also typed out certain portions. Sri.B.R.Seshadri  
typed all mathematical symbols in this work.

While A.Vagiswari readily spared the services from  
our library, Sri.R.Krishnamoorthy of our Institute worked  
hard to provide multiple copies of several graphs and elegantly

prepared the bound copies of the thesis. He also provided some photographic prints.

Sri.P.S.Dixit of SHAR(ISRO), Sri.A.K.Gurjale of NAL and Sri.N.S.Asathanarayana Rao, A.E. Department, Indian Institute of Science., mainly contributed for many of the photographs in this thesis.

My wife, Dr.Swarupa Nadig, checked certain calculated results and made helpful suggestions for the final get-up of the thesis.

I very sincerely thank them all.

Finally, I would like to record my sincere thanks to the remaining members of the staff of the Indian Institute of Astrophysics who provided every required help from time to time.

Bangalore

  
VENKATESH.S.L.



## CONTENTS

	Page
Synopsis                    ...                    ...	i-iv
Chapter I... Astronomical Seeing	
1.1. Introduction	1
1.2. Aberrations	2
1.3. Atmospheric Effects	6
1.4. Seeing and Scintillation	10
1.5. Description of the Turbulence	14
1.6. Refractive index and Turbulence	14
1.7. Image Distortion in presence of Seeing and Scintillation	16
1.8. Seeing, Scintillation and Meteorological Phenomena	18
Chapter II... Observations of Seeing and Scintillation	
2.1. Observational Methods of Seeing	20
2.2. Some results of Seeing Observations	22
2.3. Minimization of Seeing effects	24
2.4. Observational Methods of Scintillation	28
2.5. A Few results of Scintillation Studies	28
2.6. Some Methods of Minimization of Scintillation	32

	Page
Chapter III... Instrumentation	
3.1. Introduction	33
3.2. Experimental arrangement: Optics and Associated Electronics	33
3.3. Experimental arrangement for recording Wind speed fluctuations	43
3.4. Magnetic Tape Recorders	66
3.5. Experimental set-up for recording Atmospheric Temperature	70
3.6. Details of Observations	81
3.7. Diaphragms	88
3.8. Digitization	89
Chapter IV... Power Spectrum Analysis of Seeing Data	
4.1. Introduction	96
4.2. Mathematical Method	96
4.3. Pilot Analysis for the choice of t (sampling frequency) and m (percentage lag)	102
4.4. Observing conditions at Kavalur	109
4.5. Trend removal from raw data	111
4.6. Interpretation of Autocorrelation functions and Power Spectral Densities in respect of Seeing Phenomenon	118
4.7. Interpretation of results on Normalized Autocorrelation and Power Spectral Densities in respect of Scintillation Phenomenon	133
4.8. Weather Conditions	148

	Page
Chapter V... Coherence Analysis	
5.1. Introduction	153
5.2. Mathematical Method	153
5.3. Installation of Micrometeorological sensors	156
5.4. Interrelations: Seeing Vs Wind speed	165
5.5. Interrelations: Seeing Vs Temperature	173
5.6. Interrelations: Amongst different Turbulent Layers	180
Summary                   ...                   ...	197
Appendix-A	<del>200-212</del>
Appendix-B	213-216
References	217-221

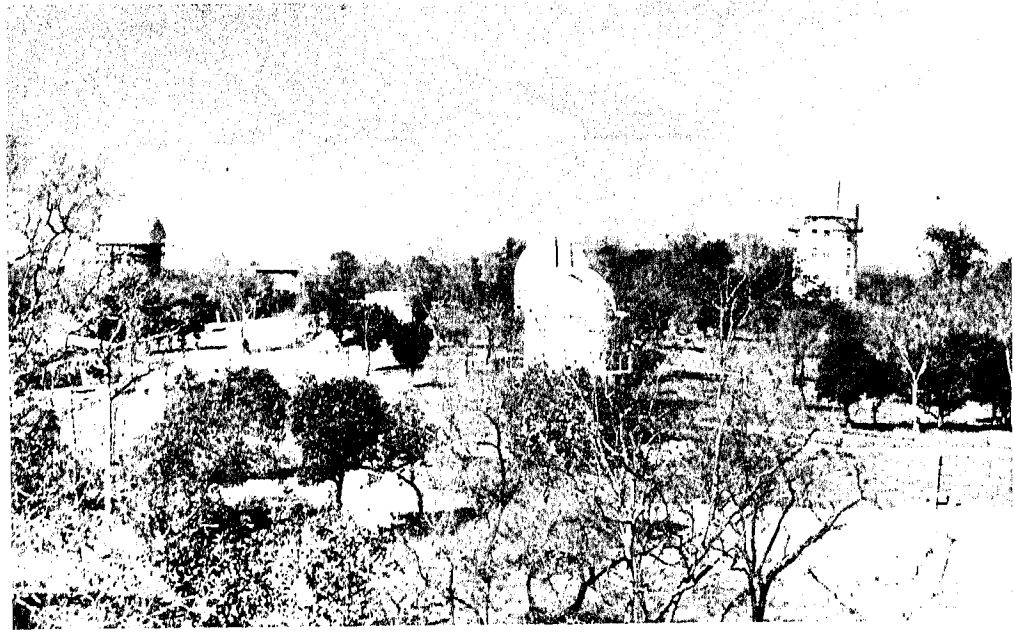
## S Y N O P S I S

Images of astronomical objects formed by optical telescopes are considerably disturbed by refraction, absorption and scattering in the atmosphere. Parallel rays originating from the distant sources undergo differential extinction and phase retardation over the telescope aperture which result in unsteady distorted images. Although these disturbing effects were known for a long time and qualitatively studied, detailed studies are rather meagre. A few attempts at sites at middle latitudes have been made throwing some light on the physics of the astronomical seeing. It is known that properties of the atmospheric layers have qualitative differences between sites in equatorial and low latitudes from those in high latitude areas. The present work aims to study these phenomena from a low latitude location by using sophisticated instruments.

In the past, the knowledge of the exact nature of seeing fluctuations had little more than academic interest but in the context of recent introduction of detector matrices for astronomical image recording, the subject has gained importance. Characteristic frequencies and amplitudes of the different components of these disturbances and their relations with the atmospheric parameters provide some vital bits of knowledge which could be employed in the building up of clear images of astronomical bodies.

The basic data for the present study was obtained at the Kavalur Observatory, Indian Institute of Astrophysics (Alt. 725 M above mean sea level, Lat: +12 Deg 34 min 32.2 Sec, Long: 78 Deg 49 min 54 Sec East). The 40-inch (1-m) telescope at the observatory is located at a height of 20 metres above surrounding ground atop a tall tower. Consistent differences were being noticed in seeing as observed in this telescope and other telescopes closer to ground, implying considerable influence of the layers adjacent to ground level. The 40-inch (1-m) telescope is used in conjunction with a sensitive system employing high gain photomultipliers, when temperature and wind flow detectors are located at different levels. Fast fluctuations in the recorded photometer signals and those of atmospheric turbulence are analysed by employing appropriate mathematical methods. Astronomical seeing as caused by the turbulent layers of the atmosphere at different levels in the neighbourhood of the 25 metre high dome of the telescope is investigated.

The present study makes observational investigation of image distortions caused essentially by optical inhomogeneities i.e., refractive index variations in the atmosphere. The 40-inch telescope is used in its cassegrainian configuration for collecting seeing and scintillation data. The temporal intensity variations of a star on account of bloating up and shrinking down of its image, a manifestation of astronomical seeing, are obtained by monitoring the intensity of a small



A view of the Indian Institute of Astrophysics  
observatory at Kavalur.

patch in the focal plane of the telescope. Information regarding scintillation fluctuations is also obtained by using a larger diaphragm about 9 seconds of arc in diameter. Records of temporal fluctuations in wind speed and temperature, representative of the movements of local optical inhomogeneities in the medium, in the vicinity of the telescope are obtained simultaneously with the seeing data. Sensitive micrometeorological instruments such as hot-wire anemometer, chromel-alumel thermocouple and bead-in-glass type thermistors are used to obtain data on atmospheric turbulence.

All data pertaining to seeing and atmospheric turbulence are recorded in the appropriate channels of a 7-channel philips tape recorder. The data is processed using computer programs for " power spectral " and " coherence " analyses. The choice of these mathematical methods and their details are discussed in the thesis. The results obtained from such an analysis are depicted in the form of plots of spectral densities against frequencies and plots of coherence between astronomical seeing and atmospheric turbulence at different frequencies. These results reflect the hidden periodicities in the observed phenomena of astronomical seeing and scintillation and the extent of relationship between astronomical seeing and atmospheric turbulence.

Finally, a detailed sum-up of the salient features of the problem under investigation is given along with a statement of the limitations involved. Further improvements in instrumentation and theoretical work which would lead to a clearer and deeper understanding of the physics underlying the observed phenomena have also been mentioned.



## C H A P T E R I

### ASTRONOMICAL SEEING

#### 1.1. Introduction

The sole source of our knowledge of the visible universe is the light that the distant stars and planets send us. It is remarkable that so much knowledge concerning the universe has been obtained by means of a simple instrument, the telescope. A simple looking telescope was invented in the early 17th century and Galileo made a series of spectacular discoveries using it. With the construction of more powerful and sophisticated telescopes, progress in astronomy became rapid and during the second half of the 19th century came the development of astronomical photography and the spectroscope. Telescopes used for collecting light from celestial objects and forming their images are of two types, viz., the refractor and the reflector. The first refractor was made in Holland in about 1608 while the first reflector was constructed by Sir Isaac Newton and submitted to the Royal Society in 1671. Many large refractors were constructed during the latter part of the 19th century. In recent times, the emphasis has been on reflectors since a large mirror is easier to make than a large lens.

## 1.2. Aberrations

No image-forming system can form a perfect image of a finite object. Every image has defects, called aberrations and the best that can be done in practice is to see that the aberrations that would be most noticed in a particular experimental arrangement are made as small as possible. von Seidel introduced in about 1860 the following classification of aberrations.

1. Spherical aberration: Lenses and mirrors with large spherical surfaces cannot form an accurate image of a point object on the axis. Usually the more extreme rays are too greatly deviated resulting in spherical aberration. This defect can be minimised in several ways.

- (i) The refracting or reflecting surface can be made aspheric and the aberration removed empirically.
- (ii) Spherical aberration produced by a single converging lens cannot be totally eliminated but may be minimised by proper design. For a single annular zone of the lens, spherical aberration may be eliminated by combining the positive lens with a negative lens. The lenses are so shaped that the spherical aberration of the negative lens nullifies that of the positive lens<sup>1</sup>.

2. Coma: Even if spherical aberration is minimised, we may still find that the image of a point slightly off the axis is not perfect. This defect is particularly important in astronomy, since the image of a star may look like that of a comet and hence the name coma. It can be eliminated by the following methods.

(i) Coma can be eliminated by choosing radii of curvature appropriate to a given object position - the so-called 'bending' of the lens. This usually also leads to minimum spherical aberration.

(ii) Coma and spherical aberration are absent in any system that obeys Abbe's sine condition.

3. Astigmatism: Astigmatism can be regarded as an extreme form of coma; it occurs for very oblique rays. Then a bundle of rays cannot pass through an image point. Instead, it forms a tapering wedge-shaped pencil, the edge of the wedge forming what is known as a focal line; all the rays pass through this line and then diverge. The rays then pass through another focal line, perpendicular to the first. The consequence of this defect is that it is impossible to produce a focused image of the outer parts of a plane object perpendicular to the axis. For example, if the object is

a spoked wheel, radial detail may appear to be in focus in one focal line and tangential detail in the other. Moreover, the surfaces in which these focal lines occur may not even be approximately plane, thus leading to the fourth aberration, viz., the curvature of field.

4. Curvature of field: The removal of astigmatism can be regarded as causing the two line surfaces to coincide, and the removal of curvature of field as making these surfaces plane. The defects are particularly important in cameras in which the image has to be focused on a flat plate. The lens which is corrected for astigmatism and curvature of field is called an anastigmat. Complex lens systems such as the Zeiss Sonnar lens system are designed to obtain the necessary correction for astigmatism and curvature of field.

5. Distortion: An image in which the previous aberrations have been corrected is still not necessarily a perfect representation of the object; if the magnification varies with obliquity of the rays then the shape of the object may not be reproduced and the image is said to be distorted; if the magnification increases with obliquity the image of a square will have the shape of a pin-cushion and if it decreases with obliquity the image will be barrel shaped. By using a symmetrical arrangement of two similar meniscus convex lenses placed with their concave surfaces facing each other

and with a stop midway between them, the positive distortion of the first element may be nullified by the negative distortion of the second element. For such a lens, distortion is absent only when object and image are symmetrically positioned. When used at other object-image distances some distortion is present. A symmetrical lens that corrects for distortion and spherical aberration is called ORTHOSCOPIC, or RECTILINEAR.

6. Chromatic aberration: Because the refractive index of glass is a function of wavelength, an image produced by using white light usually has coloured edges. This defect is known as chromatic aberration.

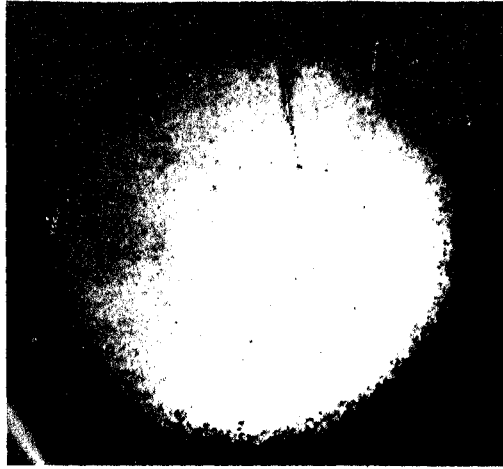
A rough correction can be made by using two lenses separated by a distance. The violet ray is more deviated than the red and so reaches the second lens nearer to the axis than the red ray; it is therefore less deviated by the second lens. The deviations can be arranged to combine in such a way that the red and violet rays emerge parallel to each other. A more precise correction can be achieved by cemented doublets of two different glasses; such a lens is known as an achromatic doublet.

Further, the wave nature of light gives rise to diffraction effects and thereby introduces limitations in the use of telescopes. Even in the absence of all aberrations, any optical component forms diffraction patterns characterised by

a central maximum surrounded by circular fringes. Two point objects are resolvable by an optical system if the two diffraction patterns produced by them are sufficiently small or are well separated.

### 1.3. Atmospheric effects

The ultimate choice of a telescope will, however, be dictated by the uses to which it is to be put. But even a fine telescope cannot surmount certain restrictions imposed upon it by our turbulent atmosphere. Pioneering theoretical and experimental work related to the propagation of waves in a turbulent medium has come from Tatarski<sup>2</sup> and Chernov<sup>3</sup>. This includes the propagation of starlight through the atmosphere. Clearly, the most well-known effect of turbulent atmosphere is the twinkling i.e., scintillation of stars, which refers to irregular changes in the brightness of stellar images. In the early 1950's, scientific interest in the twinkling and quivering of stellar images in telescopes became quite pronounced. Early experimental work on scintillation was reported by Mikesell<sup>4</sup> and others. Quivering refers to displacements of the image of a star in random directions and is obviously related to the fluctuation in the angle of arrival of the incoming light wave. Experimental work on this problem was renewed by Kolchinski<sup>5</sup>. Since then, many attempts have been made to investigate this phenomenon.



- Cross section of a laser beam before propagation



- Cross section of a laser beam after propagation through a 800 m path.

---

Fig. 1.1. Effect of atmospheric turbulence on a laser beam.

When an optical beam propagates through the atmosphere, it undergoes attenuation and fluctuations of amplitude and phase. The first effect is due to absorption and scattering by the constituents of the atmosphere i.e., water vapour, molecular oxygen, carbon dioxide, aerosols, clouds. The absorption is a quantum mechanical process due to the interaction between photons of the beam and molecules under resonance conditions. For this reason, absorption is markedly dependent on frequency. The scattering consists of changes in the direction of radiation incident on particles.

A turbulent atmosphere causes the beam parameters to fluctuate at random and distorts the beam producing one or more of the following effects<sup>6</sup>. For example Fig. 1.1 shows the effect of atmospheric turbulence on a laser beam.

1. Intensity fluctuations: Interference between waves of light reaching the image plane from different parts of the telescope objective produces amplitude fluctuations on the receiving surface, scintillation. These fluctuations depend upon the telescope aperture and the path length traversed by the optical beam.

2. Spatial phase fluctuation: The phase at different points on an arriving unperturbed wavefront is not the same but changes in a random way. Thus two points on the wave surface of the unperturbed wave, do not have, generally the same phase.



3. Temporal phase fluctuations: Because of variations in temperature, humidity and windspeed, changes occur in refractive index of the atmosphere. This results in fluctuations in the propagation velocity followed by random phase changes over a point of the telescope.

4. Fluctuations in the angle of arrival: The angle of arrival is the angle formed by the normal to the wavefront and the propagation direction. These fluctuations produce displacements of the image point in the focal plane i.e., image dancing or quivering. When the path is long, the wavefront can be thought of as being divided into separate coherence regions. Each coherence region presents its own incidence angle which suffers casual changes i.e., crumbling of the wavefront, boiling or image blurring.

5. Beam deviations: The unperturbed beam, if well established mechanically, maintains a well defined direction of propagation. In the presence of turbulence, the beam axis changes its direction in a casual way i.e., illumination dancing or spot dancing or beam steering.

6. Beam spreading: The unperturbed beam has its own spread due to diffraction. Turbulence causes further beam spread and the beam cross-section fluctuates in size, i.e., breathing.

7. Polarisation fluctuations: An initial polarisation may be perturbed by the turbulent atmosphere. Suppose at first the beam is totally polarised. When it arrives at the telescope objective it could present a depolarisation which depends upon the turbulence and the path characteristics.

Not all these phenomena are mutually independent. Distortions of the optical images formed by the telescopes are not known in detail. This knowledge is necessary to plan optical and digital systems for better image construction. The present study is intended to provide some of this knowledge. Studies of this type have not been made at low latitudes in the tropics and hence this study was undertaken.

In this work scattering and absorption are not considered. The problem of the fluctuations of wave parameters as manifest through intensity fluctuations experienced by an optical beam propagating through the turbulent atmosphere is examined, making an attempt to investigate the frequency composition of the seeing phenomenon. Also the extent of correlation between the two processes i.e., optical seeing and atmospheric turbulence existing at the time of observation is examined.

#### 1.4. Seeing and Scintillation

When a stellar image is observed through a telescope with high magnification, the observed image structure does not in

general correspond to diffraction pattern computed theoretically, even if the optics are excellent. The diffraction rings may be resolved only partly or not at all. In addition, an irregular motion of the image is often observed. The random fluctuations in the direction of part or all of the starlight received by the telescope are called seeing.

The random fluctuations of the intensity of starlight received on the ground are referred to as scintillation. The twinkling of stars falls into this category. The refractive index inhomogeneities causing the phenomena of seeing and scintillation are expected to occur in the turbulent parts of the atmosphere.

If a plane wavefront enters a turbulent layer, it will emerge as a distorted wavefront and travel as such to the ground. Fig 1.2 shows distortion of wavefront of a light wave. Two phenomena may follow from this situation:

(1) Below the turbulent zone the direction of light will show a dispersion. This dispersion is independent of the distance of the telescope from the turbulent zone. (2) The intensity in the wavefront below the turbulent zone is not uniform. The lack of uniformity increases with increasing distance of the telescope from the zone, at least until the average lateral displacement of a light ray is comparable with the average separation of the turbulent elements.

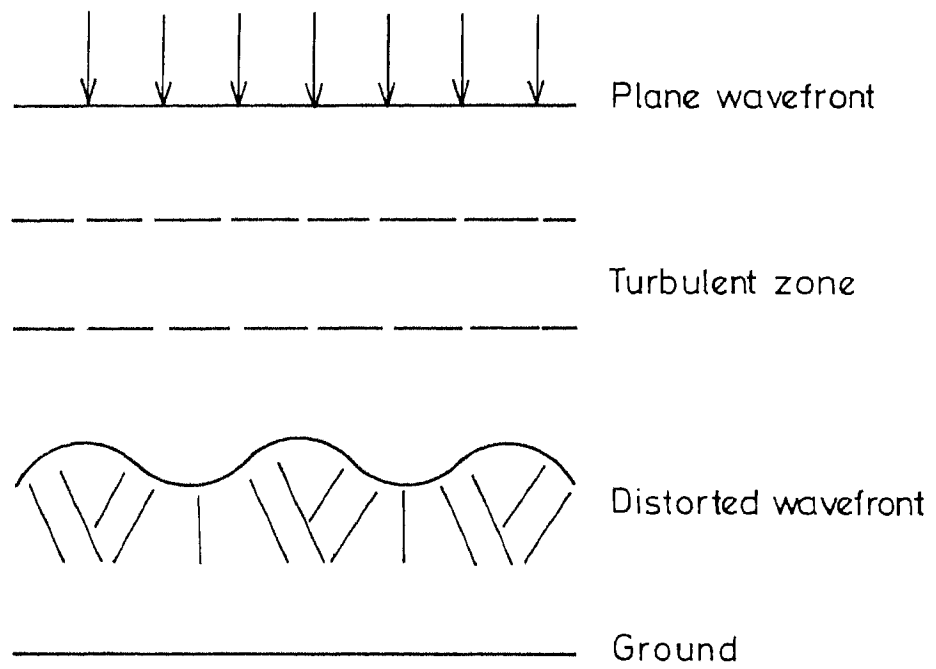


FIG-1.2. WAVEFRONT DISTORTION ON  
PROPAGATION THROUGH  
ATMOSPHERIC ZONE OF TURBULENCE.

Changes in the turbulence pattern in the light-path cause the temporal changes associated with seeing and scintillation. Suppose the turbulent layer consists of cells of various sizes with a refractive index different from that of their surroundings and that such cells are near the telescope. Then these cells with horizontal dimensions of the order of the aperture of the telescope or lesser will, in a first approximation, act as small lenses and defocus all or part of the light entering the telescope thus causing blurred images. In other words, light reaching different parts of the telescope objective is at different angles of arrival depending on the cells, their size and number. Thus seeing occurs. Such cells may also be present within the telescope dome and contribute to seeing, viz., dome seeing. On the other hand, if the cells are much larger than the telescope objective, they act as prisms since at a given moment the whole of the telescope aperture is covered by a single cell. Thus again we have seeing.

If the cells of varying refractive index are far above the telescope, the changes in direction due to cells at different heights average out and light of varying intensity reaches the objective. This results in scintillation. Obviously, scintillation is more prominent when objective is small. For example, more scintillation i.e., twinkling is observed with the naked eye as compared with visual observations through binoculars. Often scintillation and seeing occur together.

The image of a star in a small telescope may both move about in the field of view and vary in apparent brightness. Therefore it is possible to have poor seeing but no scintillation but it is not possible to have good seeing with strong scintillation.

### 1.5. Description of the turbulence

A laminar flow of a fluid is specified by its Reynold's number, relating the velocity  $V_f$  of the flow, the kinematic viscosity  $\eta$  and the dimension  $L$  of the fluid as a whole.

$$R = \frac{V_f L}{\eta}.$$

If Reynold's number  $R$  does not exceed a critical value  $R_{cr}$  the flow is stable. On the contrary, if  $R$  is greater than  $R_{cr}$  the flow becomes unstable and vortices are created. For each vortex an "inner" Reynold's number may be considered and the vortex will be stable if its Reynold's number does not exceed  $R_{cr}$ . If each vortex is not stable it breaks up into small eddies. Further break-up will occur until the vortex is reduced to a sufficiently small size. At this point the eddy is stable and its energy is dissipated into heat.

### 1.6. Refractive index and Turbulence

It is well known that the velocity of propagation of electromagnetic waves in vacuum is a constant

$$c = 3 \times 10^{10} \text{ cm/sec.}$$

When the radiation propagates in a medium, the velocity changes by a factor  $\frac{1}{n}$  where  $n$  is called the refractive index of the medium. If  $v$  denotes the velocity in a medium, one has  $V = \frac{c}{n}$ . The quantity  $n$  depends upon the wave frequency and the characteristics of the medium. The optical characteristics of a turbulent element depend on the difference  $dn$  between the refractive index of the air in the turbulence and that of the surroundings.

$$\text{Now,} \quad dn = \frac{d\rho}{\rho_0} (n_0 - 1)$$

where  $d\rho$  is the difference in density between the turbulent element and the surroundings;  $\rho_0$  is the density of air at normal temperature and pressure; and  $n_0$  is the corresponding index of refraction. Since the velocities of the turbulent air are highly subsonic, it may be assumed that density differences between adjacent air elements are the result of temperature differences and not pressure differences. Under these conditions, for a perfect gas

$$\frac{d\rho}{\rho} = - \frac{dT}{T}$$

where  $dT$  is the temperature difference of the turbulent element and  $\rho$  is the mean density of the surrounding air.

Thus

$$dn = - \left(\frac{\rho}{\rho_0}\right) \left(\frac{dT}{T}\right) (n_0 - 1)$$

### 1.7. . Image Distortion in presence of Seeing and Scintillation

A qualitative discussion may be made considering two extreme kinds of seeing, termed " good " and " bad ". In good seeing the turbulent layer may be likened to a thin, irregular diffracting screen wherein the optical thickness of the diffracting elements is so small that a good fraction of the incident light passes through the layer in an undiffracted (zero-order) plane wave. Images are then obtained of a quality limited primarily by halos of diffused light caused by diffraction in the turbulent layers. Conditions may be termed " good " when the quantity

$$K^2 = \frac{2\pi^3}{\lambda^2} N L_m^2 d_n^2 < 1 .$$

Here N is the average number of turbulent elements which the light rays pass through on their way;  $L_m$  is a measure of the average size of the elements;  $d_n^2$  is the mean square fluctuation of the refractive index and  $\lambda$  is the wave-length of light. Since the length\* of the optical path through the turbulent layer increases with the zenith distance of the object observed, N also increases. Hence good seeing is promoted by

- (1) thin turbulent layers
- (2) small zenith distances
- (3) small element sizes



- (4) small temperature fluctuations  
 and (5) use of a long wavelength of  
 light for observations.

Thus the phenomena of seeing and scintillation are related, in a statistical manner, with cells of hot and cold air in the atmosphere. Suppose that these air cells are confined to a horizontal layer of thickness  $\Delta z$  lying at a vertical height of  $z$  above the observer. Further, suppose that the variations in the index of refraction  $n$  in this layer are described by a Fourier series.

If we assume that the turbulence is homogeneous and isotropic we can describe the frequency of occurrence of turbulent elements of different sizes by the spectrum function  $b(\omega)$ , for which  $\omega$  is the wave number in  $\text{cm}^{-1}$  of a Fourier component and  $4\pi\omega^2 b(\omega)d\omega$  is the sum of the squares of all the Fourier coefficients with wave numbers lying in the interval  $\Delta\omega$  about  $\omega$ . If the turbulence and hence the scintillation are not unusually severe, a number of authors have shown that a relation between  $b(\omega)$  and the spectrum function for the shadow pattern  $B(\omega)$  can be obtained (the illumination of a lens or a mirror in the light of a single star is never completely uniform. The irregular patchwork of illumination which is present at any time is called the shadow pattern) as

$$\frac{B(\omega)}{h_0^2} = \frac{16 \pi^2 \Delta z b(\omega) \sin^2(\pi z \omega^2)}{\lambda^2}$$

Here  $\lambda$  is the wave length of light in centimetres. The formula indicates in a general way the manner in which atmospheric conditions are related to the characteristics of the shadow pattern and hence to the amplitude of scintillation. Large temperature fluctuations cause large differences in the index of refraction, hence large values of  $b$  and  $B$ . A thick layer produces a larger  $B$  than a thin layer<sup>7</sup>.

#### 1.8. Seeing, Scintillation and Meteorological Phenomena

If mixing of air masses of different temperatures occurs, extensive turbulence zones are produced and large values of  $dT$  may exist. This occurs in two typical situations:

- (1) in a cold front and
- (2) in an inversion layer

A rapid temperature decrease, lasting for several hours or more, indicates that a cold air mass is moving into the area. Temperature inversion is typical of dry climates. At night the surface cools rapidly by radiation, and little of this radiant energy is absorbed by the atmosphere because of lack of water vapour. Thus cold air forms close to the ground. The higher layers of the atmosphere show little change in temperature, unless there is wind. The thickness of the layer of cold air steadily increases during the night. The vertical temperature gradient shows an inversion at the top of the cold

air. Turbulence with large values of  $\Delta T$  may exist near the inversion.

When shadow-pattern velocities are compared with wind velocities at various altitudes by different meteorological instruments, it is found that in nearly all cases the velocity pattern agrees with the wind velocities at those altitudes. Scintillation is essentially caused by a turbulent layer of mixed hot and cold air located in different parts of the atmosphere.

Conditions for good observation:

1. Good observing conditions ensue when the ground heating is minimum, as otherwise there exist thermal inhomogeneities in presence of ground radiation by cooling.
2. Good conditions would prevail if there is minimum of wind turbulence, since this turbulence gives rise to thermal inhomogeneities and thereby inhomogeneities in the refractive index of the medium.

## C H A P T E R II

### OBSERVATIONS OF SEEING AND SCINTILLATION

#### 2.1. Observational methods of Seeing

1. Image diameter: The only seeing feature observed through a large aperture is the profile of an image. It is observed that an image does not have sharp edges. It has been shown that the profile is usually nearly Gaussian. Sufficient magnification must be used so that the images look like discs. The magnification has to be chosen according to the seeing conditions. Photoelectric measurements through diaphragms of different sizes show what fraction of the starlight is included in a visually estimated diameter.

2. Image motion: In the case of small apertures, it is sufficient to estimate the maximum excursion of the image from its average position. Such estimates again yield a radius within which the image will stay for 80 to 90 per cent of the time; this radius nearly has the same value as obtained in the previous method.

3. Photographic trails: Image motion can be studied readily by trailing the image of bright stars across a photographic plate. This procedure also allows for the deduction of the entire image profile expected for large apertures. This method works quite satisfactorily if the seeing effects are manifest as image motion.

4. Image intensifiers: The use of image intensifiers has a great advantage in studying this problem, since it enables one to use shorter exposures and to work with fainter sources. Frederick (1960)<sup>8</sup> has been able to photograph binary stars having separations as small as 0.3 second of arc with the aid of a two-stage cascaded-image intensifying tube and exposures of the order of  $\frac{1}{100}$  second of time.

5. Observation through two apertures: If two small apertures are placed in front of a telescope of large aperture and images slightly out of focus are observed, two sharp but separated images can be seen. The relative image motions and structure of the two images provide very useful measures of what the image appearance would be in a telescope of aperture equal to the separation between the holes. From photographic trails of the images, image profiles for the larger telescopes can be deduced.

6. Study through diffraction pattern: One of the most widely used methods was proposed by Danjon (1926)<sup>9</sup>. It is based on the estimates of the resolution of the diffraction pattern of stellar images observed through apertures of 20-25 cms. The estimates made in a scale described by Danjon are then transformed by an empirical relation to angular measures. Allowance for the actual aperture used can readily be made. Such estimates can be carried out easily and with accuracy. Seeing effects which appear as image motion through a 20-25 cm

error in the basic assumptions. The phase shift at a point on the disturbed wavefront is dependent on the wavelength, being only half at 8000 Å of that at 4000 Å. In this manner the phase-shift autocorrelation function appears to be dependent on the wavelength in such a way as to yield a correlation function independent of colour in the image plane of the telescope.

Recent balloon studies, both manned and unmanned have added information on high-altitude seeing effects. Seeing and scintillation greatly diminish upward in the first 20,000 feet ( 6000 m ) above the earth and are negligible above 50,000 feet ( 15,000 m ). It has been found, however that a light source on a balloon observed from the ground does not begin to scintillate until high altitudes are reached.

Systematic changes in seeing with latitudes and longitudes appear to be smaller than the variations between the best and the poorest seeing at any one site. Records for many years are therefore needed to yield a significant average. The jet-stream shows an annual variation in latitude from  $15^{\circ}$  to  $60^{\circ}$ , while polar frontal systems range from  $20^{\circ}$  to  $80^{\circ}$ . The principal sources of thermal inhomogeneity in the free atmosphere thus cover almost the entire globe, though the frequency of disturbance varies regionally.

A large number of experimental papers are devoted to the study of the quivering of images, a review of which is contained in the papers of Kolchinski<sup>14</sup>. This author arrives at the conclusion that the mean square fluctuations of the angle of arrival of the light from the star is directly proportional to the secant of the zenith distance of the star. Dependence of the amount of quivering of stellar images on the zenith distance is as shown in Fig. 2.1. Also empirical dependence of the amount of twinkling on the diameter of the telescope diaphragm is shown in Fig. 2.2.

### 2.3. Minimization of seeing effects.

Couder (1953)<sup>15</sup>, Rosch (1955)<sup>16</sup>, and Sisson (1957)<sup>17</sup> suggested methods for suppressing seeing effects in optical instruments. Devices with combination of ventilation and temperature-control system were made to ensure that the temperature of the air within the instrument is as nearly uniform as possible and at the same time maintaining the same temperature existing outside the dome. These methods have their own drawbacks. Brief periods of good instrumental seeing have been obtained by Leighton (1957)<sup>18</sup> by utilising the first 100 seconds after first opening the 60-foot Mount Wilson solar tower to the sun's light.

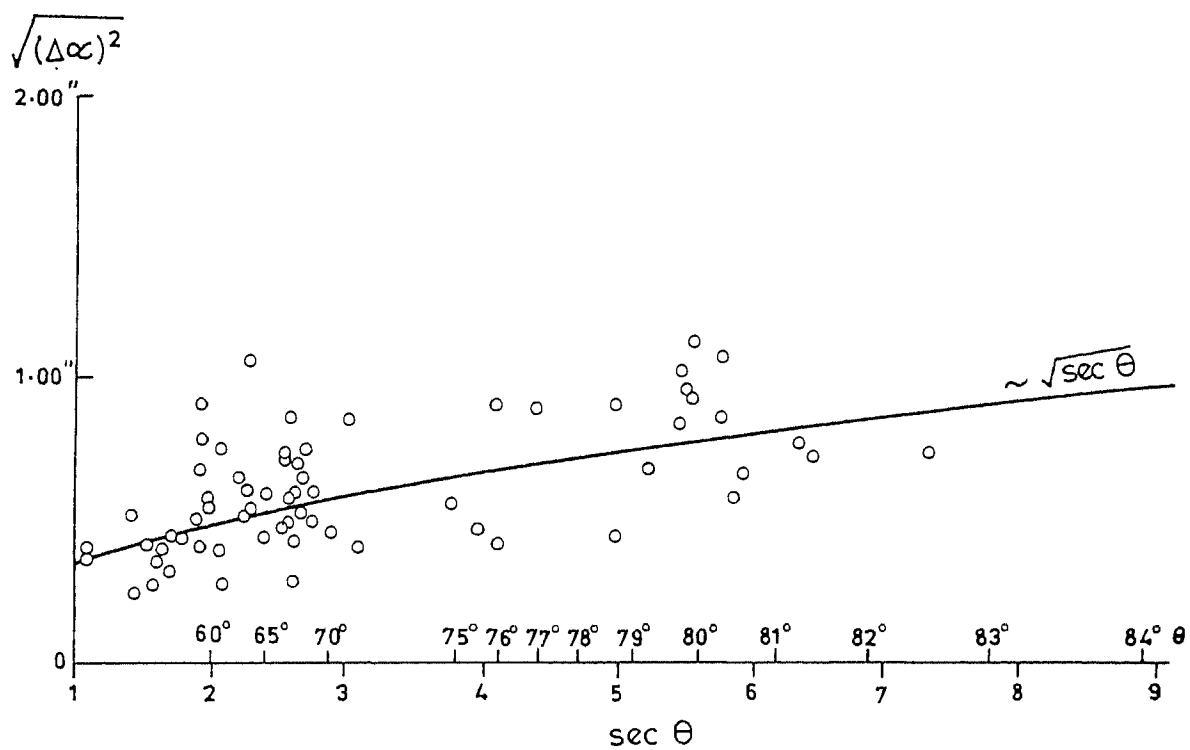
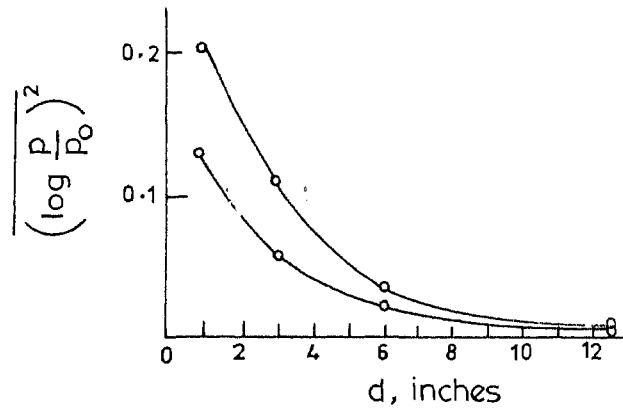


Fig. 2.1. Dependence of the amount of quivering of stellar images on the zenith distance.

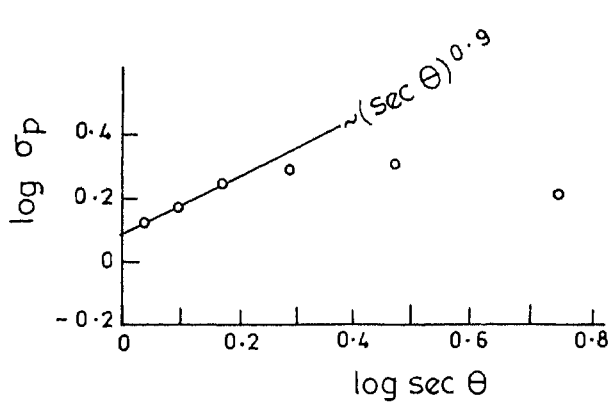
$$\sqrt{(\Delta\alpha)^2} = A^2 \sec^2 \theta = (\text{rms fluctuation of the propagation directions of the wave})$$

The quantity  $A$  is a few tenths of an angular second in order of magnitude, and depends upon meteorological conditions

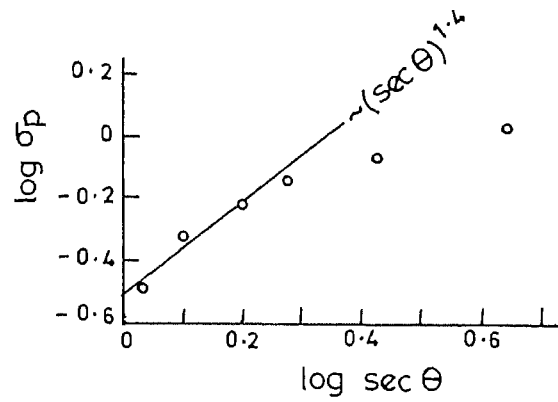




Empirical dependence of the amount of twinkling on the diameter of the telescope diaphragm.



Dependence of the amount of twinkling on the zenith distance when the telescope diaphragm has a diameter of three inches.



Dependence of the amount of twinkling on the zenith distance when the telescope diaphragm has a diameter of 12.5 inches.

Fig. 2.2.

$$\frac{\left(\log \frac{p}{p_0}\right)^2}{\log \sigma_p} >$$

Quantities representing fluctuations in light intensity.

Another approach to the problem is based on the fact that, at any given instant, the wavefront being focused at adjacent points in the focal plane have traversed pretty much the same elements of inhomogeneities in the atmosphere. To the extent that this is true, the images of the adjacent sources will be displaced and distorted in the same manner, a fact that opens up the possibility of analysing one or more of the images to determine the nature of the distortion and using this information to introduce optical corrections, as suggested by Babcock (1953)<sup>19</sup> and actually achieved, so far as lateral displacements are concerned, by Leighton (1956)<sup>20</sup> and Dewitt, Hardie (1957)<sup>21</sup>.

McMath (1955)<sup>22</sup> offered a complete solution to all seeing problems by placing the entire equipment at an altitude sufficiently high that a negligible amount of air lies in the light path to the instrument. Using a 12-inch reflector suspended from a balloon at an altitude of 80,000 feet, Schwarzschild (1959)<sup>23</sup> has obtained photographs of the solar granulation of unprecedented definition. Using exposure times of approximately 1/1000 second, the theoretical optical resolution of 1/3 second of arc has been achieved in the best photographs. However, such experiments are rare and generally the observations have to be made with the ground-based telescopes. As such detailed studies of seeing are quite vital and useful.

#### 2.4. Observational methods of Scintillation

The rapid temporal changes in the shadow pattern are accompanied by changes in the integrated illumination, and scintillation results.

Direct observation of instantaneous shadow pattern is difficult because even the brightest stars do not furnish enough light to permit the use of exposure times needed to stop the motion ( of the order of 1/500 second ) with ordinary photographic techniques. So the statistical properties of a shadow pattern can be studied by the use of high-efficiency photomultipliers at points separated by a preassigned amount. Barnhart, Keller and Mitchell (1959)<sup>24</sup> have obtained fairly typical autocorrelation function  $Q$  for stars near the zenith which can be approximated by the expression

$$Q = \exp - \frac{(\Delta r)^2}{2(\Delta r_0)^2}$$

where  $\Delta r$  is the separation of the correlated points in centimeters and  $\Delta r_0$  is of the order of 2 cm.

#### 2.5. Some results of scintillation studies

Protheroe (1955)<sup>25</sup> found that a mean value of the scintillation at Columbus, Ohio, is of the order of 40 per cent of the mean intensity for an aperture of 2.5 cm when one

observes close to the zenith during the night.

Mikesell, Hoag and Hall (1951)<sup>26</sup> determined the frequency spectrum of stellar scintillation. Nights of both good and bad seeing were used and observations were made at Washington D.C. and Flag Staff, Arizona. Representative scintillation spectra are shown in Fig. 2.3.

The authors consistently found that when the seeing is good, the high-frequency components are missing and the low-frequency components are much less pronounced than they are under bad seeing conditions. They also derived the dependence of scintillation on zenith distance, showing the well-known fact that stars near the horizon scintillate more slowly and with greater amplitude than do stars near the zenith. Also, scintillation were found to decrease with increase in telescope aperture and the scintillation amplitude was roughly proportional to the inverse of telescope diameter.

The colour dependence of scintillation was found to be slight or nil and there was no evidence of dependence on the plane of polarization.

Protheroe (1955)<sup>25</sup> and Mikesell et al (1951)<sup>26</sup> have made observations of the frequency spectrum of scintillation. It is found that the fluctuations in intensity of the light have frequencies varying upto perhaps 500 cps. The r.m.s. amplitude per unit bandwidth is more or less constant upto 75 cps

(a) Washington 4-inch Aperture  
 Copella,  $Z=54^\circ$ , Seeing poor  
 Observations taken over 30min.  
 Polaris,  $Z=51^\circ$ , Seeing good  
 Observations taken over 60min.

(b) Flagstaff 4" Telescope Polaris  
 Seeing: 11.26.50: Good. Image  
 excellent with considerable  
 motion. 12-4-50: Very bad. Image  
 exploded, motion very large and fast

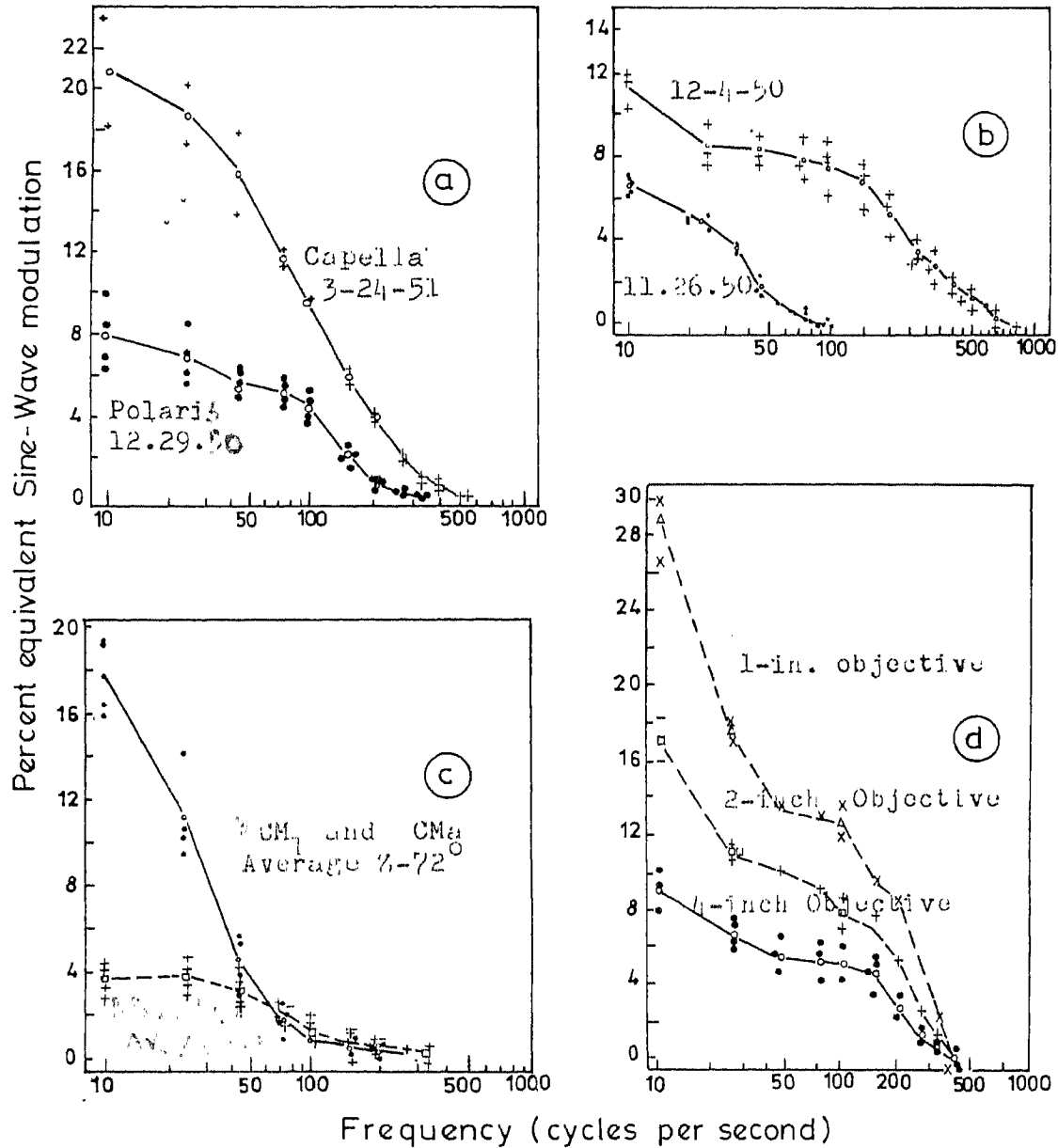


Fig.2.3. Above: Scintillation spectra obtained with good and bad seeing, both at Washington and at Flagstaff. Below, left: Scintillation spectra showing increase of scintillation with zenith distance; right: variation of scintillation spectra with aperture of telescope; open point represent means.

(c) 12-21-50 Washington 15-inch Telescope  
 8-inch Aperture Visual Seeing: Fair

(d) 12-5-50 Flagstaff Polaris  
 Seeing: Very poor. Image large and fuzzy, motion large and fast  
 Strong N wind: very clear.

and decreases fairly smoothly to zero at the high-frequency limit. During winter months, when meteorological conditions at those places are more severe, it is found that the amplitudes at all frequencies are larger, but those at the higher frequencies relatively more so, probably because of the higher wind velocities that prevail at that time of the year.

A number of studies have been made of the relation of upper-air phenomena to the behaviour of the shadow bands and scintillation by Protheroe (1955), Gifford and Mikosell (1953)<sup>27</sup>, Mikosell (1955)<sup>28</sup> and Barnhart et al (1959)<sup>24</sup>.

The autocorrelation method can be used with considerable accuracy to measure the speed and direction of motion of shadow patterns. Although the most striking of the temporal changes in the shadow pattern is its lateral motion, important intrinsic changes occur fairly rapidly. Barnhart et al (1959) found for a sample of 12 nights that the pattern changes completely in periods of time varying from 6.5 to 13 milliseconds. During this period the pattern as a whole moves distances of the order of 15-27 cms.

Two-dimensional spatio-temporal power spectra of shadow patterns associated with the stellar light scintillation has been determined experimentally by optical filtering of the spatial frequencies. The results show evidence for a multi-layer structure of the air turbulence in the upper troposphere.

Altitude and windspeed can be deduced for each layer. They are in good agreement with wind profiles from meteorological data as stated by Vernin and Roddier (1973)<sup>29</sup>.

#### 2.6. Some methods of minimization of scintillation

It would be expected that the use of a large aperture has the effect of partially averaging out fluctuations in the total light received in the focal plane. Protheroe (1955) has obtained data in this experiment from 1.25 to 16 cm apertures which agree surprisingly well with the theoretical expression for the same effects. It seems clear therefore that scintillation effects can be suppressed by using a large aperture.

Those methods adopted for reducing the effects of seeing can also be used in this case for achieving good results ultimately.

C H A P T E R IIIINSTRUMENTATION3.1. Introduction

The plan of observations and the method of analysis in the present investigation were designed to obtain simultaneous records of temporal variations in seeing and scintillation and two of the atmospheric parameters, viz., wind speed and temperature. The one-meter ( 40-inch ) telescope at Kavalur is used in its cassegrainian configuration with photoelectric photometer as the detector for recording seeing and scintillation data. Separate micrometeorological instruments have been employed for collecting wind speed and temperature data within the lower layers of the atmosphere in the neighbourhood of the telescope dome. The individual and simultaneous records of data of astronomical seeing and atmospheric turbulence have been subjected to mathematical analysis to detect hidden periodicities in the phenomena and to investigate the extent of relationship between the optical image distortions and inhomogeneities in the atmosphere.

3.2 Experimental arrangement: Optics and associated electronics

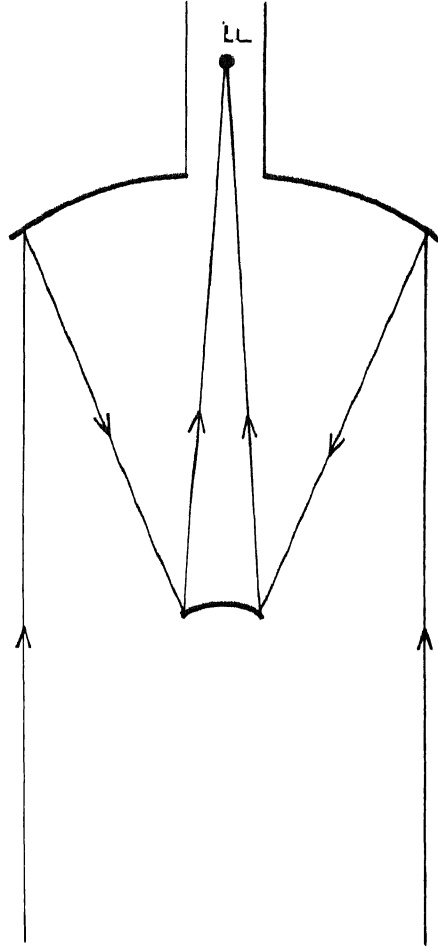
1. Optics: The one-meter ( 40-inch ) telescope at Kavalur ( Alt: 725 M above MSL, Lat:  $+12^{\circ} 34' 32.2''$ , Long:  $78^{\circ} 49' 54''E$  )



is set up in its cassegrainian configuration. The schematic diagram of this optical set-up is as shown in Fig. 3.1. The primary mirror is a paraboloid while the secondary takes the form of a convex hyperboloid. The secondary is placed within the focus of the primary mirror. Reflected light from the secondary passes through a hole in the middle of the primary mirror and the image is formed behind the primary. A suitable detecting system placed at the position of the image collects the light.

This telescope, a Carl-Zeiss make, works in both Cassegrainian and Coude configurations. Observations in both photometry and spectroscopy of stars are made using this telescope, besides astronomical photography. A range of f-numbers can be chosen depending upon the type of observation. A digital computer, TDC-12, is used to operate the telescope according to a preassigned programme in an on-line mode in some observations. This telescope is placed on an equatorial type of mounting. The situation of the telescope is ideal for making extensive observations of the southern skies. Attached to the main telescope are three smaller telescopes of 10", 8" and 3" aperture which are used for preliminary adjustments and viewing purposes.

2. Facilities with the telescope: The movements of the telescope along right ascension and declination are achieved electronically. A separate electronic system takes care of



The converging rays are intersected by the small hyperboloidal mirror before reaching the focus F.

FIG- 3.1. THE CASSEGRAINIAN CONFIGURATION.

compensation against earth's rotation rendering the position of the telescope steady during observation of an object. Handsets are provided for making fast, intermediate and fine movements of the telescope. By means of the handset, focusing can be done by the observer stationed at the spot of observation itself. The entire status of the telescope position is displayed on the console, when required. One can obtain right ascension, hour angle, local sidereal time and air mass.

Since the telescope is used with different accessories for different observational programmes, it is necessary to counter-balance it according to the accessory used. This is done by adjusting the position of the counterweight. The telescope is installed atop a high tower and a large dome covers the telescope from above. The dome can be rotated to any desired position and the large slits upon the dome can be opened at the time of observations. The movements of the dome and the dome slit are made automatically. The switches for this purpose are provided at the console. The external surface of the hemispheric dome is painted white using titanium oxide so as to reflect all heat radiation and to keep the inside temperature as steady as possible. The primary mirror is exposed to the sky only at the time of observations by opening the flaps covering it. The switch to open and close the mirror flaps is also provided at the console.

The observatory maintains clocks showing Universal Time, Local Sidereal Time and Indian Standard Time. These clocks are controlled by quartz crystal oscillators. The clocks are set every day prior to the commencement of the observations with the help of BBC time signals. In case power fails, power to operate the telescope can be drawn from two stand-by power generators without causing any interruptions to the observations.

In the present studies appropriate choice of diaphragm and filter has been made to suit the particular requirements of the individual experiments being performed, whether seeing or scintillation, the type of photomultiplier tube used, the spectral class and magnitude of the star and the existing sky conditions. A Fabry lens is used as shown in Fig. 3.2 to illuminate the photocathode of the photomultiplier tube uniformly. Further, the entire detecting system is cooled to dry ice temperatures for overcoming the disturbances from thermal noise. Fig. 3.3 is a view of this optical telescope.

The star signals from the photomultiplier are amplified and fed to a recording system. Gain settings of the photometer are suitably selected depending upon the existing conditions of the levels of the sky background. The signals that are recorded are simultaneously monitored with the aid of the display on CRT screen of an oscilloscope.

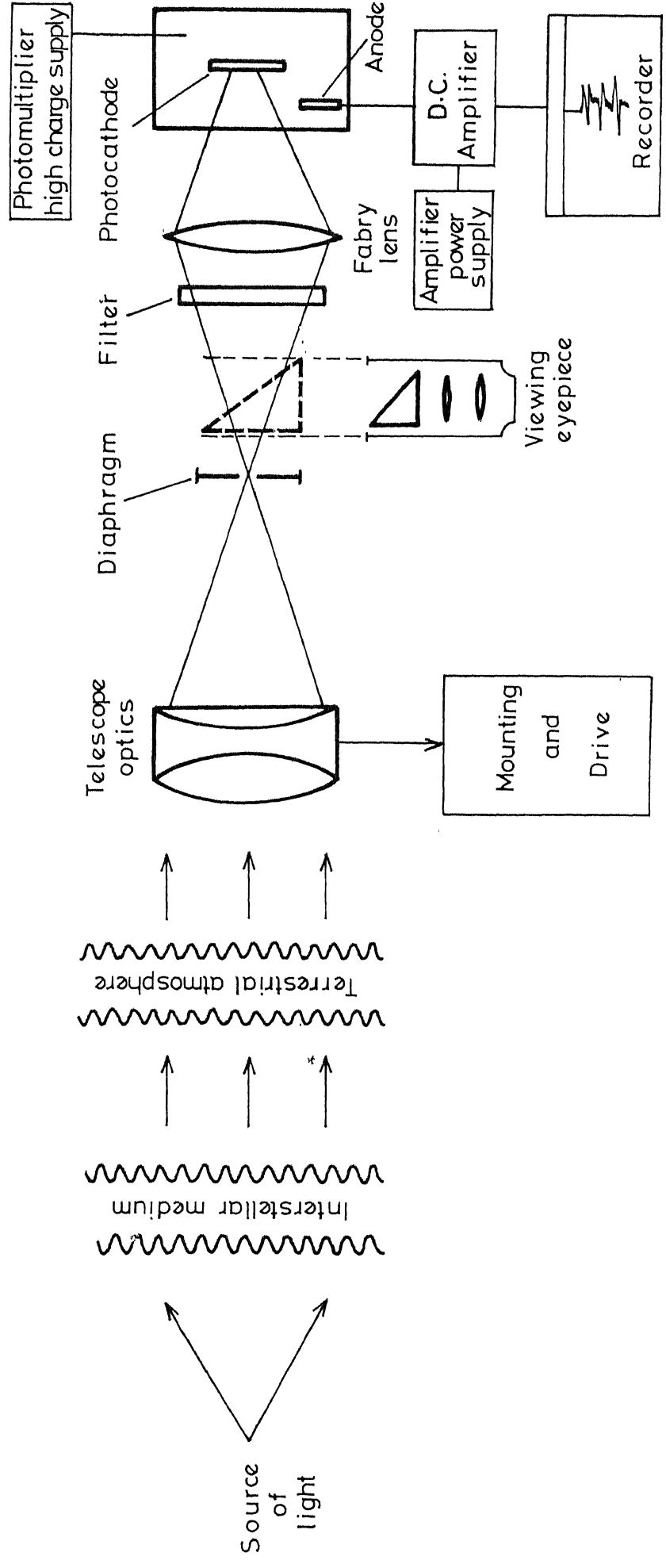


FIG-3.2. RAY DIAGRAM SHOWING THE PHOTOELECTRIC PHOTOMETRY SET-UP FOR COLLECTING DATA ON SEEING AND SCINTILLATION USING 1-M OPTICAL TELESCOPE AT KAVALUR.

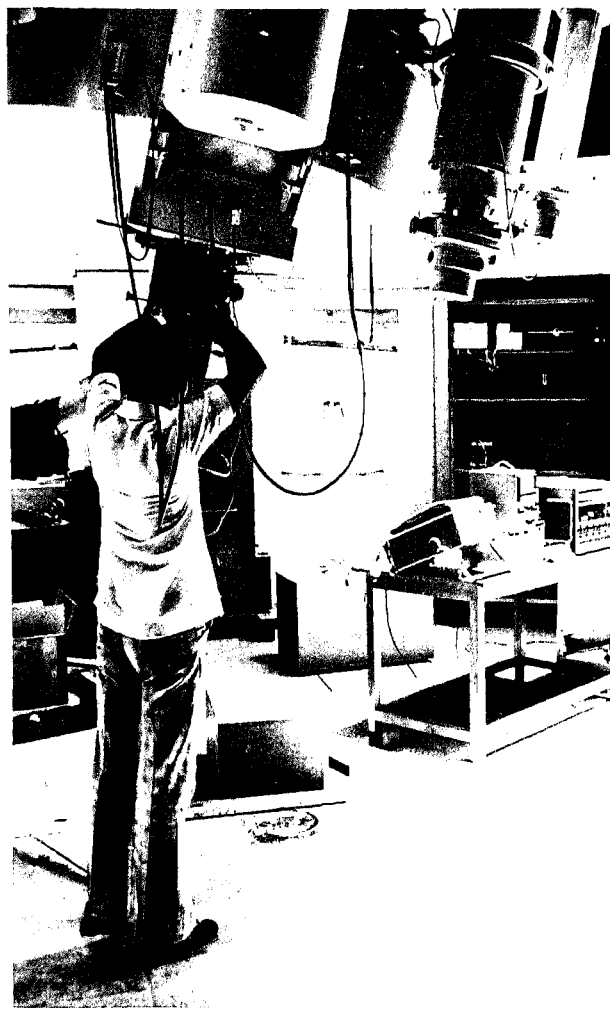
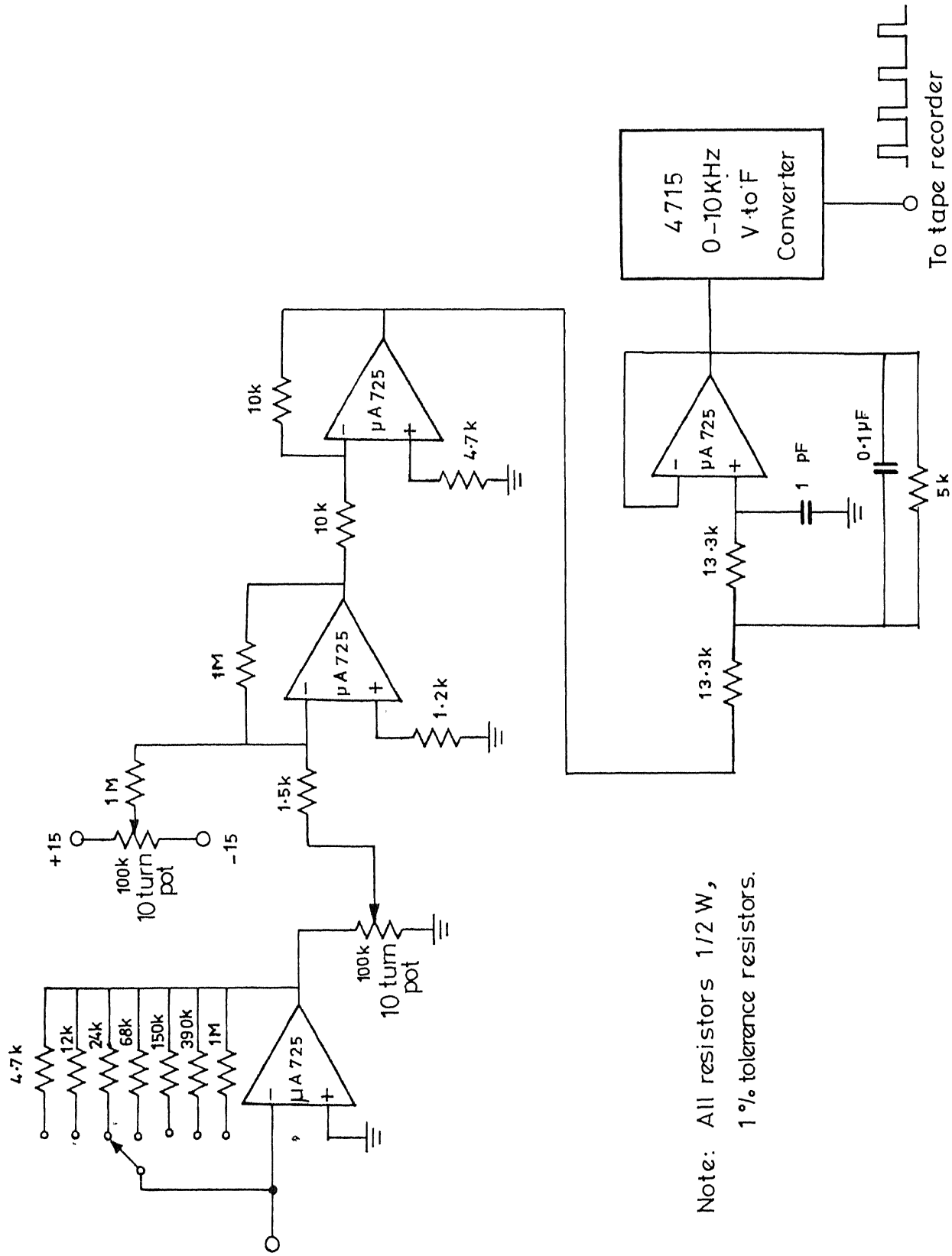


Fig.3.3. 1-m optical telescope in its cassegrainian configuration with photoelectric photometer being set up at its focus.

A range of sensitive photomultiplier tubes like EMI 9501, EMI 9558B, 1P21 has been used in this work. Such a situation arose **because the** observational programmes of seeing were combined with some other programmes which demanded the use of specific photomultiplier tubes. However, the collection of data on seeing and scintillation through different photomultiplier tubes did not affect the subsequent analysis and interpretation of results arrived at.

3. Associated electronics of the recording system: An analog system<sup>30</sup> has been employed for recording fluctuations in seeing and scintillation. This system provides for the storage of data and timing signals on two tracks of a magnetic tape. The same recorder also reproduces the stored data on a cathode ray oscilloscope screen as an analog record. Fig. 3.4 shows photomultiplier tube signal amplifier electronics. A quartz clock as shown in Fig. 3.5 is incorporated in the equipment and it provides time resolution better than a millisecond in the frequency analysis of astronomical seeing. A crystal clock followed by a divider chain generates a train of pulses of pulse frequency  $10^4$  cycles per second as well as bunches of 1 KHz signal at 1 second intervals. The printed circuits are produced in the electronics laboratory of the Indian Institute of Astrophysics. This system is capable of giving high accuracy with low level analog input signals typically in the order of  $10^{-7}$  amp. It consists of a current-to-voltage converter which



Note: All resistors 1/2 W,  
1% tolerance resistors.

Fig. 3.4 . Photomultiplier tube signal amplifier electronics.



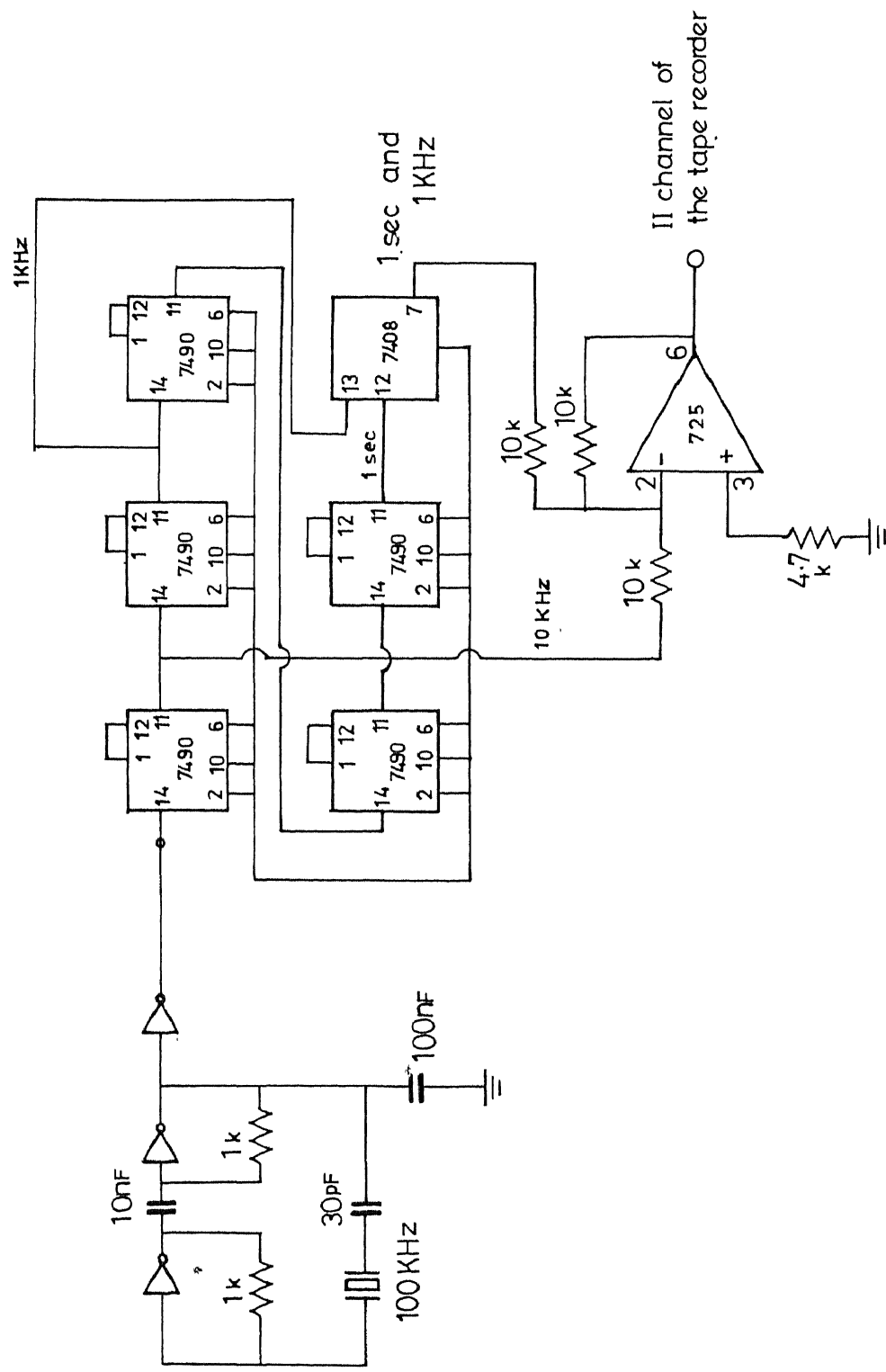


Fig. 3.5. Quartz crystal clock providing time signals of 1 ms.

accepts the PMT output and provides the voltage directly. The filtered signal voltage is given to a voltage-to-frequency converter. It uses a frequency modulation technique. This consists of a low-drift voltage-to-frequency converter providing an output pulse train whose repetition rate is a precision linear function of the input voltage. This low-drift, ultralinear device has the ability to handle positive, negative and differential input signals. This output is directly recorded on one of the FM channels of a tape recorder. The recorded output from the tape recorder goes through a frequency-to-voltage converter. This provides a linear conversion of frequency information to an analog voltage whose amplitude is proportional to the input signal frequency.

### 3.3. Experimental arrangement for recording wind speed fluctuations

1. Hot-wire anemometer: It is used to record the fluctuations in wind speed. The principle of its working is that when a sensor wire of very low thermal inertia such as superfine Platinum-Iridium or Tungsten is electrically heated in a bridge network and the sensor wire is exposed to the wind, the wire loses heat to the surroundings and hence its temperature and resistance drop. Such a drop can be taken to represent the fluctuation in the wind speed. Initially, the temperature of the wire is maintained at a constant and high value. Due to the

passing winds, the temperature of the wire is reduced because of increased cooling<sup>31</sup>. The temperature is brought to the original value by passing more current through the wire. This is achieved by a feed back amplifier as shown in Fig. 3.6. The unbalanced output across the bridge is fed to a feedback amplifier<sup>32</sup> which drives a current through the bridge for restoring the bridge balance. The detailed electronic circuitry typical of the device is as shown in Fig. 3.7.

The bridge arm ratio is set to unity and the fixed resistance value kept low to reduce the loading of the bridge by the feedback amplifier. For the sake of compactness, the usual decade resistance is eliminated but flexibility in operation is maintained by providing a choice of six operating resistances ranging from 5.7 to 8.2 ohms. With a typical 4.5 ohm wire this provides overheat ratios roughly in the range of 1.3 to 1.7.

(i) Construction of the hot-wire probe: The hot-wire probe consists of bare Platinum-Iridium of about 1 to 2 mm in length and 2 to 5 microns in diameter. This is spot-welded to the tips of two stainless steel prongs which are fixed to a ceramic body, porcelain. The length of the sensor material is carefully chosen to be compatible with the other bridge resistances. Electrical leads are soldered to the other end of the needles and taken out through the porcelain tube for connecting them to the terminals of the hot-wire bridge. The electrical leads are

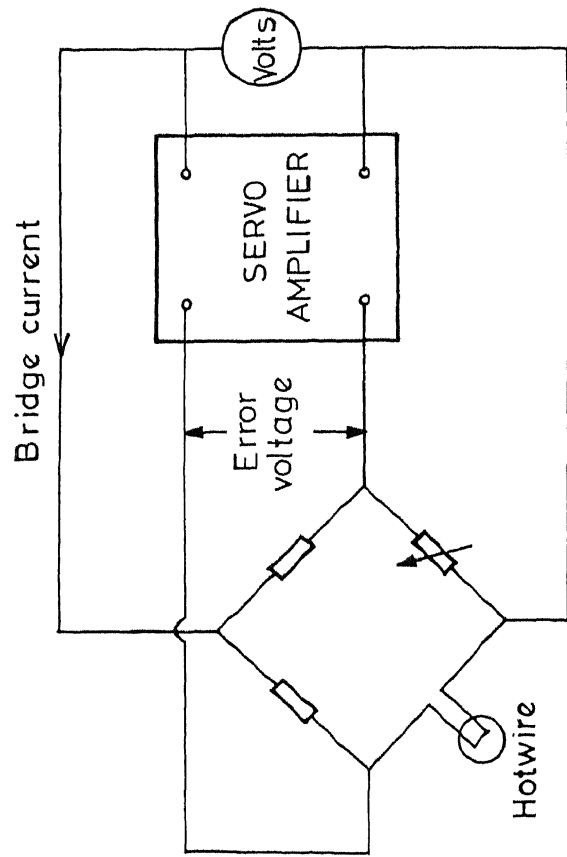


FIG-3.6. PRINCIPLE OF CONSTANT TEMPERATURE ANEMOMETER.

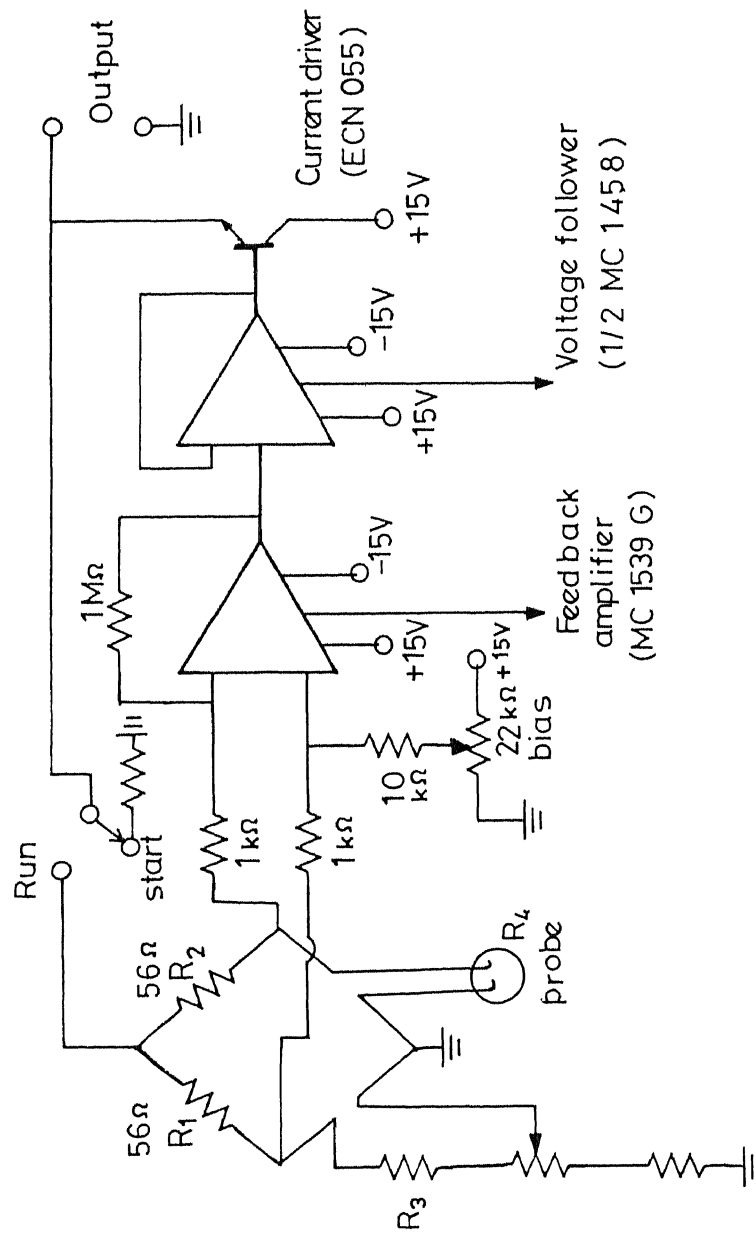


Fig.3.7. Electronic circuit typical of a constant temperature hot-wire anemometer.

insulated to avoid any shorting. The probe is as shown in Fig. 3.8. Figs 3.9 and 3.10 show the close-up view of the hot-wire anemometer sensor and its material. The probe was used in conjunction with the electronics of a DISA 55M anemometer. Fig. 3.11 shows the electronics set. For ruggedness, uncoated tungsten may be used as a sensor. It cannot be soldered and so has to be spotwelded. Silver coated Platinum-Rhodium can also be used as a sensor material. In this case, the sensor can be soldered to the needle tips as there is silver coating on them. Subsequently, a little silver is removed by what is known as etching from the wire to make it a sensor ( using 30% nitric acid ). The resistance value has to be compatible with the other bridge resistors.

(ii) Calibration: Calibration of the hot-wire anemometer is carried out at the National Aeronautical Laboratory, Bangalore. The calibration is made by keeping the wire in a wind tunnel and measuring the voltage  $V$  across the bridge as a function of wind speed  $U$ .  $U$  is obtained using the values of the air pressure in the wind tunnel as given by the formula

$$U = 12.56 (\sqrt{h})$$

Here,  $h$  is the height in mm of the liquid (alcohol) in the U-tube manometer employed to observe the air pressure. The experimental set-up for the calibration is as shown in Figs. 3.12 and 3.13.

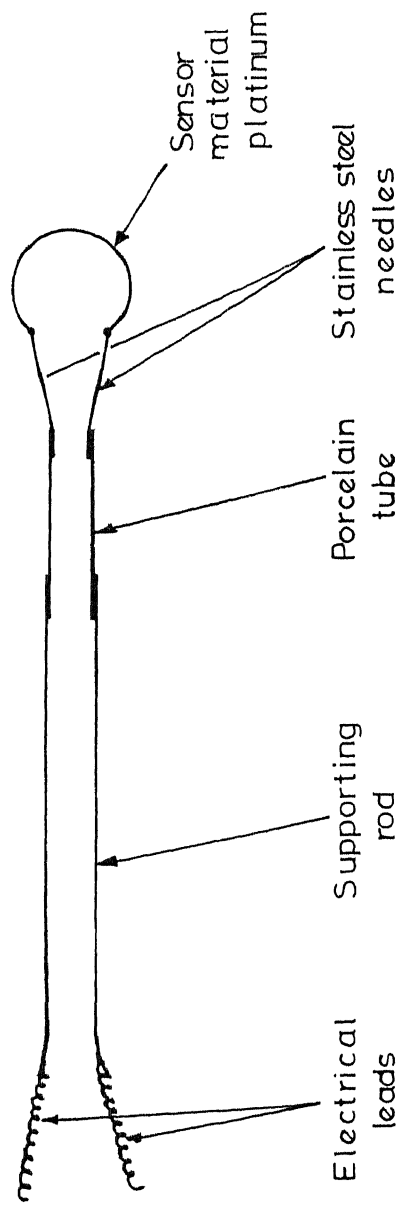


Fig. 3.8. Construction of the hot-wire anemometer sensor probe.

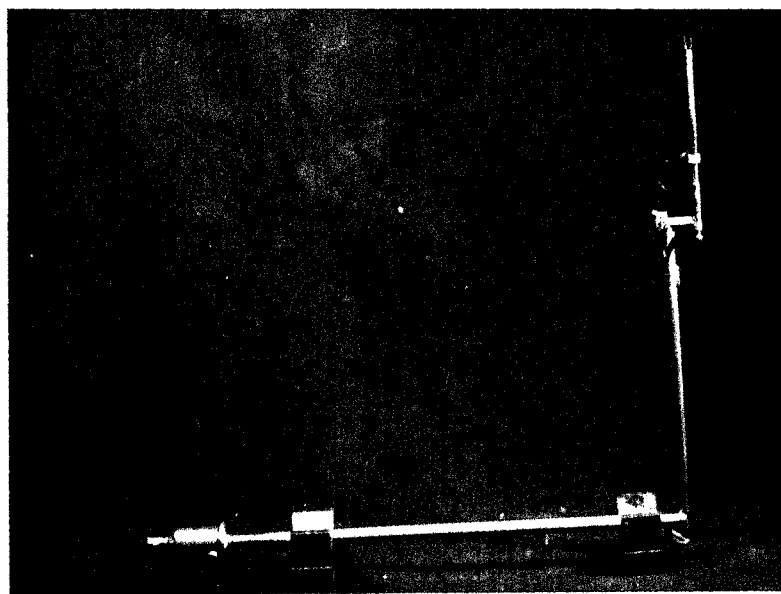


Fig. 3.9. Close-up view of a hot-wire anemometer sensor (Pt-Ir alloy) mounted on a probe and supported by a long rod.



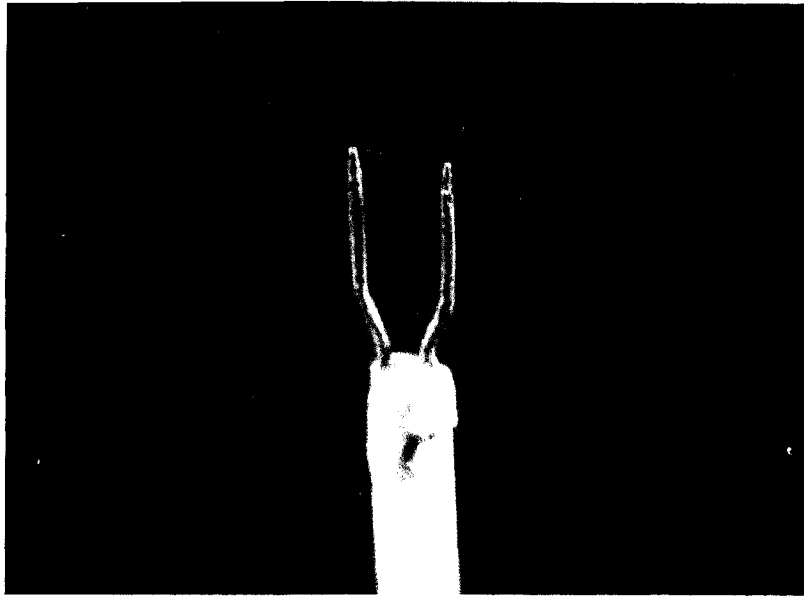


Fig. 3-10 Close-up view of the hot-wire  
(sensor)

Material: Pt-Ir alloy, 3mm in  
length and 10 microns in dia.

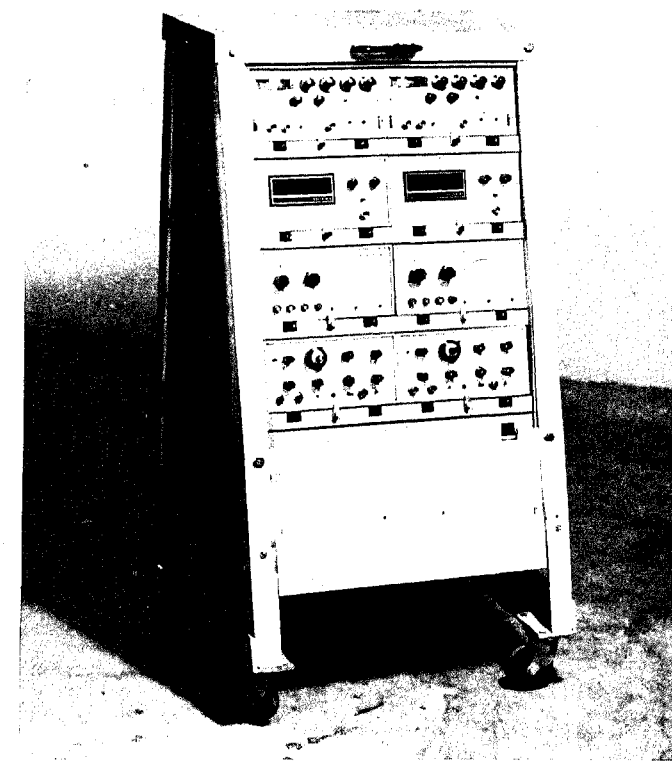


Fig. 3.11. DISA hot-wire anemometer electronics. Model 55M. Has monitoring meters, controls for gain setting, filtering, zero suppression facility when long cables are used.

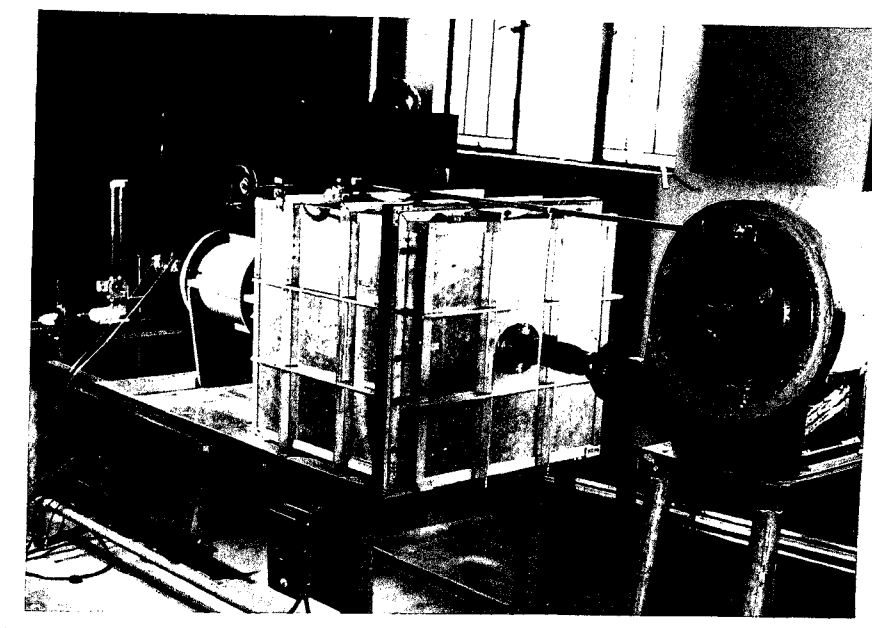


Fig.3.12. Wind jet facility for hot-wire sensor calibration.

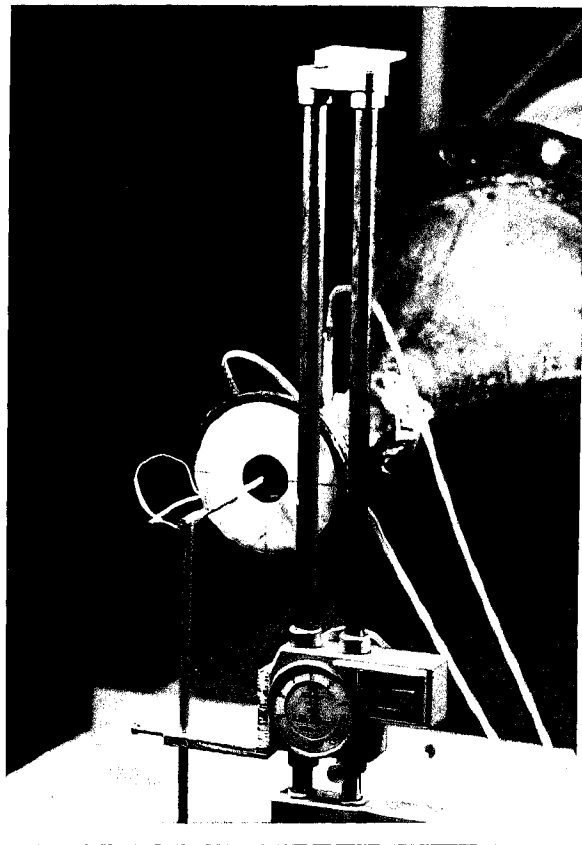


Fig.3.31. Calibration of a hot-wire sensor in "Free Wind Flow."

The output voltage of the anemometer is compared with the air speed as calculated above. This calibration is done for a few probes. The data is used to determine the constants 'n' and 'B' in the modified king's law <sup>34</sup>.

$$V^2 = V_0^2 + BU^n$$

which relates the output voltage (V) to the air speed (U).

$V_0$  is the out-put voltage at "no flow" condition. The constants are evaluated by the method of least squares by using 15 data points. The values of n and B are given in table 3.1. The details of location of the different sensors are given in table 3.2.

The sensitivity,  $\frac{\partial V}{\partial U}$  is obtained from the relation

$$\frac{\partial V}{\partial U} = \frac{n}{2} \frac{V^2 - V_0^2}{VU}$$

The plot of  $\frac{\partial V}{\partial U}$  Vs U for one of the sensors (used over the dome) is shown in Fig. 3.14.

(iii) Specification of sensor material:

- i) Material of the sensor : Platinum-Iridium alloy
- ii) Diameter of sensor : 10 microns
- iii) Length of sensor : 3-4 mm approx.
- iv) Material of sensor support : Ceramic body with steel prongs
- v) Diameter of sensor support : 0.5 mm approx.

TABLE 3.1  
CALIBRATION DATA FOR HOT WIRE SENSOR

PROBE IDENTI- FICATION	DATE OF CALIBRA- TION	n	B	V <sub>0</sub> VOLTS
02	22.6.81	0.481	13.45	5.75
	3.7.81	0.487	12.44	5.70
03	22.6.81	0.399	29.58	5.56
	24.7.81	0.400	20.00	5.54
04	17.6.81	0.450	12.97	4.41
	24.7.81	0.449	12.81	4.40
05	22.6.81	0.441	21.87	5.85
	24.7.81	0.440	20.07	5.84
10	20.5.81	0.463	14.105	5.06
	11.6.81	0.466	13.80	4.98
	3.7.81	0.464	14.60	5.00

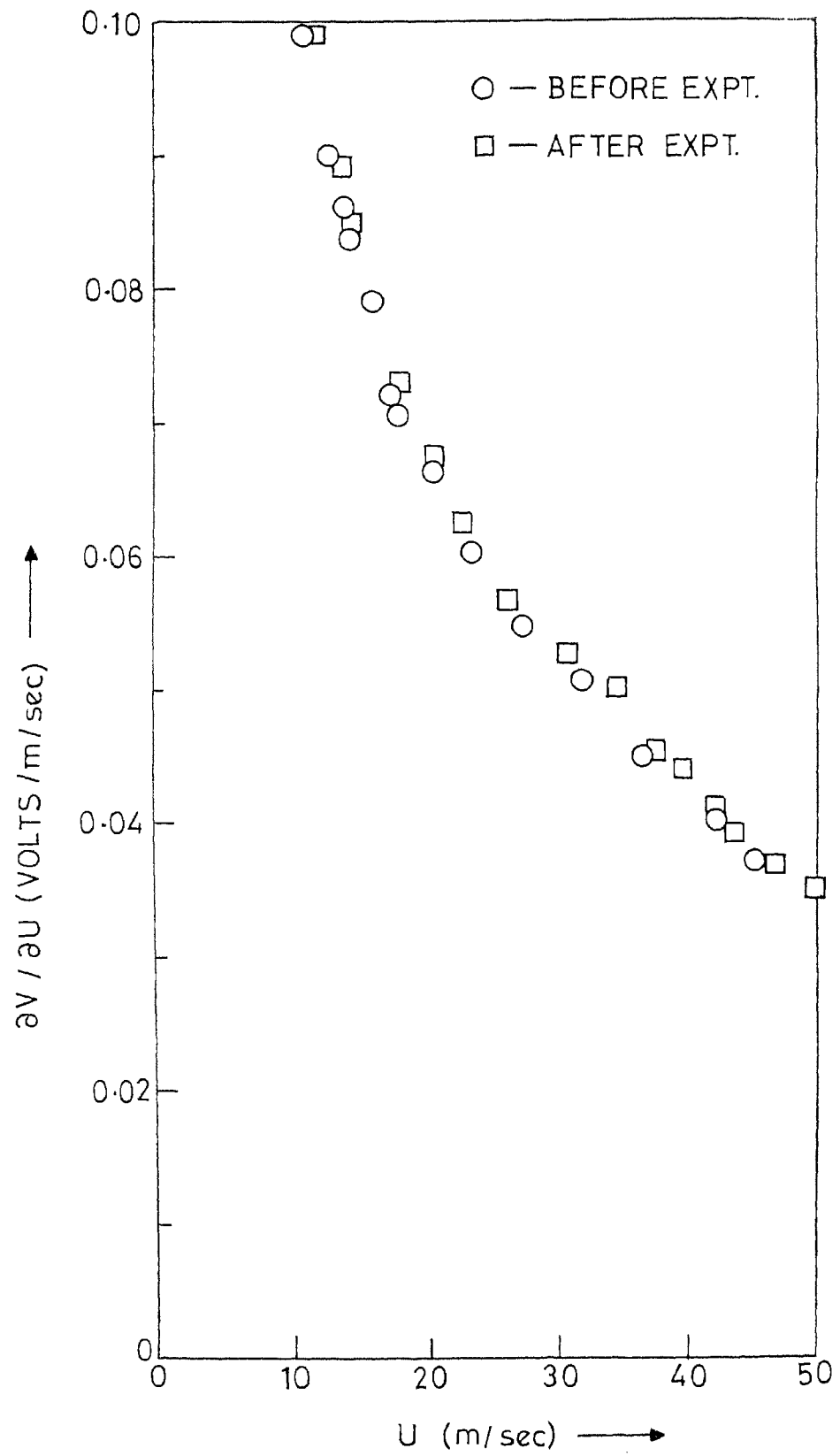


FIG-3.14. Sensitivity of the probe located over the dome.

TABLE 3.2

DETAILS OF PROBE LOCATION

PROBE IDENTIFICATION	LOCATION AT KAVALLUR	CHANNEL IN TAPE RECORDER	TAPE NO.	REMARKS
02	REFERENCE ( On the cat walk)	1	02	Used partly for experiments on 22.5.81. Replaced by 04 due to sensor dislodgement.
03	* AZIMUTH	2	02	Used near the cup anemometer at the top of the dome.
04	REFERENCE ( On the cat walk)	1	02	Used for experiments from 22.5.81 to 26.5.81
05	TRAVERSE	2	02	Used to explore flow field at four heights along the building.
08	CAT WALK	2	02	Used on the cat walk at a position approx. 90° with the Ref. 04.
10	DOME	2	02	Used in the vicinity of the telescope and the slit.



(iv) Limitations: Although hot-wire anemometer has earned a predominant place in such measurements, it has its own limitations, viz.,

(a) The atmospheric dust gets deposited on the wire and changes its calibration and frequency response. This can be set right by frequent cleaning of the hot-wire using acetone or alcohol.

(b) Since the sensor material ( Pt-Ir ) is very fragile, it is extremely exacting to keep it intact for long intervals of time. So, much care is exercised in preserving the delicate wires.

(v) Motivation in using hot-wire sensors: The motivation for using such sophisticated micrometeorological instruments in this research project in which extremely high frequency response instruments are to be employed, is being well brought out in Fig. 3.15 where it is indicated that hot-wire anemometers are best suited for measurements in atmospheric turbulence where eddy sizes and their frequencies are of such minute scales. This figure is drawn from the work of Daniel A. Mazze<sup>35</sup>lla.

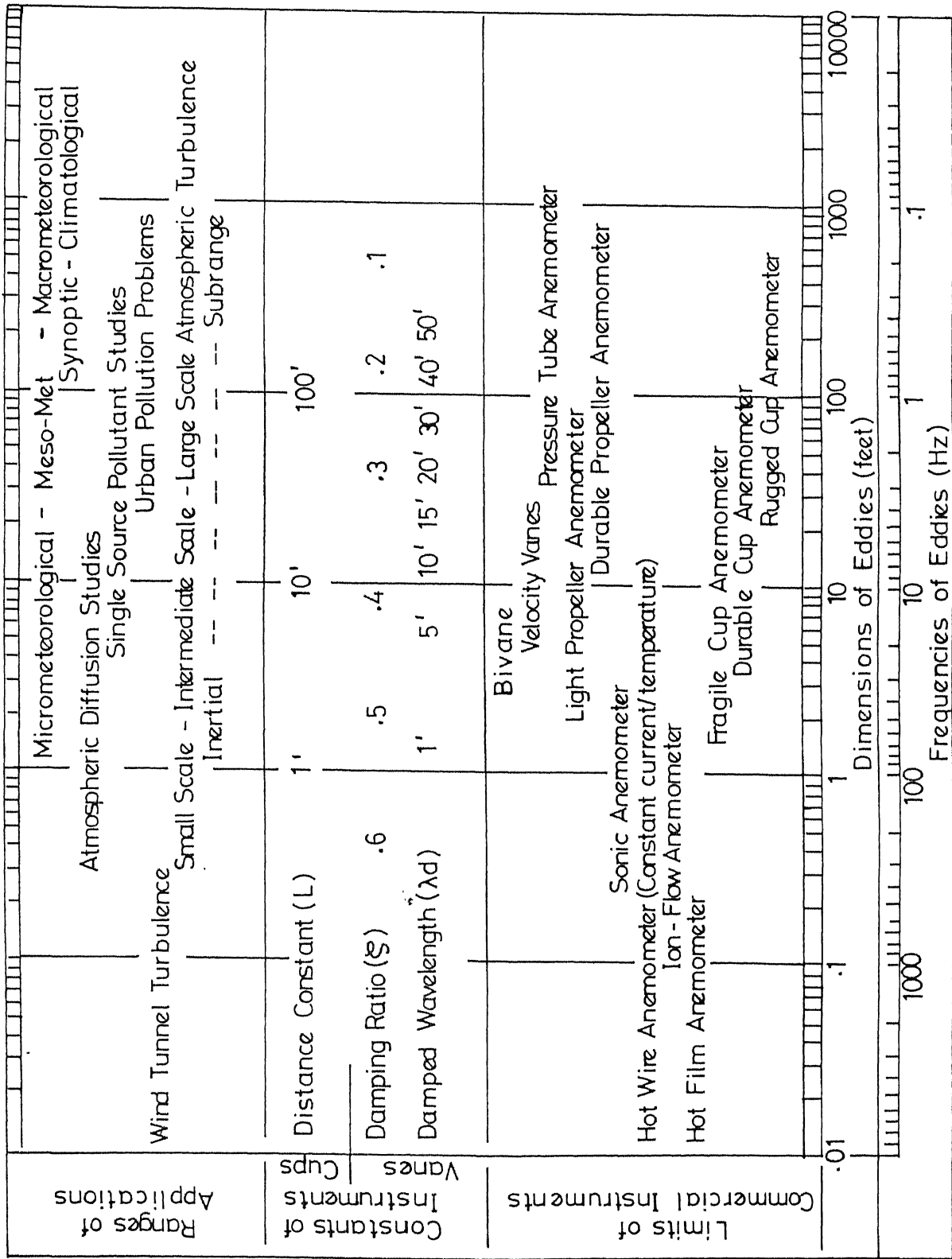


FIG-3.15. APPROXIMATE RANGES, CONSTANTS & LIMITS OF WIND SENSORS.

2. Cup anemometer: Because hot-wire sensor is very fragile, another stand-by wind speed recording instrument is maintained and used. This is Young Company cup anemometer that is provided with a windvane also to indicate the direction of wind flow. Data from this instrument is recorded in one of the channels of the tape recorder for using it when required.

Principle of cup anemometer: The cup wheel makes one revolution for each 75 cm ( 2.46 feet ) of wind passage. The cup wheel is supported on a stainless steel shaft which rotates in two stainless steel precision instrument grade ball bearings. The cup wheel drives the miniature d.c. tachometer generator through a unique flexible coupling consisting of a circular bristle disc mounted on the cup wheel shaft and a small coupling with two sharp pin projections mounted on the generator shaft<sup>36</sup>.

The voltage output of the generator is  $2400\text{mv} \pm 10\%$  at 1800 rpm and is very linear throughout the working range. Internal resistance of the miniature generator is 71 ohms nominal. The output signal is suitable for magnetic tape recorder.

Fig. 3.16, 3.17 and 3.18 show Model 6101 3-cup anemometer, windvane and recorder respectively.

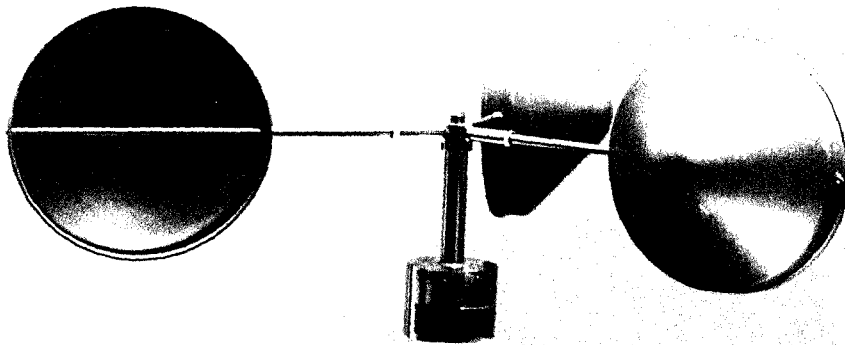


Fig. 3.16 Cup anemometer.

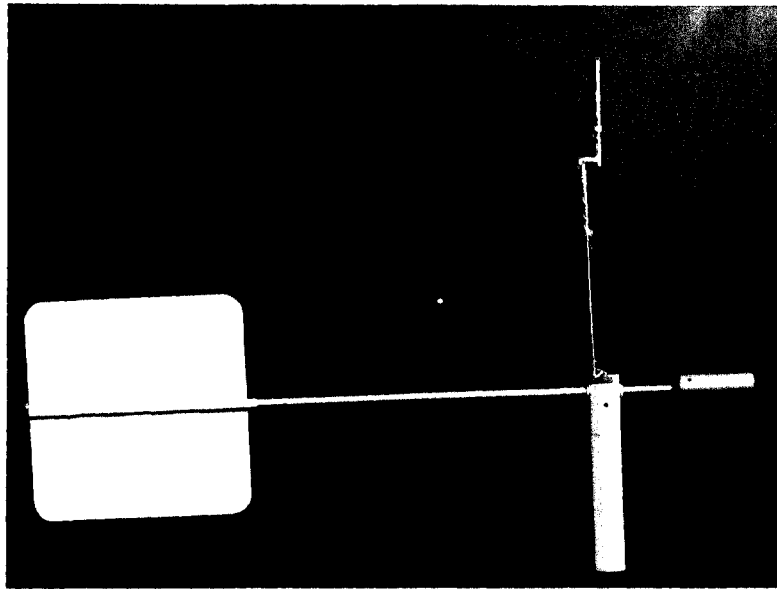


Fig.3.17. Close-up view of Young Company Windvane; attached to the vertical rod is a hot-wire sensor.

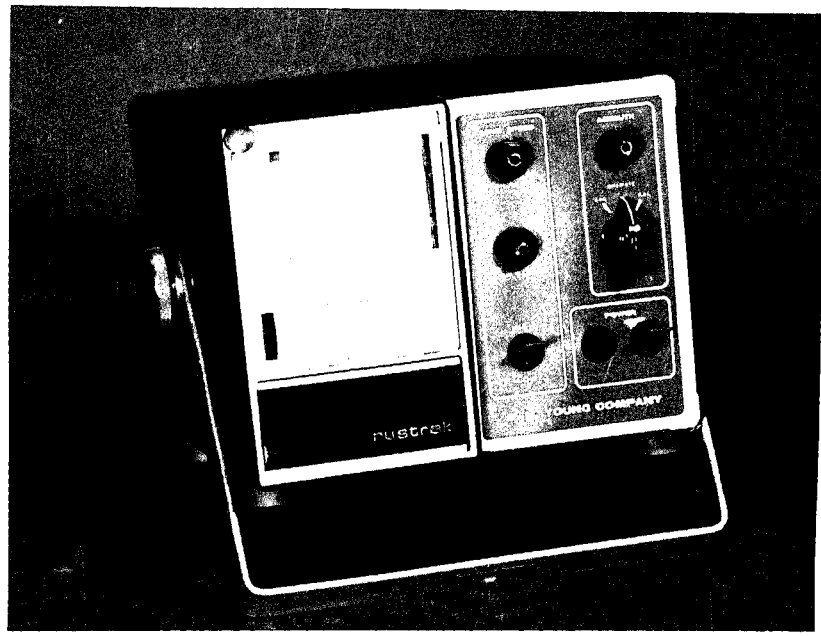


Fig. 1-18 Van Dyne / Cup anemometer chart recorder.

3. Nichrome Bridge Network: This network is used as a back-up to the above two instruments. A suitable bridge network employing nichrome wire as the sensor is used as a stand-by device for recording the fluctuations in the wind speed. This arrangement is considered necessary for meeting any emergency, like equipment failure in case of DISA hot-wire anemometer in field experiments at Kavalur. A soldering iron heating element of 35 or 65 W rating is also suitable as the sensor material. The sensing element forms one of the arms of a Wheatstone's net as shown in Fig. 3.19.

The principle of its working is that when the heated sensor experiences variations in wind speed, it undergoes changes in its degree of hotness. This change in its temperature causes a change in its resistance. This in turn leads to the variations in the voltage measured across the vertical diagonal of the bridge. Thus, these variations in voltage, as an output, will provide a measure of wind speed fluctuations.

The average signal strength of the wind speed during observations in an ordinary night without any signal amplification is about 30 mv. It has been observed that the tape recorder that is used for recording these fluctuations, itself gives small signal levels of about 50 mV, when unrecorded empty tape is run through it. Therefore the output from the bridge is preamplified so that the signals of the wind speed fluctuations do not get drowned in the recorder noise.

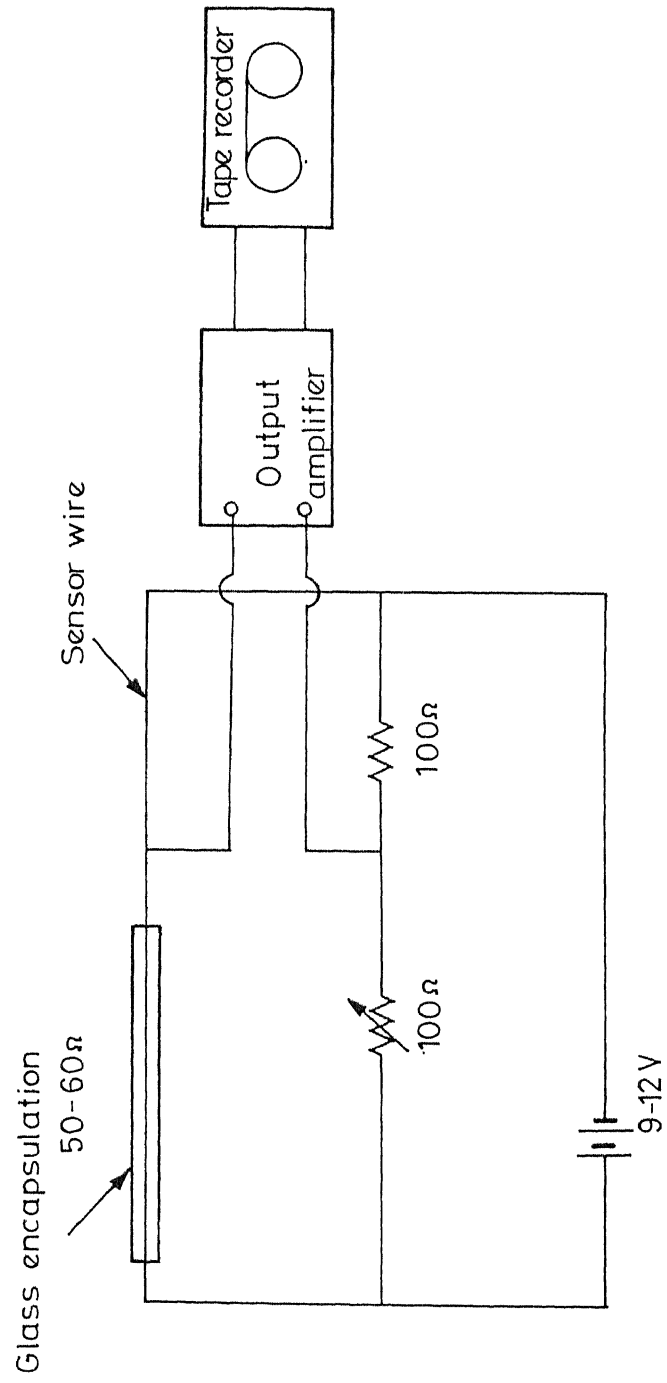


Fig. 3.19. Nichrome wire bridge network shown with amplifier and tape recorder.



Overall frequency response:

Tape Speed	Frequency range	Tolerance
$3\frac{3}{4}$ " / s ec	0Hz-1250Hz	30Hz-0dB $\pm$ 0.5dB
		625Hz-0.5dB $\pm$ 0.5dB
		1250Hz-2.5dB $\pm$ 0.5dB

Input level (for maximum frequency sweep)

0.1V-0.2V-0.5V-1V-2V or 5V  
(selection by calibrated attenuator switch)

Input Impedance: 10,000 Ohms

Output level : 1V peak across 10,000 Ohms

Output Impedance: 30 Ohms

Fig. 3.20 and 3.21 show EMI 4-channel and Philips 7-channel analog tape recorders used in this work.

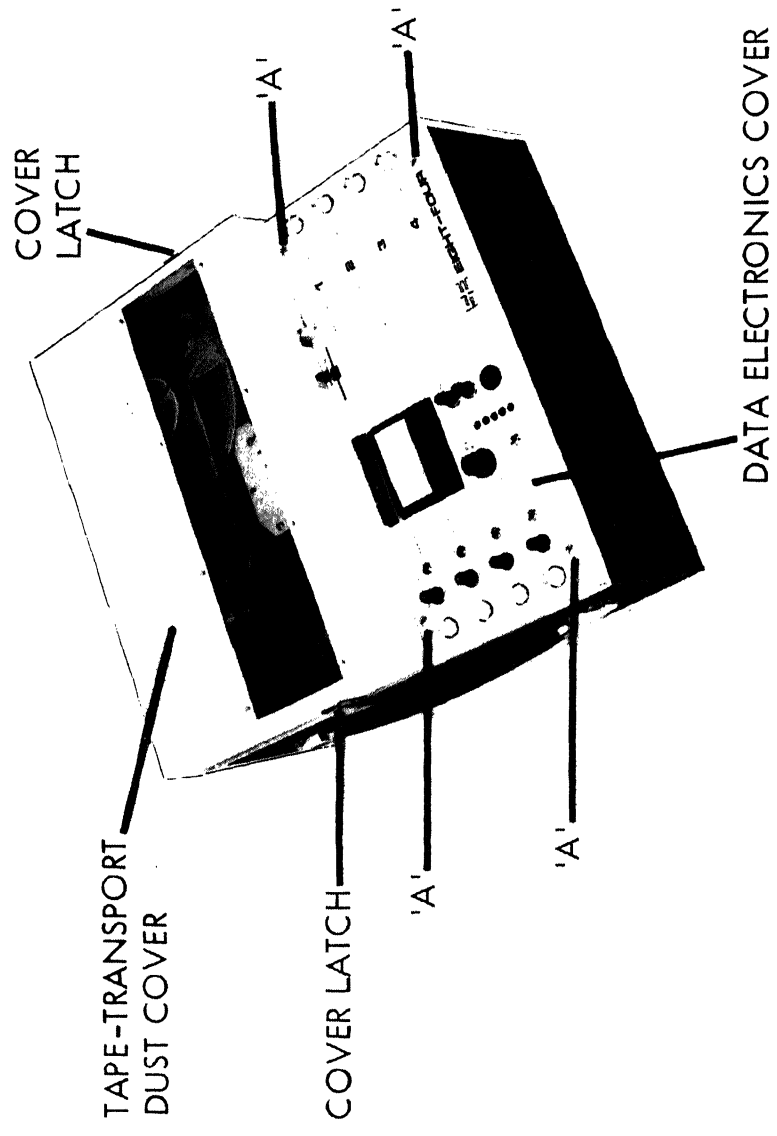


Fig. 3.20. General view of the EMI 4-cf analog tape recorder with cover.

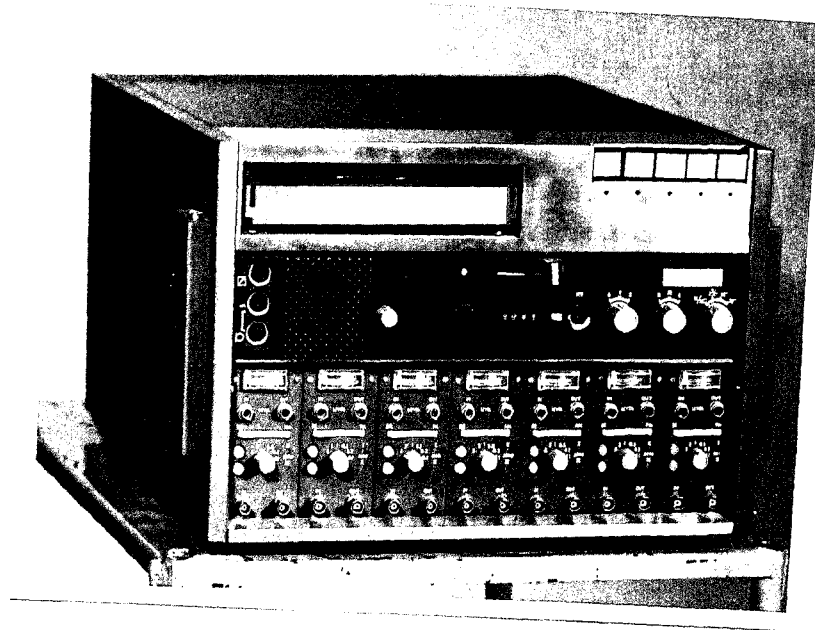


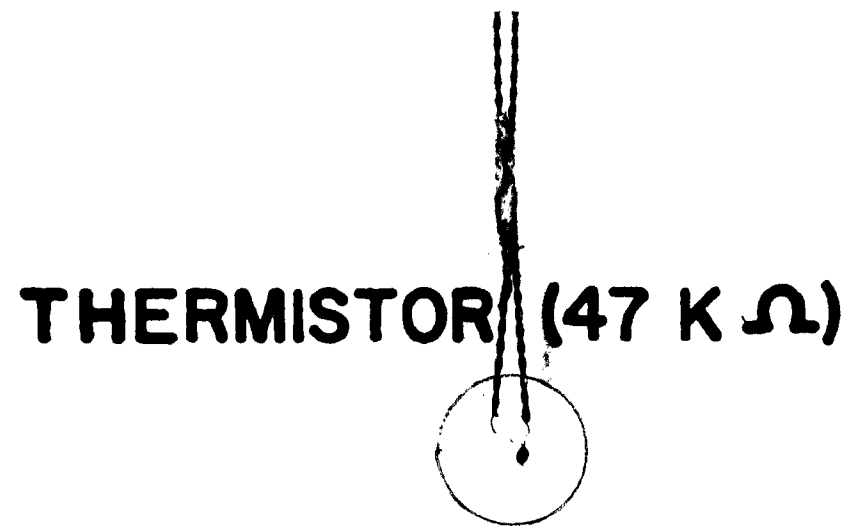
Fig. 3.21. Philips 7-channel analog tape recorder. Has controls for AM/FM recording, variable tape speed and gain settings.

### 3.5. Experimental set-up for recording atmospheric temperature

1. Wheatstone's net : This is used to record the fluctuations in the atmospheric temperature. The sensor element, one of the arms of the bridge, is the bead-in-glass type thermistor with its glass encapsulation removed. The sensor is as shown in Fig. 3.22. Here the sensor responds by changing its resistance mainly due to the variations in ambient temperature, unlike the nichrome wire which responds mainly to the wind speed variations on account of its being hot. The net work diagram is as shown in Fig. 3.23.

Whenever there is a variation in atmospheric temperature, the temperature of the thermistor also varies resulting in changes in its resistance. These changes in resistance will finally reflect as voltage fluctuations across the vertical diagonal of the bridge. If these voltage fluctuations are taken as output information and recorded, they will provide a measure of temperature variation with time. These signals are recorded in one of the FM channels of a tape recorder.

The bridge is excited by a stabilized 5V D. C. supply. The bridge null is adjusted at  $0^{\circ}\text{C}$ . The bridge output is amplified by a suitable amplifier that gives null output for  $0^{\circ}\text{C}$ .



---

Fig. 3.22 Bead-in-glass type thermistor  
with glass encapsulation removed.

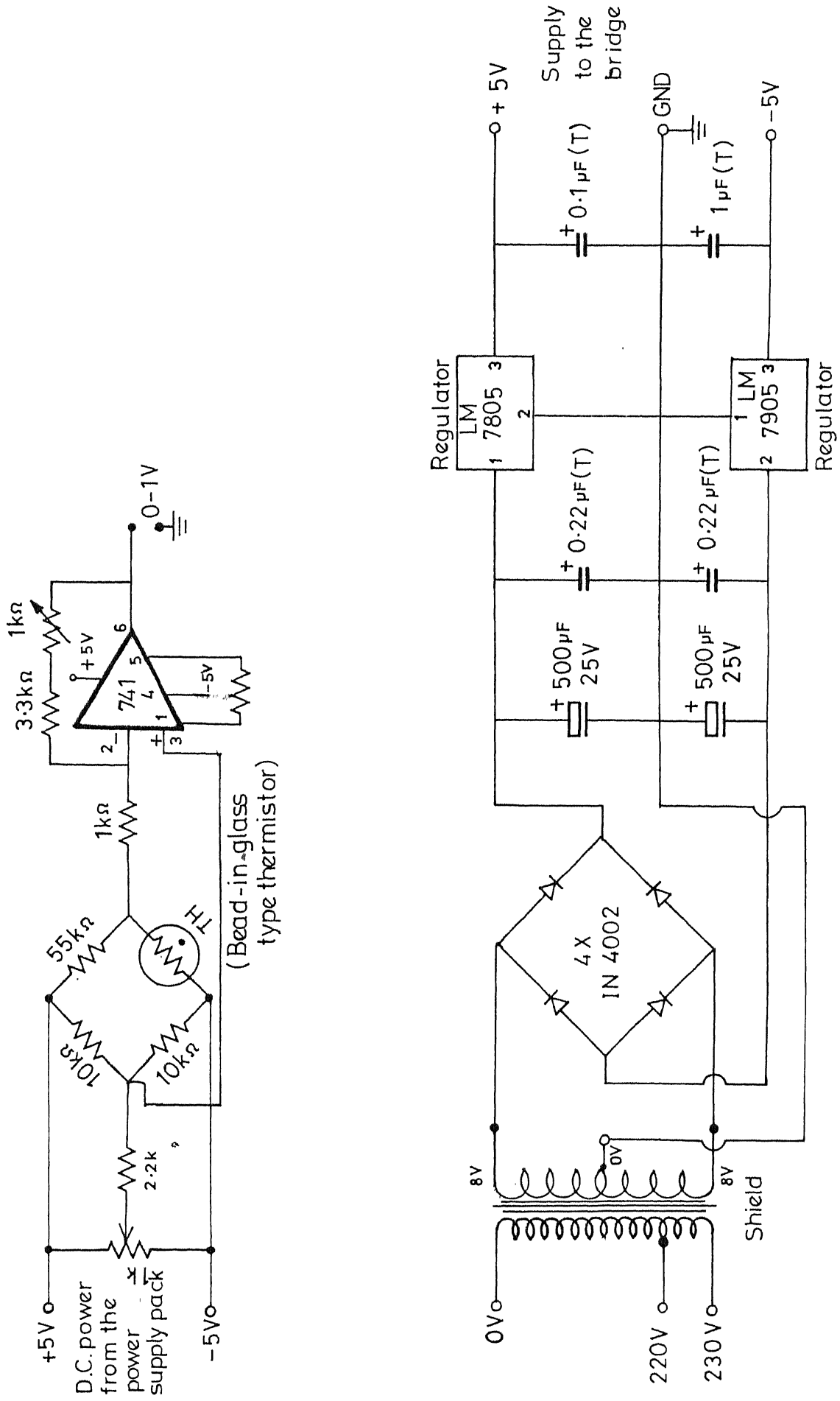


FIG-3.23. THERMISTOR BRIDGE AMPLIFIER.

The amplification is such that at  $30^{\circ}\text{C}$  the output is 300 mV. This is being done to obtain a fairly linear output in the temperature range of  $10^{\circ}$  to  $50^{\circ}\text{C}$ . The range is extended liberally on either side of the actual range of temperature encountered in the atmosphere. The electronic circuitry is powered by a supply circuit consisting of a step-down transformer, 4 diodes bridge, a capacitor input filter, a + 5V D.C. regulator, a - 5V D.C. regulator. The unit works on 230V, 50Hz, single phase A.C. Mains.

(i) Calibration: The thermistor is immersed in a bath of melting ice and the zero output of the unit is adjusted. Then the thermistor is immersed in a standard temperature bath at  $30^{\circ}\text{C}$  and the output is adjusted for 300 mV as indicated by a precise digital voltmeter. The calibration set-up is as shown in Fig. 3.24. The outputs for different temperatures between  $0^{\circ}$  and  $100^{\circ}\text{C}$  are taken and the calibration done. Calibration is checked every time before a set of readings is taken. Table 3.3 shows the values of output voltage for different temperatures. Fig. 3.25 shows the variation of the output with temperature.

(ii) Limitations: (a) Thermistors are not very sensitive to minute variations in atmospheric temperature.

(b) Frequency response of such thermistors is not satisfactory.

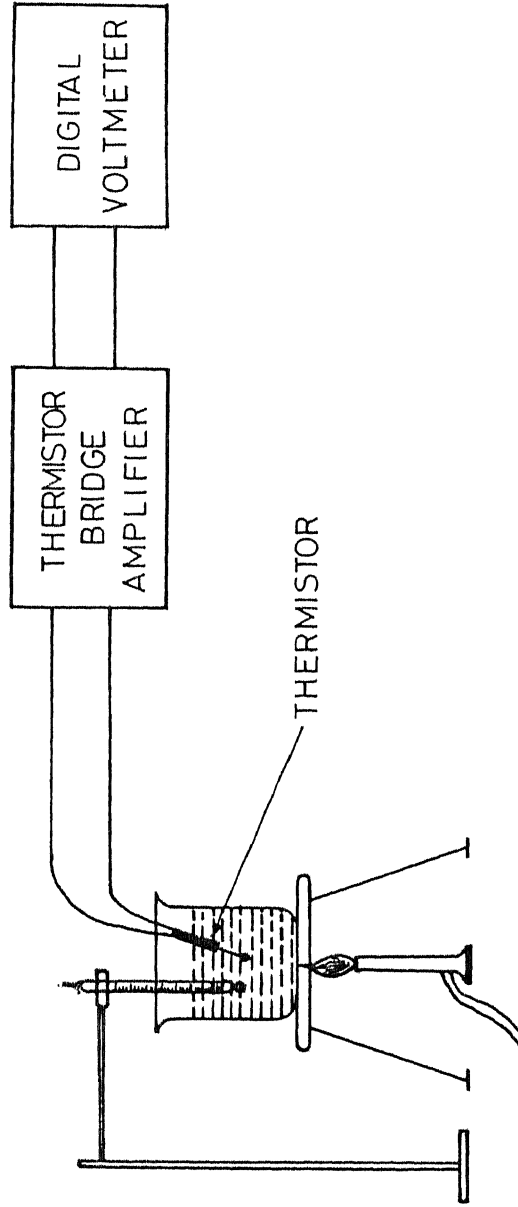


Fig. 3.24. Calibration set-up for thermistor.



TABLE 3.3

Table showing the variation of Thermistor bridge amplifier output ( in mV ) with change in Temperature

Temperature ( In degrees Celsius )	Thermistor bridge amplifier output ( in mV )
8.0	23
11.0	50
16.0	102
18.5	130
22.0	190
24.0	220
30.0	300
35.0	380
40.0	480
45.0	610
50.0	760

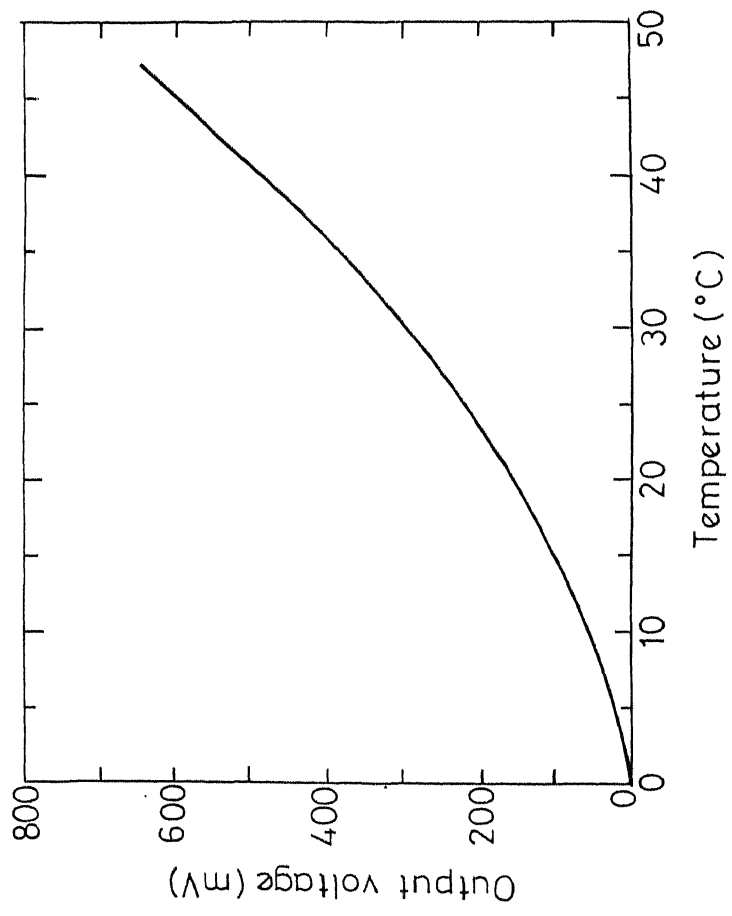


Fig.3.25. Plot of variation of analog output from thermistor bridge amplifier (mV) with temperature (°C).

2. Chromel-Alumel Thermocouple: Since thermistors are not very sensitive to small fluctuations in temperature, a thermocouple using Chromel and Alumel elements, is used for recording minute fluctuations. The bead of chromel-alumel material is made as tiny as possible for better frequency response and greater sensitivity. Since the output from the thermocouple is of about  $40 \mu\text{V}$ , that is to be amplified before recording. This device is specially used for recording low-frequency components in the temperature variations.

The electronics designed for amplifying the thermocouple output consists of a 2-stage preamplifier, since amplification from a single stage is found to be inadequate. Two low input-noise voltage operational amplifiers (LM725) are used in cascade<sup>39,40</sup>. The first stage of the preamplifier provides a voltage gain of 100 and the second stage provides a gain of 20. The incoming signals are passed through a low pass filter<sup>(741)</sup> with a cut-off frequency of 40Hz. This eliminates high frequency noise components and allows to record the low-frequency components of the atmospheric temperature variations alone. The final output is fed to one of the FM channels of the tape recorder. Figs.3.26 and 3.27 show the thermocouple probe and the tiny chromel-alumel bead. Fig.3.28 shows the electronic circuitry employed. In the present study, temperature data has been obtained using both the devices.

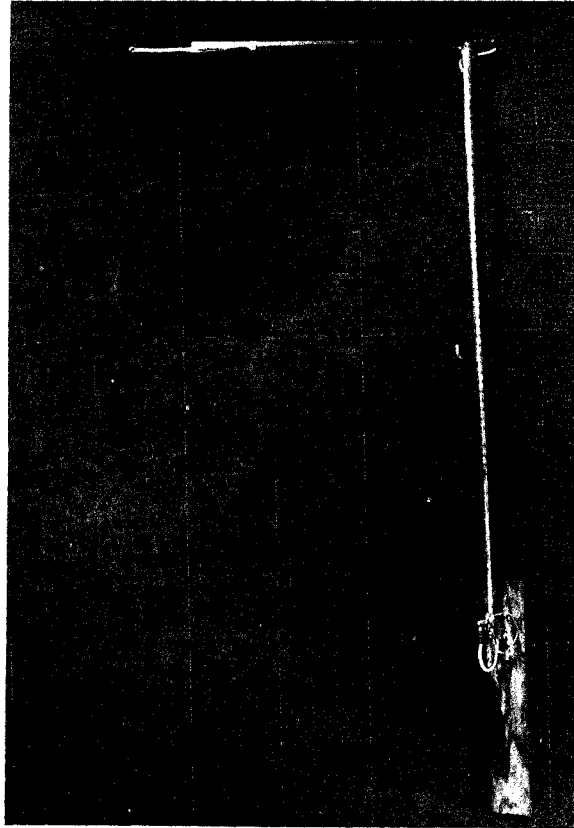


Fig. 3.26. Close-up view of a Cr-Al thermocouple mounted on a probe and supported by a long rod.



Fig. 3.27 Close-up view of the Cr-Al thermocouple. (Temperature sensor)  
Material: Chromel-Alumel in bead form; bead size: 50 microns in dia.

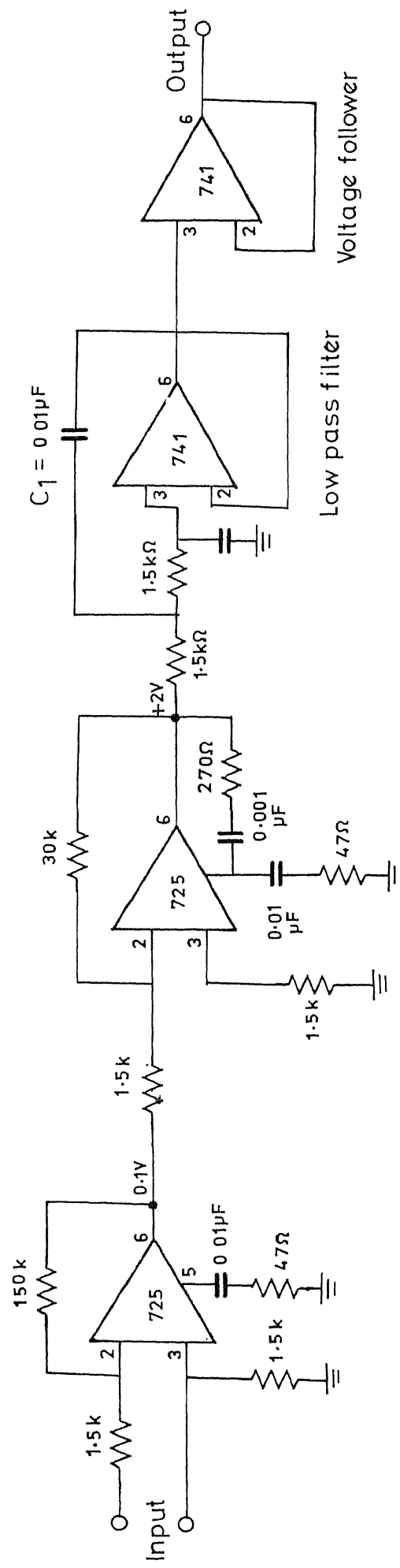


Fig. 3.28. Electronic circuit employed for amplifying the thermocouple output.

### 3.6. Details of observations

With the above set of instruments, simultaneous records have been obtained of the fluctuating parameters. The following table furnishes details of some observations carried out on different nights, the instrument at focus, diaphragms used, filters chosen and the photo-multiplier tubes employed. Details of the stars chosen for observations also are given. Sky and weather conditions existing during each night have been recorded. Details regarding the tape recorder channel numbers in which different parameter information was recorded, were carefully noted for subsequent retrieval of data in a systematic fashion.

TABLE 3.5

DETAILS OF SOME OBSERVATIONS

Sl. No.	Date and time in UT & star	R. A.	Dec.	Mag.	Filter	Diaph- ragm	Instrument at focus & Gen. remarks
1.	22.12.1977 18 00 00 to 18 02 30 <u>64 Cancri</u>	8 58 00	+32 30 00	5.64	Yellow	1 mm	EMI 9558B PMT. Cloud and Mist
2.	22.12.1977 18 05 37 to 18 08 07	8 58 00	+32 30 00	5.64	Blue	1 mm	EMI 9558B PMT Cloud and Mist
3.	22.12.1977 18 40 48 to 18 43 18 <u>51 Gemini</u>	7 12 07	+16 11 30	5.31	Yellow	1 mm	EMI 9558B PMT Cloud and Mist
4.	22.12.1977 18 44 10 to 18 46 40	7 12 07	+16 11 30	5.31	Blue	1 mm	EMI 9558B PMT Cloud and Mist
5.	22.12.1977 18 56 34 to 18 59 04 <u>60 Orionis</u>	5 57 43	+0 32 55	5.25	Yellow	1mm	EMI 9558B PMT Cloud and Mist



Sl. No.	Date and time in UT & star	R. A.	Dec.	Mag.	Filter	Diaphragm	Instrument at focus & Gen. remarks
6.	18 53 33 to 18 56 03	5 57 43	+ 0 32 55	5.25	Blue	1mm	EMI 9558B PMT Cloud and Mist
	<u>60 Orionis</u>						
7.	22.12.1977 19 09 13 to 19 11 43	* 3 39 27	+25 15 00	6.15	Yellow	1 mm	EMI 9558B PMT Cloud and Mist
	<u>11 Tau</u>						
8.	22.12.1977 19 13 19 to 19 15 58	:3 39 27	+25 15 00	6.15	Blue	1 mm	EMI 9558B PMT Cloud and Mist
9.	13.01.1978 16 23 00 to 16 25 30	23 28 18	-01 54 45	6.6	Yellow	1 mm	EMI 9558B PMT Transparency & seeing favourable
	<u>SAO 14 67 33</u>						
10.	20.01.1978 18 11 50 to 18 14 20	5 22 15	+18 34 43	7.5	Yellow	1 mm	EMI 9558B PMT Transparency & seeing favourable
	<u>SAO 094510</u>						

Sl. No.	Date and time in UT & star	R. A.	Dec.	Mag.	Filter	Diaph-gram	Instrument at focus & Gen. remarks
11.	21.01.1978 13 05 44 to 13 08 14 <u>SAO 095263</u>	6 06 42	+18 24 08	7.7	Yellow	1 mm	EMI 9558B PMT Good sky conditions
12.	21.01.1978 17 56 35.5 to 17 59 05.5 <u>SAO 095397</u>	6 12 17	+18 41 04	6.2	Yellow	1 mm	EMI 9558B PMT Good sky conditions
13.	21.01.1978 19 24 55.2 to 19 27 25.2 <u>SAO 095456</u>	6 14 25	+18 18 09	6.8	Yellow	1 mm	EMI 9558B PMT Good sky conditions
14.	21.01.1978 20 22 03.4 to 20 24 33.4 <u>SAO 095484</u>	6 15 51	+18 23 04	8.1	Yellow	1 mm	EMI 9558B PMT Good sky conditions
15.	22.01.1978 16 04 51.6 to 16 07 21.6 <u>SAO 096407</u>	7 01 10	+17 47 04	6.2	Yellow	1 mm	EMI 9558B PMT Good sky conditions

Sl. No.	Date and time in UT & star	R. A.	Dec.	Mag.	Filter	Diaph- ragm	Instrument at focus & Gen. remarks
16.	22.01.1978	7 02 58.6	+17 45 36	9.0	Yellow	1 mm	EMI 9558B PMT
	17 39 08.2 to 17 41 38.2						Good sky conditions
	<u>SAO 096440</u>						
17.	22.01.1978	7 05 02.6	+17 46 31	7.1	Yellow	1 mm	EMI 9558B PMT
	19 42 52.8 to 19 45 22.8						Good sky conditions
	<u>SAO 096487</u>						
18.	21.01.1978	7 07 23.4	+17 23 12	8.5	Yellow	1 mm	EMI 9558B PMT
	21 12 52.8 to 21 15 22.8						Good sky conditions
	<u>SAO 096541</u>						
19.	21.02.1978	9 16 41.8	+11 35 23	6.3	Yellow	1 mm	EMI 9558B PMT
	18 10 37 to 18 13 07						Good sky conditions
	<u>SAO 098476</u>						
20.	27.02.1978	14 23 31.2	-11 34 17	6.5	Yellow	1 mm	EMI 9558B PMT
	21 13 21.6 to 21.15 51.6						Good sky conditions

Sl. No.	Date and time in UT & star	R. A.	Dec.	Mag.	Filter	Diaphragm	Instrument at focus & Gen. remarks
21.	28.02.1978 22 21 45.6 to 22 24 15.6 <u>SAO 159199</u>	15 20 36.5	-15 04 57	8.6	Yellow	1 mm	EMI 9558B PMT Good sky conditions
22.	16.01.1979 20 08 30 to 20 11 00 <u>SAO 118286</u>	10 24 29.8	+ 0 53 22	5.9	Yellow	1 mm	EMI 9558B PMT
23.	16.01.1979 20 17 12 to 20 19 42 <u>SAO 118292</u>	10 24 29.8	+8 52 52	7.7	Yellow	1 mm	EMI 9558B PMT Sky condition not fair
24.	22.12.1980 16 32 00 to 16 41 50 <u>56 Erdiani</u>	4 43 00	-8 32 00	5.87	Yellow	1 mm	EMI 9558B PMT Sky conditions good along with temperature
25.	13.03.1981 IST- 5 A.M. <u>Y -Sagittarii</u>	18 04 34	-30 25 24		Yellow	25 micron	EMI9558B PMT Good sky
			LST at 1300 Hrs IST: 5Hr 39Min 37Sec				Seeing Vs Temperature

Sl. No.	Date and time in UT & star	R. A.	Dec.	Mag.	Filter	Diaph-gram	Instrument at focus & Gen. remarks
26.	13.03.1981 $\gamma$ -Sagittarii around 5 AM	18 04 34	-30 25 24 Scintillation	Yellow	1 mm	EMI 9558B PMT Good Sky	
27.	28.03.1981 Experiments around 11 PM for 5 minutes	7 17 00	+16 34 00 Scintillations (LST at 1300 Hr IST: 6Hr 35 m. 46 sec.)	3.65 Yellow	1 mm	IP21 Good sky	
<u><math>\lambda</math>-Geminorum</u>							
28.	28.03.1981 for 5 minutes	7 17 00	+16 34 00 Scintillations	3.65 Yellow	1 mm	IP21 Good sky	
<u><math>\lambda</math>-Geminorum</u>							
29.	28.03.1981 for 5 minutes	7 17 00	+16 34 00 seeing Vs. Wind Speed	3.65 Yellow	25 mic-ron	IP21 Good sky	
<u><math>\lambda</math>-Geminorum</u>							
30.	28.03.1981	7 17 00	+16 34 00 Seeing Vs. Temperature	3.65 Yellow	25 mic-ron	IP21 Good sky	
31.	28.03.1981 for 10 minutes	-	- Wind Speed Vs. Temperature	-	-	-	

### 3.7. Diaphragms

While recording stellar intensity fluctuations, two diaphragms of different diameters were used separately for obtaining data exclusively on scintillation and seeing. While a fairly large diaphragm, 9 secs of arc or 1 mm in diameter, has been used to record stellar intensity fluctuations (scintillation), a tiny diaphragm, 25 microns in diameter equivalent 0.4 sec of arc has been employed for recording the bloating up and shrinking down ( a manifestation of seeing ) of the star image. Stars of fairly good magnitude at different zenith distances are chosen for recording these stellar image intensity fluctuations. This data is used for subsequent analysis to account for the effects of the depth of the atmosphere the light wave would propagate in reaching the telescope. Observations have been carried out at the observatory during different nights and for each night the data is collected at different hours.

The amount of variation in light intensity with bloating up and shrinking down of the stellar image can be likened to a similar effect of variation of illumination produced on a screen when it is moved towards and away from a source of light. Here the inverse square law  $E = \frac{1}{d^2}$ , which indicates the pattern of illumination ( E ) drop with increase in separation ( d ) between the screen and the source, is quite evident. Therefore, in the present case of seeing monitoring

the variations in intensity during seeing fluctuations may be assessed by simulating similar variations of intensity of light using a screen and a source of light and by varying the distance of separation between them.

### 3.8. Digitization

All the above data have been obtained as mentioned earlier using different instruments and storing the data so acquired on analog tapes. This data requires to be digitized for processing by using large digital computers with high memories. Data obtained in the observatory at Kavalur, and stored in analog tapes are digitized at the school of Automation in Indian Institute of Science, Bangalore using the hybrid computer facility. The hybrid computer section in the School of Automation is shown in Fig. 3.29. The digitized data are stored in 9-track computer compatible magnetic tapes. These tapes are used as input media subsequently with DEC-1090 computer system for processing the data. The large memory (256 K) of this system is needed for processing data on astronomical seeing & atmospheric turbulence, which are very large even when the analog data is digitized at sampling frequencies of 500 Hz and 1 KHz. Data from Kavalur has been digitized at 500 Hz and 1 KHz with due regard to the implications of the Nyquist's criterion<sup>41</sup> and the fluctuating phenomena under investigation.



Fig. 3.29. Hybrid computer laboratory at Indian Institute of Science where analog data of Astronomical Seeing and Atmospheric Turbulence collected at Kavalar Observatory, was digitized.



To be sure of what has been digitized conforms to what is to be digitized, the following step is followed. First, the display of analog data from EMI or philips tapes is seen for over a particular length of the tape. This portion is digitized and stored on a 9-track magnetic tape. The 9-track magnetic tape is now used to give the stored data for display on a CRO screen after the same has gone through D-to-A conversion. If this display is comparable to the one seen earlier within the tolerance limits of the sampling frequency chosen, then it can be said that digitization has been done fairly well. Digitized data is stored on 9-track magnetic tapes in 16-bit format by this computer. For purposes of record, a paper print-out of the digitized data from the hybrid computer is taken of a few sample files.

Since DEC-1090 computer system handles information in 36-bit format, the format of the hybrid computer in 9-track tapes has to be changed suitably. This is achieved by using a standard subroutine " SWAP " in the system software of DEC-1090. After the format change, a print-out of the same sample files chosen earlier with the hybrid computer is taken from DEC-1090 also. Both of them are compared and found to tally with each other perfectly. Figs 3.30 and 3.31 show these print-outs from the two computers for a couple of files. Thus it is verified that no stage of digitization and/or format conversion, the original data collected at Kavalur undergoes

DIGITAL OUTPUT OF KVL R NO.3/12/1,2,3,4 : AS OBTAINED FROM DEC-10

-133	-259	512	-730	-100	-118	510	-728	134	-128
509	-727	-91	-103	508	-732	490	-168	504	-725
-5	-149	508	-728	-11	-129	511	-721	259	-155

STOP DIGITAL OUTPUT OF KVL R NO.5/12/1,2,3,4 + AS OBTAINED FROM HYBRID COMPUTER,  
S.A., I.I.Sc.,

-133	-259	512	-730	-100	-118	510	-728	134
-128	509	-727	-91	-103	508	-722	490	-168
504	-725	-5	-149	508	-728	-11	-129	511
-721	259	-155	508	-728	110	-281	509	-725
81	-281	506	-729	-92	-274	515	-726	129
-260	511	-726	210	-282	514	-724	129	-144
510	-720	284	-119	513	-720	11	-1	514

Fig. 3.30. Print-outs from the two computers of digitized data from a sample file.

DIGITAL OUTPUT OF KVLK NO.3/9/1,2,3,4 : AS OBTAINED FROM DEC-10

147	786	512	-777	-429	621	508	-710	-90	805
512	-785	18	871	502	-713	-9	727	511	-681
<del>-239</del>	<del>622</del>	<del>511</del>	<del>-679</del>	<del>-376</del>	<del>898</del>	<del>511</del>	<del>-718</del>	<del>133</del>	<del>632</del>

DIGITAL OUTPUT OF KVLK NO.3/9/1,2,3,4 : AS OBTAINED FROM HYBRID COMPUTER, S.A., I.I.Sc.,

147	786	512	-777	-429	621	508	-710		
805	512	-785	18	871	502	-713	-9		
511	-681	-239	622	511	-679	-376	898	511	
-718	133	632	509	-711	-47	613	513	-705	
360	762	507	-762	580	883	512	-706	407	

Fig. 3.31. Print-outs from the two computers of digitized data from another sample file.

any distortion.

This method of digitization has saved considerable amount of time and labour in inputting the data to digital computers. The storage medium in magnetic tapes is quite compact and elegant, allowing processing of data with computers located in different places.

The details of the peripherals of the hybrid computer system are shown Fig. 3.32. This hybrid computer 511 at the School of Automation in Indian Institute of Science, consists of PDP-11/35 digital computer. It has 96 KW of memory, a magnetic tape drive, (800 bpi), two RK05 disc drives, one 10MB disc drive, one line printer, a card reader, a DEC-writer VT-11 graphic subsystem and an analog computer (AD 5). The analog computer has 16 channels, 15 bit ADC and 8 DAC. The system is capable of digitizing analog data upto a maximum sampling rate of 10 Khz.

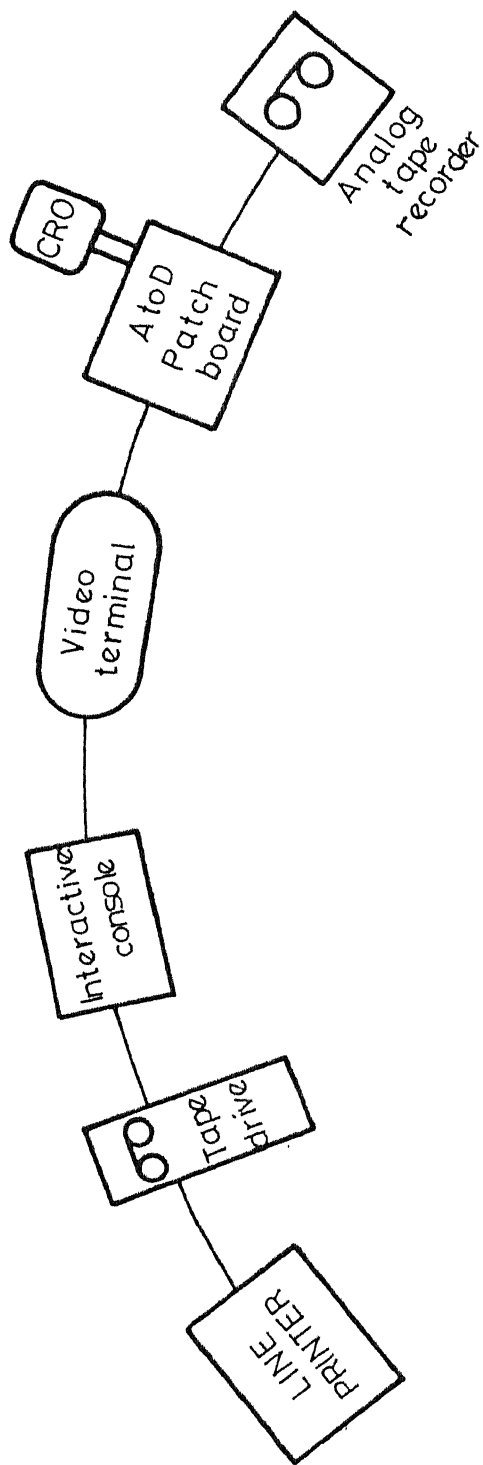


FIG-3.32. BLOCK DIAGRAM SHOWING THE PERIPHERALS OF THE HYBRID COMPUTER USED FOR DIGITISING THE ANALOG DATA COLLECTED AT KAVALLUR.

C H A P T E R IV

POWER SPECTRUM ANALYSIS OF SEEING DATA

4.1. Introduction

The temporal fluctuations of astronomical seeing and atmospheric turbulence form a random time series and can be subjected to mathematical analysis for obtaining vital information regarding the physics underlying the phenomena. The relevant statistical properties of such time series are normally contained by their autocovariance function and the power spectrum. These are the most useful interesting and important properties. The only requirement in their practical computation is the extensiveness of the data required for highly precise estimates. This requirement is an inherent characteristic of such random phenomena.

4.2. Mathematical method<sup>42</sup>

We shall assume that the random process is Gaussian. This means that the joint probability distribution of the values at successive instants of time  $t_1, t_2, t_3, \dots, t_n$ , namely  $X(t_1), X(t_2), X(t_3), \dots, X(t_n)$  is n-dimensional normal distribution. This distribution is completely determined by the average

$$\bar{X}(t_i) = \text{ave} \{ X(t_i) \},$$

and by the covariance

$$\begin{aligned} C_{ij} &= \text{Cov} \{ X(t_i), X(t_j) \} \\ &= \text{ave} \left\{ [X(t_i) - \bar{X}(t_i)][X(t_j) - \bar{X}(t_j)] \right\} \end{aligned}$$

The autocovariance function with lag  $\tau$  is given by

$$C(\tau) = \lim_{T \rightarrow \infty} \frac{1}{T} \int_{-T/2}^{T/2} X(t) \cdot X(t+\tau) dt$$

This may be reduced to the form

$$C(\tau) = \int_{-\infty}^{\infty} P(f) \cdot e^{i2\pi f\tau} df$$

where

$$P(f) = \lim_{T \rightarrow \infty} \frac{1}{T} \left| \int_{-T/2}^{T/2} X(t) \cdot e^{-i2\pi ft} dt \right|^2$$

and where  $P(f)$  describes the power spectrum of the random process under consideration.

The relation exhibiting autocovariance function as the Fourier transform of the power spectrum may be inverted to express the power spectrum as the Fourier transform of the autocovariance function.

Thus we have

$$P(f) = \int_{-\infty}^{\infty} C(\tau) \cdot e^{-i2\pi f\tau} d\tau$$

If we consider the real part of the solution, the relation between  $P(f)$  and  $C(\tau)$  can more simply be expressed as

$$C(\tau) = \int_{-\infty}^{+\infty} P(f) \cos 2\pi f \tau df ,$$

and

$$P(f) = \int_{-\infty}^{+\infty} C(\tau) \cos 2\pi f \tau d\tau ;$$

or perhaps even more simply as one-sided cosine transform, viz.,

$$C(\tau) = 2 \int_0^{\infty} P(f) \cos 2\pi f \tau df$$

and

$$P(f) = 2 \int_0^{\infty} C(\tau) \cos 2\pi f \tau d\tau$$

The theoretical study of sampling variability is much simpler in the case of the estimates of the power spectrum than in the case of the estimates of the autocovariance function.

If  $X_t$ ,  $t = 0, 1, 2, \dots, n$  are the given observations which are treated as equispaced, prewhitening of these is done by

$$\bar{X}_{t+1} = X_{t+1} - 0.6 X_t \quad (\equiv \quad \bar{X}_t = X_t - 0.6 X_{t-1})$$

This generally improves the spectrum estimate because the prewhitened spectra will be flatter and therefore less influenced by the finiteness of the number of data points.



The constant 0.6 is chosen because it works normally well over a wide range of circumstances.

This operation multiplies  $P(f)$  by

$$1.36 - 1.20 \cos 2\pi f$$

a factor increasing from 0.16 to 2.56.

We calculate the mean lagged products as following:

$$C_r = \frac{1}{n-r} \sum_{t=1}^{n-r} \bar{X}_t \bar{X}_{t+r} - \left( \frac{1}{n} \sum_{t=1}^n \bar{X}_t \right)^2,$$

upto a carefully chosen value of  $r$ . " $r$ " is the percentage of lags, generally kept at 5 or 10% of the total number of data points  $N$ .

Here  $(1/n-r)$  is chosen to keep  $C_r$  bias free and occasionally this results in ambiguous values.

The above is calculated with an adjustment for the mean. Further adjustment for any trend may be necessary. Next, we calculate the finite cosine series transform upto ' $m$ '. The choice of ' $m$ ' depends upon the frequency separation between the adjacent estimates of the power spectrum and is therefore guided by the amount of separation considered acceptable. ' $m$ ' should not normally exceed 5 to 10% of  $N$ . We now calculate the finite cosine series transform of  $C_r$ 's above,

$$V_r = [C_0 + 2 \sum_{q=1}^{m-1} C_q \cos (qr\pi/m) + C_m \cos(r\pi)]$$

Now to these values certain carefully chosen windows are applied for minimising the effects of having a finite amount of data. Hanning is just a simple, but very useful window. Fig. 4.1 shows the behaviour of this window. This is used in order to make the main lobe in the spectral curves prominent and to reduce the side lobes<sup>43</sup>. This window is represented by

$$D(\tau) = \begin{cases} (1/2)(1 + \cos \pi \tau/T_m) & \text{for } |\tau| < T_m \\ 0 & \text{for } |\tau| > T_m \end{cases}$$

Where  $T_m$  is the maximum lag which we desire to keep.

The corresponding spectral window is also indicated in the figure.

As a result of Hanning, we obtain estimates of the power spectral density as

$$U_0 = (1/2)(V_0^* + V_1)$$

$$U_r = (1/4) V_{r-1} + (1/2) V_r + (1/4) V_{r+1},$$

$$1 \leq r \leq m-1,$$

$$U_m = (1/2)V_{m-1} + (1/2)V_m.$$

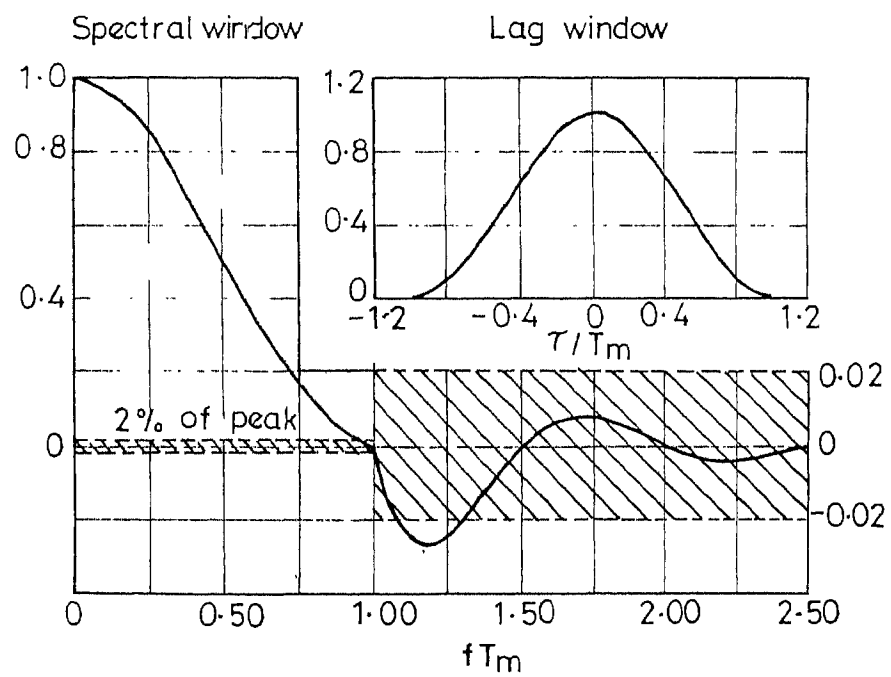


Fig. 4.1. Lag window (Hanning) and its corresponding spectral window.

These can be corrected for the prewhitening and the mean by forming

$$\left[ \frac{n}{n-m} \frac{1}{1.36 - 1.20 \cos 2\pi/6m} \right] U_0,$$

$$\left[ \frac{1}{1.36 - 1.20 \cos 2r\pi/m} \right] U_r, \quad 1 \leq r \leq m-1,$$

$$\left[ \frac{1}{1.36 - 1.20 \cos(1 - 1/6m)2\pi} \right] U_m.$$

These will now be the smoothed estimates of the " power spectral density " ,  $P(f)$  . Estimates with subscript  $r$  apply to a frequency near  $r/2m$  cycles per observation.

#### 4.3. Pilot analysis for choice of $\Delta t$ (sampling frequency and $m$ ( percentage lag )

Scintillation data from 60-Orionis and 51-Geminorum collected on 22.12.1977 is subjected to mathematical analysis. A sample of the recording in respect of these two stars is shown in Fig. 4.2. This data is obtained through a yellow filter. A scheme of computation as shown in table 4.1 is followed.  $N$ , the total number of points is varied first. For each set of  $N$ ,  $m$ , the percentage of lag is varied. Three different values of  $m$  are adopted. For these different  $N$ 's and  $m$ 's, power spectral densities have been calculated according to the above formulae. While the nature of the resulting power spectral density values has been the same throughout by showing a decrease with increasing

R.A.: 7hrs 12min 7sec  
Decl.: +16° 11' 30"

R.A.: 5hrs 57min 49sec  
Decl.: 0° 32' 55"

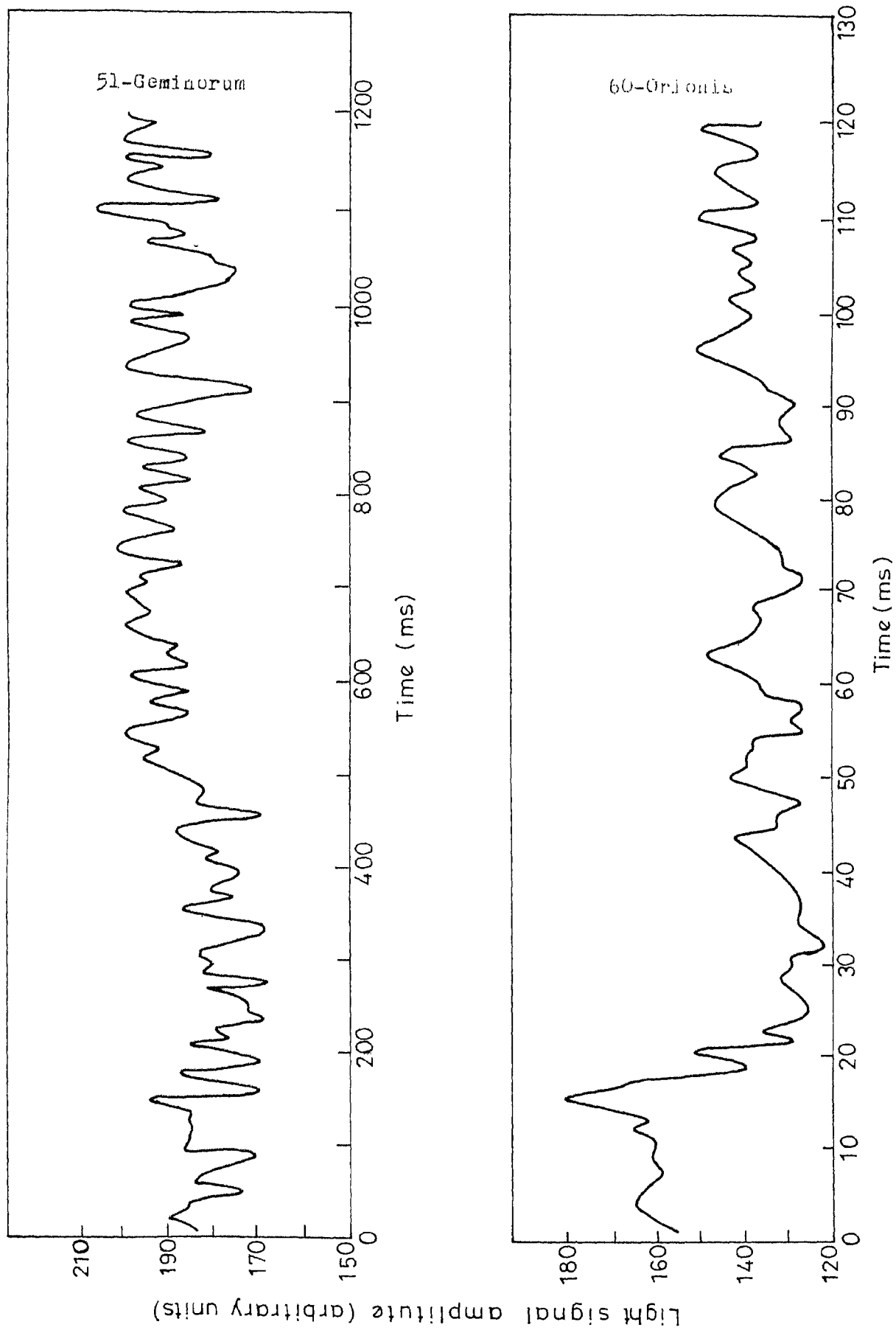


Fig. 4.2. Sample recordings of two stars.

TABLE - 4.1.

Case No.	Date	Star	N	t	T	m/N
1.	22/23.12.77	60-Orionis	2500	1ms	2.5 sec	(i) 250/2500 (ii) 500/2500 (iii) 750/2500
2.	22/23.12.77	60-Orionis	5000	1ms	5 sec	(i) 500/5000 (ii) 1000/5000 (iii) 1500/5000
3.	22/23.12.77	60-Orionis	10000	1ms	10 sec	2000/10000
4.	22/23.12.77	51-Gem	10000	10ms	100 sec	2000/10000
5.	22/23.12.77	51-Gem	10000	10ms	100 sec	500/10000

frequency, these power spectral densities are plotted for a particular combination as in case No. 3 in the table. This plot is as shown in Fig. 4.3.A. It is observed that most of the power is concentrated within relatively lower frequency region. A similar plot as in Fig. 4.3.B. is drawn for case No. 4 in the table. It is noticed even in this case that significant power lies within relatively low frequency region. This has led to the safe choice of 500 Hz and 1000 Hz for the sampling frequencies of analog data corresponding to 2 ms and 1 ms for interdata gap in time.

Incidentally the above plot in Fig. 4.3-B, shows ambiguous power spectra for certain frequencies. It may be noted that this is an artifact of the computational process and has been caused by the large value of  $m$ . With  $m$  as 5% of  $N$  ( case No. 5 in the table ) the same data is subjected to power spectral analysis and its  $\log P(f)$  is drawn against frequency. This plot is shown in Fig. 4.3.C. In this case there is no ambiguity in regard to the values of power spectral density. Hence, it has been maintained throughout in this study to keep  $N$  large and  $m$  at 5% only. It has been varied from case to case to study the fluctuations in seeing and scintillation as also atmospheric turbulence parameters in different frequency regions.

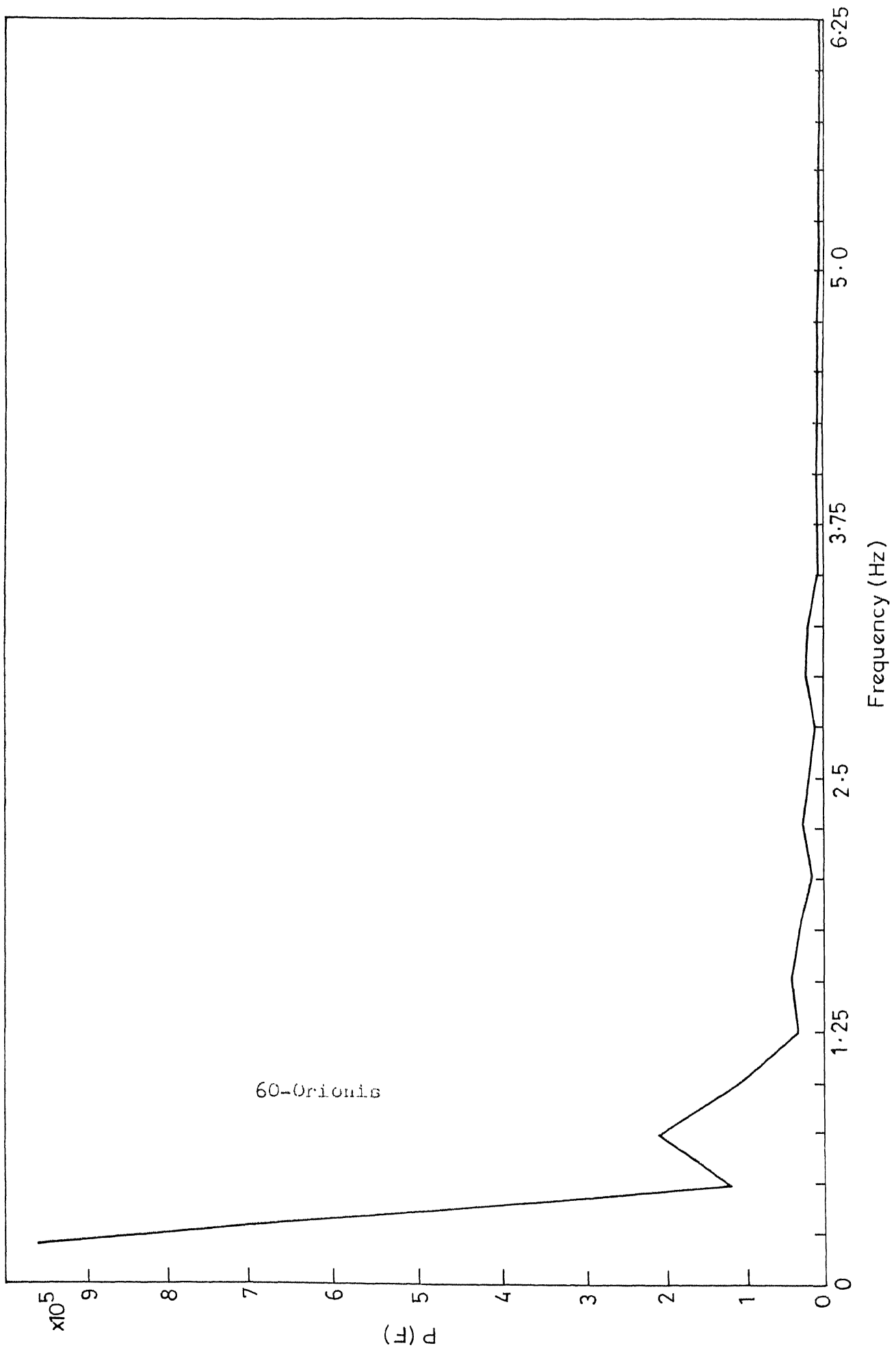


Fig. 4.3a. Power spectra of astronomical seeing at Kavalur. (Shorter data)



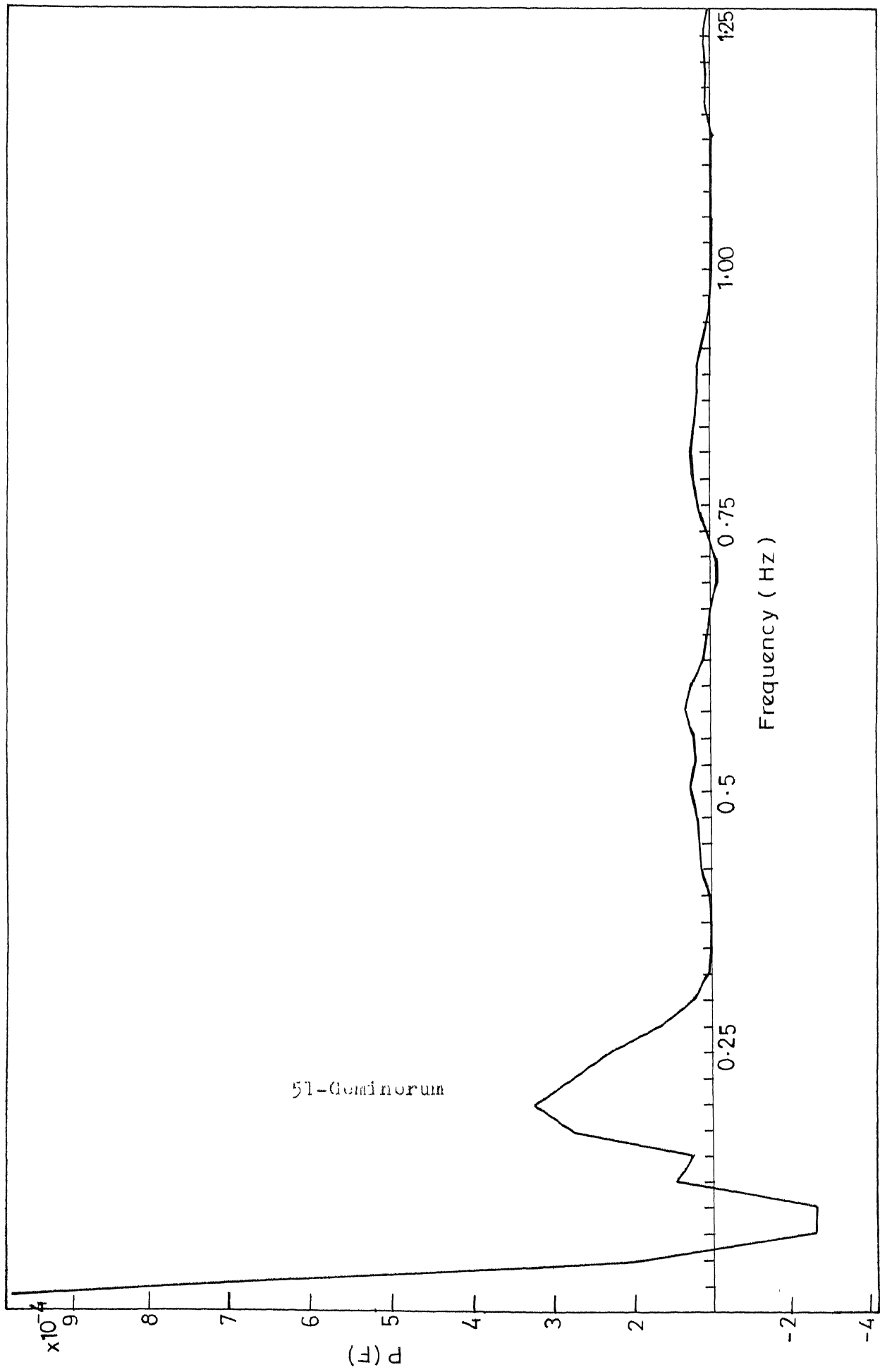


Fig. 4.3b. Power spectra of astronomical seeing at Kavalur. ( Longer data )

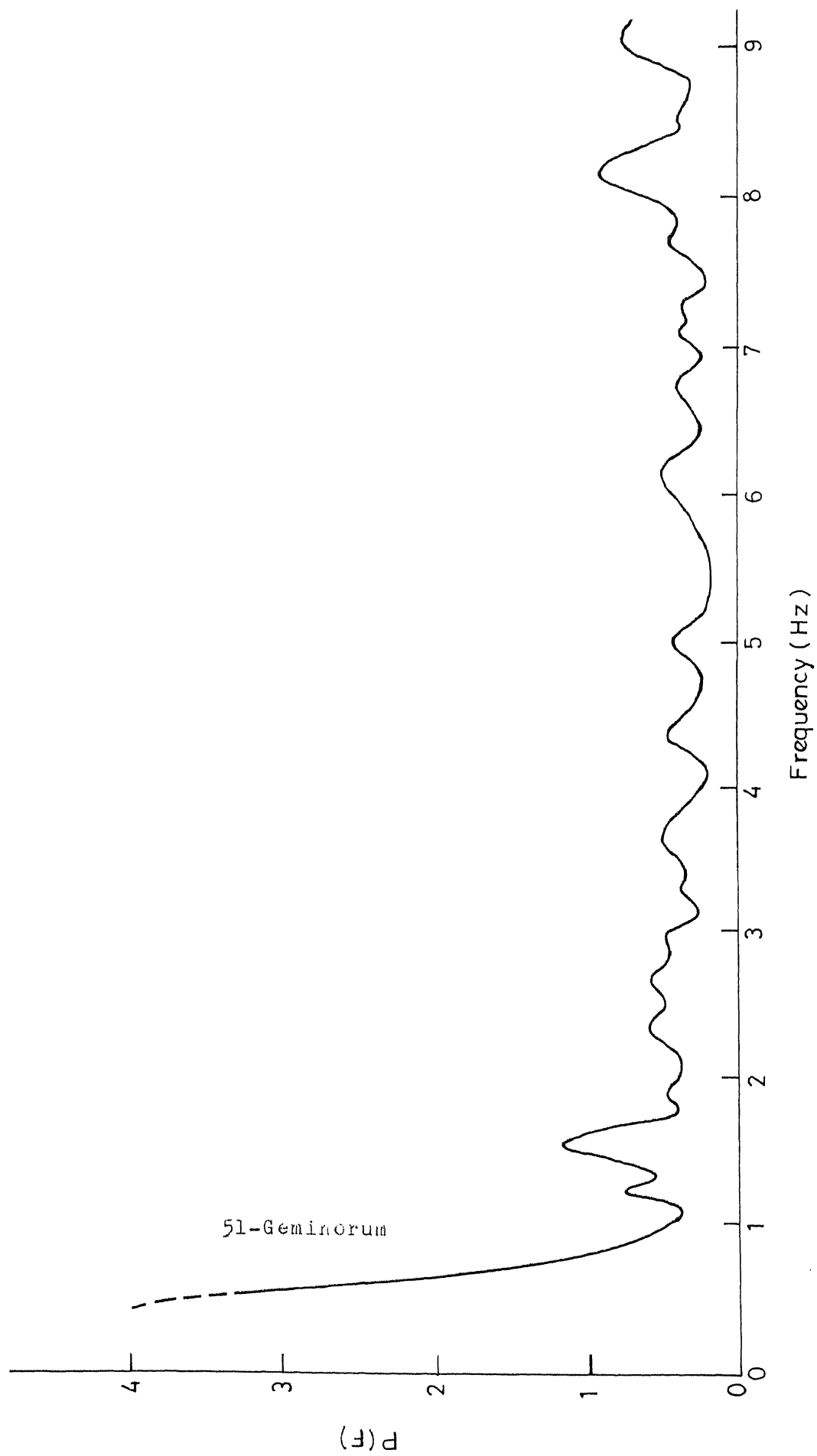


Fig. 4.3c. Power spectral density vs. Frequency plot pertaining to case No.5 of table 4.1.

#### 4.4. Observing conditions at Kavalur

While the above gives us a brief pilot survey of the seeing phenomenon at Kavalur on a quantitative basis, the following provides a more detailed and elaborate qualitative studies of the phenomenon. A summary of observing conditions at Kavalur observatory<sup>43</sup> states that nearly fifty percent of nights on which observations can be made have been better than 1.5 arc seconds. Among the southern locations in India from which access to southern skies is possible, it is seen that the south-eastern part of the peninsula is relatively cloud free. This is shown in Fig. 4.4. Even during monsoon months, 20 clear mornings which is about 25 percent of the time are available. During most of the year, more than 50% of the mornings are cloud free.

Best observing conditions are in the months of December to April when a higher percentage of the nights is also photometric. There is some correlation of seeing with humidity. Very good seeing is usually followed by a very low ground fog that fills in the valleys and ravines around Kavalur and seldom reaches the telescope that is located 20 meters above ground. Three component layers apparently contribute to seeing effects in the tropics. These are:

1. thermal effects in the immediate vicinity of the telescope,

The Astronomical seeing at Kavalur

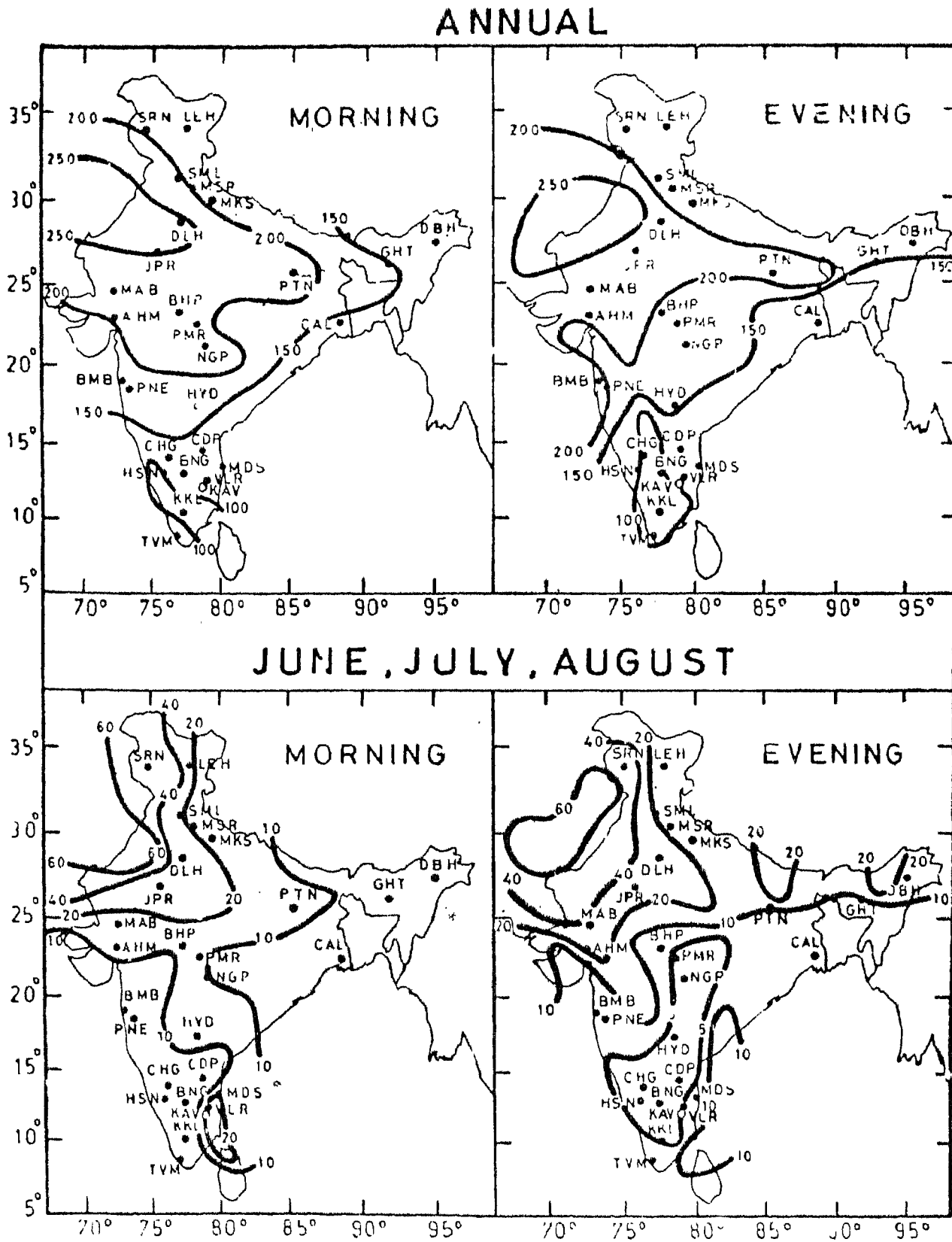


Fig.4.4. Number of days with cloud amount less than three octas.

2. a layer, two to three hundred metres high which is the principal contributor and orography dependent,
3. a high level contribution which is a part of the large-scale global circulation.

Observing conditions at Kavalur in terms of spectroscopic, photometric and clear nights ( in percentage ) are shown in Table 4.2.

Table 4.3 shows the percentage of observed nights with different values of seeing. Kavalur station is compared with other locations elsewhere in the world.

A sample plot of seeing evaluation during each night is shown in Fig. 4.5. Further a sample set of histograms of Kavalur seeing is presented in Fig. 4.6.

#### 4.5. Trend removal from raw data

With the background of the above pilot quantitative analysis and elaborate qualitative studies of seeing at Kavalur, it is expected that the following detailed power spectral analysis of seeing, scintillation and coherence analysis between these two individual phenomenon and atmospheric turbulence would provide more sound basis for a clearer and definite interpretation of the mechanisms causing the observed optical image distortions. The emphasis has been

TABLE 4.2 OBSERVING CONDITIONS AT KAVAJUR

	1973			1974			1975		
	Hrs. Of spec. sky	Hrs. of phot. sky	Clear nights 100%	Hrs.of spec. sky	Hrs. of phot. sky	Clear nights 100%	Hrs. of spec. sky	Hrs. of phot. sky	Clear nights 100%
Jan	232	162	23	298	255	30	207	108	18
Feb	228	167	22	220	168	22	208	121	17
Mar	270	234	26	223	173	26	275	210	24
Apr	136	52	12	240	77	22	270	188	24
May	122	70	12	123	41	10	103	30	7
Jun	37	10	1	25	6	5	41	8	3
Jul	43	4	0	23	8	1	19	4	1
Aug	59	27	3	65	13	5	23	0	3
Sep	45	15	4	46	10	3	48	0	1
Oct	54	14	4	97	57	7	39	0	1
Nov	162	89	12	170	107	16	108	23	10
Dec	133	52	11	207	125	20	138	62	10
Annual Total	1485	686	130	1787	1034	167	1479	754	119

TABLE 4.2 OBSERVING CONDITIONS AT KAVVALUR

(Contd.)

	1976			1977		
	Hrs. of spec. sky	Hrs. of phot sky	Clear nights 100%	Hrs. of spec. sky	Hrs. of phot sky	Clear nights 100%
Jan	138	108	18	288	138	26
Feb	231	178	23	185	98	12
Mar	270	244	25	214	125	19
Apr	171	94	14	164	42	12
May	137	61	6	99	22	4
Jun	82	25	3	43	6	2
Jul	11	0	0	57	0	2
Aug	24	0	0	29	5	1
Sep	81	18	2	67	6	1
Oct	104	59	7	95	45	8
Nov	56	15	1	65	5	2
Dec	141	65	9	209	29	15
Annual Total	1446	835	100	1515	521	104

Mean Values: Spectroscopic hours = 1542  
 Photometric hours = 806  
 Clear nights of nine hour observation = 124

The following table shows the percentage of observed nights with different values of seeing. Kavalur station is compared with other locations elsewhere in the world.

Location	Best Seeing Observed	Percentage of observed nights with average seeing as indicated				Total number of nights observed
		1.0"	1.1" to 1.5"	1.6" to 2.0"	2.0"	
Tololo, Chile	0.70"	24	32	22	22	509
Junipero Serra, Chile	0.50"	26	38	13	23	558
Kitt Peak, Arizona	0.75"	15	30	16	39	253
Canary Islands		50	29	10	11	38
San Pedro Martia	0.75"	15	25	17	42	52
Flagstaff, Arizona	1.00"	1	5	29	65	80
Kavalur	0.50"	24.7	30.4	23.4	21.6	795

TABLE - 4.3.



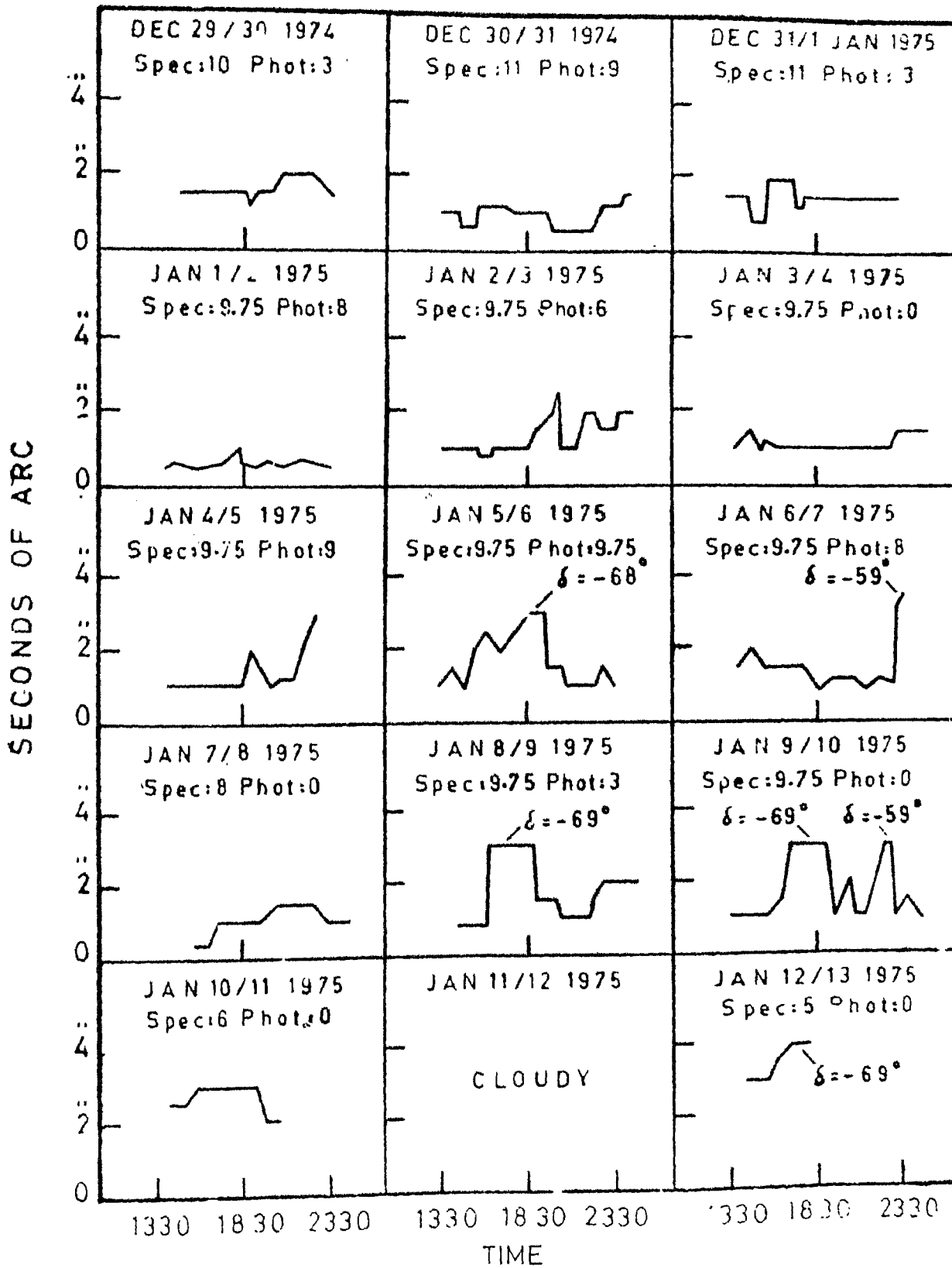


Fig. 4.5. A sample plot of seeing evaluation during

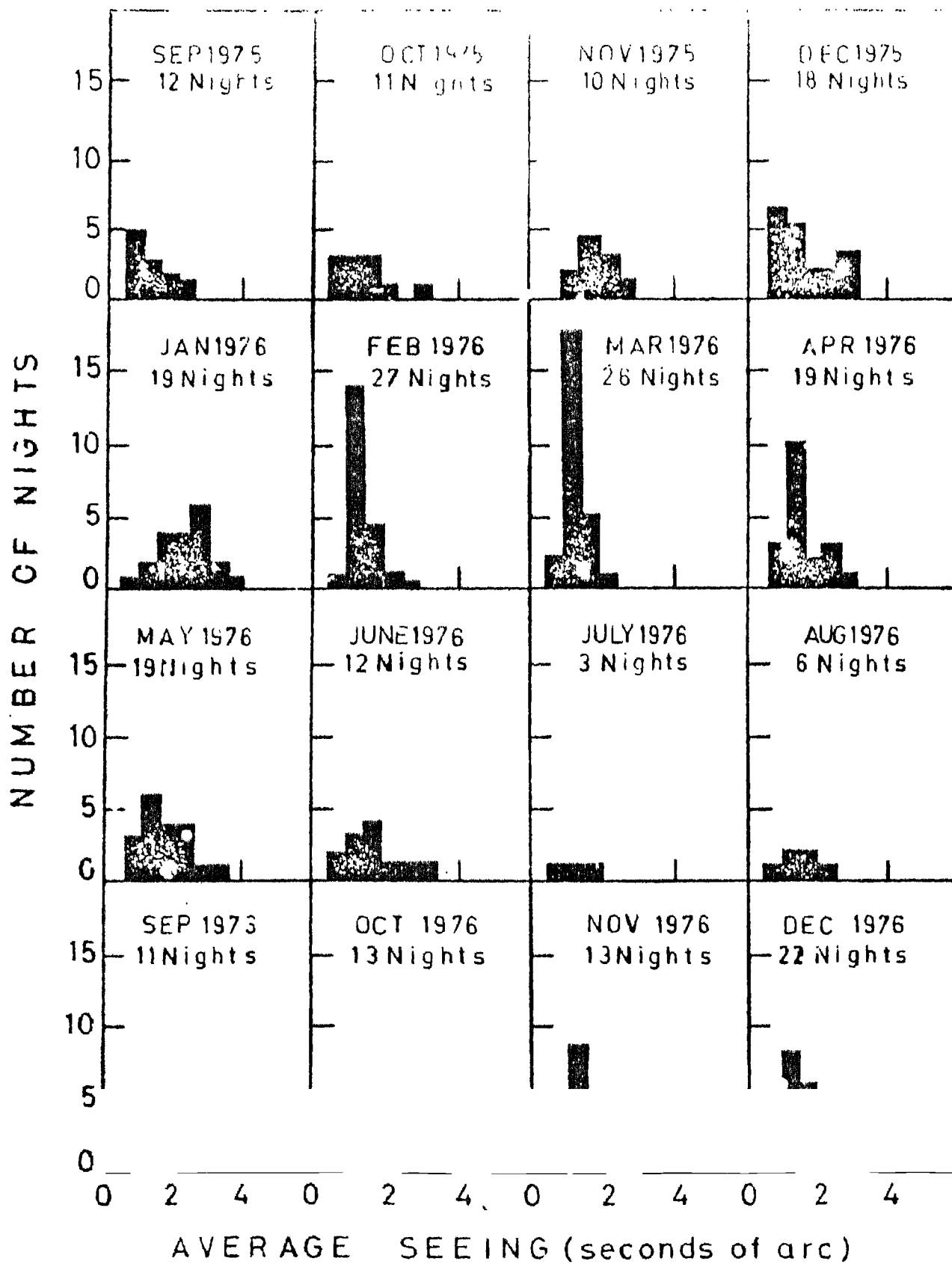


Fig.4.6. Histograms of Kavalur seeing.

to study the data of a few selected stars during certain nights more intensively.

It was suggested by earlier workers that if the data has any trend, it is better the same is removed before processing it for computation of power spectral densities and coherence values at different frequencies as otherwise it is likely that discordant values for the later quantities be encountered.

As such, when in fact, discordant values for coherence recurred despite several trials on different stretches of data, the nature of the time histories itself was examined and some of them did have the characteristics of a certain definite trend. Following the "Average slope method" given by Bendat and Piersol<sup>44</sup> as described below, the observed trend in the data was removed. Power spectral densities obtained from this trend-free data were used to get coherence values. This procedure is recommended by Blackman and Tukey<sup>42</sup> Onis and Enochson<sup>45</sup> and also by many other workers.

Average Slope Method: Let the original random record be represented by

$$U(t) = \bar{U} + \bar{\alpha}_U(t - T_r/2) + x(t) \quad 0 \leq t \leq T_r$$

( $T_r$  is the record length duration)

where  $\bar{U}$  denotes the sample mean value of  $U(t)$  over  $(0, T_r)$ , the parameter  $\bar{\alpha}_U$  denotes the average slope of  $U(t)$  with respect to  $t$ , and  $x(t)$  is the corrected sample record with

zero mean value and zero average slope. By integrating  $u(t)$  over 0 to  $T_r/3$  and subtracting from the integral over  $2T_r/3$  to  $T_r$ ; one can solve for  $\bar{u}$  as follows.

( Summation being equivalent of integration )

$$\bar{u} = \frac{1}{h(N-\nu)} \left[ \sum_{n=N-\nu}^N U_n - \sum_{n=1}^{\nu} U_n \right]$$

$h$  = Interdata gap;  $Nh = T_r$ ;  $\nu \equiv T_r/3$  (largest integer  $\leq N/3$ )  
 The change in the nature of raw data before and after trend removal is shown for a couple of sample recordings in Fig. 4.7 and 4.8

#### 4.6. Interpretation of autocorrelation functions and power spectral densities in respect of seeing phenomenon:

It is found, on autocorrelation and power spectral analyses of stellar intensity fluctuations, that the phenomenon of seeing is composed of components of different frequencies ranging upto 500 Hz or sometimes even higher. This is in keeping with the work reported earlier by Protheroe (1955)<sup>25</sup> and Mikesell et al (1951)<sup>26</sup>.

From data collected from stars at different zenith distances and on different nights, it is observed that there exist distinct peaks at different lags in their " auto-correlation vs. time lag " plots. The corresponding power

WIND SPEED DATA BEFORE AND AFTER TREND REMOVAL

( HOT-WIRE ANEMOMETER SENSOR )

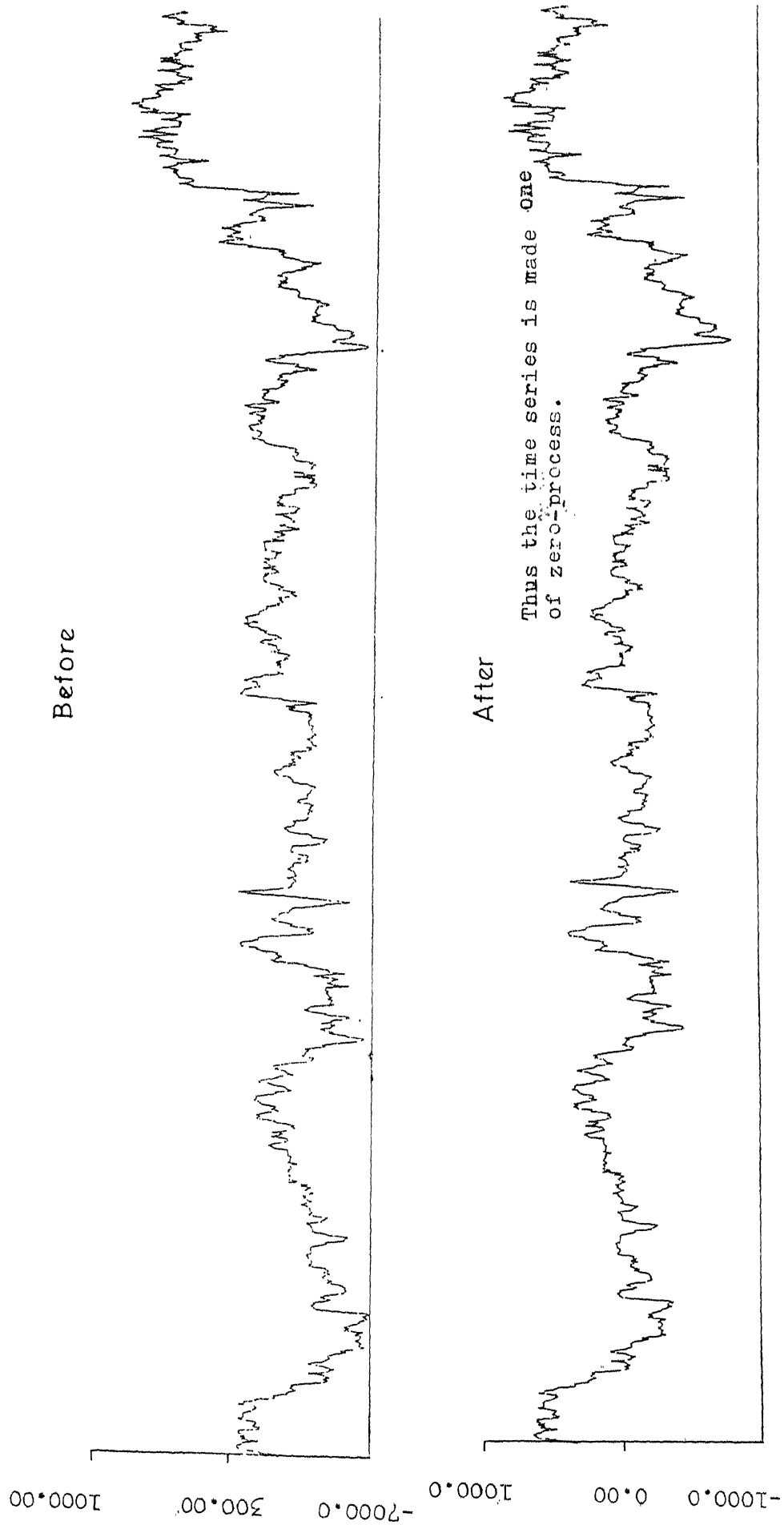
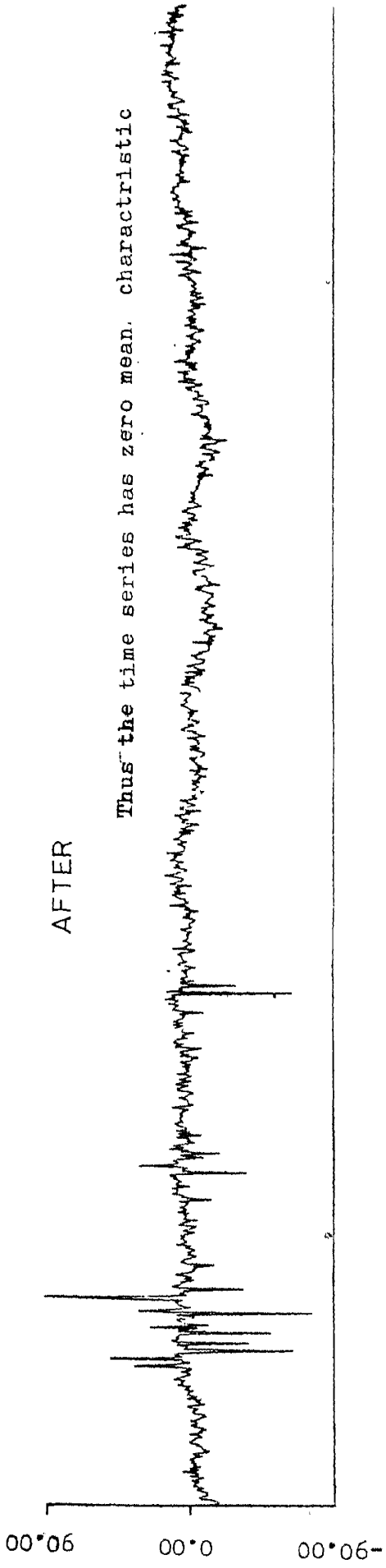


Fig. 4.7.



WIND SPEED DATA BEFORE AND AFTER TREND REMOVAL

( SENSOR : CUP ANEMOMETER )

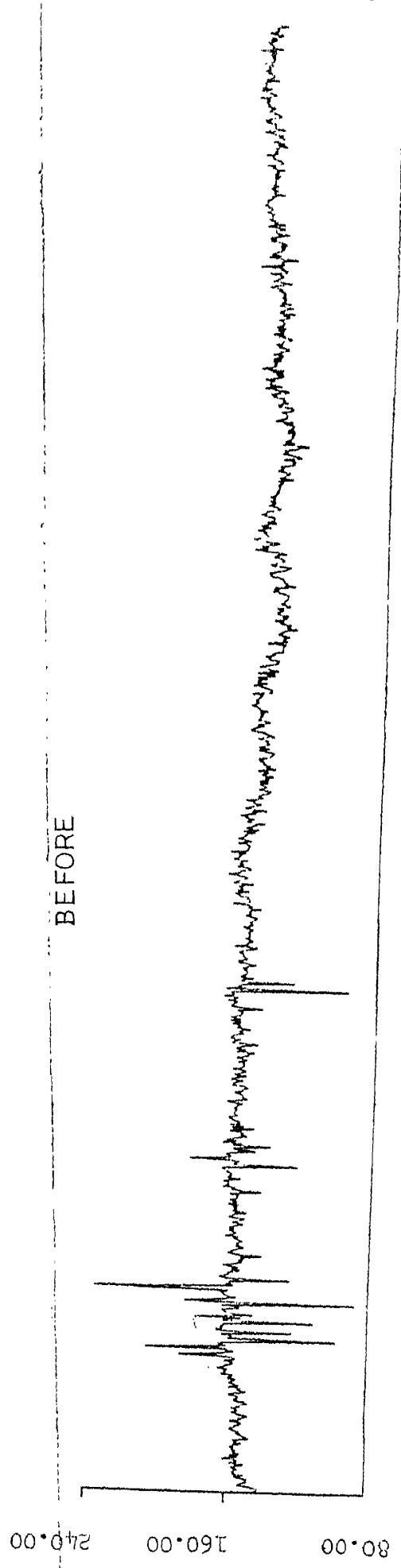


Fig. 4.8.

spectral density plots indicate the clear existence of dominant period components.

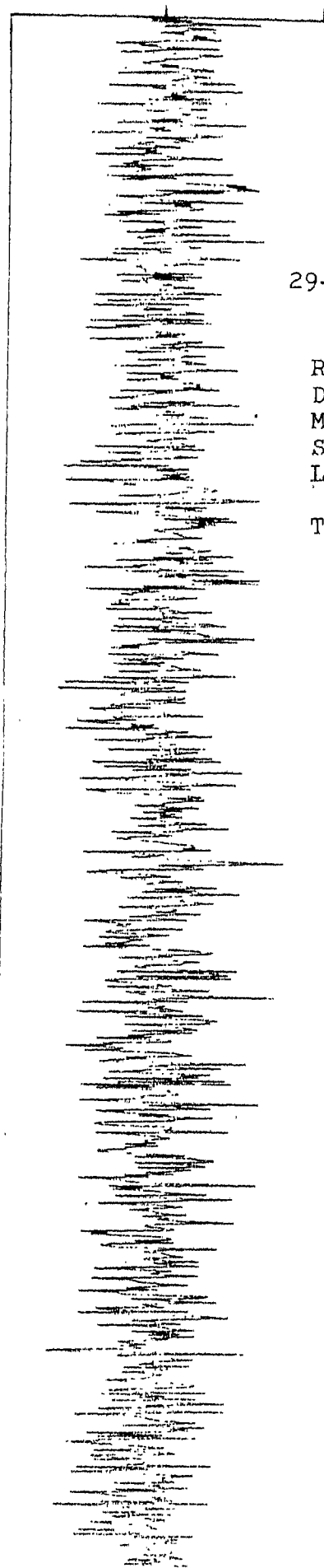
The weather conditions at the observatory station during these nights of observation were mostly normal with a tendency for humidity to increase and temperature to decrease with time. Seeing and transparency, judged qualitatively, were fair. Observations were taken in standard B and V filters. Figs. 4.9-A and B show typical records, autocorrelation plots and corresponding power spectral densities.

It is noticed that the power spectrum of seeing indicates variable nature in its pattern, which may be ascribed as due to the variable nature of the atmospheric turbulence. Further, it is found that change filters i.e., the effect on wavelength of light, of the turbulence, has been minimal.

Fig. 4.10 shows the different positions of the 1-m optical telescope while observing stars at different zenith distances. Analog data so collected was sampled, as mentioned earlier, at 500 Hz and 1000 Hz.

To study the low frequency components and also to keep down the computational time to a reasonable limit, data points at every 32 ms were taken. With  $N$  as 1000 and  $m$  as 5% and the interdata gap of 32 ms, it turns out that the effective realizable frequency region would lie within 0 and 16 Hz as per Nyquist criterion<sup>42</sup> for information sampling.

-300.00 0.00 300.00



29-Vulpeculae

R.A.: 20hrs 37min

Decln.: 21°07'

Mag: 4.78

Sp.Cl.: AD

LST at 10hrs 11min

40sec

Time of Expt 0540 Hrs

to 0545 Hrs IST

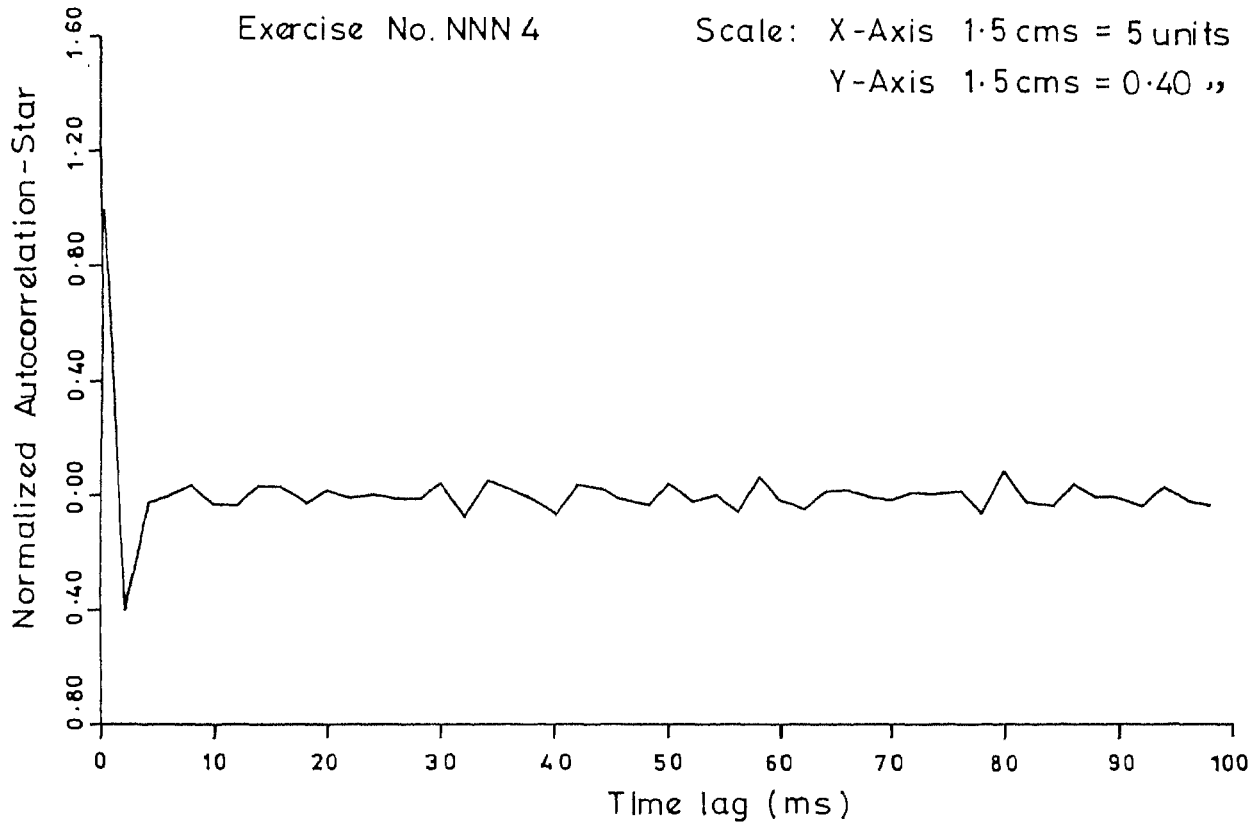
SNAR DATA

Fig. 4. 9a. A sample record of seeing fluctuations.



Normalized autocorrelation vs. Time lag  
Astronomical seeing

123



Log of power spectral density vs. Frequency  
Astronomical seeing

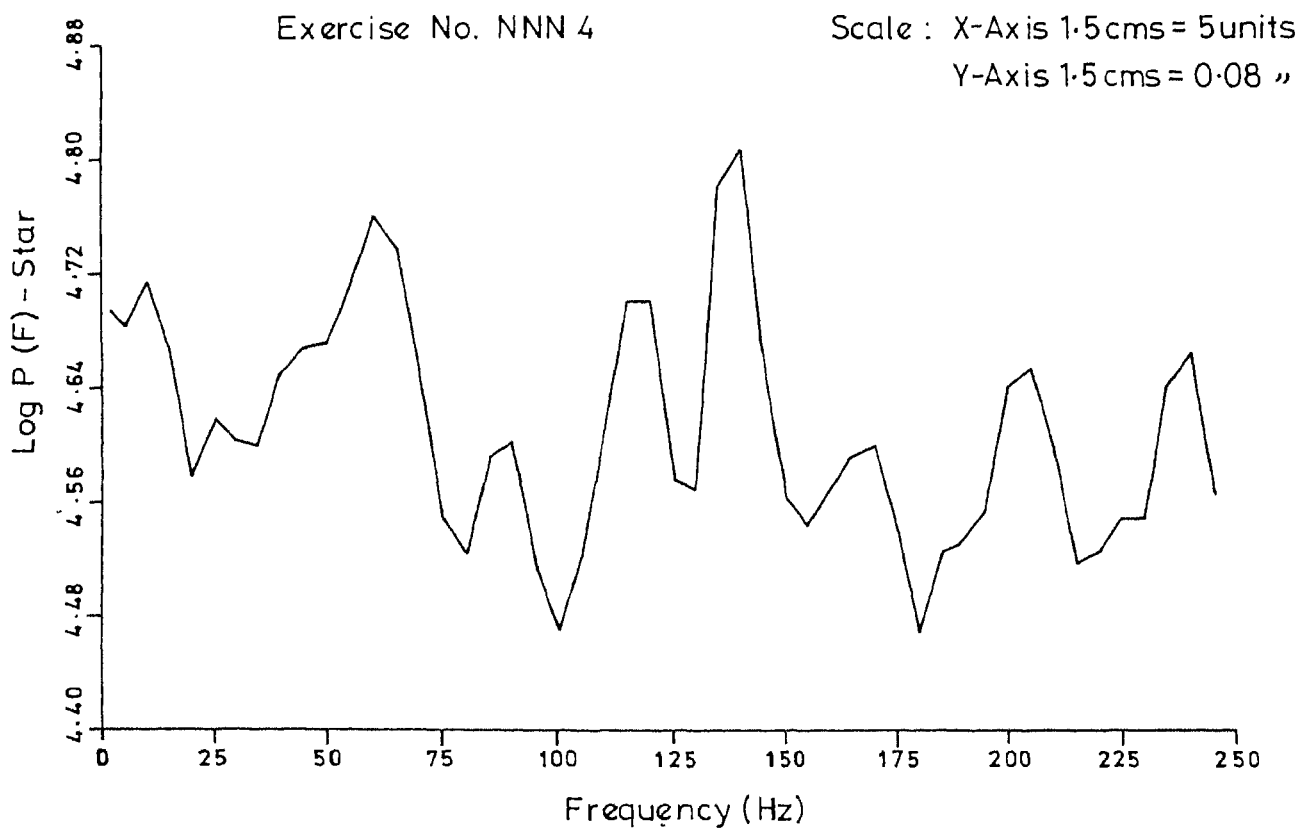


Fig. 4.9b.

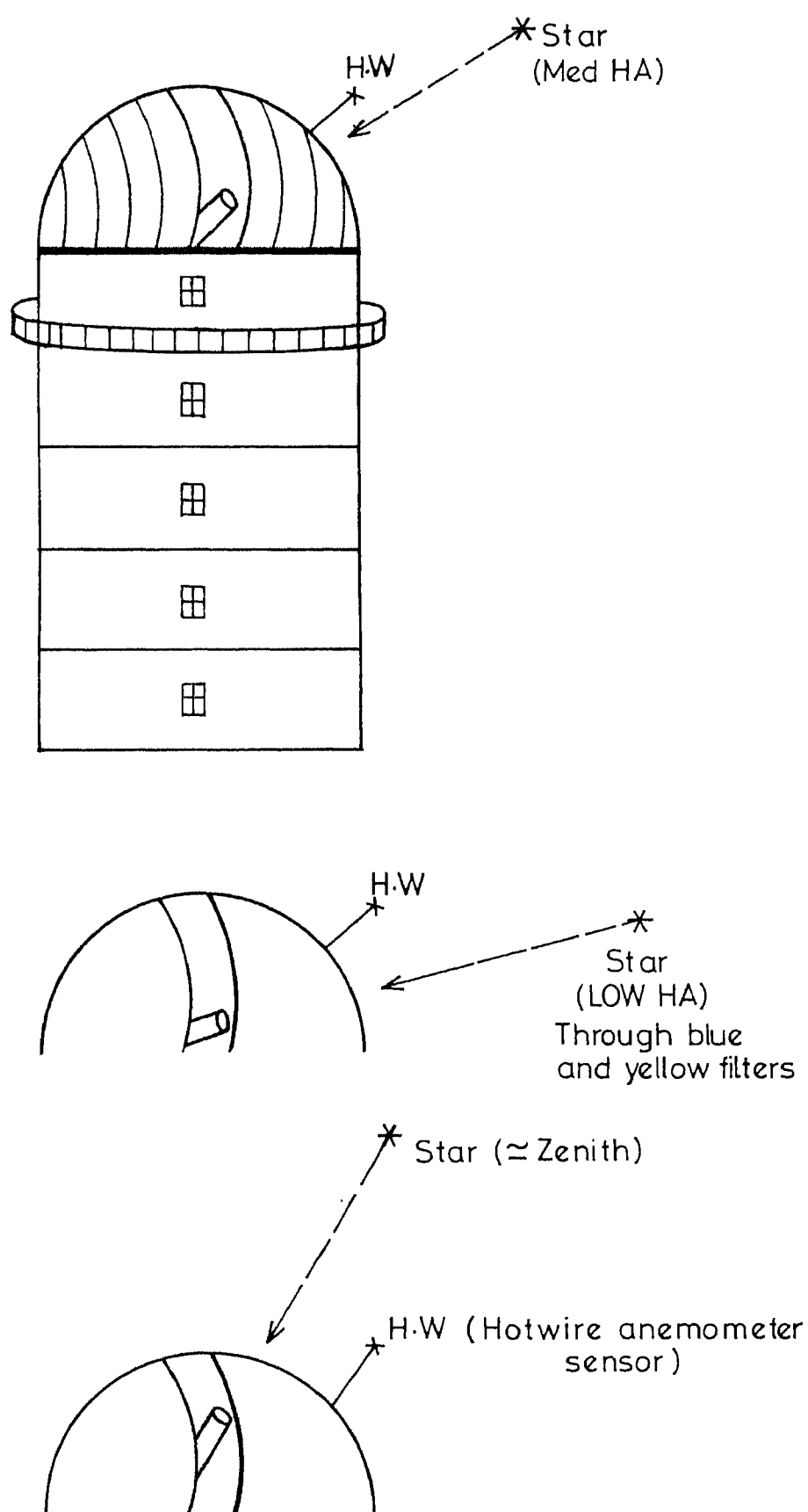


FIG-4.10. SEEING. (Diaphragm :  $25\mu$ )

Analog data sampled at  $\Delta t = 2\text{ ms}$  ( $f_c = 250\text{Hz}$ ),  
 $1\text{ ms}$  ( $f_c = 500\text{Hz}$ ),  $32\text{ ms}$  ( $f_c = 16\text{Hz}$ ),  $8\text{ ms}$  ( $f_c = 62.5\text{Hz}$ )

Their autocorrelation and power spectral density plots show many peaks whose periods and spectral densities vary from experiment to experiment. Parts of the same record have also been sampled at 2 ms intervals, the analysis yielding typical high-frequency characteristics.

Appendix-A gives computer program (Fortran-10) listings for plotting raw data, evaluating normalised autocorrelation function, logarithms of power spectral densities, coherence and phase angles. Also included is the listing for actual plotting of these values.

Some sample plots pertaining to atmospheric turbulence, data for which was collected synchronously with seeing data are shown in Appendix-B. This pertains to their power spectral densities.

An example of low-frequency spectrum in respect of the seeing phenomenon is shown in Fig. 4.11. The power spectral density plots indicate the presence of components of frequencies from less than 1 Hz to 16 Hz. The individual values varied on different occasions, but some persistent peaks e.g., at 1-2 Hz, 4-6 Hz and 10-12 Hz are seen. This is shown in fig. 4.12. The results are summarised in table 4.4.

Power spectrum and coherence analysis of Kavalur seeing

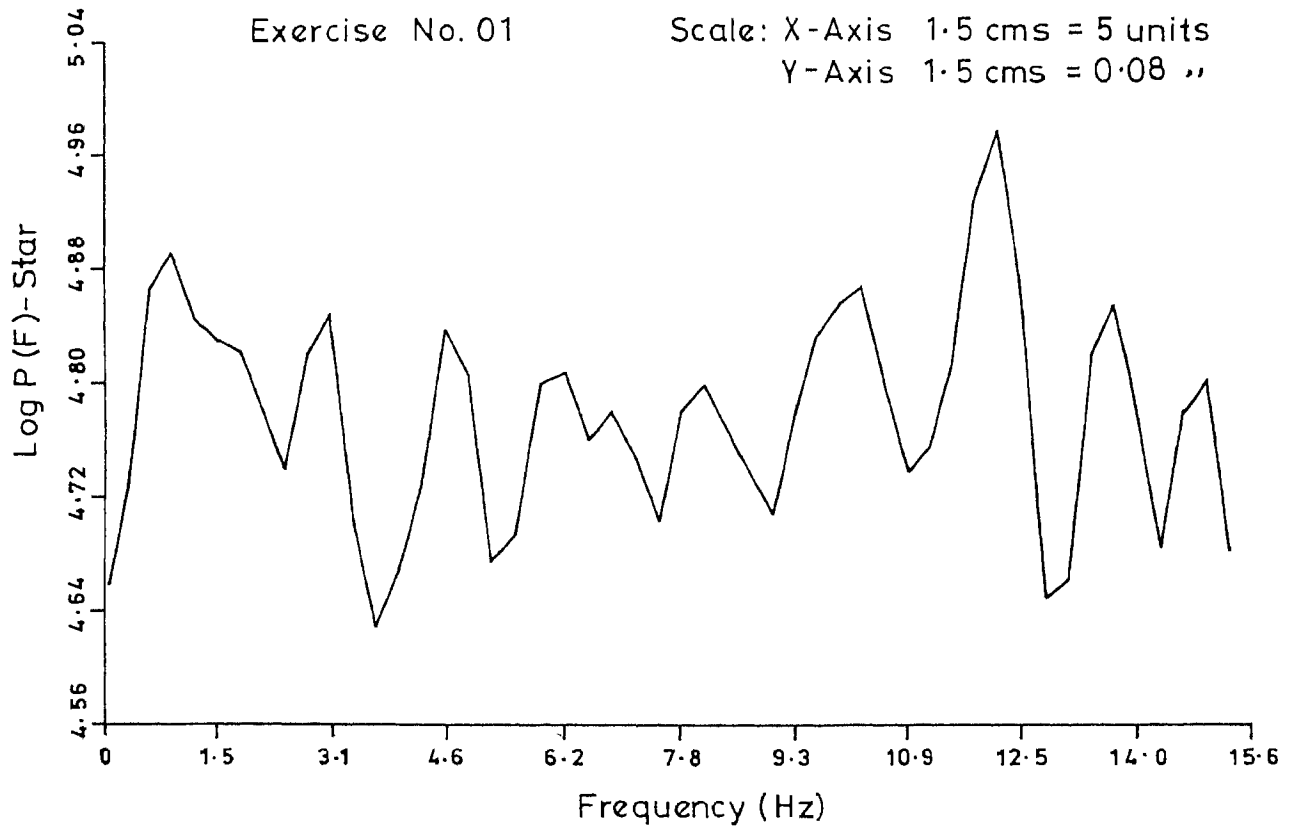
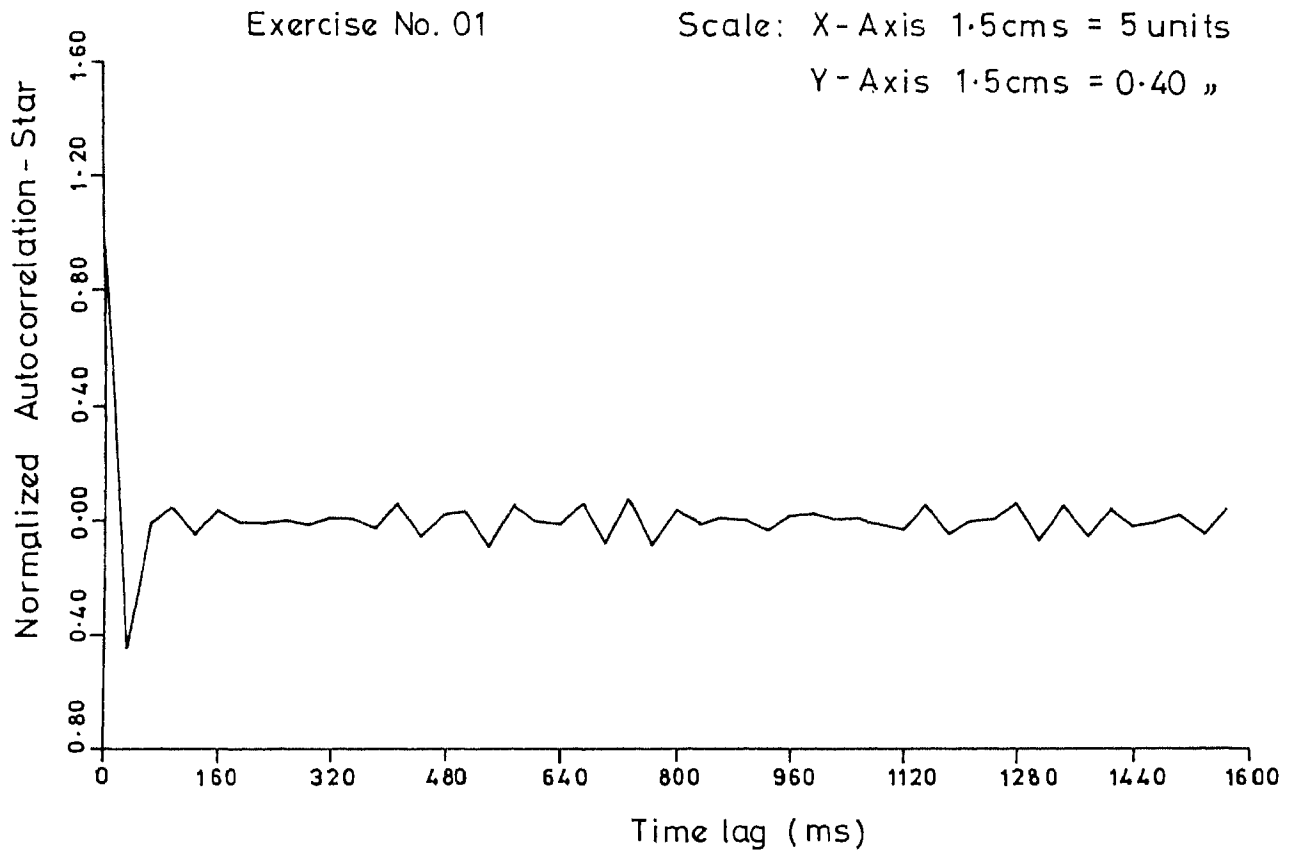


Fig 4.11.

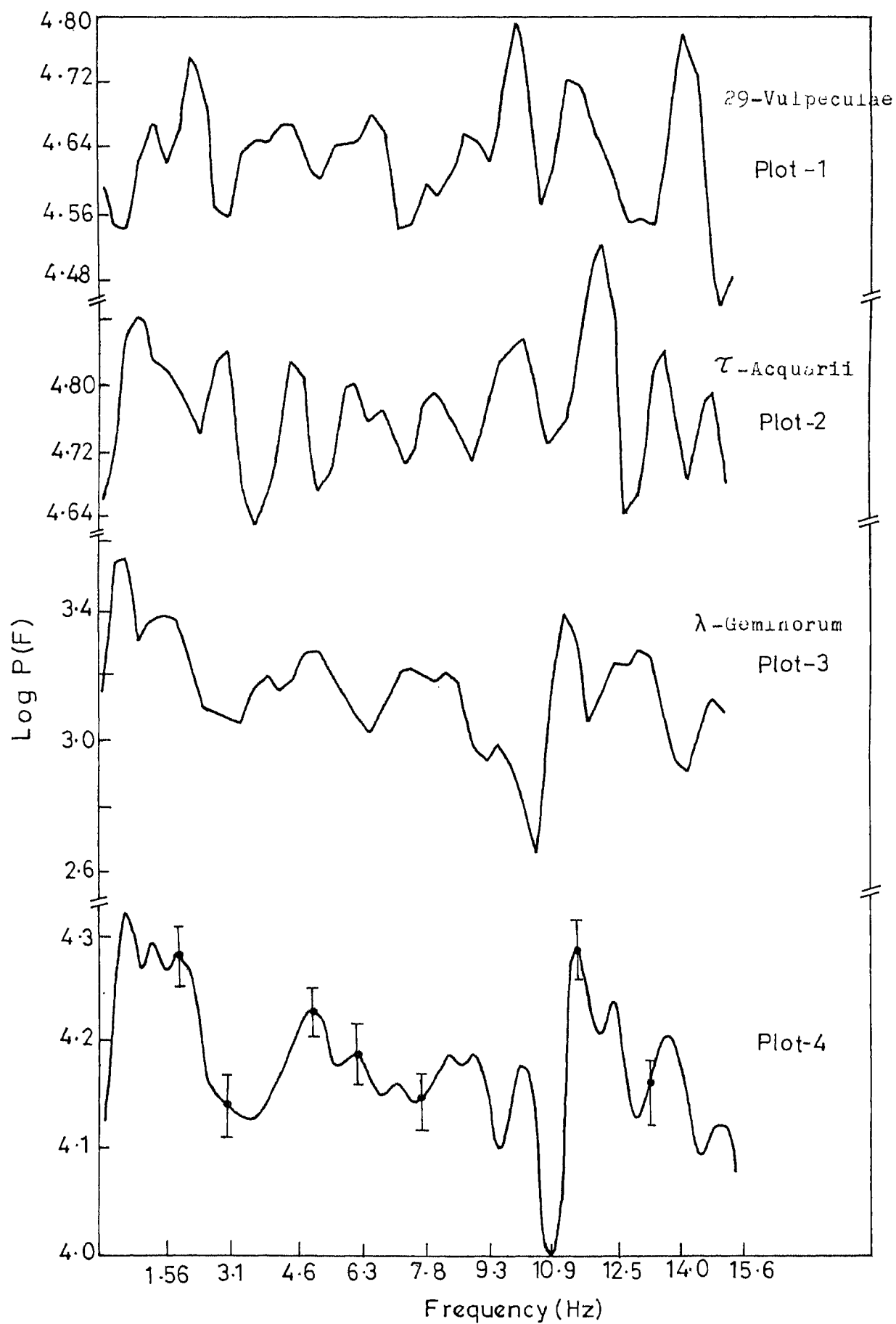


Fig. 4.12. Composite plot of low-frequency component study of seeing phenomenon.

TABLE - 4.4.  
STUDY OF LOW-FREQUENCY COMPONENTS

Frequency (in Hz)	Log Power Spectral Density (By arbitrary scale)	Remarks
0.31	4.13	-
0.62	4.27	-
0.93	4.32	Peak Region
2.5	4.26	-
3.75	4.13	-
5.0	4.22	Peak Region
6.25	4.19	-
7.0	4.16	-
8.75	4.19	-
10.0	4.17	-
11.56	4.29	Peak Region
13.12	4.13	-
14.06	4.20	-
15.0	4.12	-

A representative sample of high-frequency power spectra is shown in Fig. 4.13. This depicts power spectra from individual observations identically analysed. The summary of results is presented in table 4.5. The presence of 50 Hz and 150 Hz components can be clearly seen.

The coincidence of the components at 50 Hz and 150 Hz with the power line frequency and its third harmonic causes some doubt about its atmospheric origin. This aspect has been studied in depth and it has been found that there are ample indications in support of its non-instrumental generation.

In any detection system the recorded infiltration of the power line frequency or its harmonics is directly related to the gain introduced in the system. Measurements taken in these studies cover a wide range of star brightnesses, where different amounts of amplifications had to be employed. If the two above mentioned frequencies are of instrumental origin, there should have been a direct correlation of the spectral densities with the magnitude of the star; such an effect is not noticeable in the sample. In Fig. 4.14 is shown the values of  $\log P(f)$  at 50 Hz for a few stars of different brightnesses. The nature of variations indicates that the sources are not of instrumental origin.

Further, the dependence of the frequencies of seeing phenomenon with the zenith distance of the stars has also

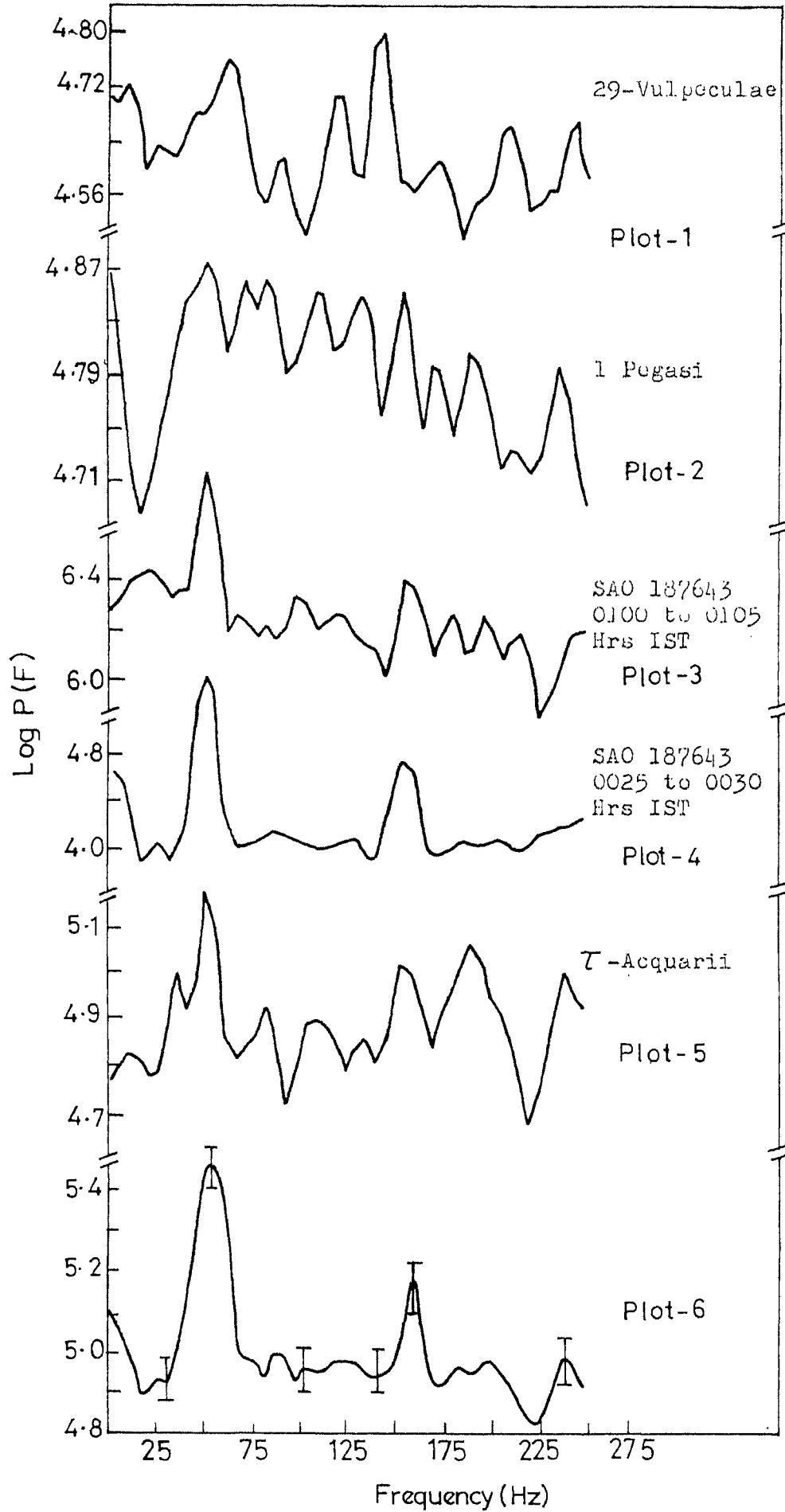


Fig. 413 A composite plot for high-frequency component study of the seeing phenomenon.



TABLE - 4.5.  
STUDY OF HIGHER-FREQUENCY COMPONENTS

Frequency (in Hz)	Log Power Spectral density (By arbitrary scale)	Remarks
10	5.07	-
30	4.93	-
40	4.99	-
55	5.44	Peak Region
70	4.97	-
80	4.93	-
100	4.99	-
120	4.96	-
155	5.16	Peak Region
175	4.92	-
200	4.93	-
225	4.80	-
250	4.93	-

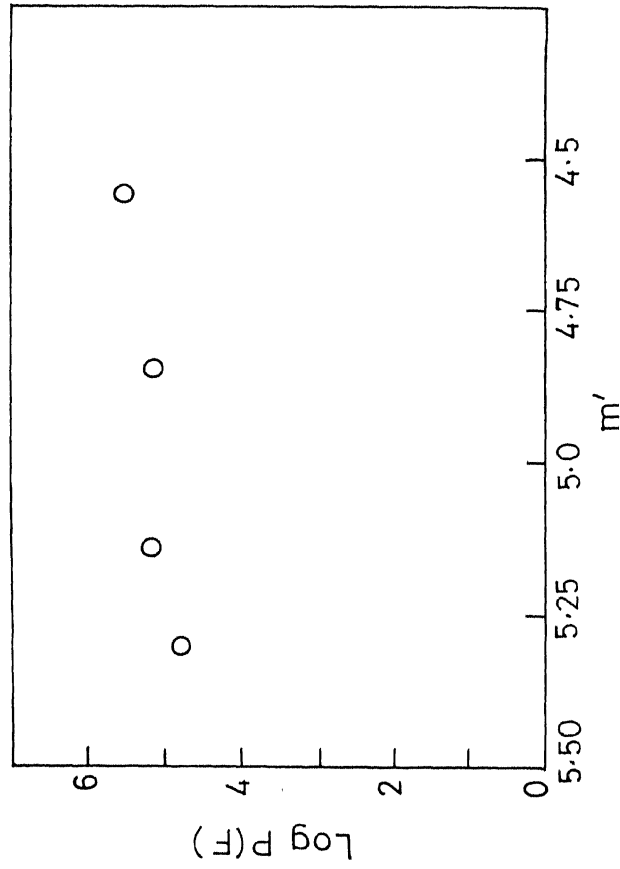


Fig.4.14. Log P(F) of seeing at 50Hz vs. m'

$$m' = m + 0.5 \text{ See } z$$

$$\cos z = \frac{\sin \phi \sin \delta + \cos \phi \cos \delta \cos h}{\cos h}$$

- $\phi$  : Latitude of the observer
- $\delta$  : Declination of the star
- $h$  : Hour angle of the star

The nature of the curve is the same even at 150 Hz

been studied. If these disturbances are of atmospheric origin, there should be slight increase of both 50 Hz and 150 Hz components in their amplitudes with sec Z. Fig. 4.15 shows  $\log P(f)$  plotted against sec Z for seeing data at the characteristic frequency of 50 Hz, showing the expected ascent of the  $P(f)$  values.

Nextly, it is noticed also in the case of power spectral analysis of wind speed data collected simultaneously with stellar intensity fluctuations that there exists similar peaks with significant coherences at specified frequencies. Additional peaks in the spectral density curves of seeing perhaps indicate variations due to upper layers of the atmosphere. This aspect has been discussed in the fifth chapter.

#### 4.7. Interpretation of results on normalized autocorrelation and power spectral densities in respect of scintillation phenomenon

Studies of astronomical seeing have been based on variation of light intensity of a small representative patch ( 0.4 arc sec ) of the smeared star image. In experiments of astronomical photometry, variations in the total light intensity known as scintillation are important. These have been studied by obtaining records of stellar intensity fluctuations through a diaphragm larger than the seeing disc.

The nature of the curve is the same even at 150 Hz

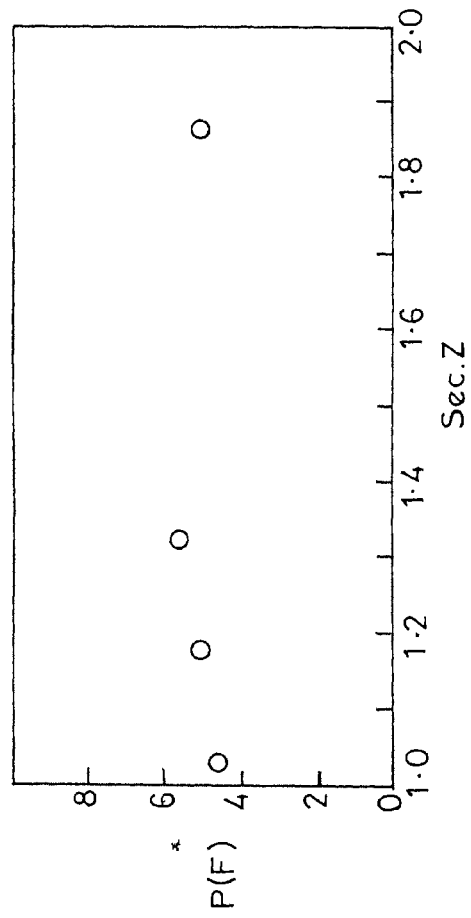


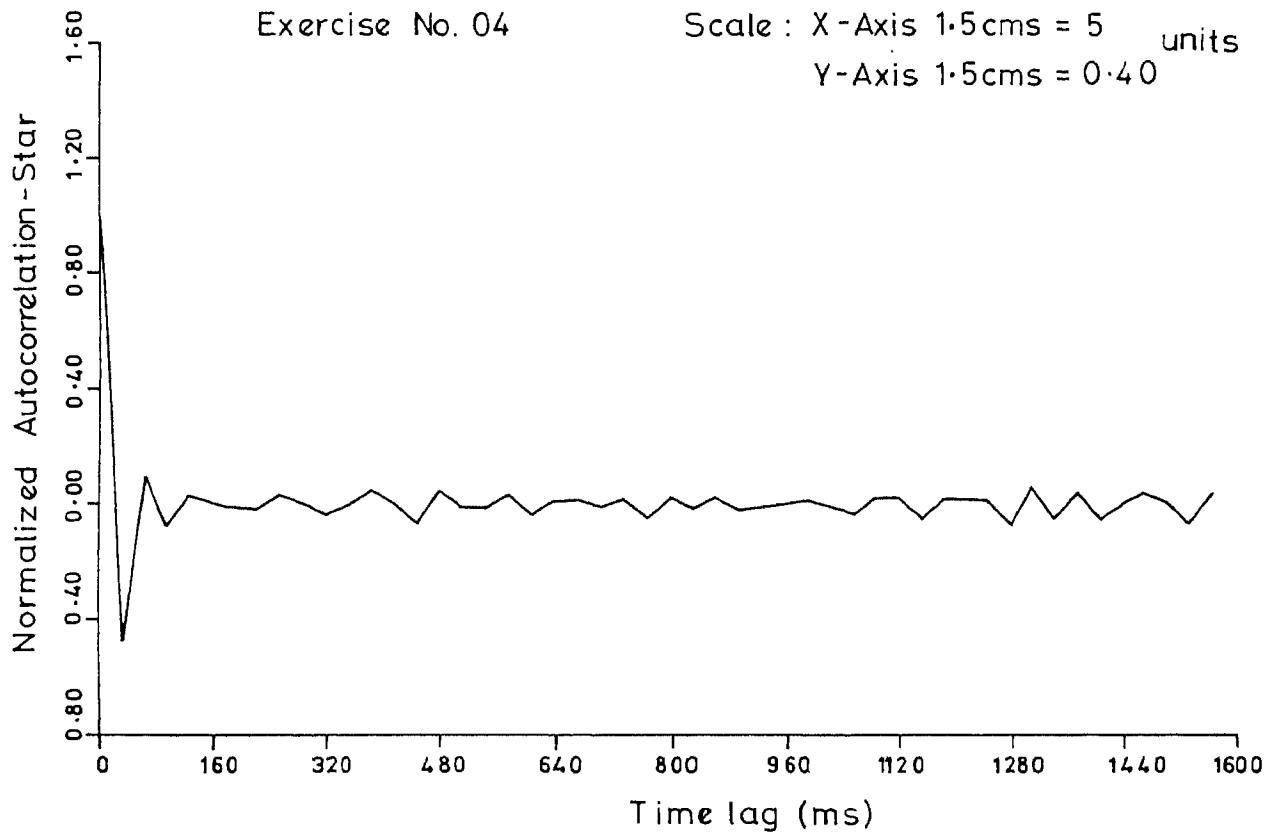
Fig.4.15. Log P(F) of seeing at 50Hz vs Sec.Z

The autocorrelation and power spectral density plots for such data as obtained through a diaphragm of 9 arc sec diameter reveal characteristics of scintillation. It is found that there are distinct peaks at specified lags signifying presence of selected periodicities. Correspondingly, there are spectral density peaks at appropriate frequencies. Records taken for stars at different elevations indicate variations in the power spectral curve. Fig. 4.16 shows normalized autocorrelation and power spectral density plots for low-frequency region, upto 16 Hz. As in the case of seeing, there exist in the case of scintillation also distinct frequencies at which power spectral densities have a large magnitude.

A comparative study is made of this phenomenon within lower frequency region between two analysed records and is found that there are very clear low-frequency components recurring consistently in these observations. These frequencies are found at 3.1 Hz, 7.13 Hz, 13.46 Hz. Fig 4.17 shows the comparative study made of the power spectral densities within the low frequency region of the scintillation phenomenon.

A couple of sample records, normalized 'autocorrelation Vs. time lag' plots and 'logarithm of power spectral densities against frequency' plots in respect of scintillation phenomenon as pertaining to the higher frequency regions

Normalized autocorrelation vs. Time lag  
Astronomical seeing



Log of power spectral density vs. Frequency  
Astronomical seeing

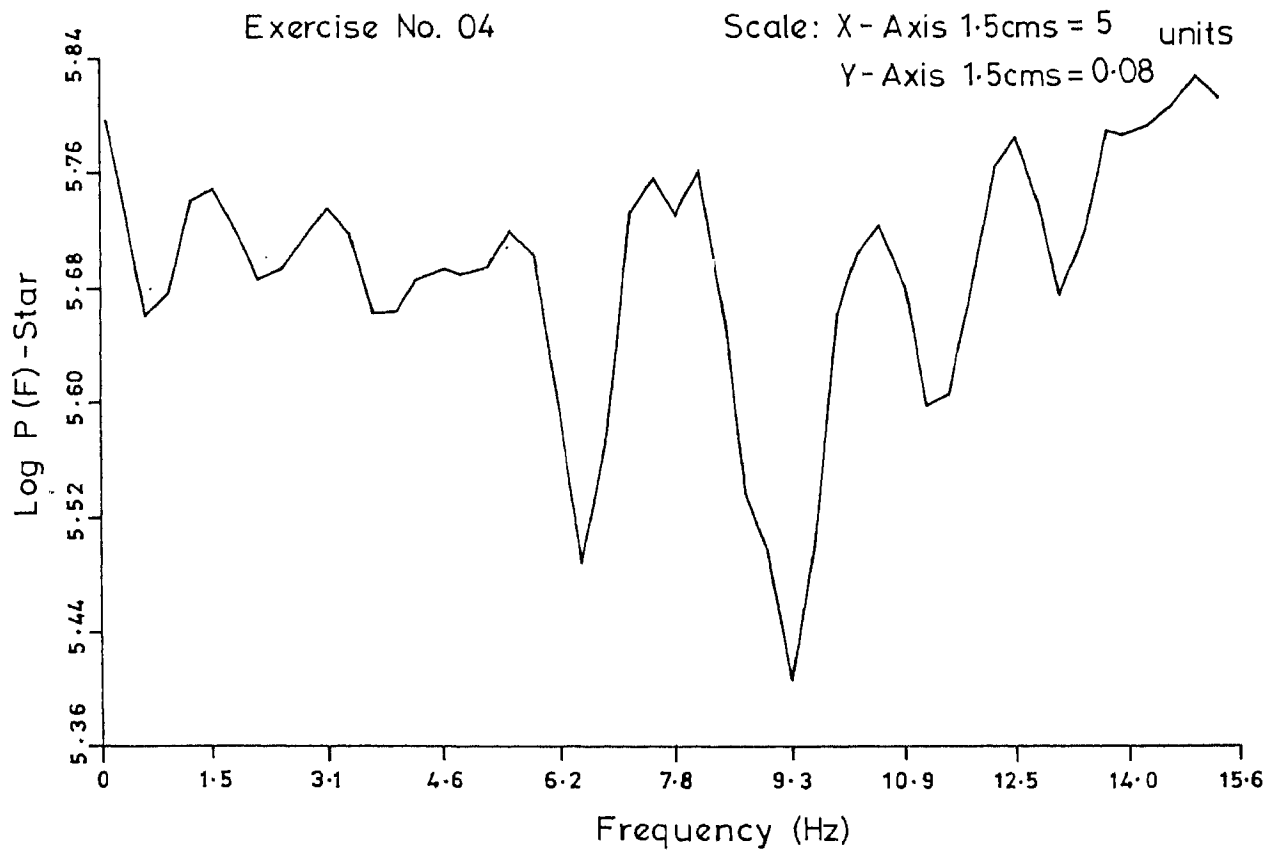


Fig. 4.16.

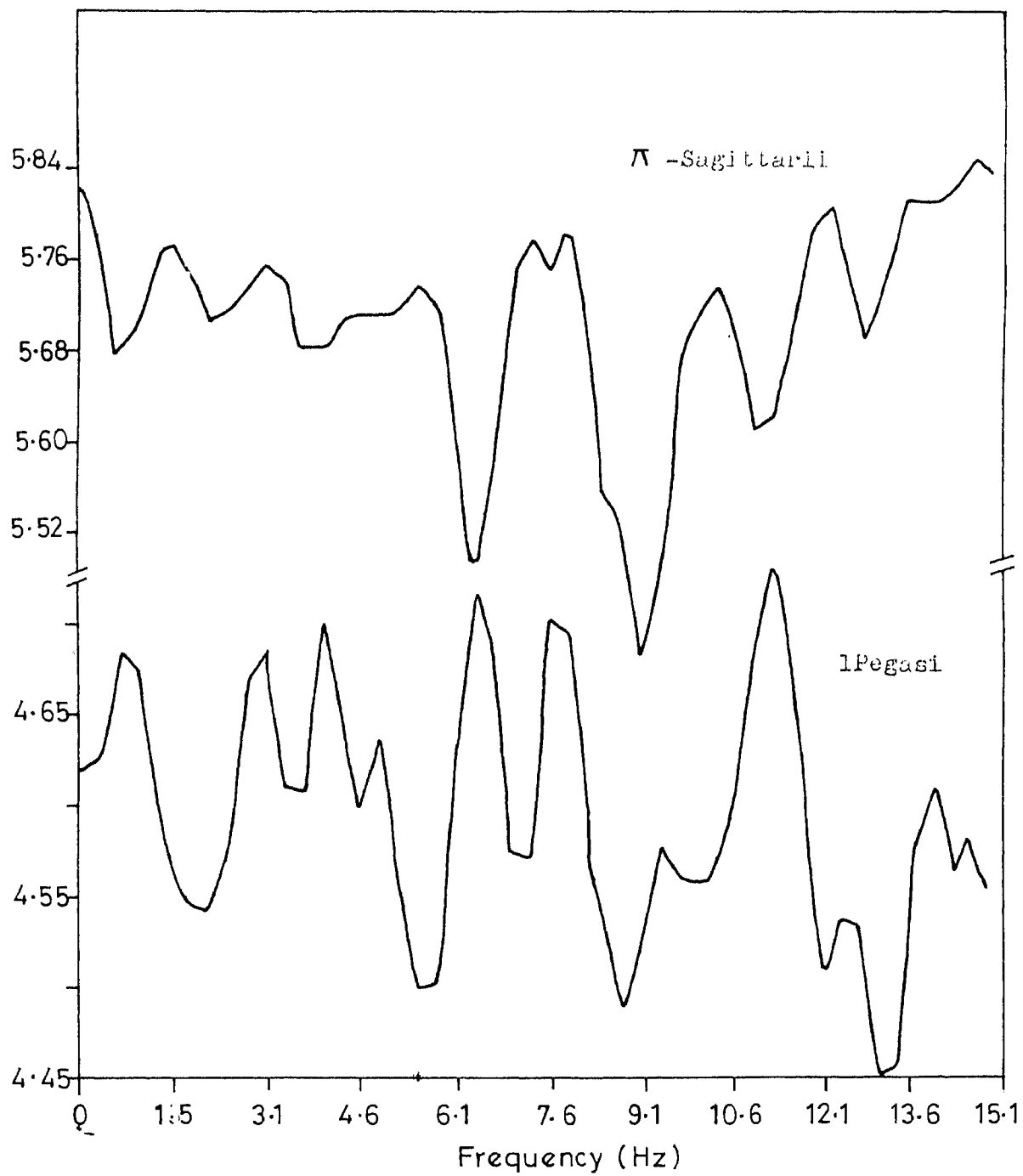


Fig.4.17. A comparative study of power spectral densities of two records of scintillation within low - frequency region.

are shown in Figs. 4.18A and B and 4.19A & B. While there exists less prominent peaks at several specified frequencies within 250 Hz, it is found that the two distinct peaks around 50 Hz and 150 Hz make their appearance in studies on scintillation also. A similar comprehensive plot of  $\log P(f)$  Vs.  $f$  is drawn, which indicates the same characteristics. This is shown in Fig. 4.20 and the values of  $P(f)$  are given in the accompanying table.

As there exist these two frequency components in these studies, a similar argument is advanced in regard to the care to be taken while classifying these components as having been caused by the intervening atmosphere between the star and the telescope. The doubt about the presence of the frequency of a power line at 50 Hz and its third harmonic at 150 Hz is dispelled by studying the values of  $P(f)$  for stars of different brightnesses as done before. Fig. 4.21 clearly shows that the cause for such a behaviour can be other than the power line frequency. Fig. 4.22 indicates the variation of  $P(f)$  for stars with different zenith distances. This is rather expected and supports further the non-instrumental origin of the two predominant frequency components.

Further, when plots of power spectral densities Vs. frequencies corresponding to turbulence at different levels are compared, there is found to be an appreciable degree of



## STAR DATA

$\Lambda$  -Sagittarii

R.A.: 19h 08<sup>m</sup> 40sec  
 Decln.: -21° 03' 11"  
 Mag: 3.02  
 Sp.Cl.: F2  
 LST at Time of Expt.  
 1300 Hrs U.T. = 10hr 15min 36sec  
 Time of Expt 0540 Hrs  
                   to 0545 Hrs IST

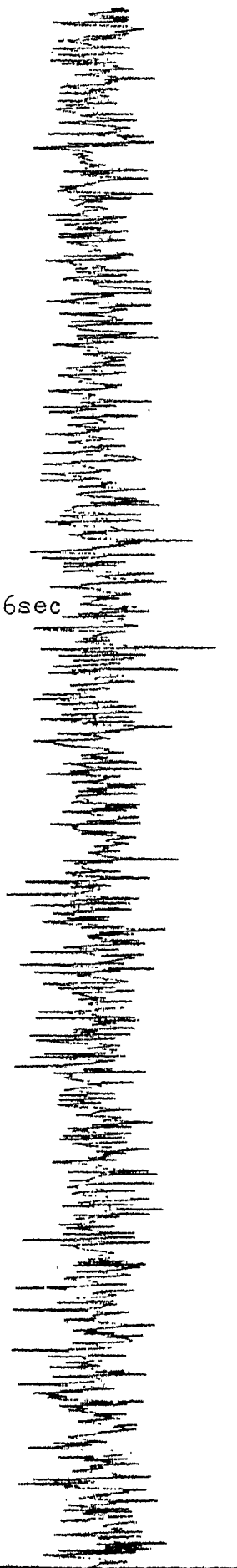
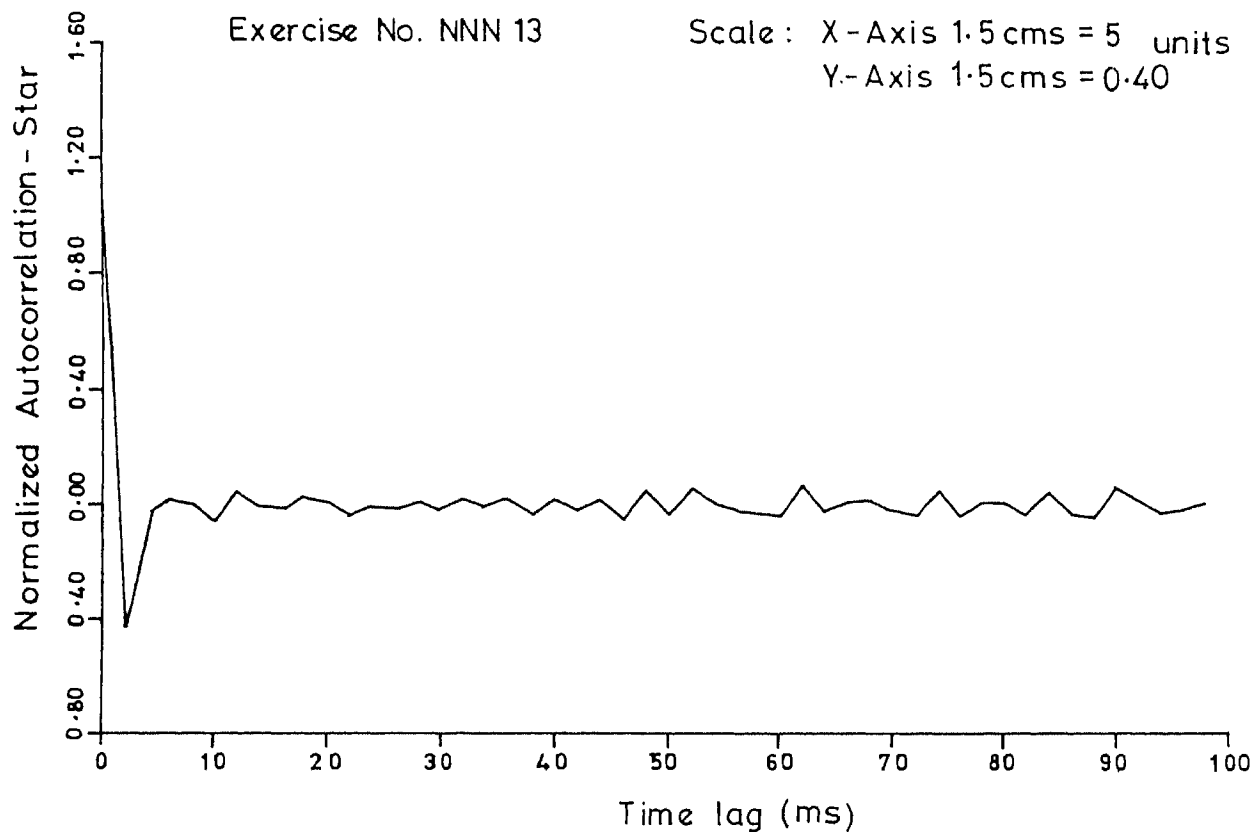


Fig.4.18a. A record of scintillation.  
 $\Delta t = 1$  ms.

Normalized autocorrelation vs. Time lag  
Astronomical seeing



Log of power spectral density vs. Frequency  
Astronomical seeing

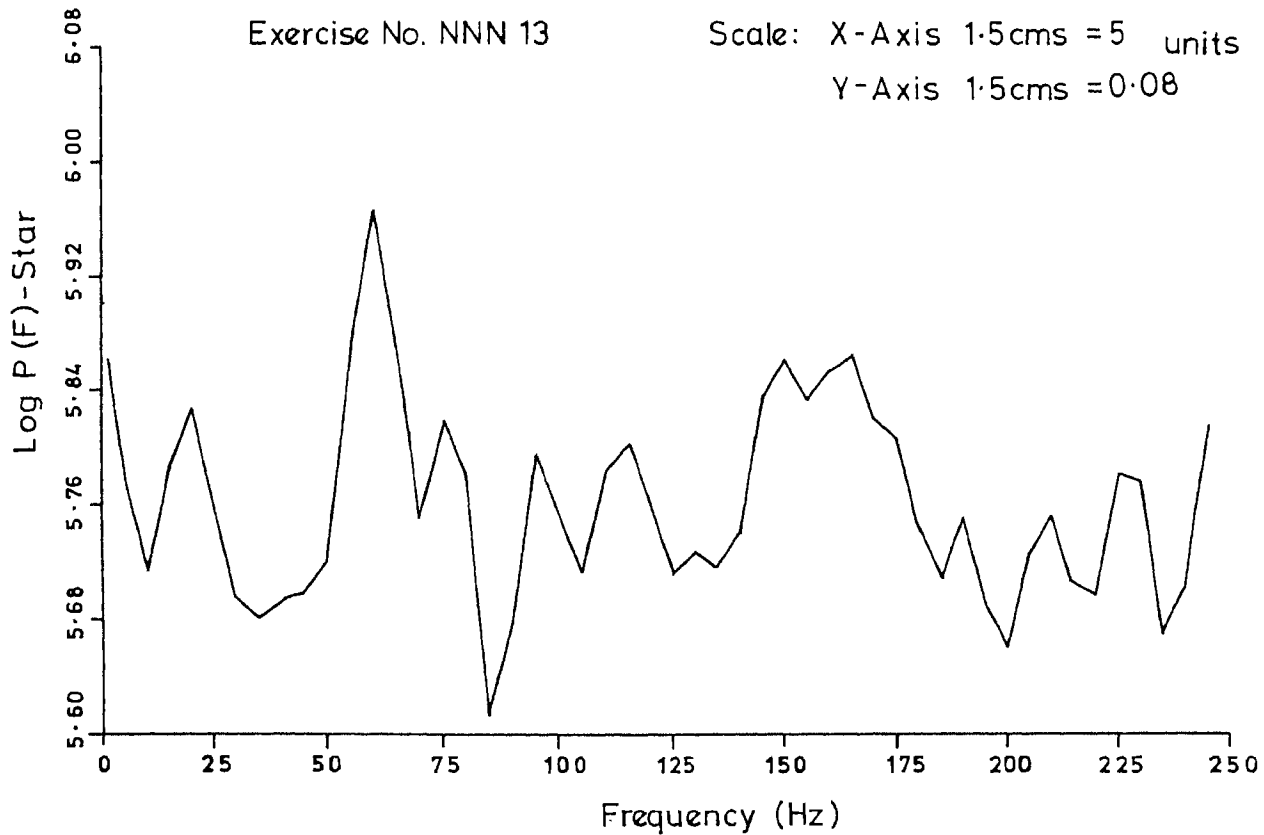


Fig 4.18b.

STAR DATA

1 Pegasi

R.A.: 21hr 21min  
Decln.: +19°43'  
Mag: 4.27  
Sp.Cl.: KO  
LST at  
1300Hrs U.T.=10hr 11min  
40sec  
Time of  
Expt. : 0235Hrs to  
0240Hrs IST

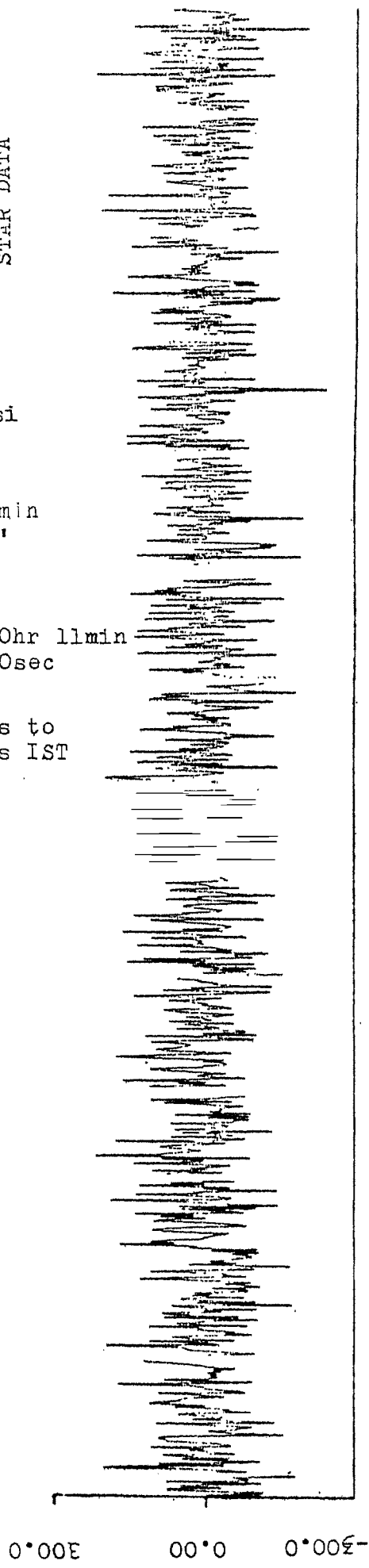


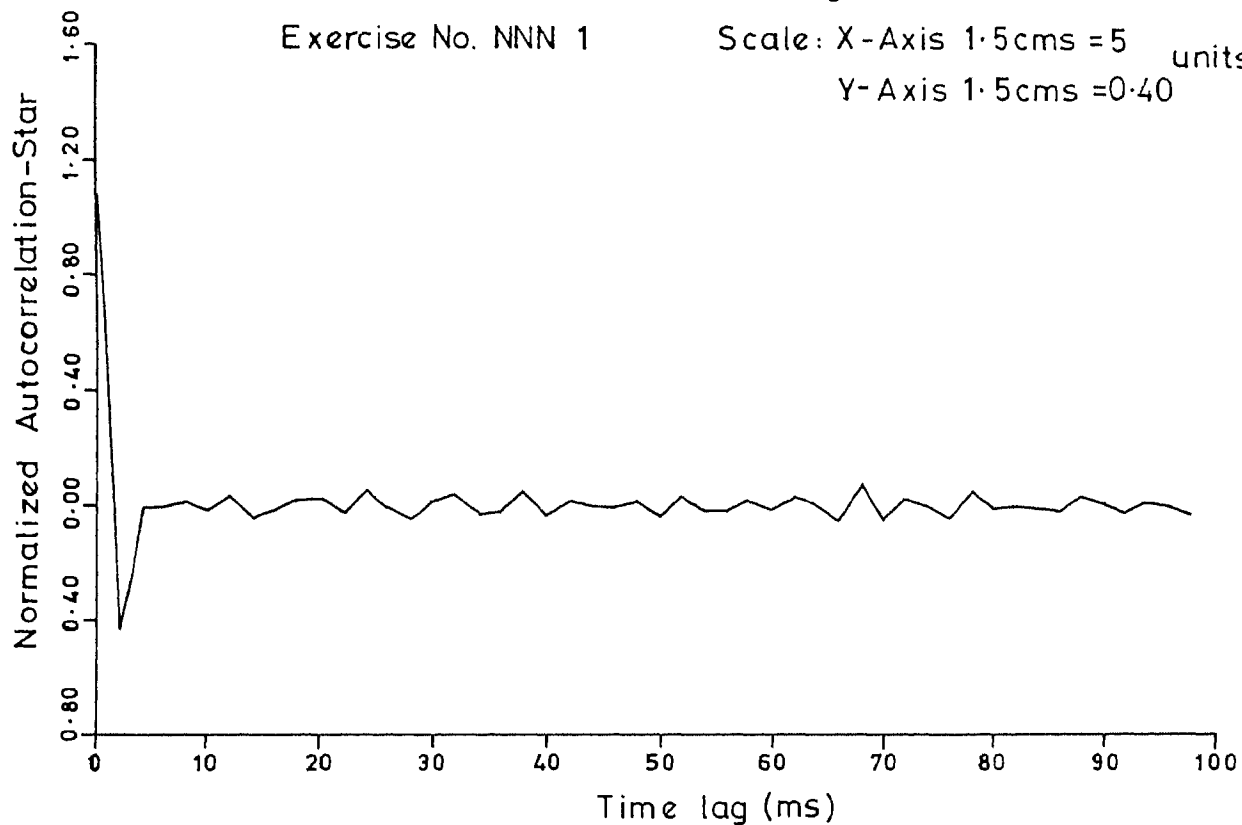
Fig.4.19a. A sample record of scintillation.

Normalized autocorrelation vs. Time lag  
Astronomical seeing

142

Exercise No. NNN 1

Scale: X-Axis 1.5cms = 5 units  
Y-Axis 1.5cms = 0.40



Log of power spectral density vs. Frequency  
Astronomical seeing

Exercise No. NNN 1

Scale: X-Axis 1.5cms = 5 units  
Y-Axis 1.5cms = 0.08

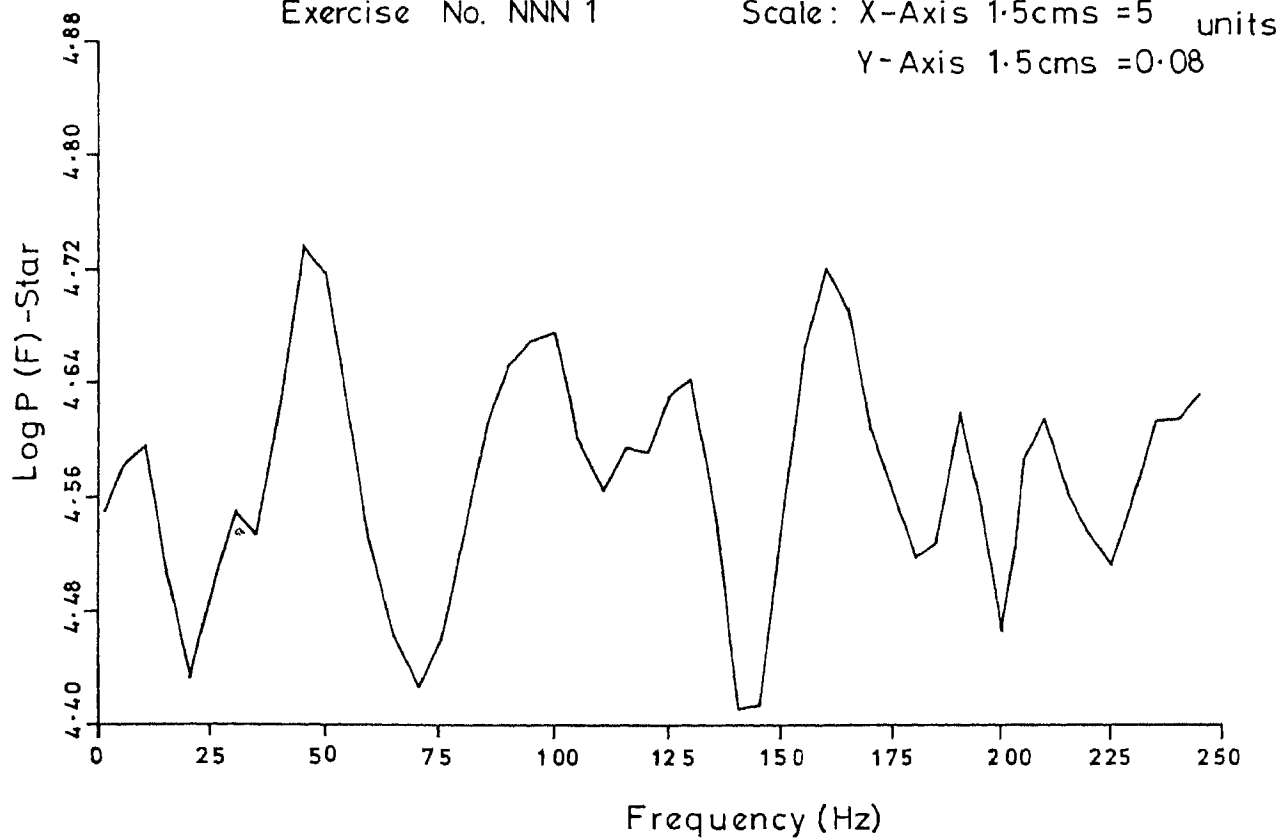


Fig. 4.19b.

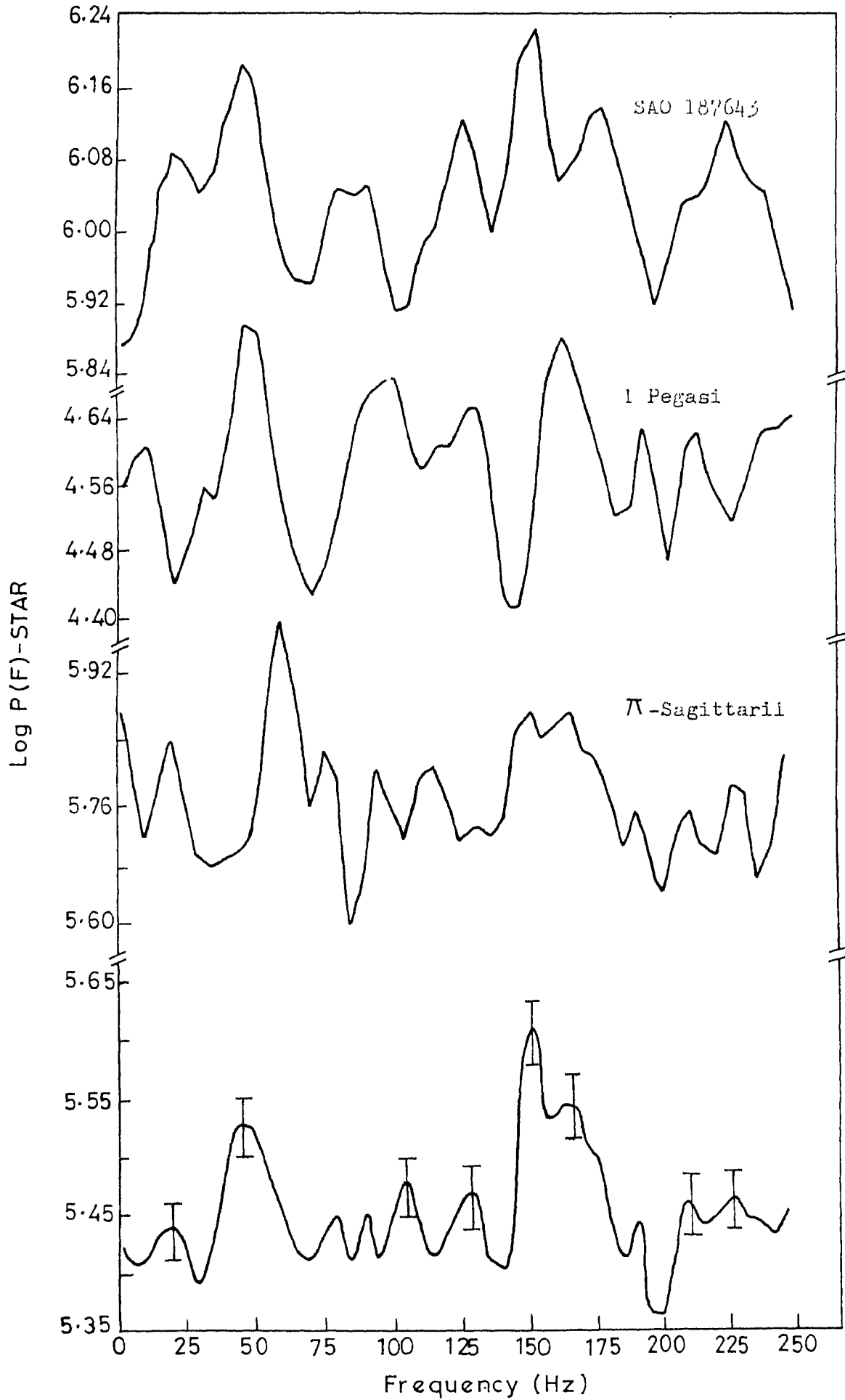


Fig.4.20. A composite plot of high frequency component study in respect of scintillation phenomenon.

TABLE - 4, F.

## STUDY OF HIGH-FREQUENCY COMPONENTS

Frequency (in Hz)	Log Power Spectral Density (on arbitrary scale)	Remarks
10	5.41	-
20	5.43	-
30	5.43	-
40	5.42	-
50	5.53	Peak Region
60	5.50	-
80	5.43	-
100	5.48	-
120	5.46	-
130	5.48	-
150	5.48	-
155	5.61	Peak Region
170	5.54	-
190	5.41	-
200	5.38	-
220	5.44	-
230	5.46	-
250	5.45	-

The nature of the curve  
is the same even at 150 Hz

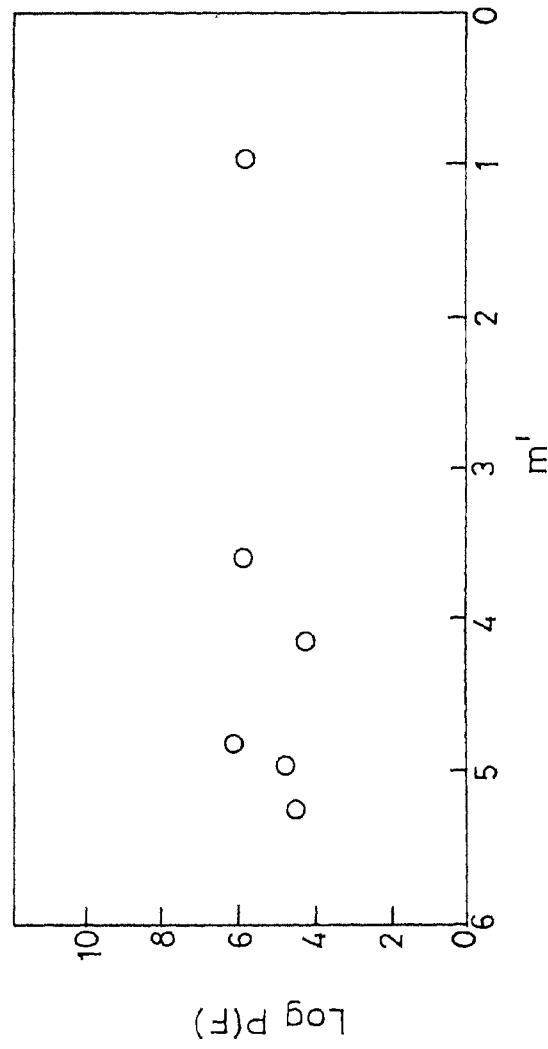


Fig.4.21. Log P(F) of scintillation at 50Hz vs.  $m'$ .

The nature of the curve  
is same even at 150 Hz

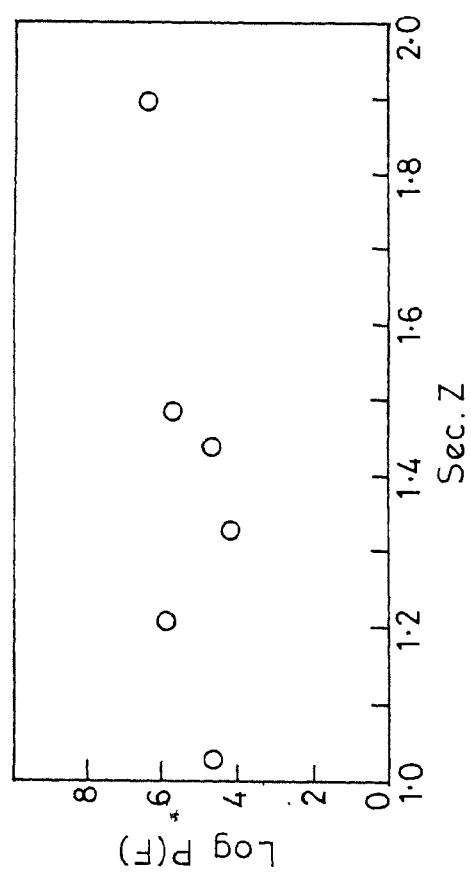


Fig.4.22. Log P(F) of scintillation at  
50 Hz. vs. Sec.Z.



correlation amongst the physical processes taking place along the height of the 1-m telescope dome and in its vicinity. As such, the effects of upper layers of atmospheric turbulence (just above the low lying atmosphere) on distortion of optical images are expected.

A sample curve of  $P(f)$  corresponding to stellar intensity fluctuation and atmospheric turbulence ( windspeed ) obtained through their simultaneous study is shown in Fig. 4.23. Apparently there are specified frequencies at which there exist a fair degree of correlation between the two quantities.

A detailed mathematical discussion of the simultaneous study between seeing and turbulence and between turbulence values at different heights is made in the following chapter.

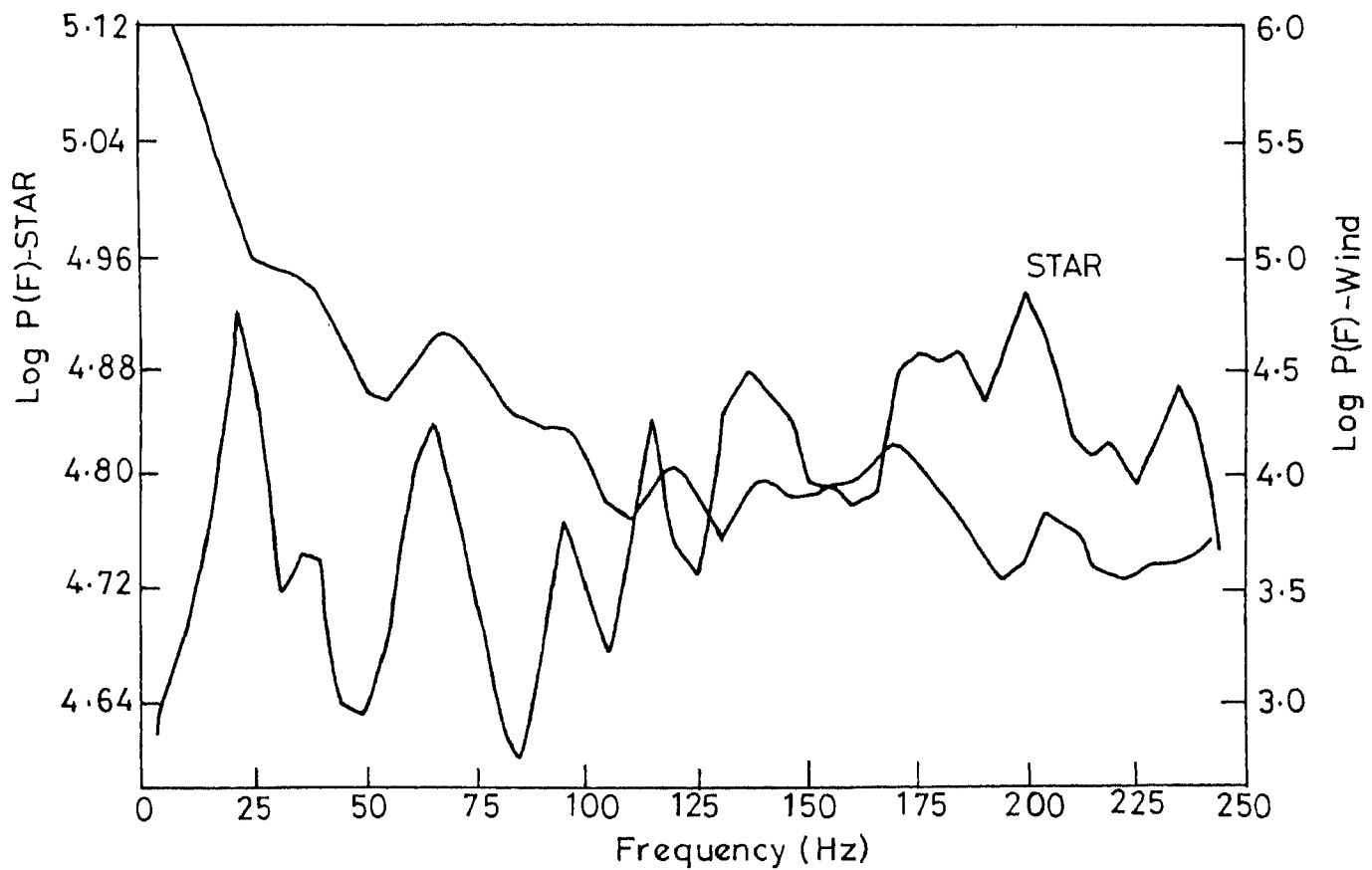
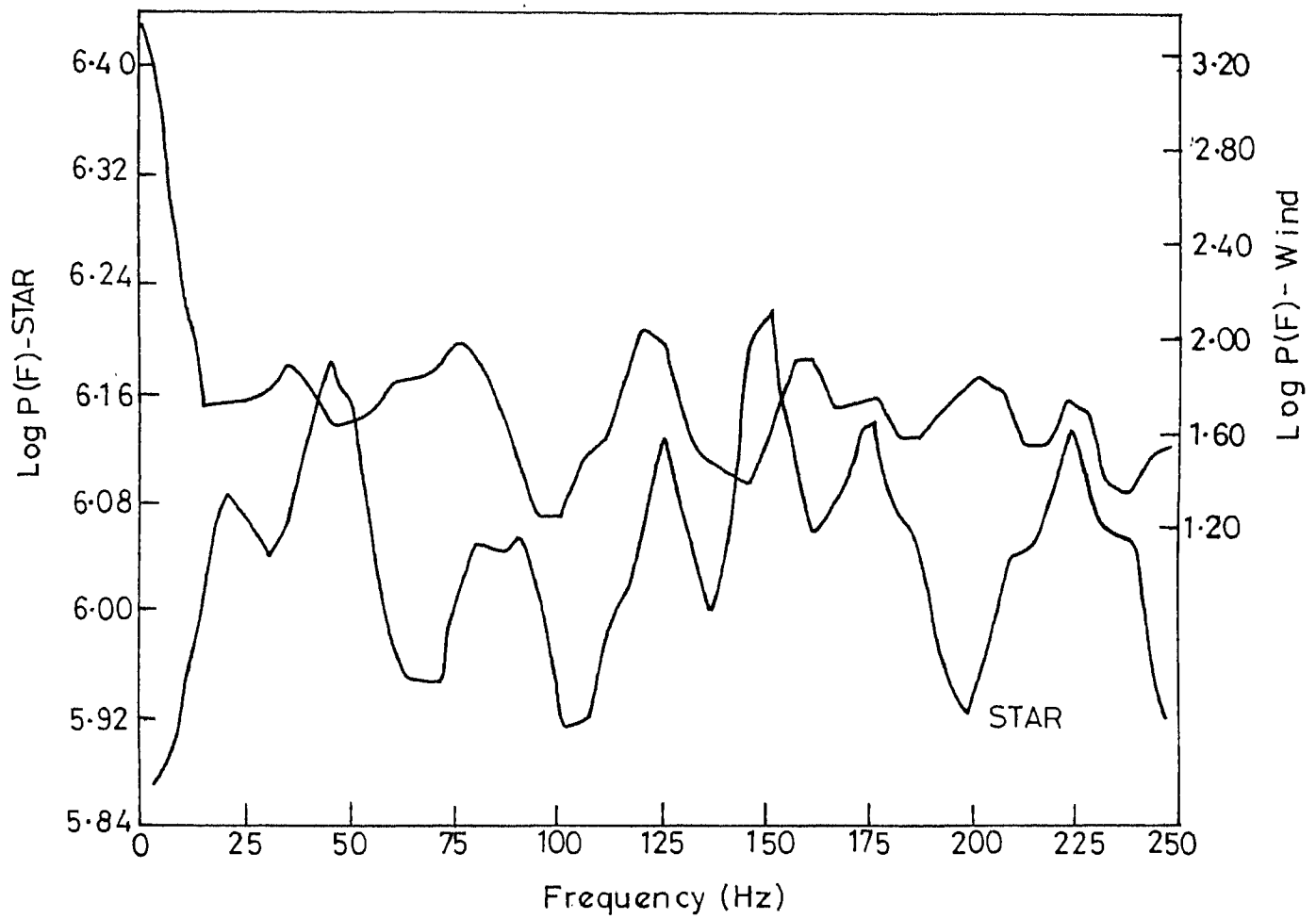


Fig. 4.23. Comparative study of power spectral densities of seeing and wind speed from two samples.

4.3. Weather conditions

The weather and sky conditions prevailing at Kavalur at the time of observations are as indicated in the following table.

TABLE-4.7.A

TABLE SHOWING WEATHER CONDITIONS BETWEEN 21ST AND 25TH MAY 1981, AT KAVALUR  
(BETWEEN 1800 Hrs IST AND 0600 Hrs IST)

Sl. No.	Particulars	21/22	22/23	23/24	24/25	25/26
1.	Transparency	Good	Good	Fair	Poor	Good
2.	Seeing	Fair	Fair	2"	-	Good
3.	Humidity	36%	36%	35%	41%	50%
4.	Temperature	31°C	31°C	31°C	31.5°C	30°C
5.	Spectroscopic hours	8	8	4	4	8
6.	Photometric Hours	4	4	0	0	2
7.	Remarks	Nil	Nil	Overcast	Passing Clouds	Nil

TABLE - 4.7.B

TABLE SHOWING WEATHER CONDITIONS BETWEEN  
21ST AND 25TH MAY 1981 AT KAVALUR

(BETWEEN 21 Hrs IST & 2400 Hrs IST)

Sl. No.	Particulars	21/22	22/23	23/24	24/25	25/26
1.	Transparency	Good	Good	Overcast	Poor	-
2.	Seeing	Good	Good	-	2"	-
3.	Humidity	38%	38%	50%	45%	-
4.	Temperature	30°C	30°C	29°C	30°C	-
5.	Spectroscopic hours	8	8	4	4	8
6.	Photometric hours	4	4	0	0	2
7.	Remarks	Nil	Nil	Overcast	Passing Clouds	-

TABLE-4.7.C

TABLE SHOWING WEATHER CONDITIONS BETWEEN  
21ST AND 25TH MAY 1981 AT KAVALUR

(BETWEEN 2400 HRS IST TO 0300 HRS IST)

Sl. No.	Particulars	21/22	22/23	23/24	24/25	25/26
1.	Transparency	Fair	Fair	Overcast	Poor	-
2.	Seeing	Good	Good	-	-	-
3.	Humidity	55%	55%	55%	51%	-
4.	Temperature	28°C	28°C	28°C	29°C	-
5.	Spectroscopic hours	8	8	4	4	8
6.	Photometric hours	4	4	0	0	2
7.	Remarks	Nil	Nil	Overcast	Passing Cloud	-

TABLE - 4.7.D

TABLE SHOWING WEATHER CONDITIONS BETWEEN  
21ST AND 25TH MAY 1981 AT KAVALUR

(BETWEEN 0300 HRS IST AND 0600 HRS IST)

Sl. No.	Particulars	21/22	22/23	23/24	24/25	25/26
1.	Transparency	Good	Good	Fair	Fair	-
2.	Seeing	Fair	Fair	3"	1"	-
3.	Humidity	78%	78%	57%	65%	-
4.	Temperature	26°C	26°C	27°C	27°C	-
5.	Spectroscopic hours	8	8	4	4	8
6.	Photometric hours	4	4	0	0	2
7.	Remarks	Nil	Nil	Overcast	Passing Cloud	-

C H A P T E R VCOHERENCE ANALYSIS5.1. Introduction

On subjecting a pair of time series, stellar intensity fluctuations and one of the atmospheric turbulence parameters ( either wind speed or atmospheric temperature ), to spectral coherence analysis, the values for coherence and phase difference between various Fourier components of the two fluctuating parameters were obtained. The mathematical method followed for evaluating coherence and phase angle is as originally formulated by N.R. Goodman. In recent literature, many forms of the formulae are found<sup>44,45,47</sup>. The method outlined in Goodman's<sup>46</sup> paper is followed in the present work. The coherence between the stellar intensity fluctuation and turbulence fluctuation is briefly discussed below.

5.2 Mathematical method

We have synchronous time histories of data pertaining to astronomical seeing and atmospheric turbulence. Let us designate them S and T respectively. Their power spectra as defined in chapter IV will be  $P_S(f)$  and  $P_T(f)$  which represent the spectral densities of the two elements at any given frequency  $f$ .

Let us now define the cross-spectrum  $P_{ST}(f)$  as

$$P_{ST}(f) = \int_{-\infty}^{+\infty} C_{ST}(\tau) e^{2\pi i f \tau} d\tau$$

which is Fourier transform of the cross-correlation function  $C_{ST}(\tau)$ . Generally the function  $P_{ST}(f)$  is a complex quantity and can be represented by

$$P_{ST}(f) = R_{ST}(f) + i S_{ST}(f)$$

the quantity  $R_{ST}(f)$  being the real part of the transform, is called the co-spectrum, and  $S_{ST}(f)$ , the imaginary part, is called the quadrature spectrum.

The cross-correlation function  $C_{ST}(\tau)$  is composed of two parts, viz., the even part

$$C_{ST}^+(\tau) = \lim_{T \rightarrow \infty} \frac{1}{2T} \int_{-T/2}^{+T/2} [S(t) \cdot I(t+\tau) + S(t+\tau) \cdot I(t)] dt$$

and the odd part

$$C_{ST}^-(\tau) = \lim_{T \rightarrow \infty} \frac{1}{2T} \int_{-T/2}^{+T/2} [S(t) \cdot I(t+\tau) - S(t+\tau) \cdot I(t)] dt$$

It can be shown that the finite cosine and sine series transforms given by

$$R_{ST}(f) = \int_{-\infty}^{+\infty} C_{ST}^+(\tau) \cdot \cos 2\pi f \tau d\tau$$



and

$$S_{ST}(f) = \int_{-\infty}^{+\infty} C_{ST}^{-1}(\tau) \sin 2\pi f \tau d\tau$$

and known as co-spectrum and quadrature spectrum contain the basic interrelation between the two series.

The quantity defined by

$$r(f) = \left[ \frac{R_{ST}^2(f) + S_{ST}^2(f)}{P_S(f) \cdot P_T(f)} \right]^{1/2}$$

is known as the " coherence " and is a measure of the cross-correlation between the Fourier components of the two variables.

The quantity

$$\theta(f) = \text{arc tan} \left[ \frac{S_{ST}(f)}{R_{ST}(f)} \right]$$

gives the phase difference between them for the frequency band centered around  $f$ .

Errors in the determination of these two quantities owing to finite length of data can be calculated in terms of equivalent degrees of freedom. For the phase angle  $\theta(f)$  the error is given by

$$\Delta\theta(f) = \text{arc sin} \left[ \frac{1 - r^2(f)}{r^2(f)} \left\{ 0.5^{-2/k} - 1 \right\} \right]^{1/2}$$

where  $k$  is the degrees of freedom as defined by Blackman and Tukey (1959)<sup>42</sup>. An approximate expression  $\Delta r(f)$  as given by

the analysis of Van Isacker (1961)<sup>48</sup>, is

$$r(f) = \frac{\Delta P(f)}{P(f)} [r^2(f) + 1]^{1/2}$$

where  $\Delta P(f)$  is the probable error of one of the associated spectra. The expression is valid provided the value of  $r(f)$  is not too small.

### 5.3 Installation of micrometeorological sensors

As mentioned earlier, data on both astronomical seeing and atmospheric turbulence is collected simultaneously, not only to study the power spectra of the individual time histories, but also to study the coherence between the two processes. Further, coherence in atmospheric turbulence amongst different layers also has been investigated, particularly in regard to wind speed data. In light of this scheme of analysis, philips 7-channel analog tape recorder is fed with inputs from PMT star signal amplifier and several micrometeorological sensors installed in different directions and heights. The network of installation of these sensors is clearly shown in Figs. 5.2 to 5.5.

Fig. 5.1 shows the telescope pointed at an object about  $45^\circ$  position. The telescope is trained at different stars, scanning the sky and thus covering a range of zenith distances and stellar magnitudes.



Fig. 5.1. 1-m optical telescope pointed at an object at medium hour angle position.

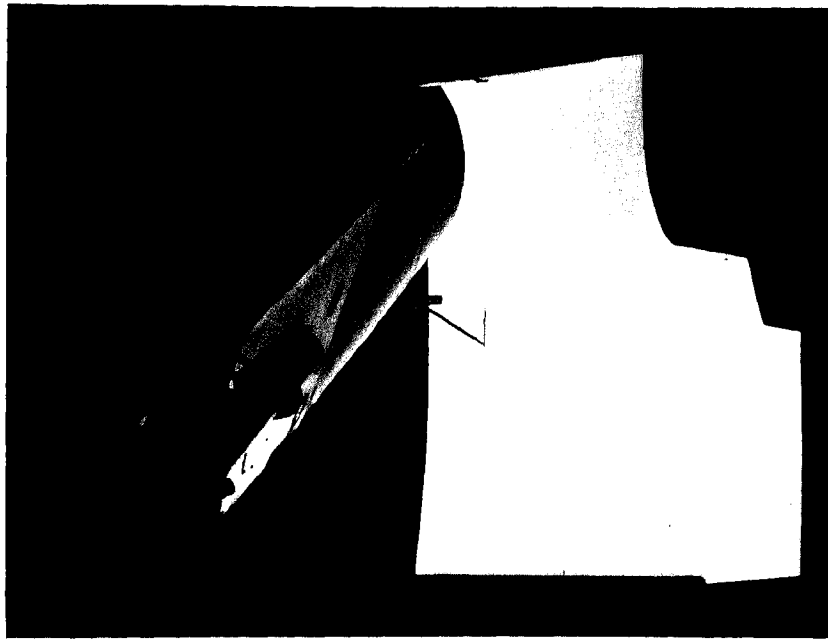


Fig. 5.2. View of a hot-wire sensor installed at the dome slit height (approximately 23 meters) when star signals were collected simultaneously with that of windspeed.

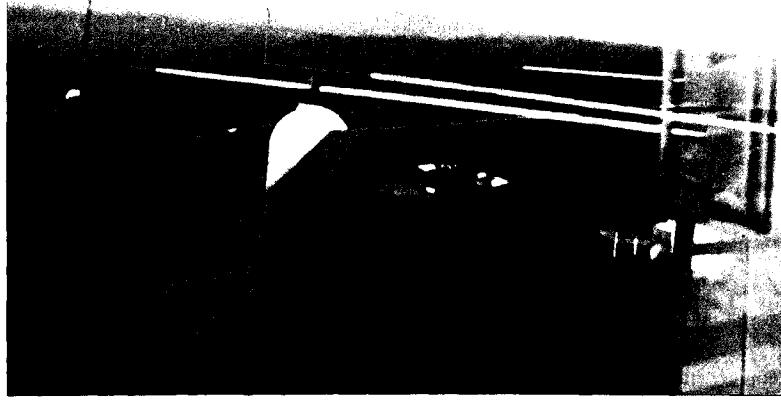


Fig. 5.3. An array of hot-wire sensors projected out at the cat-walk height (approximately 17 meters) of the 1-m telescope dome.

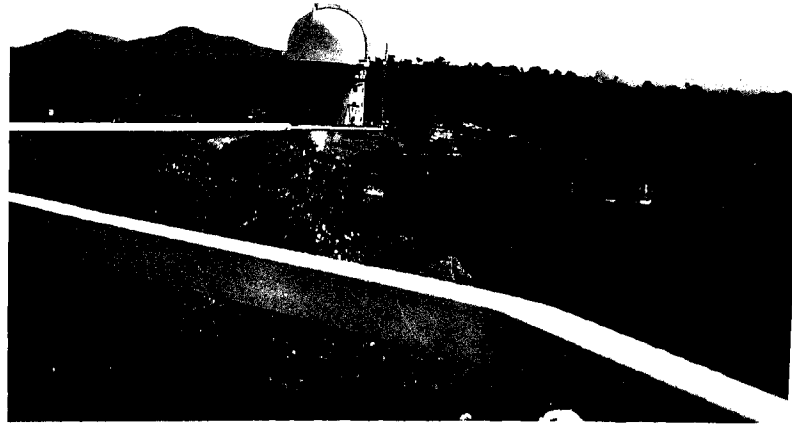


Fig. 5.4. View of the thermocouple installed at the cat-walk height (approximately 17 meters) of the 1-m telescope dome.



Fig. 5.5. View of hot-wire sensors installed outside of the dome. one at the cat-walk height and the other at the next lower floor (approximately 14 meters).

In Fig. 5.2 is shown a hot-wire anemometer sensor that is installed from the dome slit. Much of mechanical engineering effort has been put in while installing the sensor at this location and a similar one atop the dome itself at a height of nearly 80 ft. Extreme care has been exercised while rotating the dome, opening and closing the dome slit when at the same time handling the long cables trailing from different sensors.

Where-ver long cables have been used, zero suppression has been effected with the DISA hot-wire anemometer electronics in order to nullify the effects of those long cables.

Fig. 5.3 shows an array of micrometeorological sensors for recording wind speed and temperature fluctuations as obtained at the cat walk height ( about 17 meters ) and in different directions. The long rods holding the sensor probes are rigidly clamped to the cat walk railings using C-clamps. The depth through which these rods has been projected from outside the cat walk railing can be varied utilising the length of the rods. All the signals coming from different transducers have been continuously monitored at the time of recording so that appropriate gain settings and other necessary adjustments of the sensors can be made. The installation scheme of meteorological sensors for turbulence measurements is as shown in Fig.5.6. Monitoring and recording of the various signals are as shown in Fig.5.7.



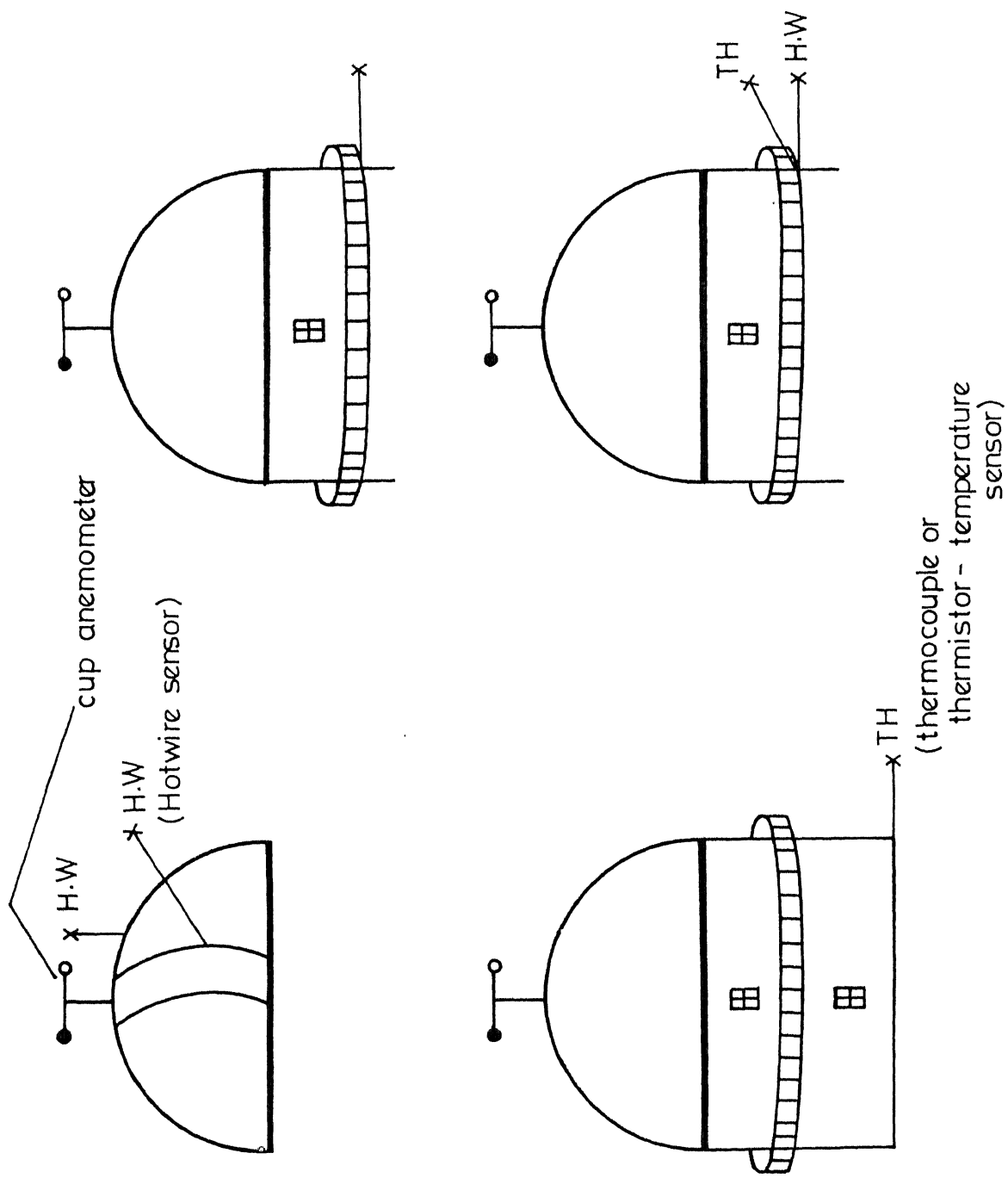


FIG-5.6. TURBULENCE.  
 Analog data sampled at  $\Delta t = 1 \text{ ms}$ , 1000 Hz;  
 $\Delta t = 32 \text{ ms}$ , 16 Hz ;  $\Delta t = 8 \text{ ms}$ , 62.5 Hz.



Fig. 5.7. Set-up showing CRO, DVM, signal amplifiers, DISA hotwire anemometer electronics, thermocouple amplifiers, recorders for monitoring and recording astronomical seeing and atmospheric turbulence data.

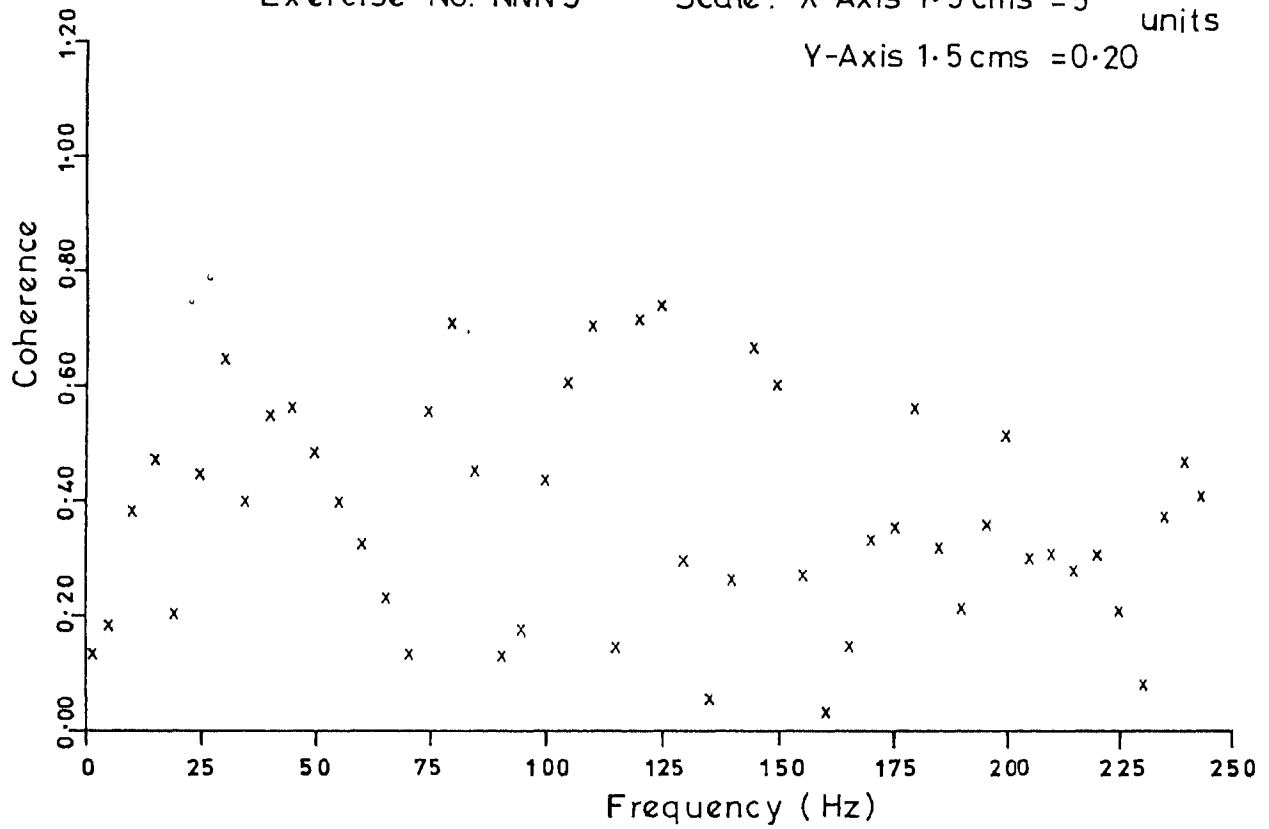
#### 5.4 Interrelations: Seeing Vs. Wind speed

In the example of the last chapter, it was clear that interrelations exist between the fluctuating phenomena of seeing and turbulence ( wind speed variations ). It is also noticed that the spectral density curves have an over all pattern which show some similarity in respect of the existence of density peaks at selected frequencies.

In order to examine the extent of such relationship, the mathematical method described above was followed and " coherence " and " phase angle " at different frequencies were arrived at. To avoid rapid fluctuations of computed values of  $\rho$  by integrals of  $2\pi$  radians which arise in the computational process, the absolute magnitude  $\rho$  at different frequencies have been plotted in the diagrams. Indeed, the plots of coherence and phase angle in the particular case shown in Fig. 4.23 in the last chapter are given in Fig. 5.8, 5.9. In order to be sur. that some physical mechanism is responsible for both phenomena, several other simultaneous recordings have been analysed. <sup>see Fig. 4.23</sup> these are shown in Figs. (5.10, 5.11). In all cases it is noticed that prominent density peaks which appear at preferred frequencies have high coherences. The phase difference between the respective Fourier components have steady values near these coherence peaks, signifying physical relations between the two parameters.

### Coherence function vs Frequency Coherence between Seeing and Turbulence

Exercise No. NNN9      Scale: X-Axis 1.5 cms = 5 units  
Y-Axis 1.5 cms = 0.20



### Phase angle difference vs Frequency Phase between Seeing and Turbulence

Exercise No. NNN9      Scale: X-Axis 1.5cms = 5 units  
Y-Axis 1.5cms = 80.0

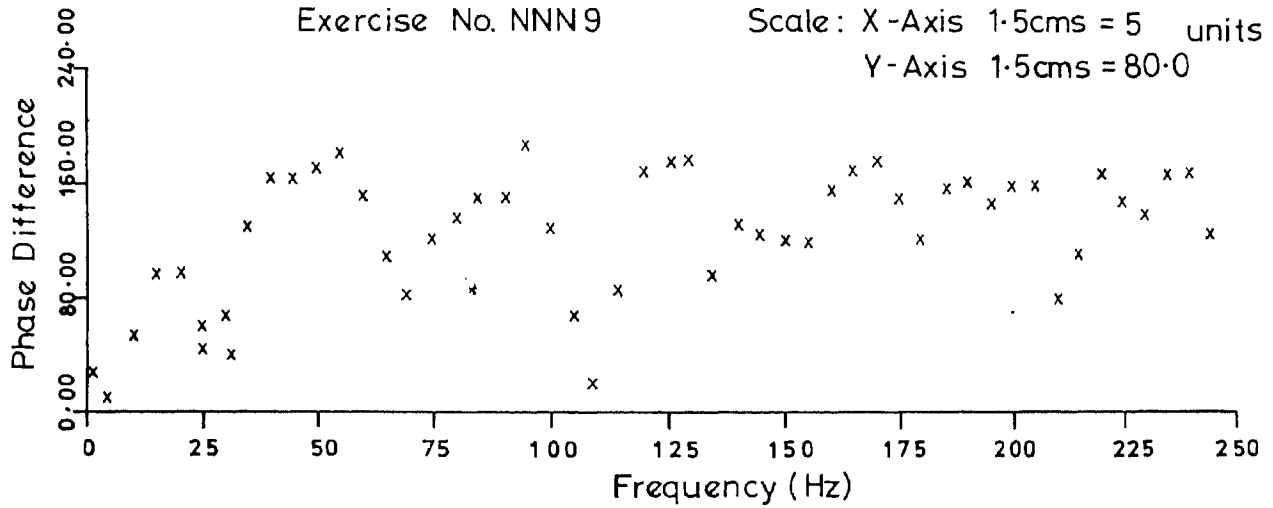
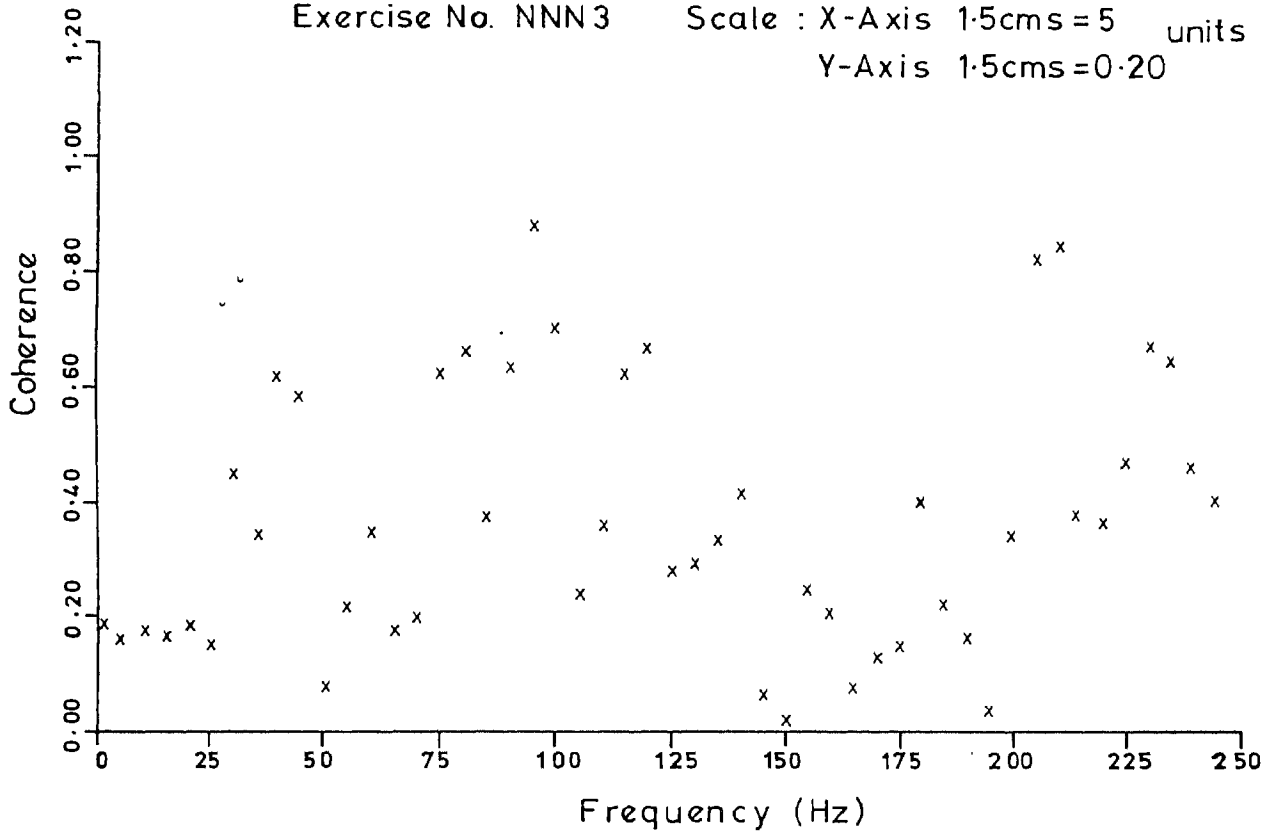


Fig. 5.8.

Coherence function vs. Frequency  
 Coherence between Seeing and Turbulence

Exercise No. NNN3      Scale : X-Axis 1.5cms = 5 units  
 Y-Axis 1.5cms = 0.20



Phase angle difference vs. Frequency  
 Phase between Seeing and Turbulence

Exercise No. NNN3      Scale: X-Axis 1.5cms = 5 units  
 Y-Axis 1.5cms = 80.0

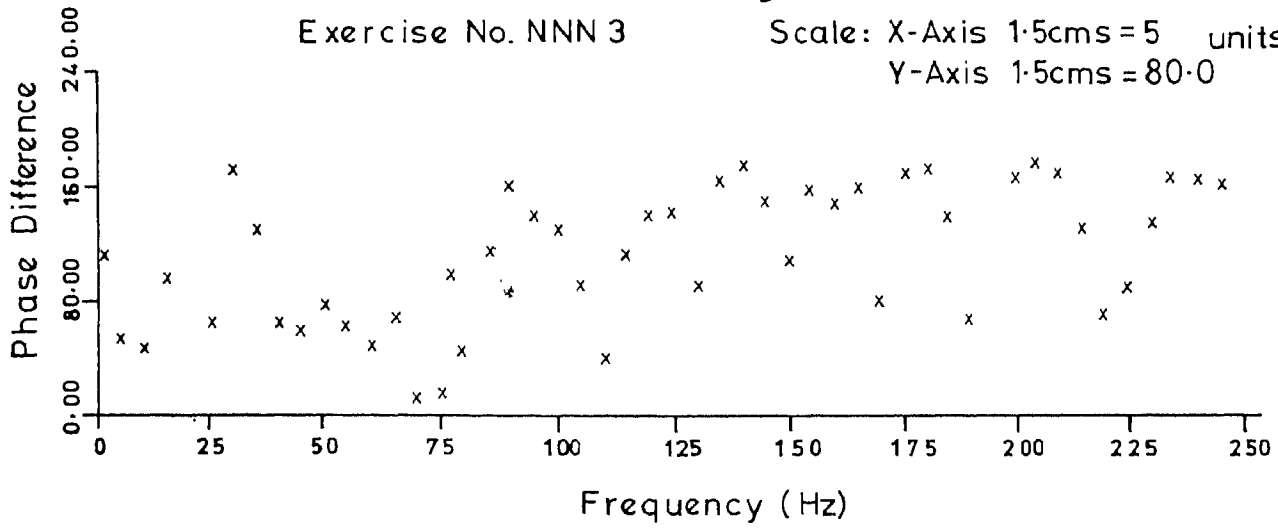


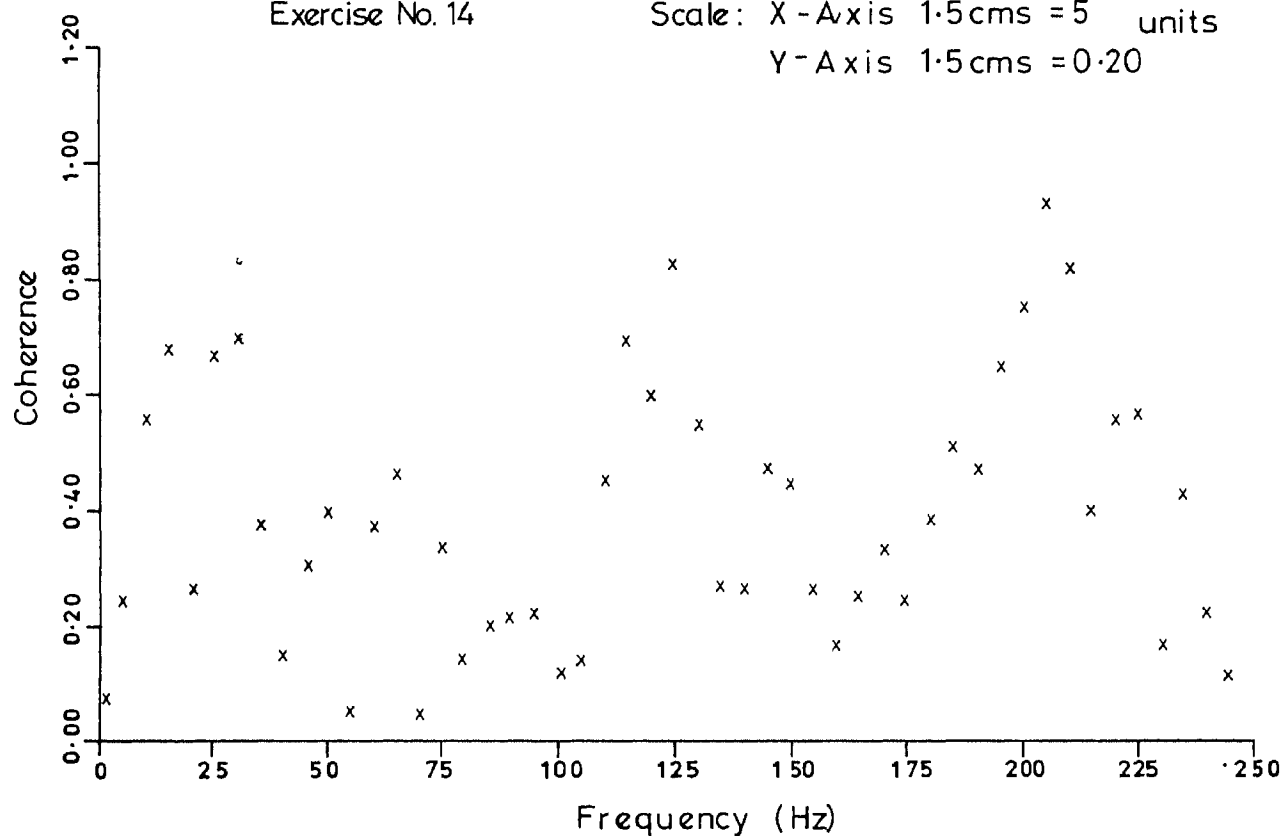
Fig. 5.9.

Coherence function vs. Frequency  
 Coherence between Seeing and Turbulence

Exercise No. 14

Scale: X-Axis 1.5cms = 5 units

Y-Axis 1.5cms = 0.20



Phase angle difference vs. Frequency  
 Phase between Seeing and Turbulence

Exercise No. 14

Scale: X-Axis 1.5cms = 5 units

Y-Axis 1.5cms = 80.0

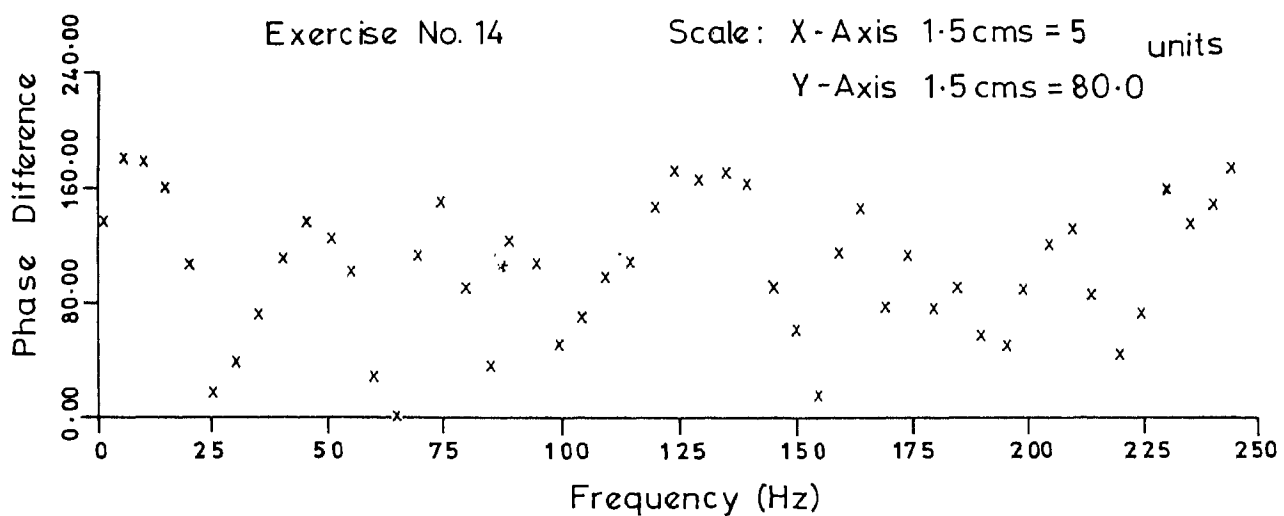


Fig. 5.10.

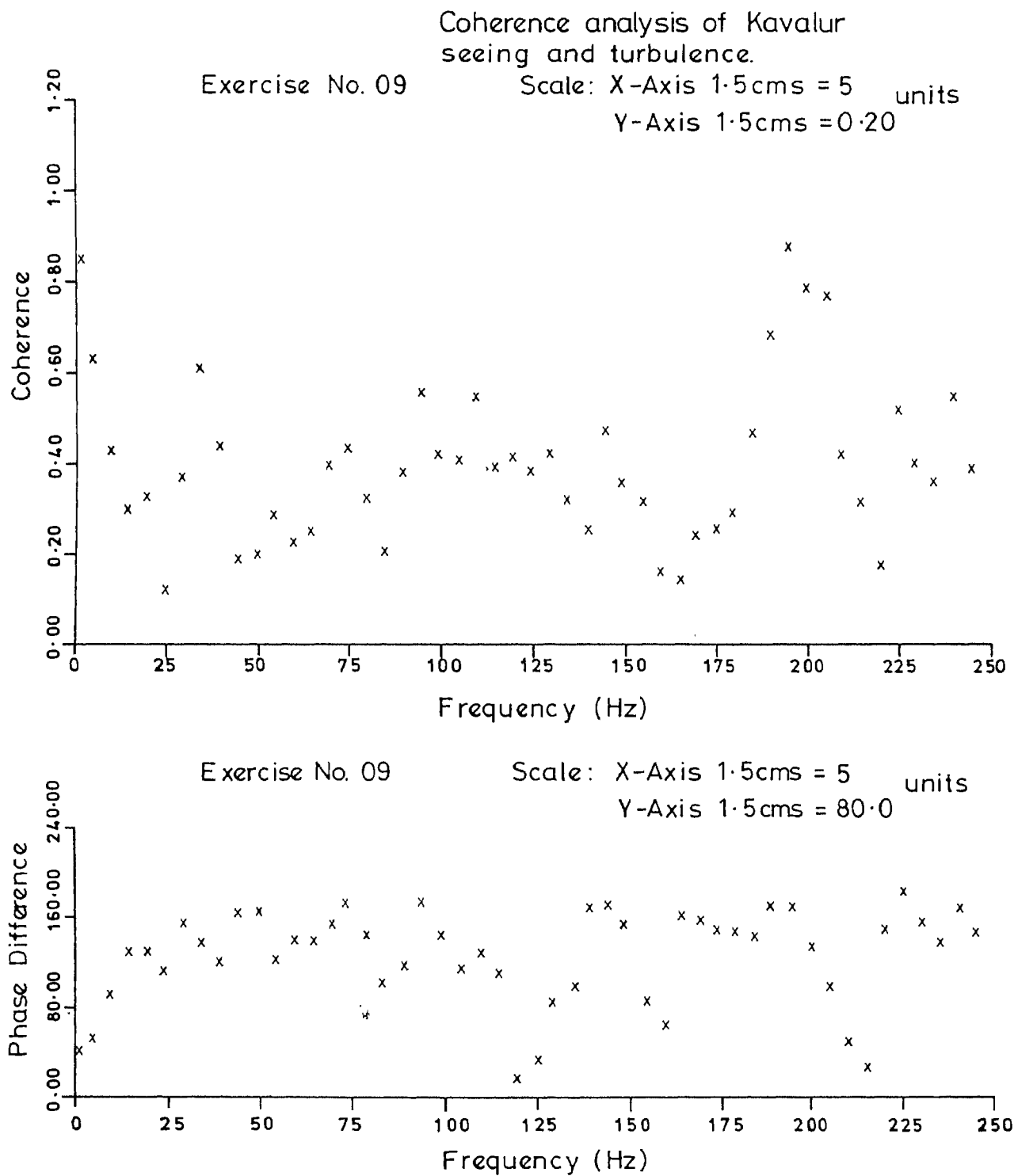


Fig. 5.11.

There are some density maxima in S curves without corresponding features in the T curves; it may be noticed that the coherence plots in these cases indicate poor interrelation. As the seeing phenomenon is the integrated effect of several layers of our atmosphere, they may not always have correspondence at all layers. Such features may not be totally unexpected.

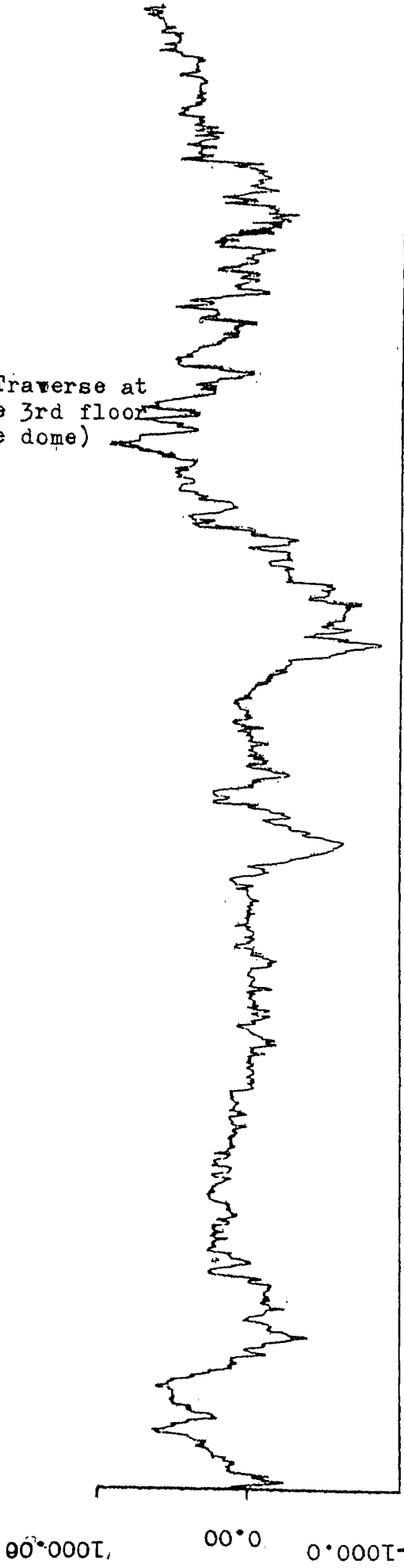
The connection between the wind speed fluctuations at different levels to the corresponding seeing fluctuations can be briefly summarised as follows.

Different wind measurements have been utilised by employing different types of instruments. Fig. 5.12 shows the record obtained by a cup anemometer as compared with that obtained by a hot-wire anemometer. The cup anemometer was placed at the top of the dome which measured the wind speed variations in the layers through which the stellar beam would have to pass. The hot wire anemometer at the observer's level records the variations immediately below this layer. Although the two records do not have much similarity because of enormous differences in their frequency response characteristics their spectral density curves bring out the correspondence very clearly. This can be seen in Fig. 5.13. The two spectral curves are remarkably similar in nature although the higher instrument has recorded certain peaks which are different from those of the lower instrument. The peaks are slightly shifted in the higher curve.



WIND SPEED DATA

(Ref: Traverse at  
at the 3rd floor  
of the dome)



WIND SPEED DATA

(Cup anemometer  
from atop the dome)

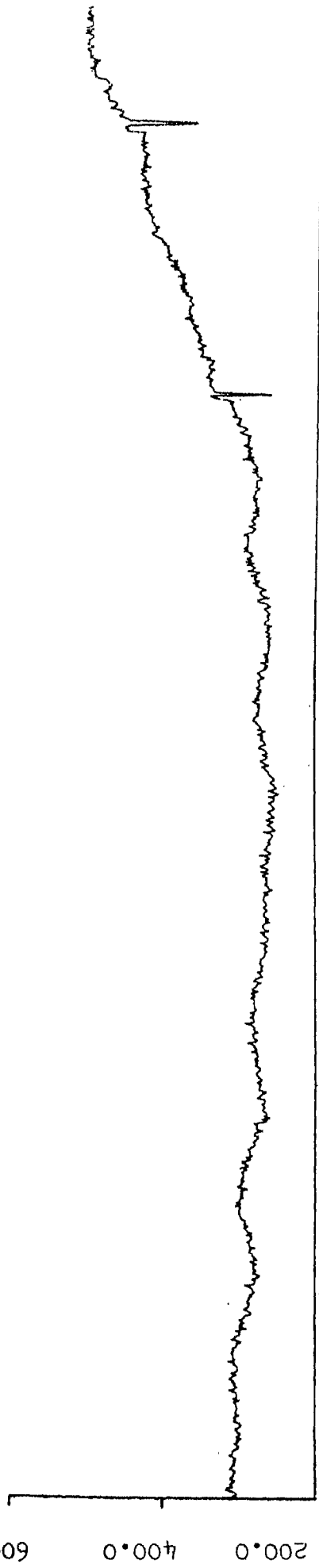


Fig.5.12. A simultaneous record of wind speed  
fluctuations at two different levels.

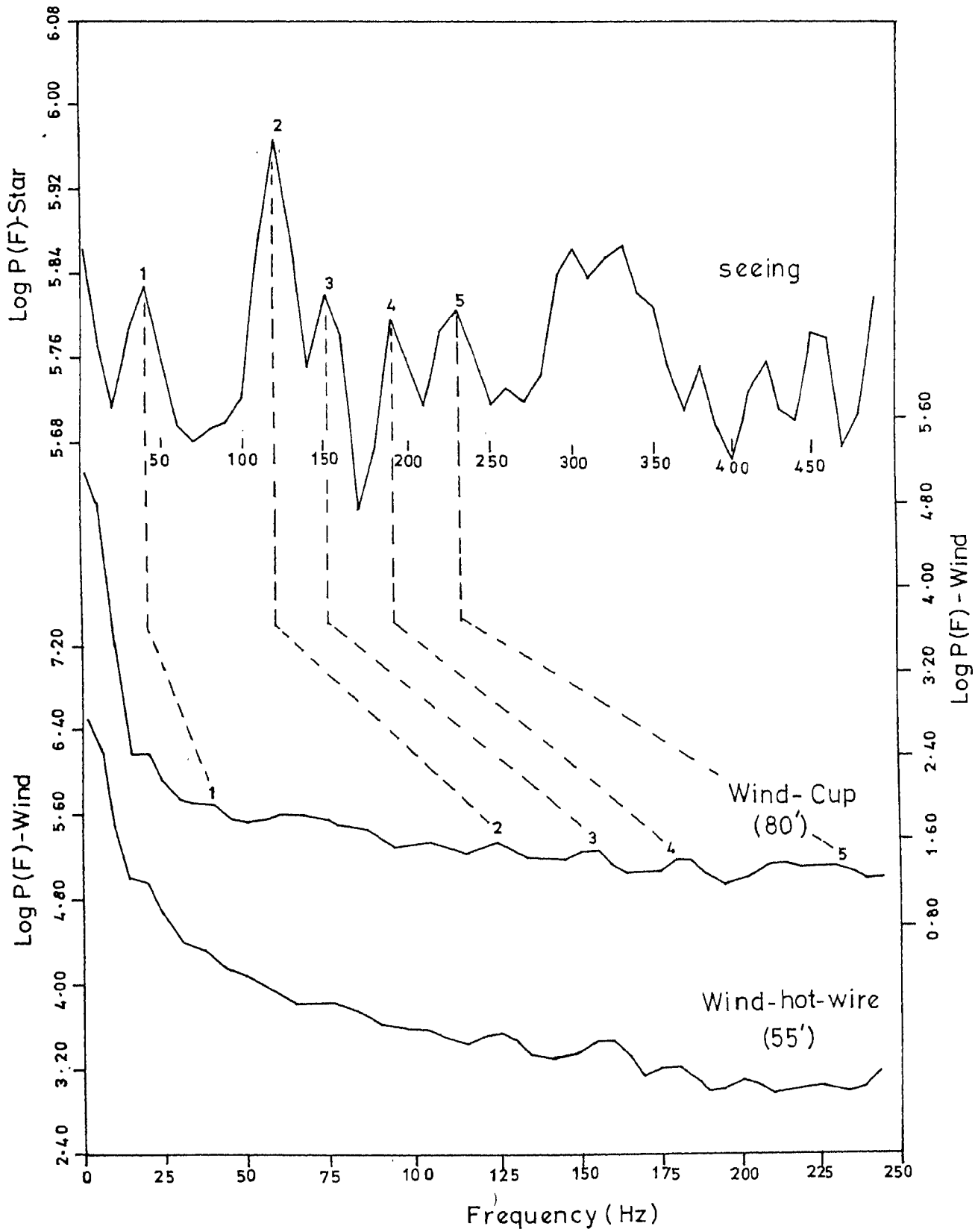


Fig. 5.13. Composite plot of spectral densities of seeing and wind speed at two levels.

Comparison with corresponding seeing fluctuations with higher curve has better correspondence than with the lower curve. This indicates that upper layers have more important role to play in seeing fluctuations. Coherence analysis also confirms this aspect. Fig.5.14 shows coherence between the two wind speed data series as obtained from the higher and lower instruments.

#### 5.5. Interrelations: Seeing Vs Temperature

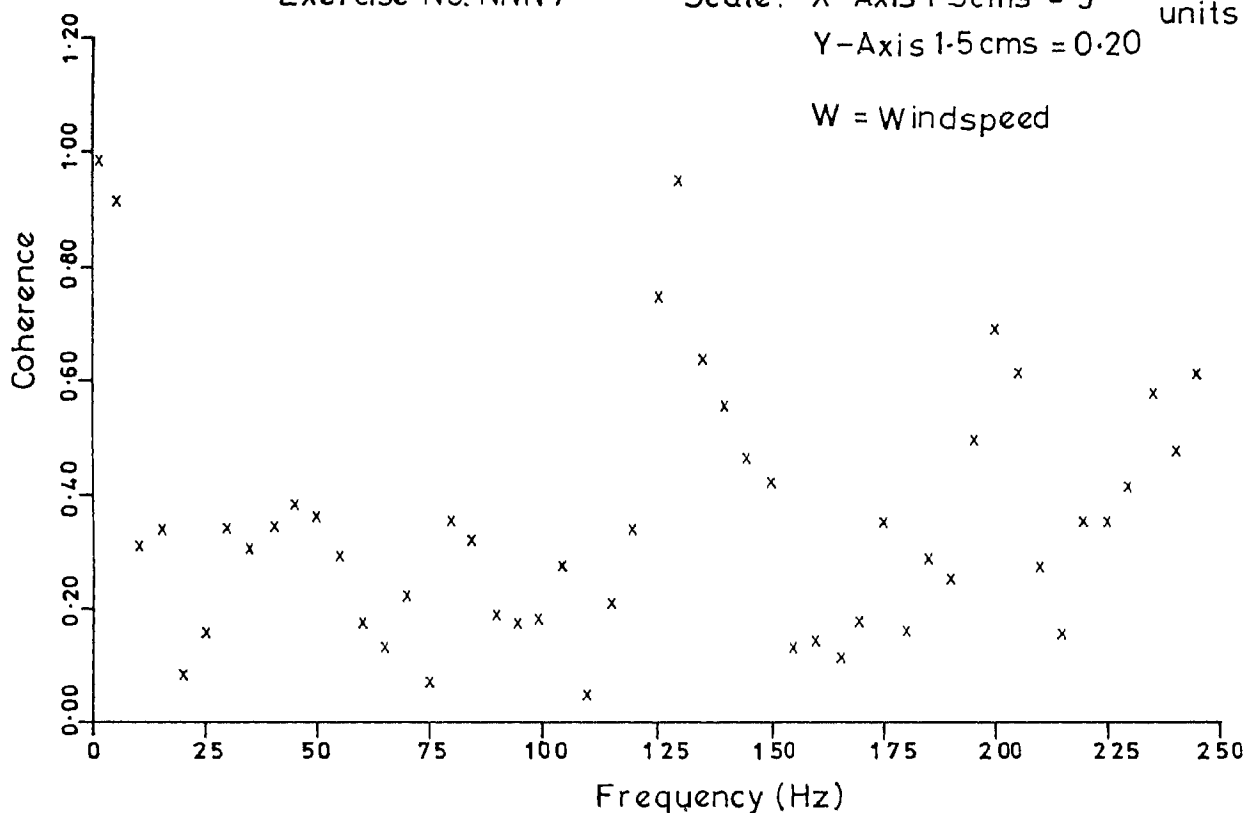
A comparative study can be made of the characteristic spectral features of seeing and temperature fluctuations with the help of Fig.5.15. The data as obtained from thermistor installed at catwalk height is shown here. There is a remarkable correspondence between the two processes. As mentioned earlier, a detailed coherence analysis between the two processes is made using temperature data as collected from more sensitive Cr-Al thermocouple, specially to study the features within the low-frequency region. The details of the records are shown in Figs.5.16 to 5.19. Figs.5.17 and 5.18 show the spectral characteristic of seeing and temperature fluctuations. It is clearly noticed that there exist distinct peaks within frequency bands centring around frequencies 7.5 Hz, 10.0 Hz, 22.5 Hz, 30.0 Hz. Fig.5.19 brings out the coherence between the two time series much more clearly. There exist a good measure of coherence at

Coherence function vs. Frequency  
 Coherence between W and W of Turbulence

Exercise No. NNN 7

Scale: X-Axis 1.5cms = 5 units  
 Y-Axis 1.5cms = 0.20 units

W = Windspeed



Phase angle difference vs. Frequency  
 Phase between W and W of Turbulence

Exercise No. NNN 7

Scale X-Axis 1.5cms = 5 units  
 Y-Axis 1.5cms = 80.00 units

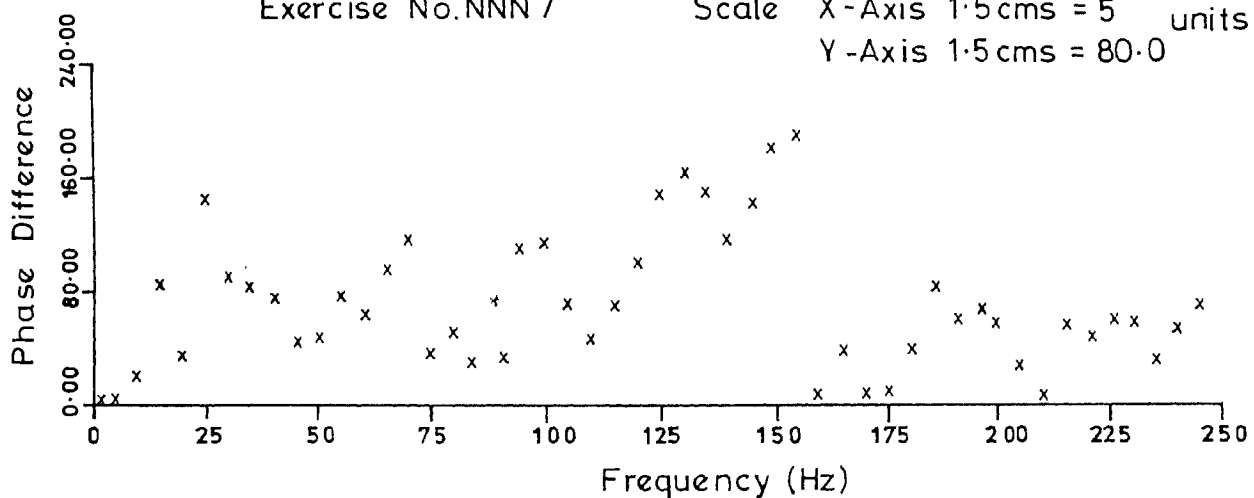


Fig . 5.14.

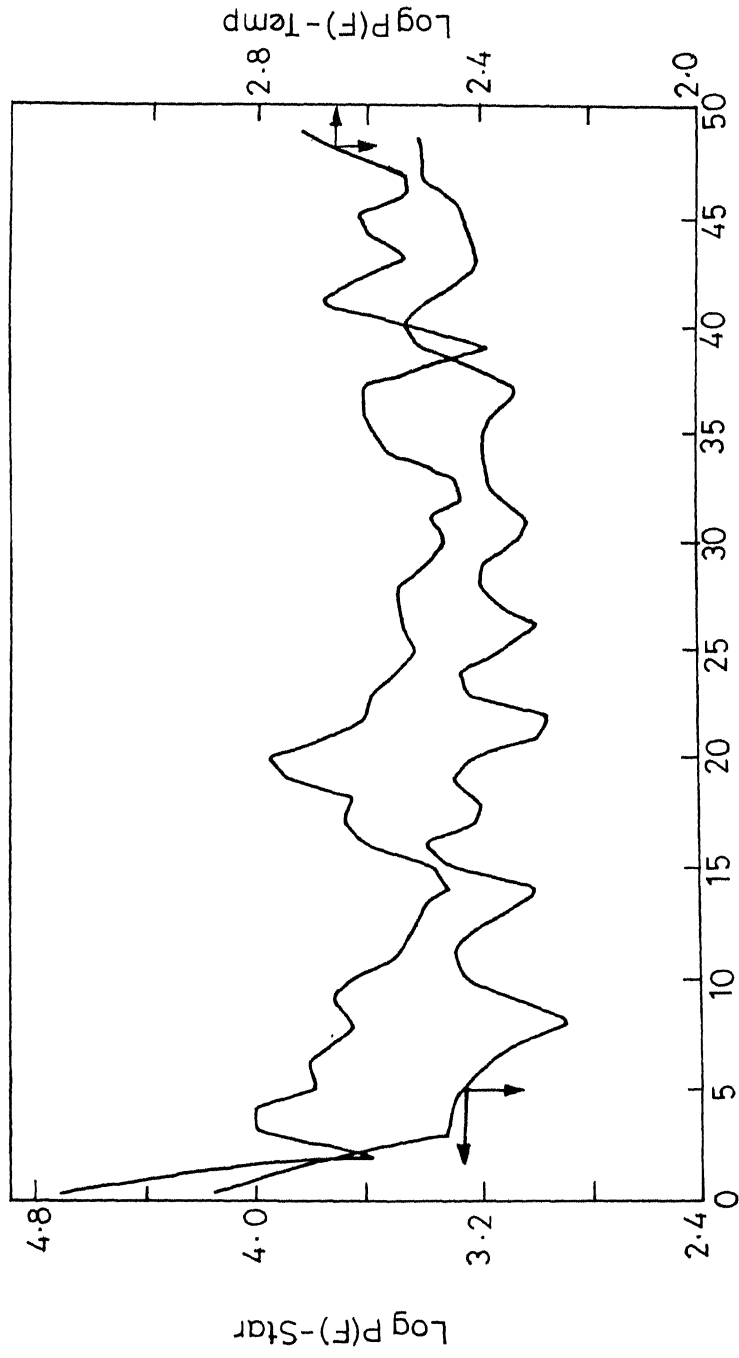
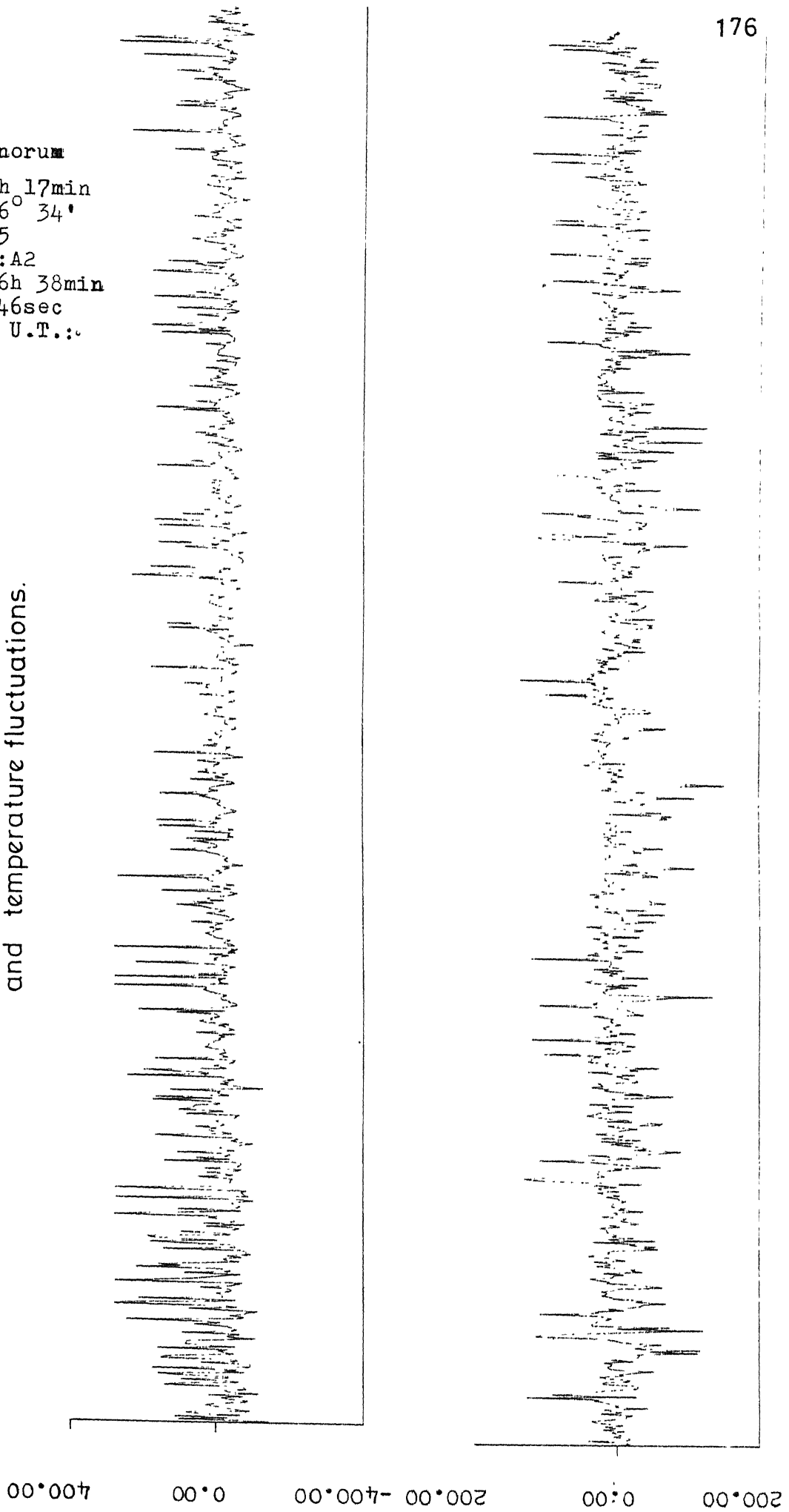


Fig. 5.15. A comparative study of  $\text{Log P(F)}^S$  of seeing and temperature variations.

$\lambda$ -Geminorum  
R.A.: 7h 17min  
Decln.: 16° 34'  
Mag: 3.65  
Sp.Cl.: A2  
LST at 6h 38min  
46sec  
1300Hrs U.T.:

Fig. 5.16. A simultaneous record of scintillation and temperature fluctuations.



Power spectrum and Coherence analysis of Kavalur Seeing.

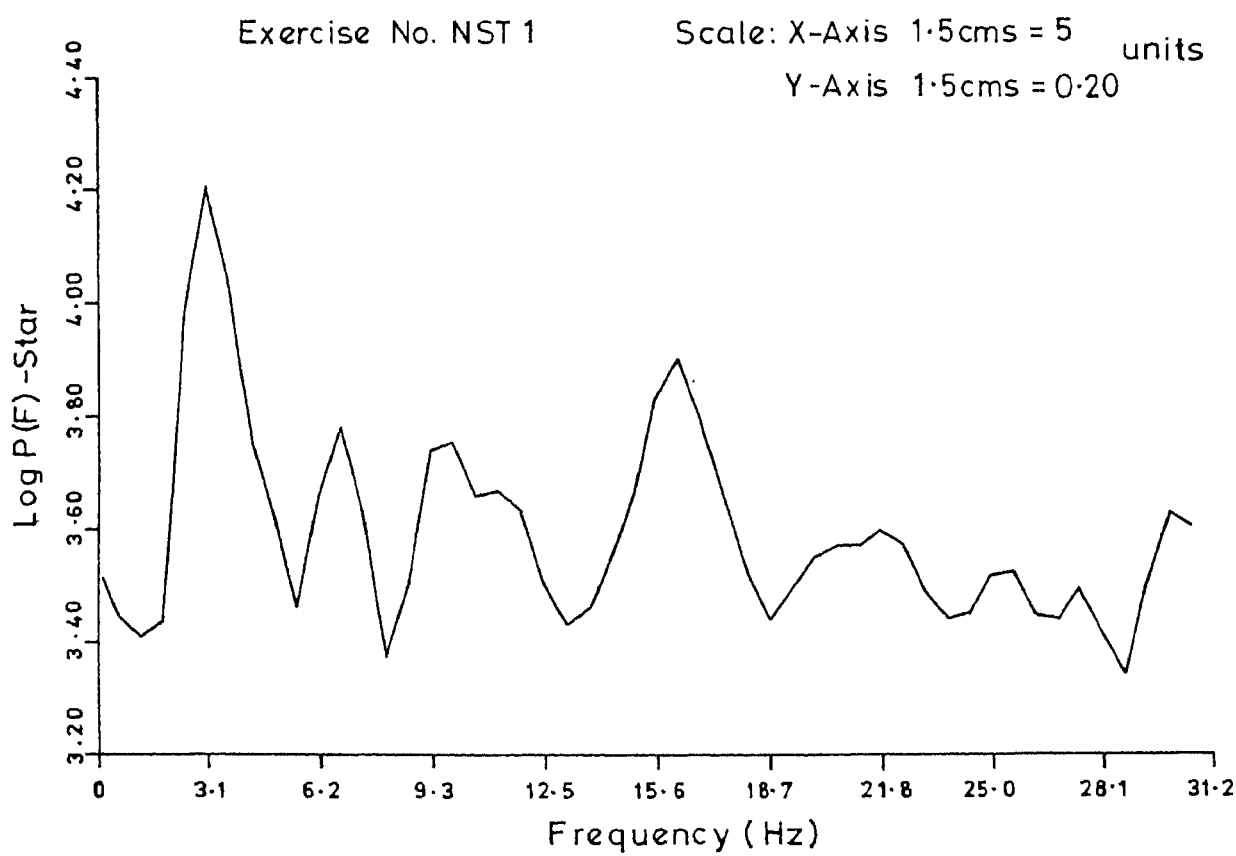
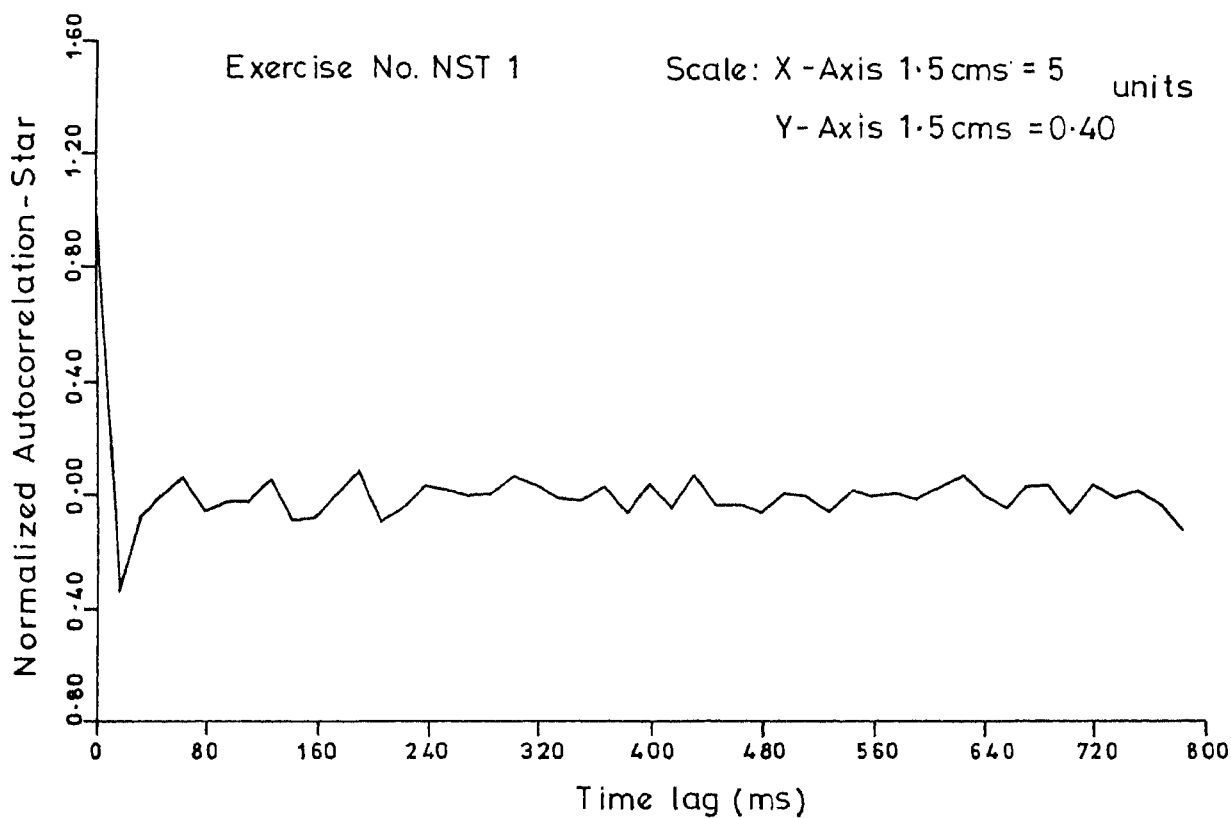


Fig. 5.17

Power spectrum and Coherence analysis of Kavalur turbulence.

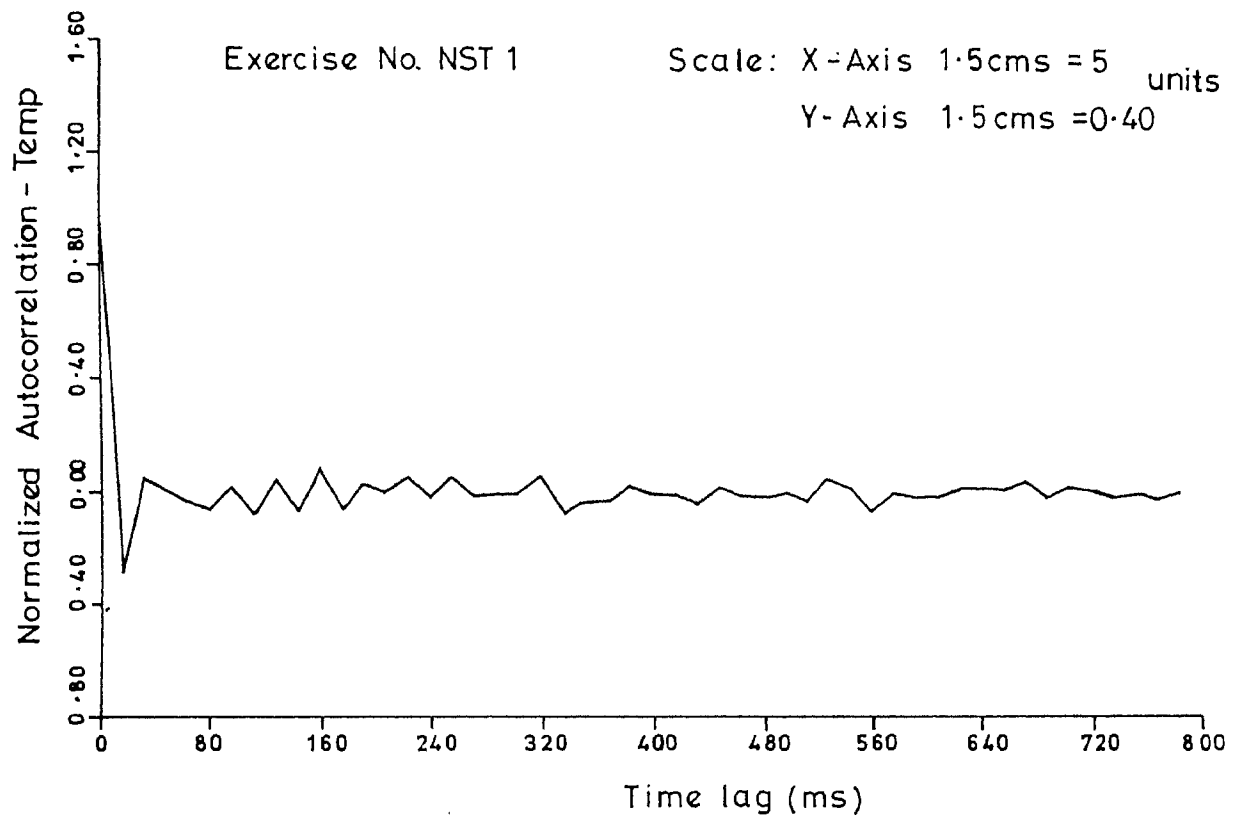


Fig. 5.18.



Power spectrum and Coherence analysis of Kavalur seeing and turbulence.

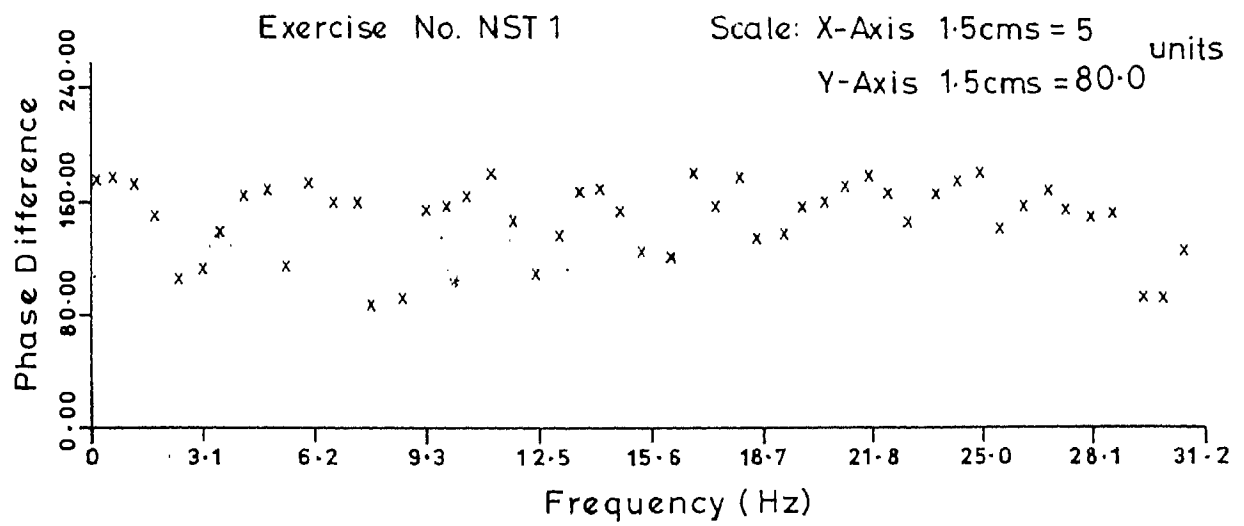
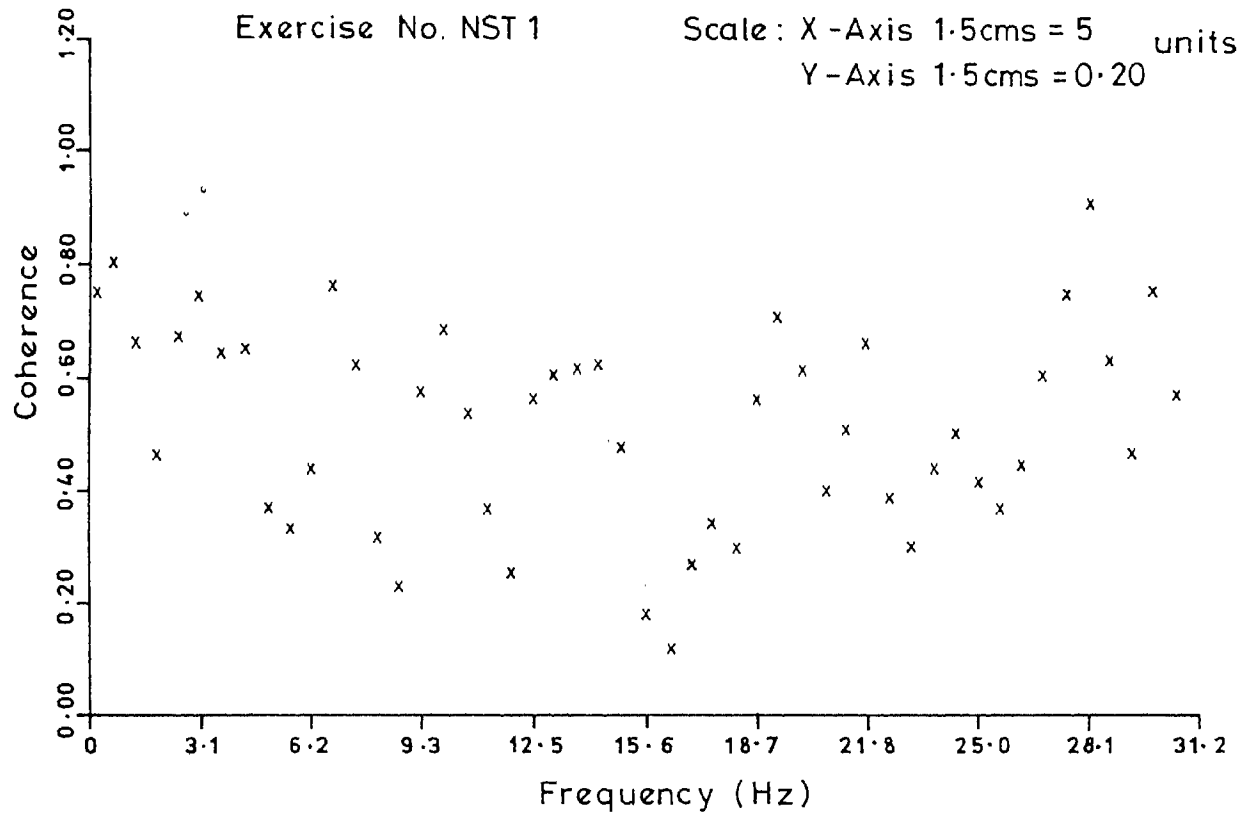


Fig .5.19.

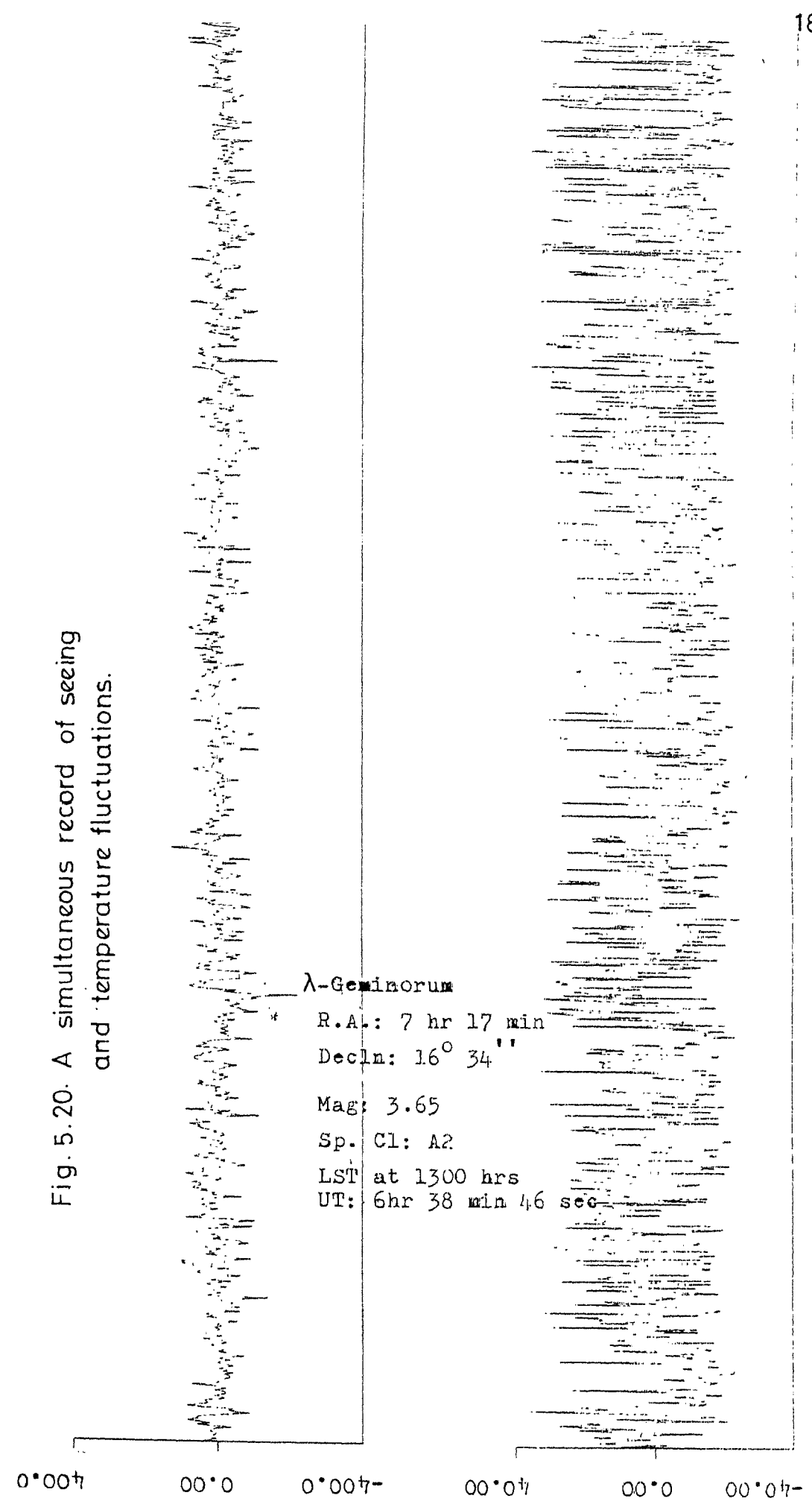
these frequencies and the values of phase angle are steady in these frequency bands. This indicates that there exist physical relations between the two processes to an appreciable extent. Yet another set of records has been presented for highlighting a similar result. These are shown in Figs. 5.20, 5.21, 5.22 and 5.23. In this case the power spectral density curves of the two processes are shown in the Figs. 5.18 and 5.19. Characteristic peaks are exhibited at specific frequencies such as 12.5 Hz, 15 Hz and 25 Hz.

The coherence value at these frequencies are quite high as shown in Fig. 5.23. The phase angles at these frequencies are once again found to be quite steady thus establishing the existence of physical relationship between the two fluctuating phenomena.

#### 5.6. Interrelations: amongst different turbulent layers

With data of turbulence collected as shown in the figures from different heights, similar power spectral and coherence analyses amongst them have been carried out to find the existence of interrelationships within the layers of the stratified structure of the low-lying atmosphere. The results are given in Figs. 5.24 to 5.34. It is seen that close relations exist between fluctuations at two levels near the ground, which suggests that not much error

Fig. 5.20. A simultaneous record of seeing and temperature fluctuations.



Power spectrum and Coherence analysis of Kavalur seeing

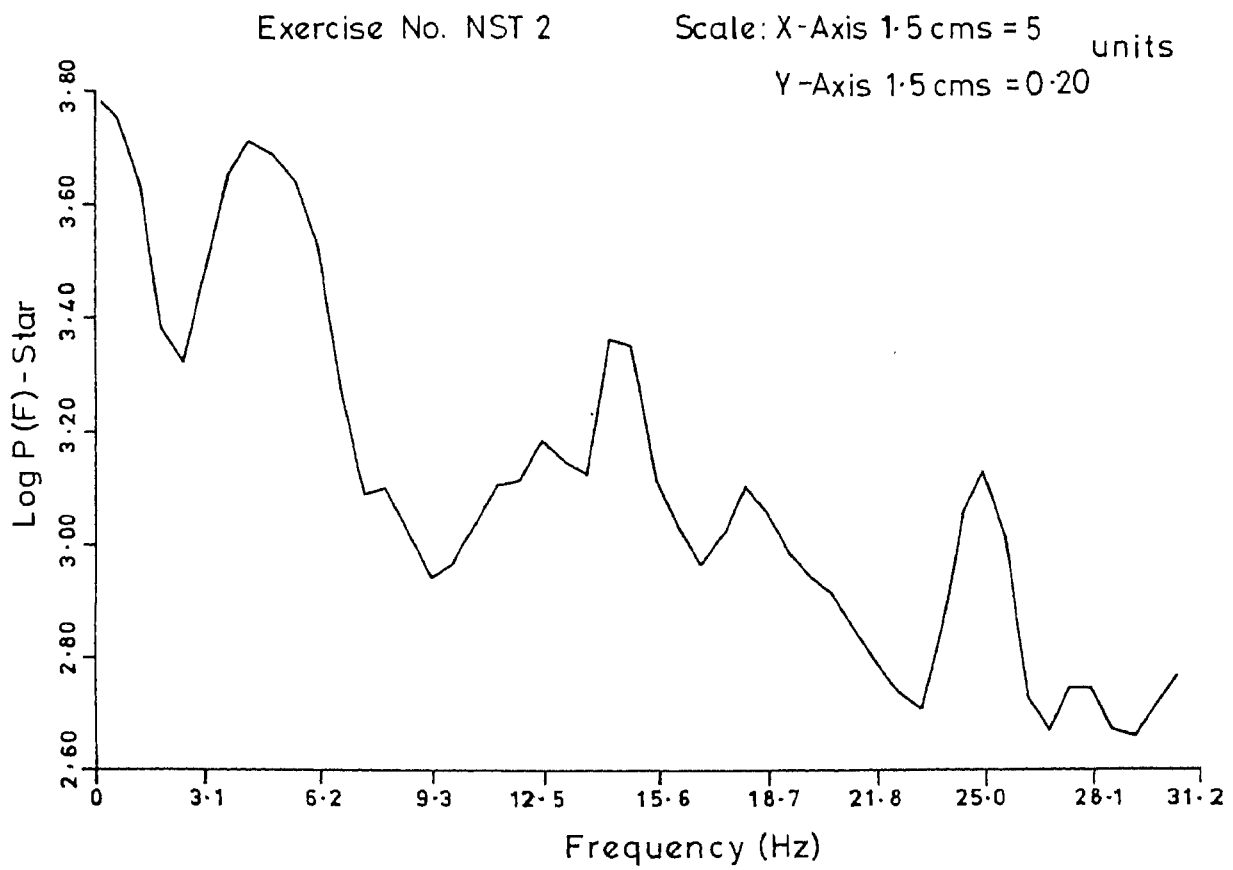
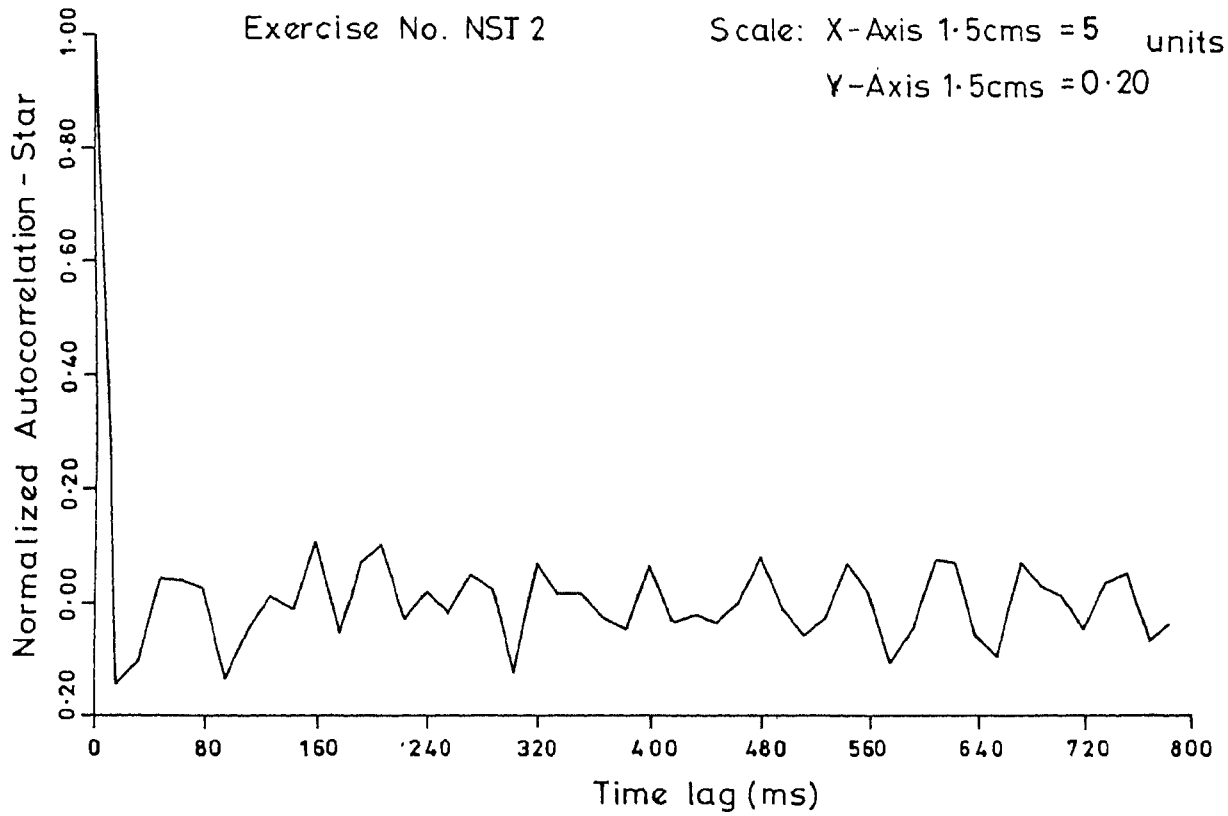


Fig. 5 21.

Power spectrum and Coherence analysis of Kavalur turbulence.

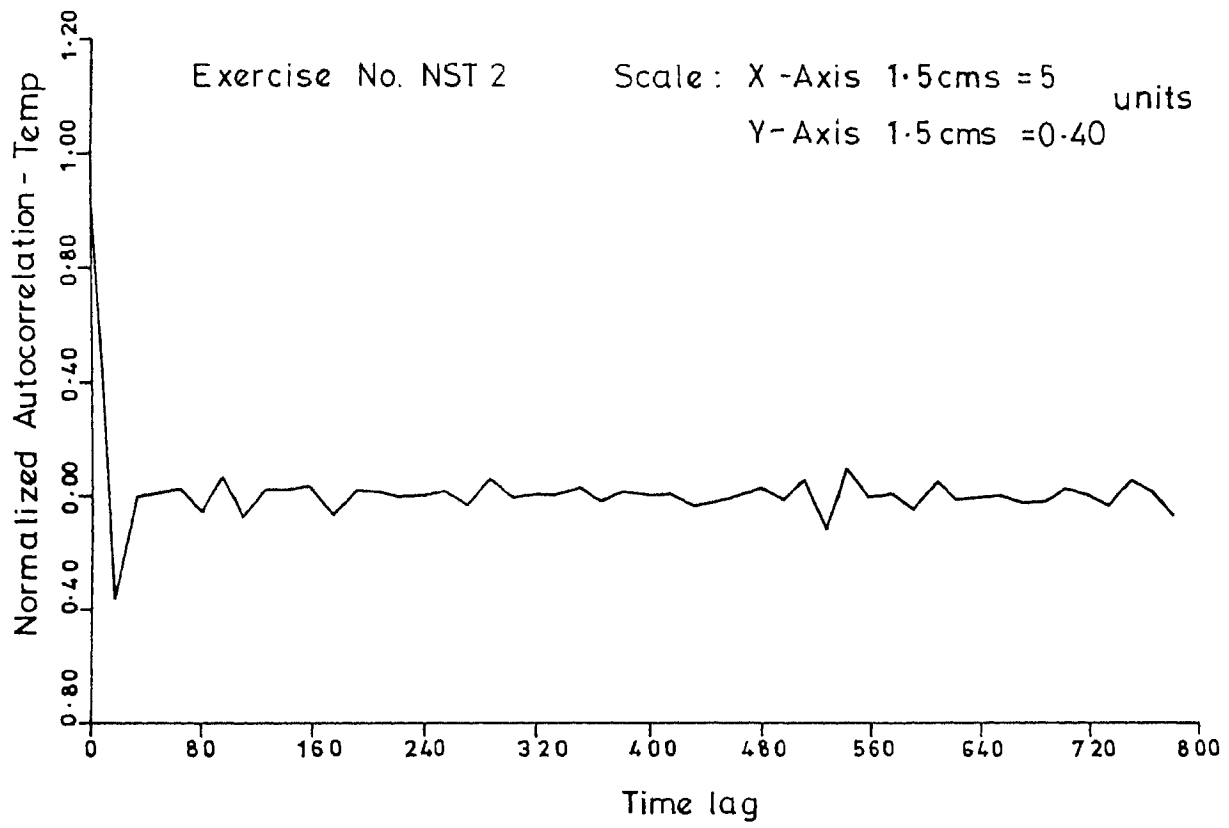


Fig. 5.22.

Power spectrum and Coherence analysis of Kavalur seeing and turbulence.

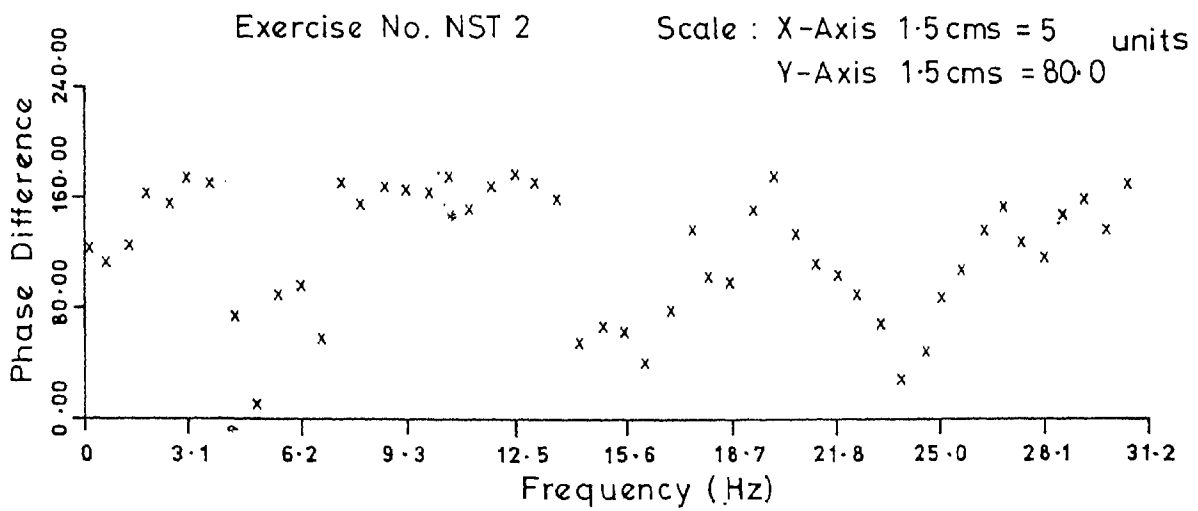
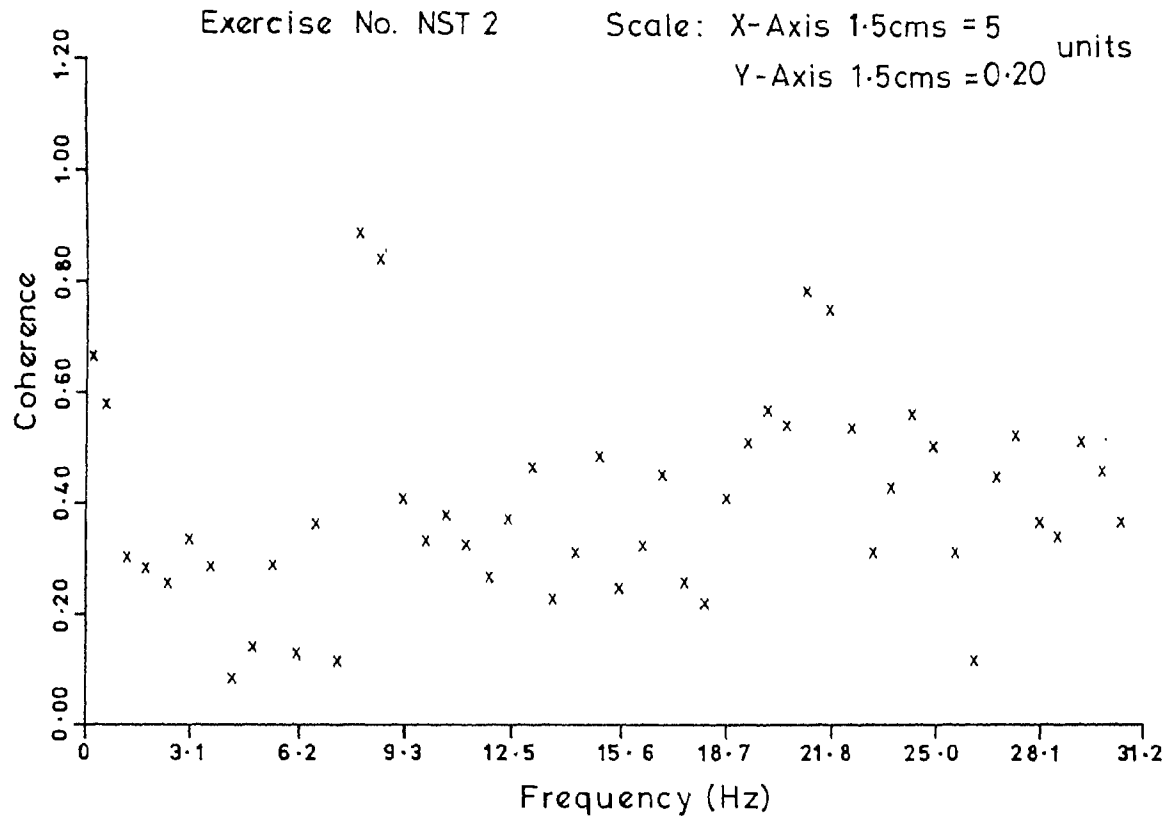
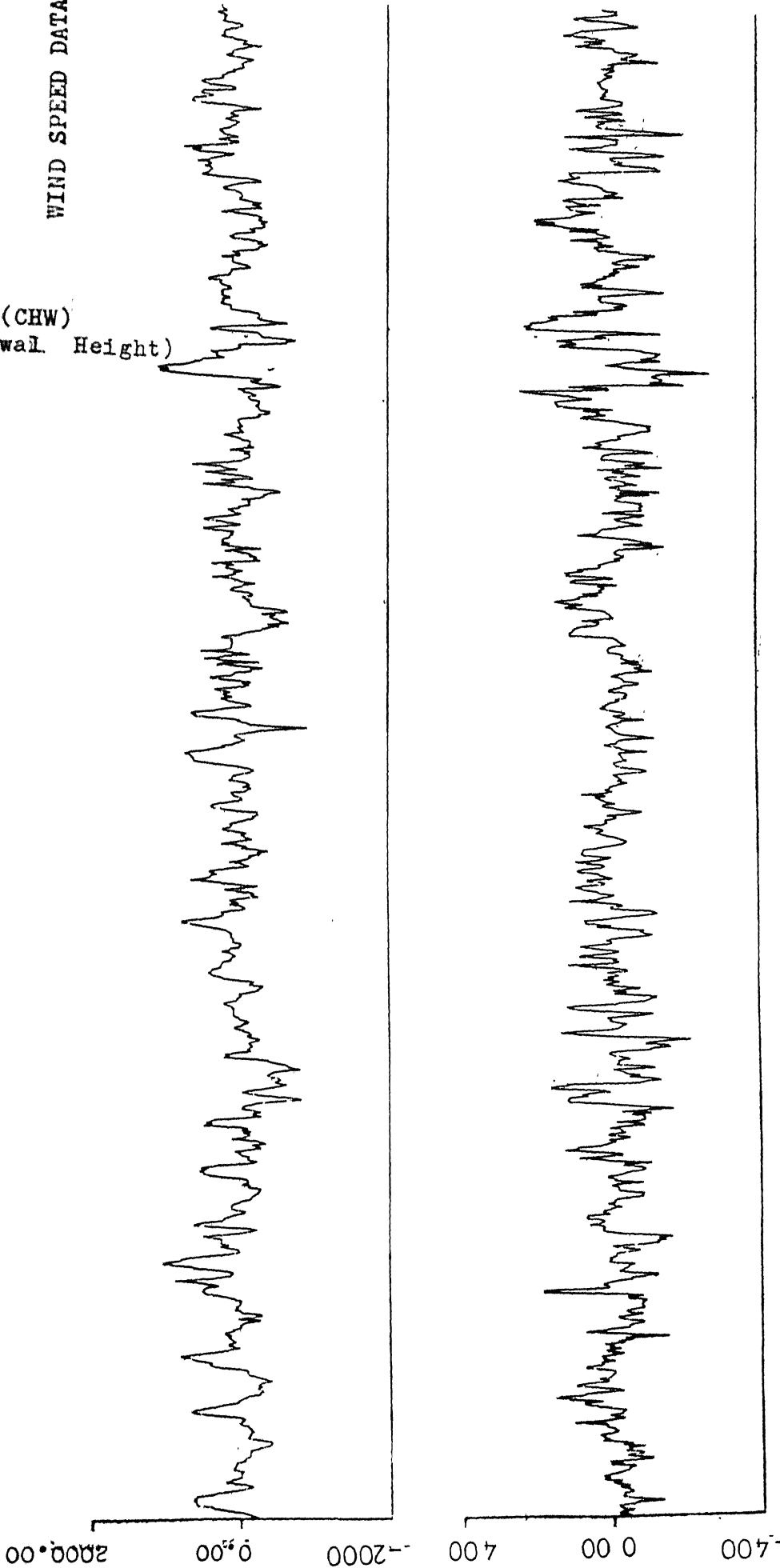


Fig. 5.23.

WIND SPEED DATA

No.8(CHW)  
(Catwal. Height)



WIND SPEED DATA

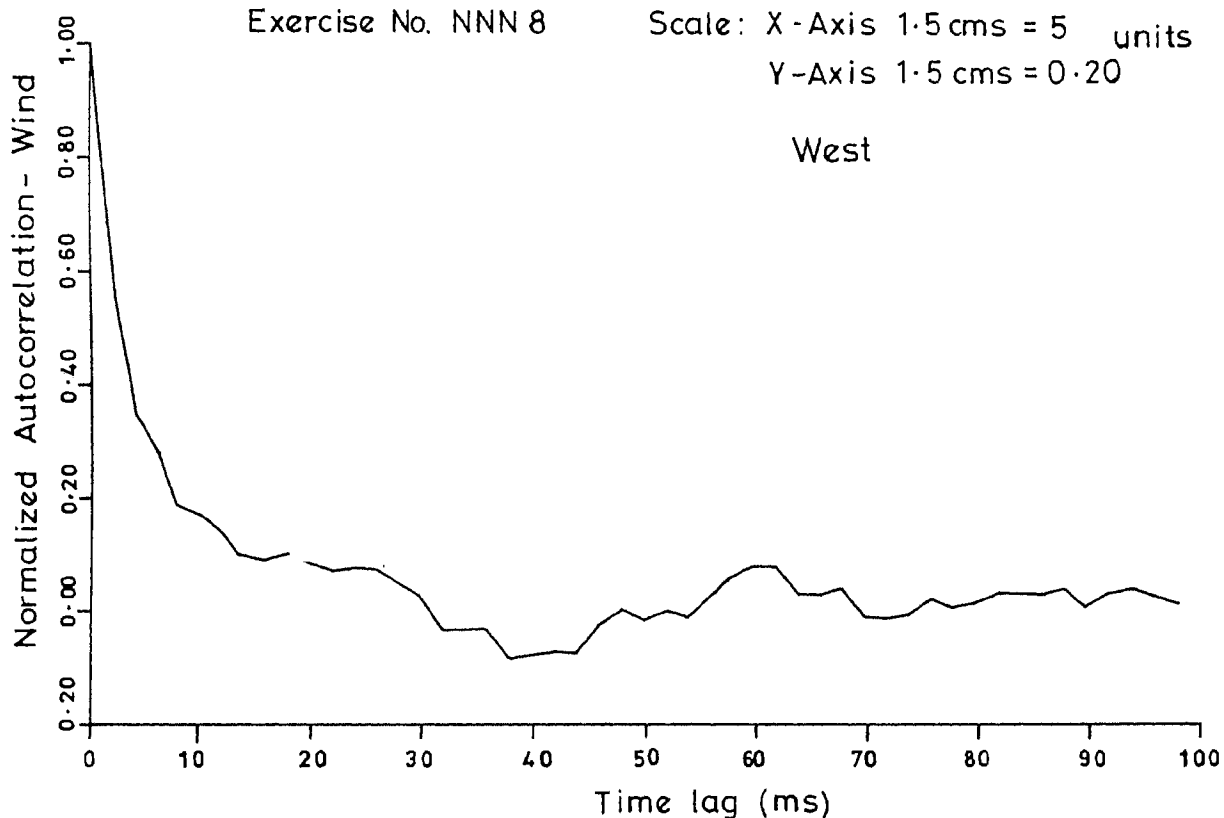
(Ref):No.4(CHN)  
(Catwal. Height)

Fig. 5.24. A simultaneous record of wind speed fluctuations at two different levels.

Normalized autocorrelation vs. Time lag  
Atmospheric Turbulence

Exercise No. NNN 8      Scale: X-Axis 1.5 cms = 5 units  
Y-Axis 1.5 cms = 0.20

West



Log of power spectral density vs. Frequency  
Atmospheric Turbulence

Exercise No. NNN 8      Scale: X-Axis 1.5 cms = 5 units  
Y-Axis 1.5 cms = 0.50

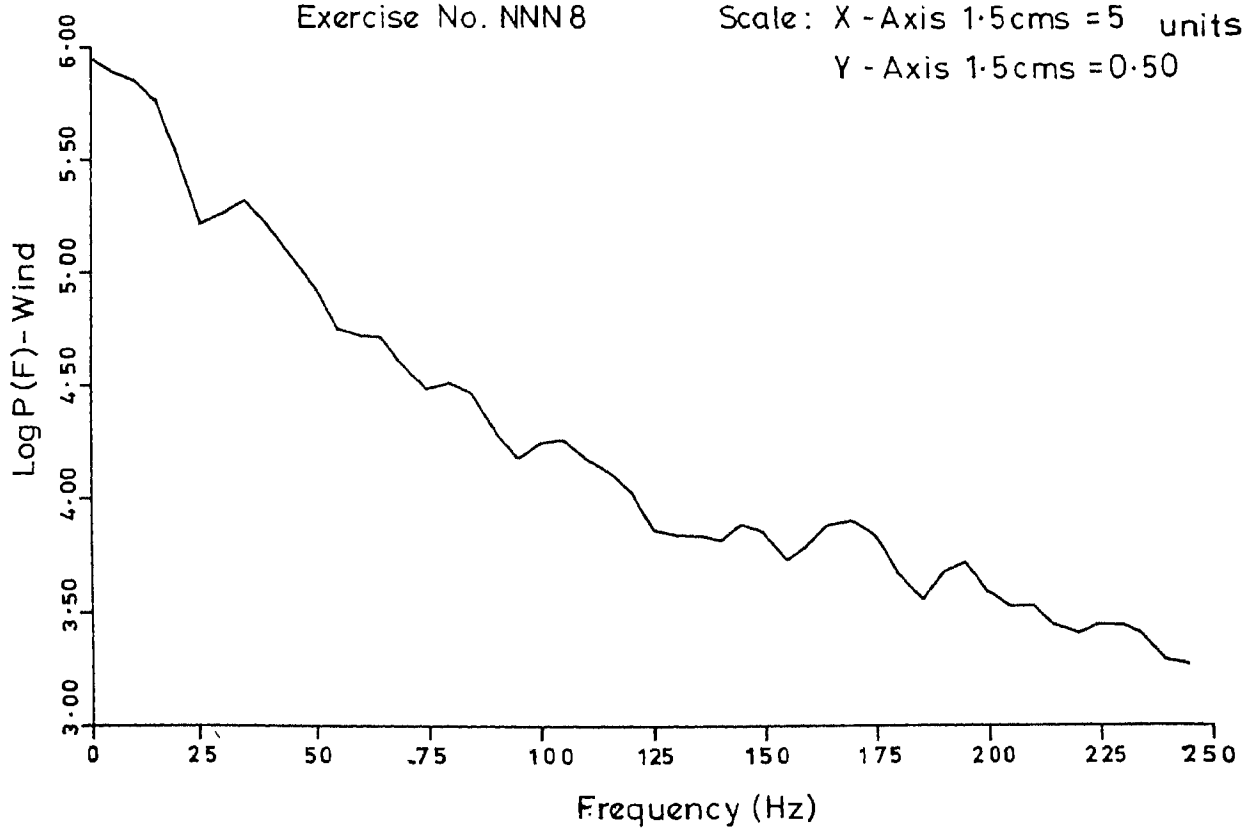
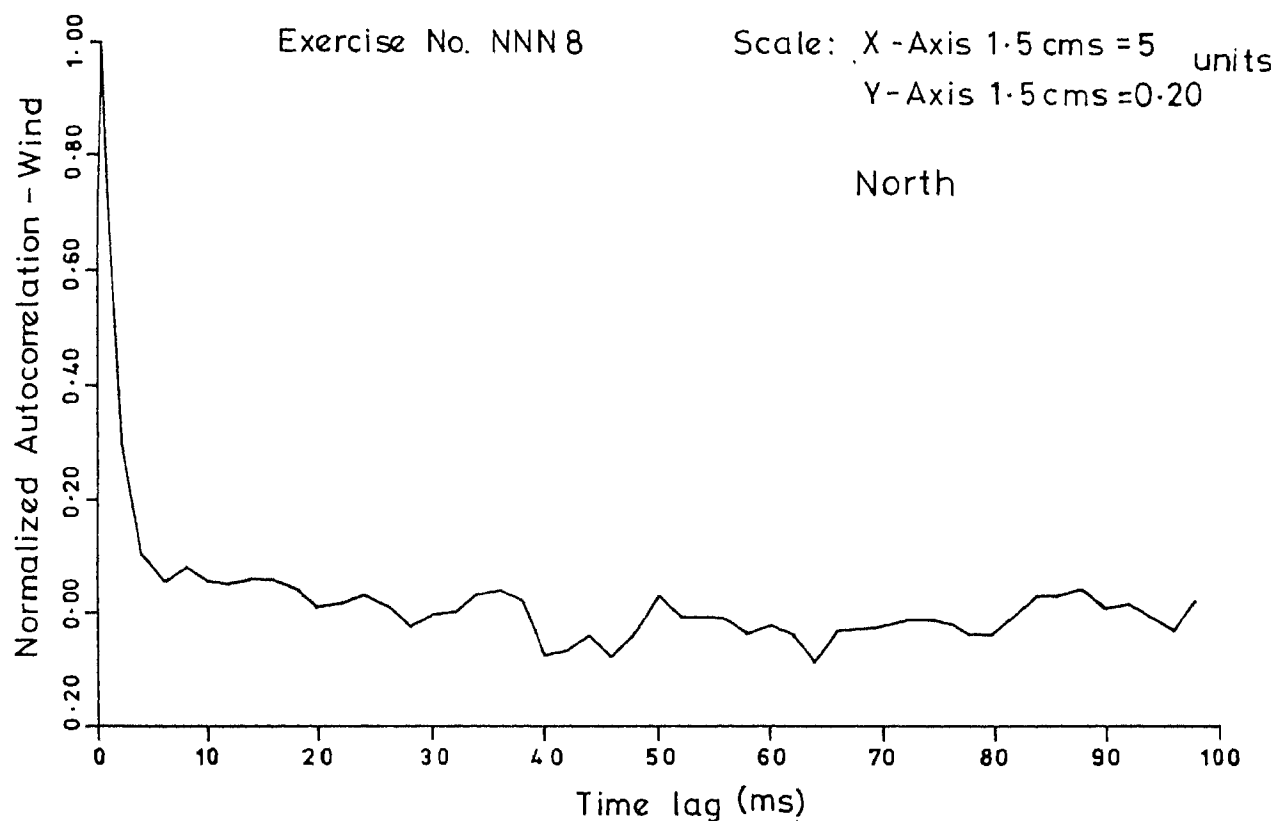


Fig. 5 25



Normalized autocorrelation vs. Time lag  
Atmospheric turbulence



Log of power spectral density vs. Frequency  
Atmospheric turbulence

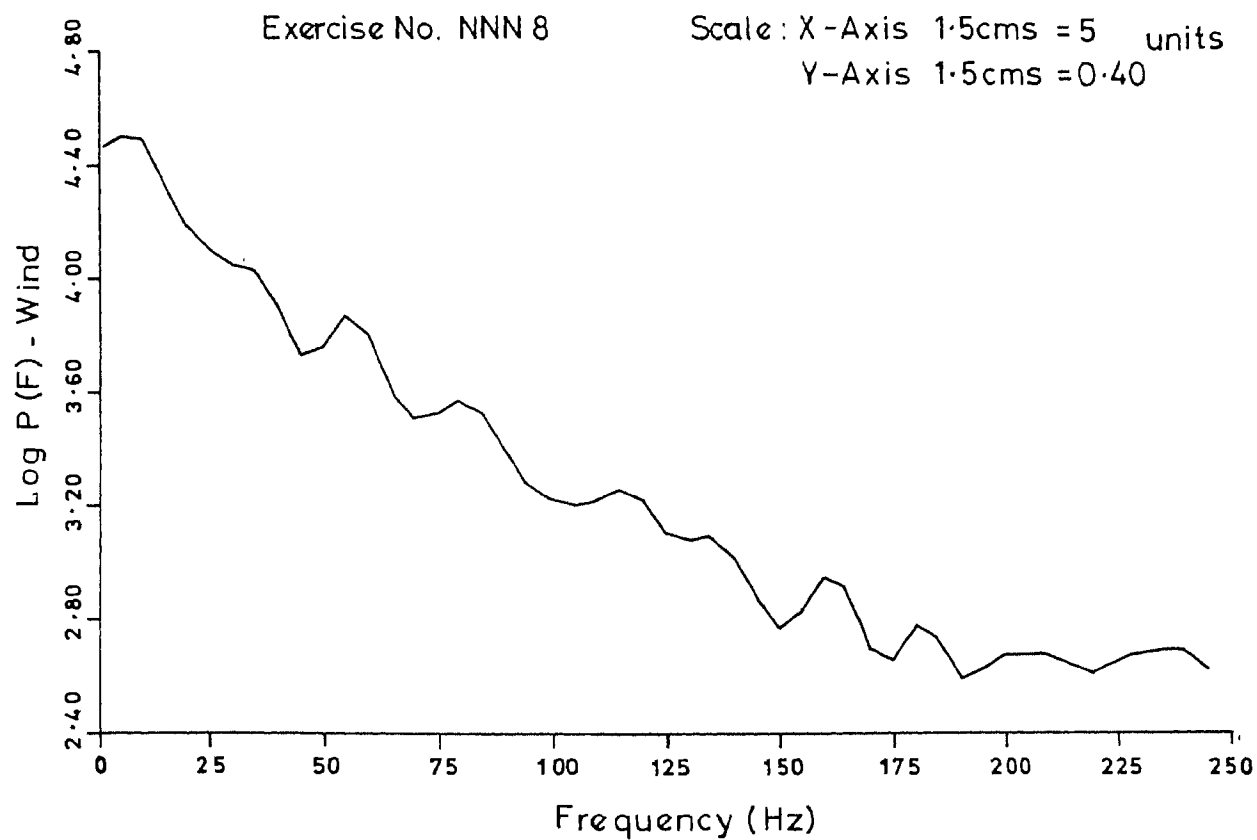


Fig . 5.26.

Coherence function vs. Frequency  
Coherence between W and W of turbulence

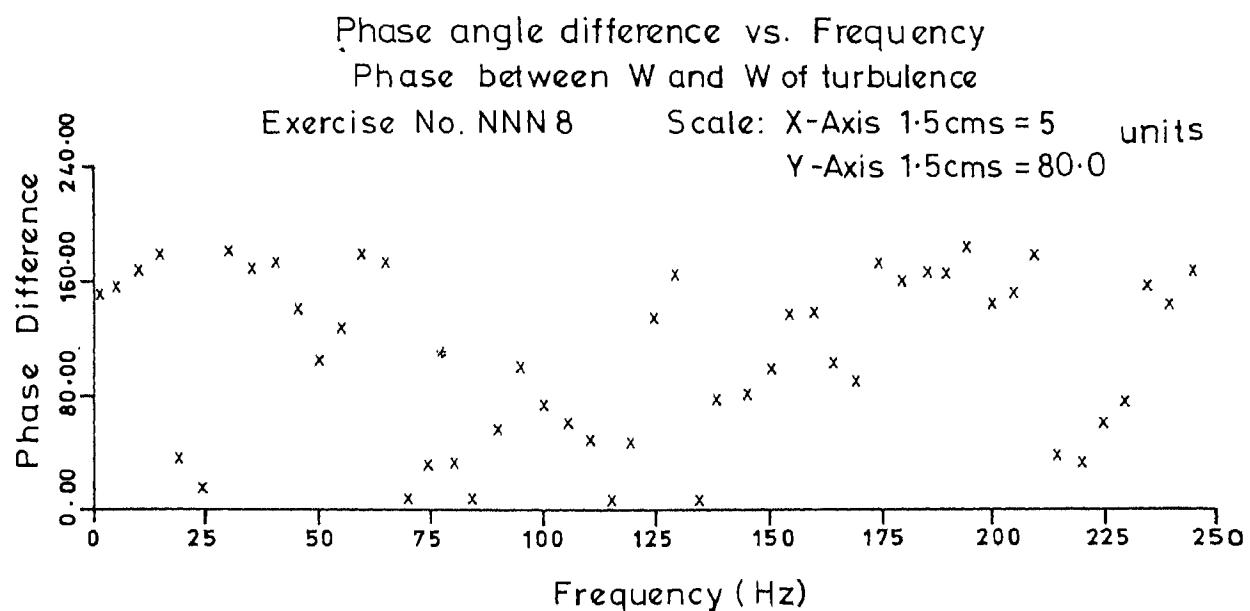
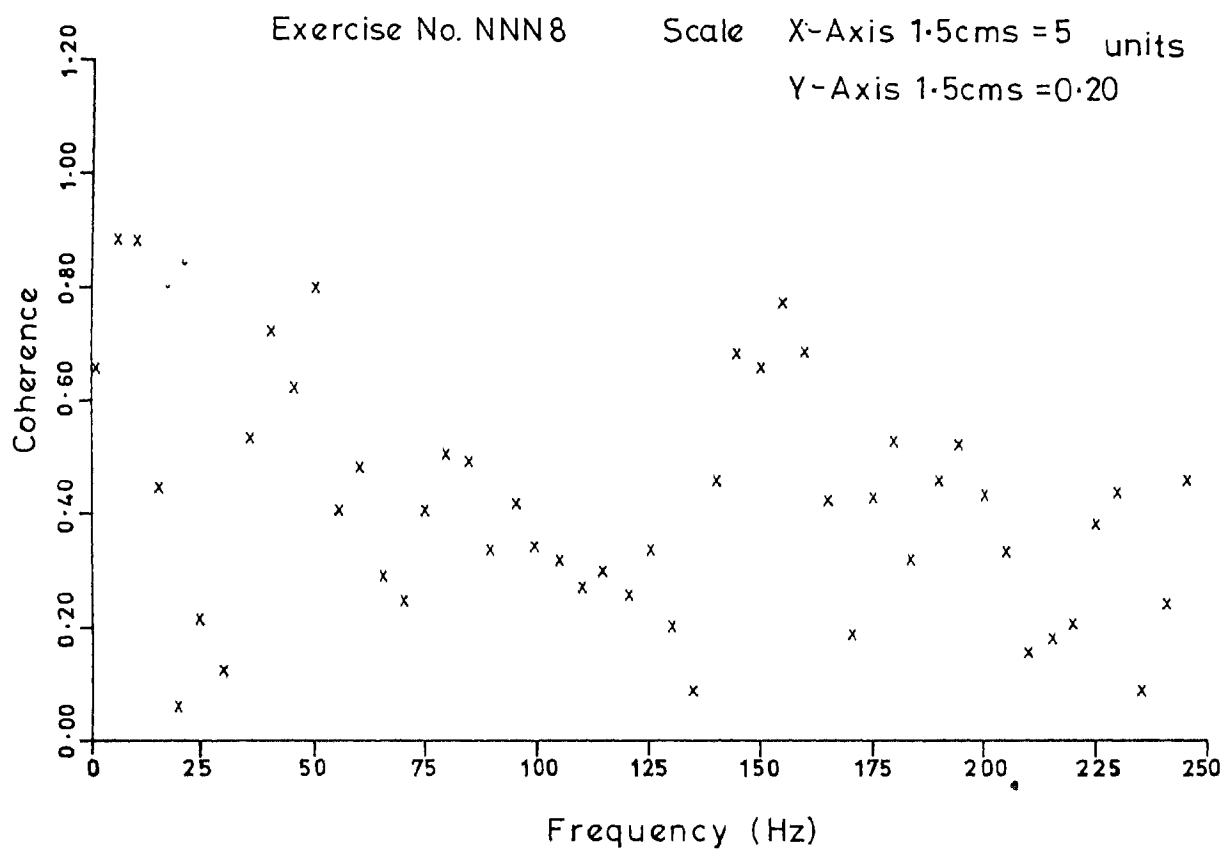
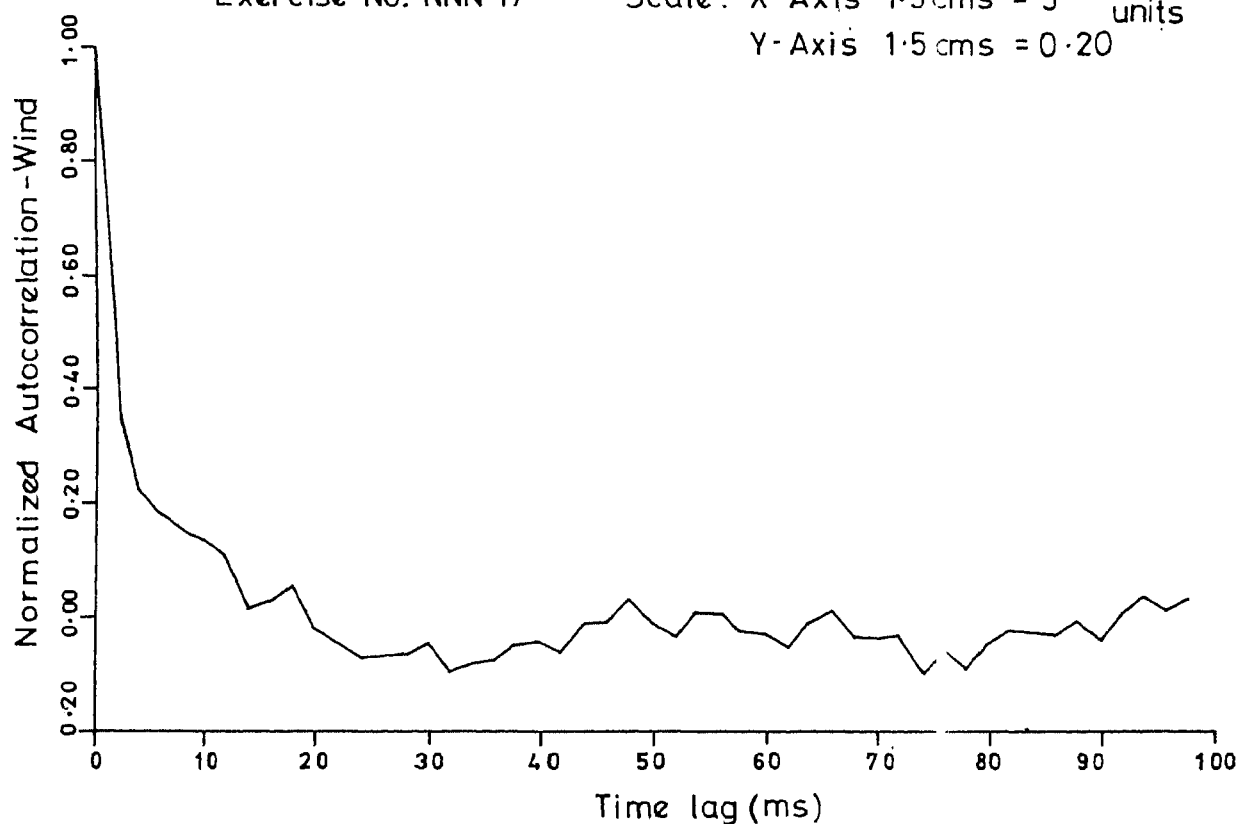


Fig . 5.27.

Normalized autocorrelation vs. Time lag  
Atmospheric turbulence

Exercise No. NNN 17      Scale: X-Axis 1.5cms = 5 units  
Y-Axis 1.5cms = 0.20



Log of power spectral density vs. Frequency  
Atmospheric turbulence

Exercise No. NNN 17      Scale: X-Axis, 1.5cms = 5 units  
Y-Axis, 1.5cms = 0.40  
Dome - slit

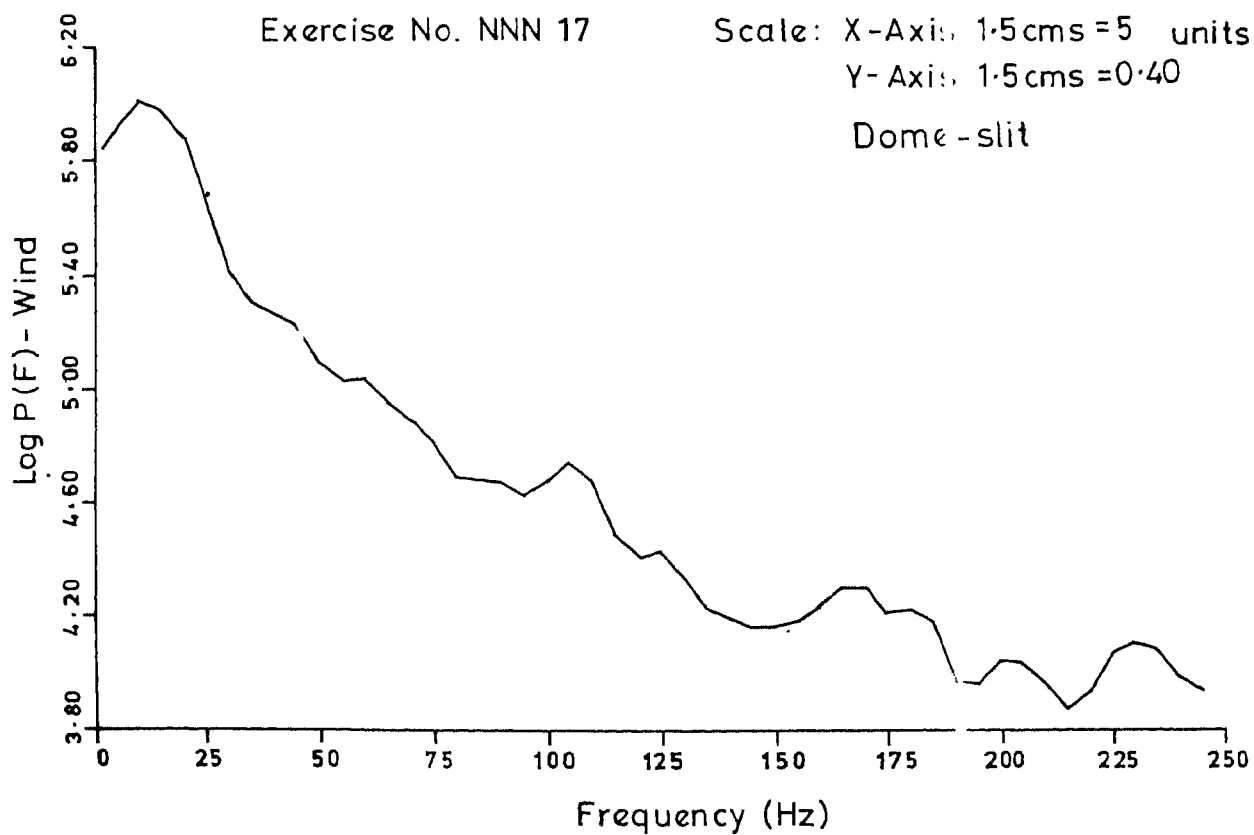
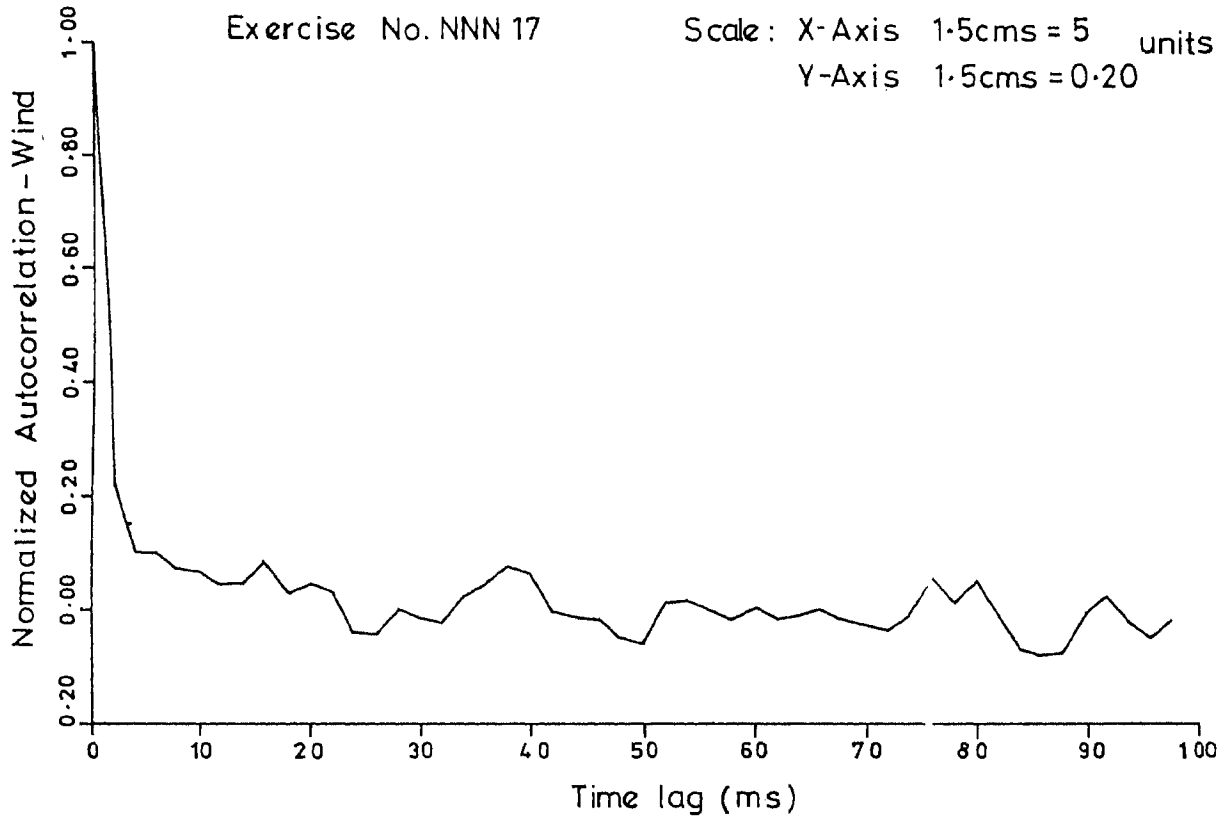


Fig 5.28.

Normalized autocorrelation vs. Time lag  
Atmospheric turbulence

Exercise No. NNN 17

Scale: X-Axis 1.5cms = 5 units  
Y-Axis 1.5cms = 0.20



Log of power spectral density vs. Frequency  
Atmospheric turbulence

Exercise No. NNN 17

Scale: X-Axis 1.5cms = 5 units  
Y-Axis 1.5cms = 0.40

Catwalk height 1.5m

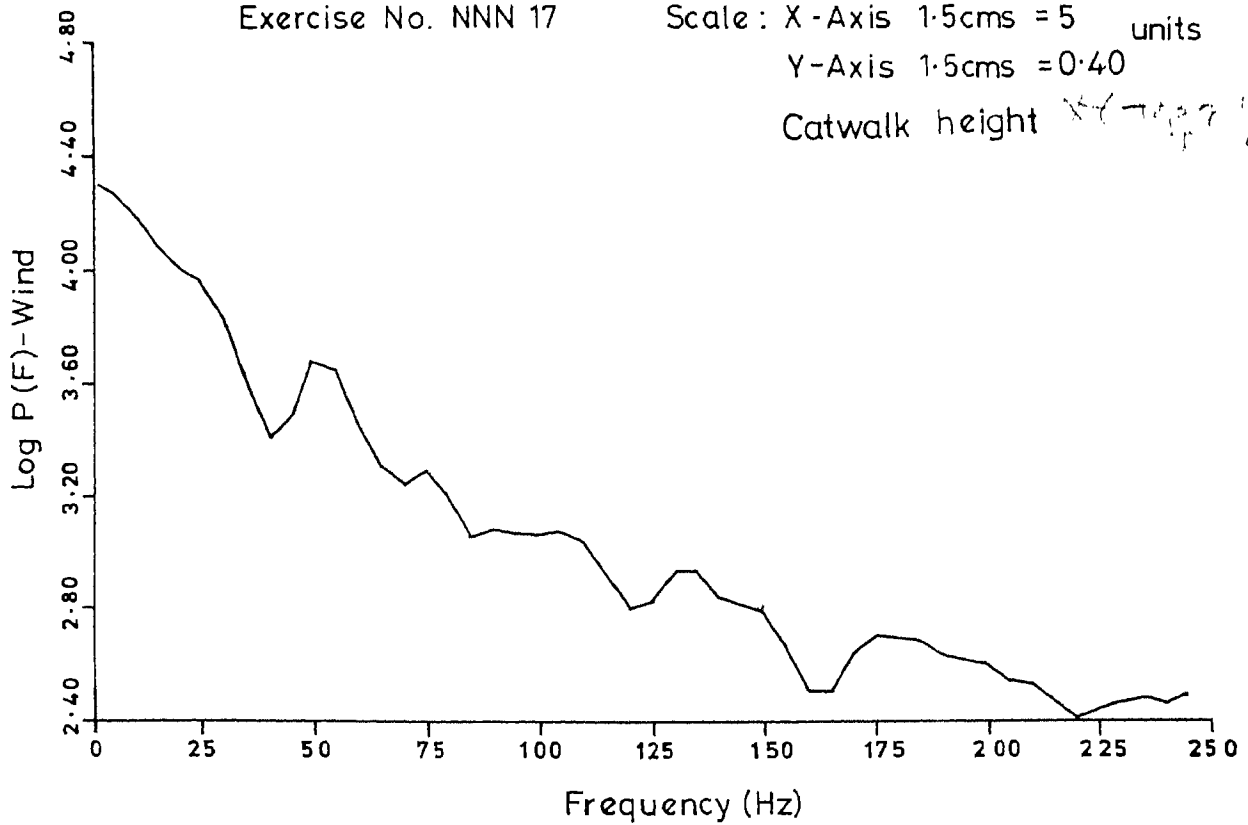
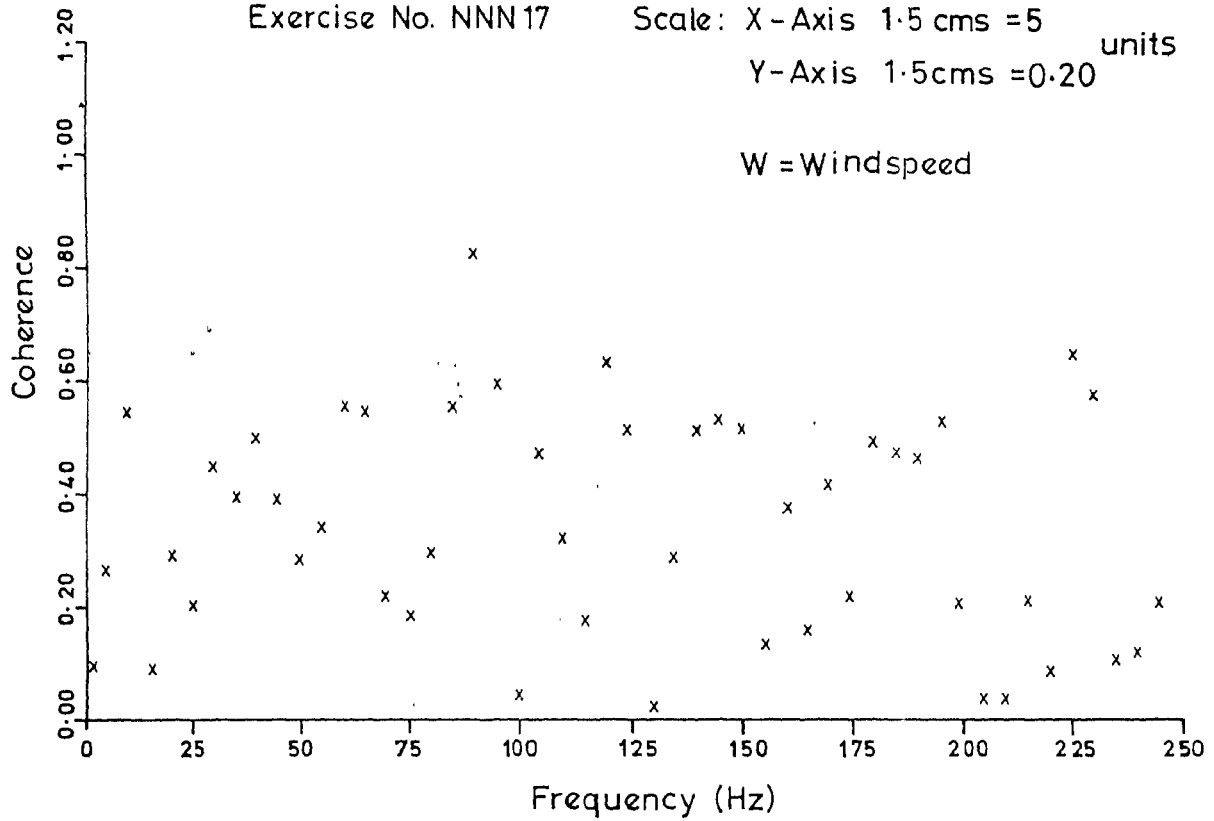


Fig. 5.29.

Coherence function vs. Frequency  
Coherence between W and W of turbulence

Exercise No. NNN17      Scale: X-Axis 1.5 cms = 5 units  
Y-Axis 1.5cms = 0.20

W = Windspeed



Phase angle difference vs. Frequency  
Phase between W and W of turbulence

Exercise No. NNN17      Scale: X-Axis 1.5cms = 5 units  
Y-Axis 1.5cms = 80.0

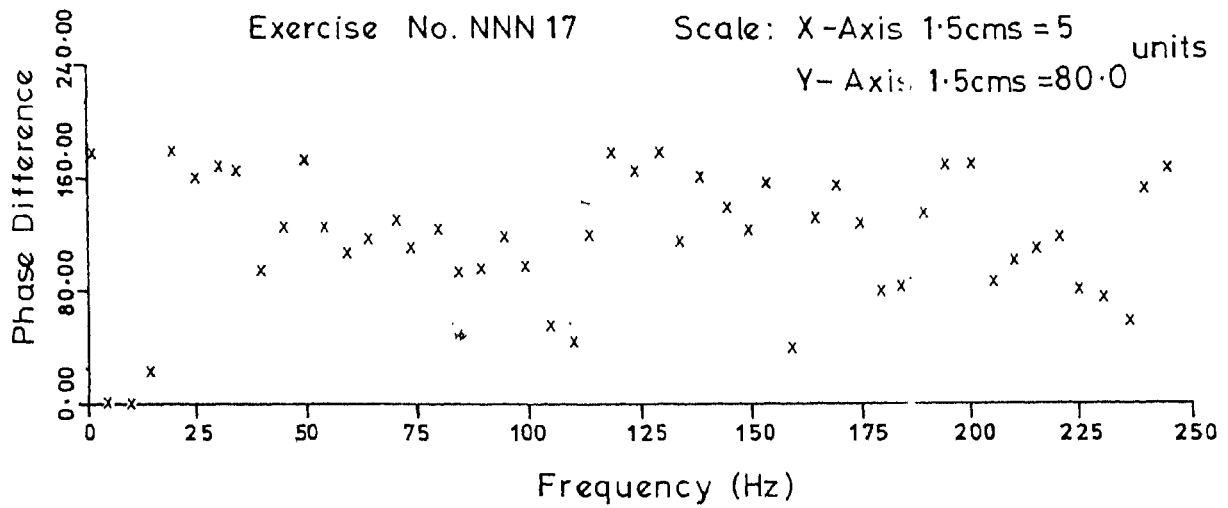
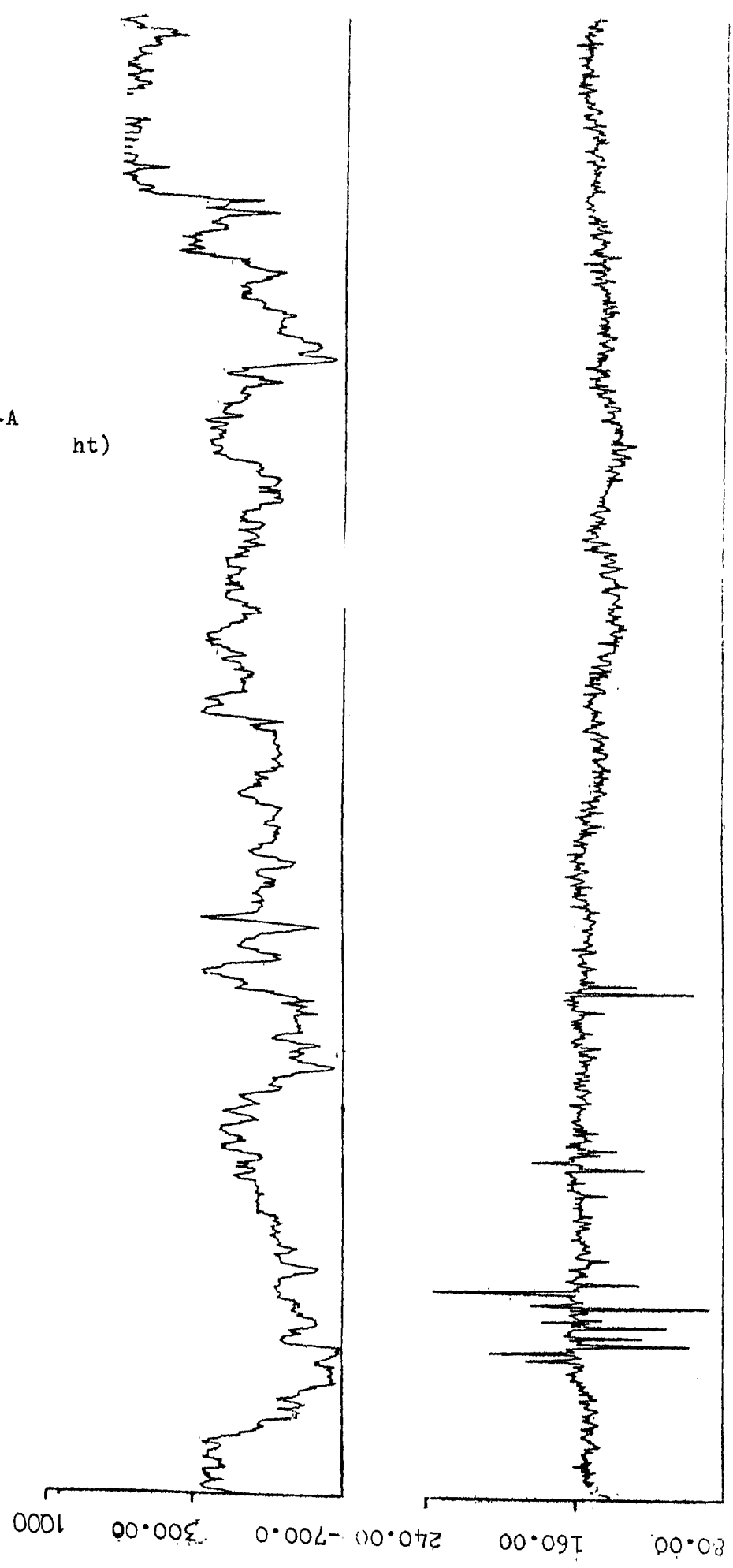


Fig. 5.30.

WIND SPEED DATA

No.10-A  
(Dome ht)



WIND SPEED DATA

Cup anemometer  
(Top of the dome)

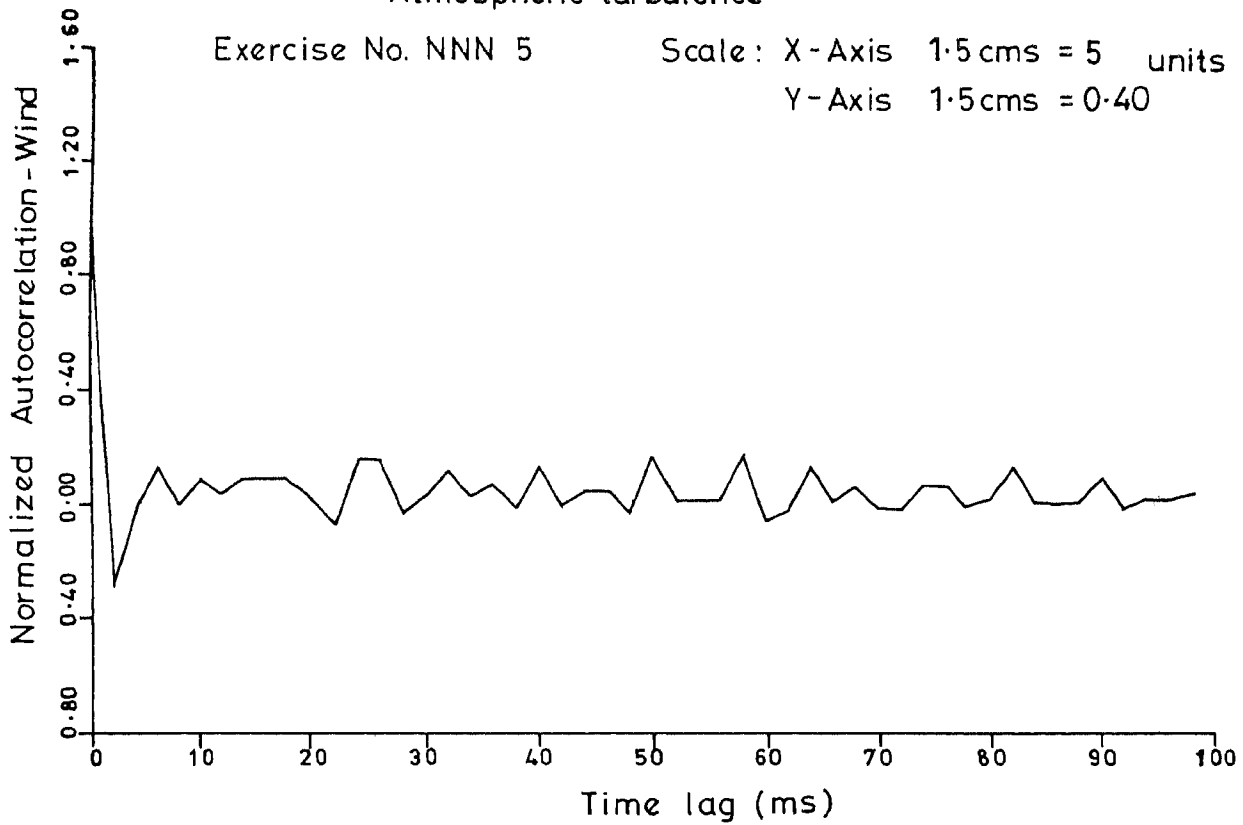
Fig. 5 31. A simultaneous record of wind speed fluctuations at two different levels.

Normalized autocorrelation vs. Time lag  
Atmospheric turbulence

Exercise No. NNN 5

Scale: X-Axis 1.5cms = 5 units

Y-Axis 1.5cms = 0.40



Log of power spectral density vs. Frequency  
Atmospheric turbulence

Exercise No. NNN 5

Scale: X-Axis 1.5cms = 5 units

Y-Axis 1.5cms = 0.40

Catwalk height

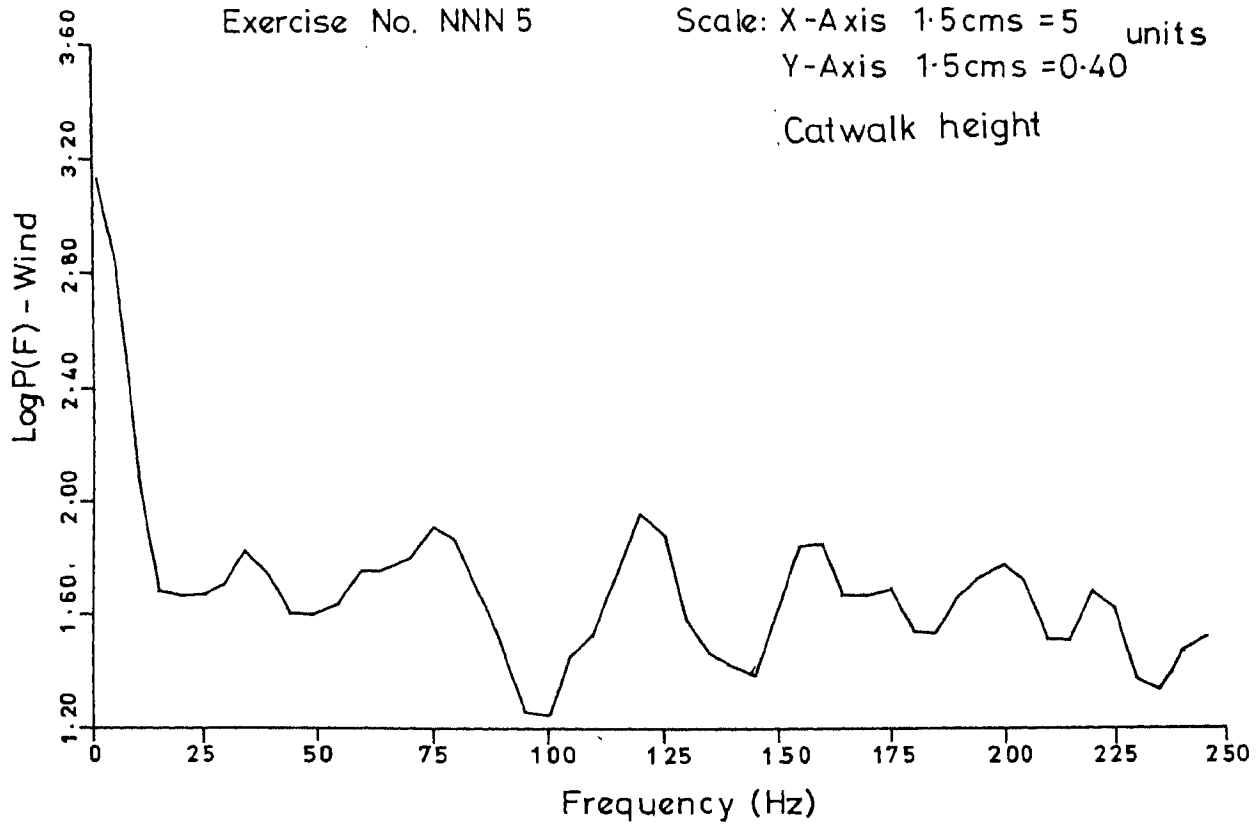
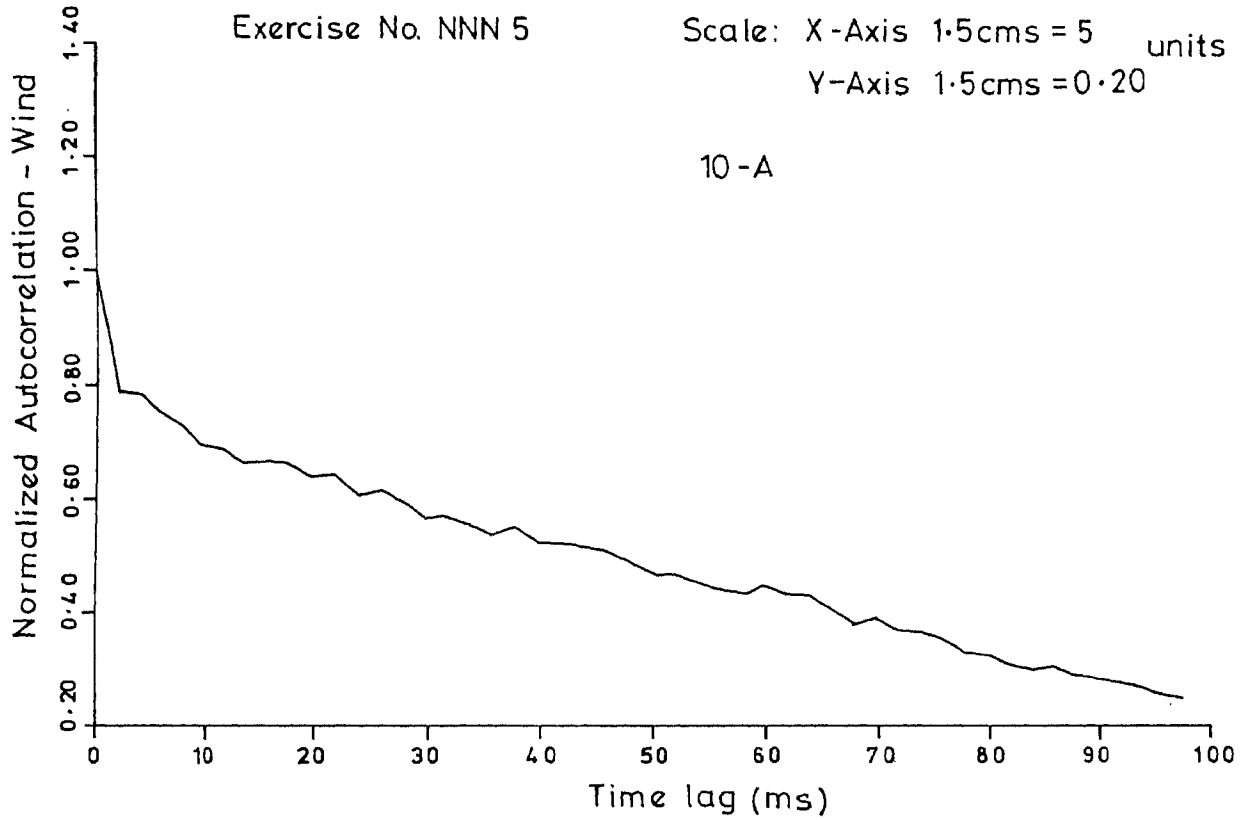


Fig. 5.32.

Normalized autocorrelation vs Time lag  
Atmospheric turbulence



Log of power spectral density vs. Frequency  
Atmospheric turbulence

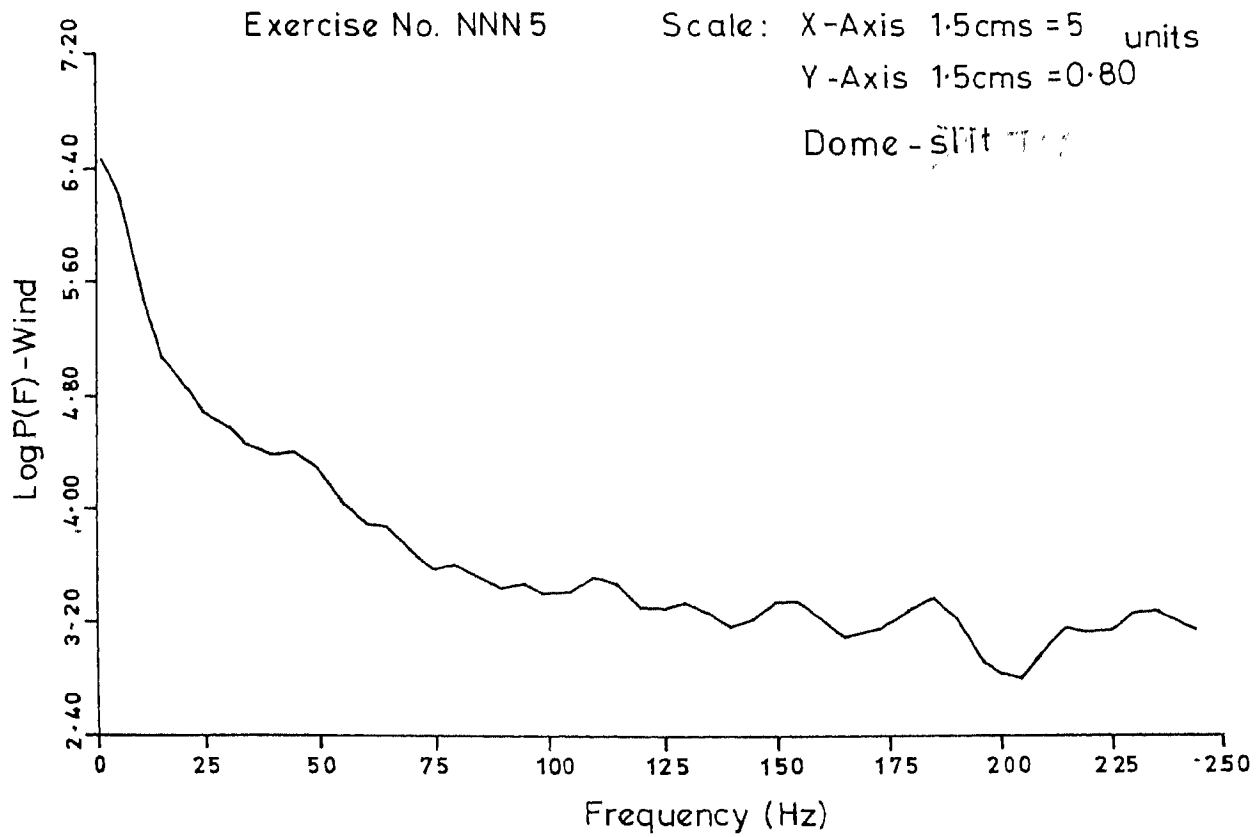
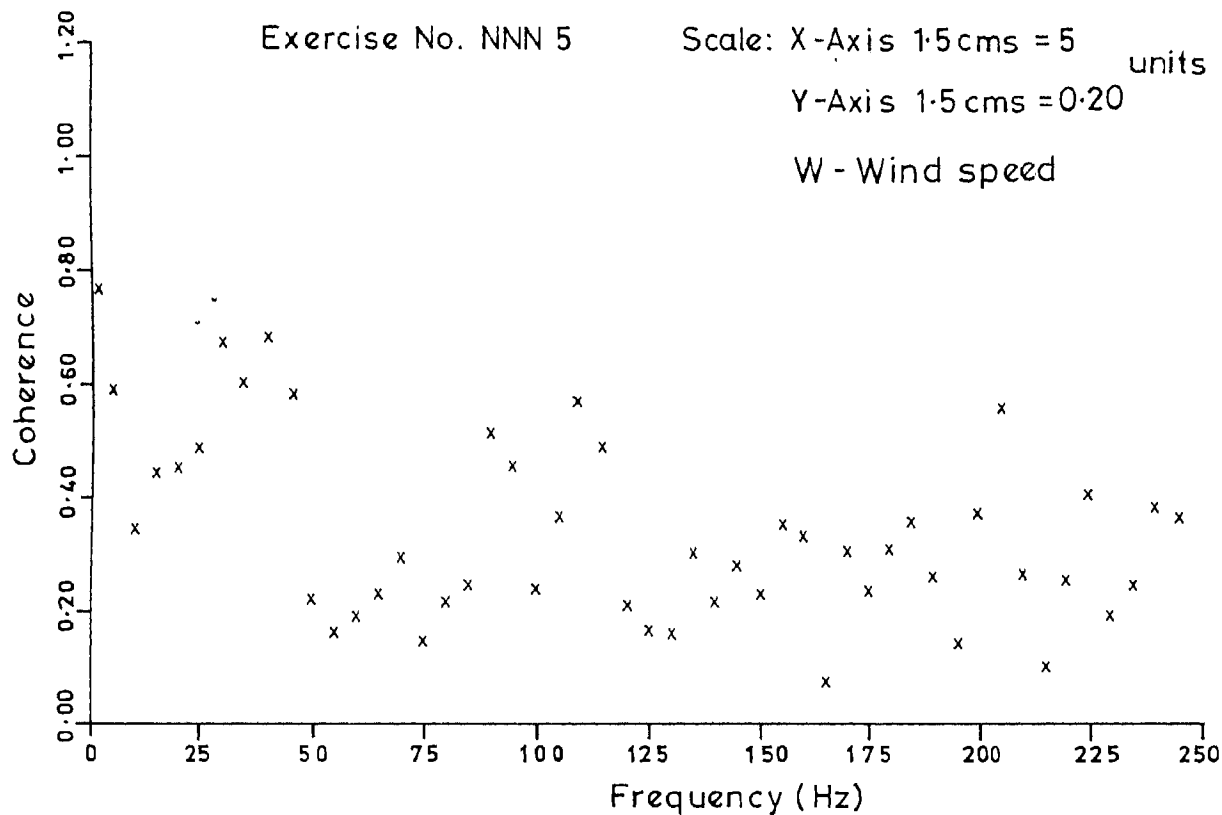


Fig. 5.33.



Coherence function vs. Frequency  
 Coherence between W and W of Turbulence



Phase angle difference vs. Frequency  
 Phase between W and W of Turbulence

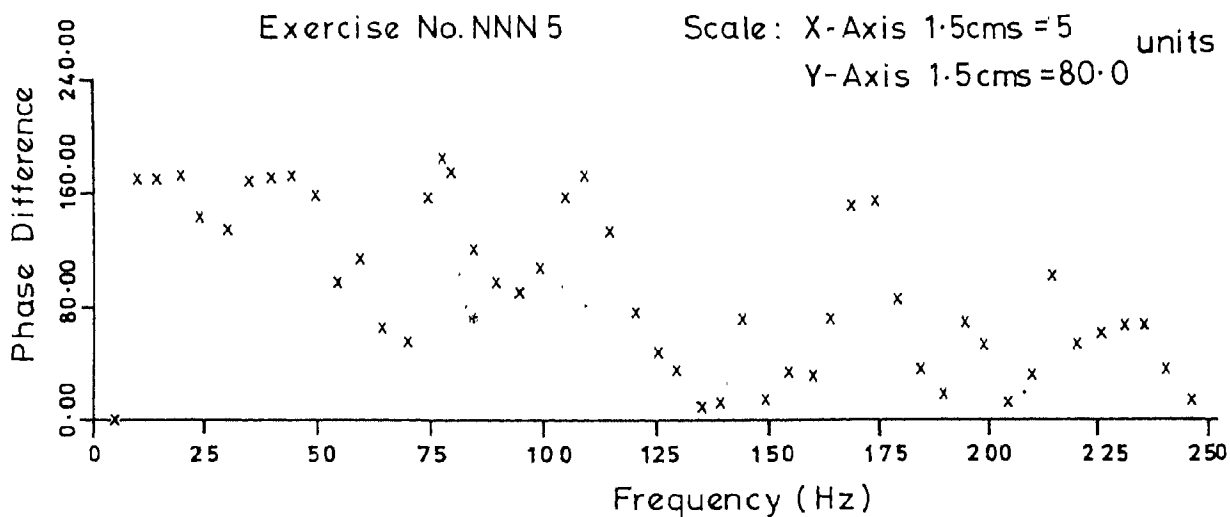


Fig. 5.34.

is introduced when spot samples of atmospheric data are considered as representative patterns of the adjacent layers. From this, it is possible to say that the interrelationship might extend to greater heights in different degrees which may cause corresponding distortions in the incoming light waves towards the ground-based optical telescope.

As mentioned earlier, seeing and scintillation phenomena are due to moving refractive inhomogeneities in our atmosphere. Depending on the atmospheric conditions the sizes and movements of these irregularities are different across the stellar beam. By physical connections, they are expected to be correlated with each other. The present studies, although not extensive, have shown that quantitative relations do exist between them.

S U M M A R Y

In this thesis the physics of the seeing phenomenon has been discussed and its relationship with the atmospheric turbulence has been shown. The work done in the past in understanding this problem has been presented. The instruments employed in this investigation are described in detail. Further the mathematical methods adopted for analysing the data collected at Kavalur observatory are described. The results of such analyses of power spectral densities and coherence have been highlighted.

The present work has been an earnest attempt to study the problem of astronomical seeing at Kavalur on a quantitative basis utilising all the data available in the observatory pertaining to this problem. In a way, it can be a very effective technique for remote sensing of clear air turbulence in the troposphere and studying the layer structure of the atmosphere, that might eventually aid in properly choosing the type of astronomical observational programmes.

A wide range of instruments may be employed towards the acquisition of the same kind of data as, for example, photographic, interferometric and simulation methods. The data may be subjected to such an analysis, for the understanding of the physical processes responsible for optical image

distortions observed in the telescopes used in astronomical studies.

This investigation has an added importance in that the same has been carried out at a low-latitude station thus fulfilling, to a measure, a major lacuna in this field of work.

The methods employed in this work may be useful in future intensive investigations on star intensity fluctuations. Through such powerful methods, optical properties of the atmosphere may be obtained, which in turn, can be made use of, for practical astronomical work, as well as studies of the micro structure of the atmosphere.

Although the ultimate choice of location of a telescope depends upon the use to which it is put, due consideration and attention are always paid to the seeing quality of the location and how this effects the image structure in the focal plane of the telescope. With the advent of high resolution detector matrices, these studies have enhanced importance in present times and their use for advanced astronomical image processing work. Hitherto unattainable fineness of measurements have been achieved by computer processing of speckle images<sup>49</sup>. These techniques offer to an astronomer very powerful tools in their researches.

By simulation studies in the laboratory, improvements over instrumentation and theoretical models may be undertaken. In fact, with the advent of lasers 50 : a wide range of useful experiments may be performed. The present studies may help in fulfilling a very necessary objective of understanding the chief causes for optical image distortions and applying appropriate corrective measures for overcoming the same.

This work attempts to provide useful experimental techniques and procedures for data analysis towards understanding of the physical processes in such phenomena.

Program for retrieval of data.

```

IMPLICIT INTEGER (A-Z)
DIMENSION IB(1024),S(1024),W1(1024),W2(1024),T(1024)
CALL INITDV(I, 'RAW.DAT')
DO I=1,5
CALL READ(XB,K)
1 CONTINUE
IT=4
OPEN(UNIT=1,FILE='RAW.DAT',ACCESS='APPEND')
C WRITE(1,200)
200 FORMAT(' I3 *****')
CLOSE(UNIT=1)
I=0
DO 2 J=1,15
CALL READ(XB,K)
IF(TI.EQ.1)TYPE=20,(IB(KL),KL=1,10)
20 FORMAT(I5,10I6)
DO 2 J=1,15
L=L+1
S(L)=IB(1+(J-1)*4)
W1(L)=IB(2+(J-1)*4)
W2(L)=IB(3+(J-1)*4)
T(L)=-IB(4+(J-1)*4)
2 CONTINUE
OPEN(UNIT=1,FILE='RAW.DAT',ACCESS='APPEND')
C WRITE(1,300)S
C WRITE(1,300)W1
C WRITE(1,300)W2
C WRITE(1,300)T
CLOSE(UNIT=1)
300 FORMAT(12I6)
STOP;END
SUBROUTINE READ(XB,K)
DIMENSION IA(1024),IB(1024)
CALL INITVA(IA,IB,1A,2,40,K)
K=K/2
CALL SWAP (IA,IB,K)
RETURN
END

```

APPENDIX A-2

Program for plotting raw data.

```

C(1)=0.0, X(1)=0.0, Y(1)=0.0, U(1)=0.0
C(2)=0.0, X(2)=0.0, Y(2)=0.0
C(3)=0.0
C(4)=0.0, X(4)=0.0, Y(4)=0.0
C(5)=0.0, X(5)=0.0, Y(5)=0.0
C(6)=0.0, X(6)=0.0, Y(6)=0.0
C(7)=0.0, X(7)=0.0, Y(7)=0.0
C(8)=0.0, X(8)=0.0, Y(8)=0.0
C(9)=0.0, X(9)=0.0, Y(9)=0.0
C(10)=0.0, X(10)=0.0, Y(10)=0.0
C(11)=0.0, X(11)=0.0, Y(11)=0.0
C(12)=0.0, X(12)=0.0, Y(12)=0.0
C(13)=0.0, X(13)=0.0, Y(13)=0.0
C(14)=0.0, X(14)=0.0, Y(14)=0.0
C(15)=0.0, X(15)=0.0, Y(15)=0.0
C(16)=0.0, X(16)=0.0, Y(16)=0.0
C(17)=0.0, X(17)=0.0, Y(17)=0.0
C(18)=0.0, X(18)=0.0, Y(18)=0.0
C(19)=0.0, X(19)=0.0, Y(19)=0.0
C(20)=0.0, X(20)=0.0, Y(20)=0.0
C(21)=0.0, X(21)=0.0, Y(21)=0.0
C(22)=0.0, X(22)=0.0, Y(22)=0.0
C(23)=0.0, X(23)=0.0, Y(23)=0.0
C(24)=0.0, X(24)=0.0, Y(24)=0.0
C(25)=0.0, X(25)=0.0, Y(25)=0.0
C(26)=0.0, X(26)=0.0, Y(26)=0.0
C(27)=0.0, X(27)=0.0, Y(27)=0.0
C(28)=0.0, X(28)=0.0, Y(28)=0.0
C(29)=0.0, X(29)=0.0, Y(29)=0.0
C(30)=0.0, X(30)=0.0, Y(30)=0.0
C(31)=0.0, X(31)=0.0, Y(31)=0.0
C(32)=0.0, X(32)=0.0, Y(32)=0.0
C(33)=0.0, X(33)=0.0, Y(33)=0.0
C(34)=0.0, X(34)=0.0, Y(34)=0.0
C(35)=0.0, X(35)=0.0, Y(35)=0.0
C(36)=0.0, X(36)=0.0, Y(36)=0.0
C(37)=0.0, X(37)=0.0, Y(37)=0.0
C(38)=0.0, X(38)=0.0, Y(38)=0.0
C(39)=0.0, X(39)=0.0, Y(39)=0.0
C(40)=0.0, X(40)=0.0, Y(40)=0.0
C(41)=0.0, X(41)=0.0, Y(41)=0.0
C(42)=0.0, X(42)=0.0, Y(42)=0.0
C(43)=0.0, X(43)=0.0, Y(43)=0.0
C(44)=0.0, X(44)=0.0, Y(44)=0.0
C(45)=0.0, X(45)=0.0, Y(45)=0.0
C(46)=0.0, X(46)=0.0, Y(46)=0.0
C(47)=0.0, X(47)=0.0, Y(47)=0.0
C(48)=0.0, X(48)=0.0, Y(48)=0.0
C(49)=0.0, X(49)=0.0, Y(49)=0.0
C(50)=0.0, X(50)=0.0, Y(50)=0.0
C(51)=0.0, X(51)=0.0, Y(51)=0.0
C(52)=0.0, X(52)=0.0, Y(52)=0.0
C(53)=0.0, X(53)=0.0, Y(53)=0.0
C(54)=0.0, X(54)=0.0, Y(54)=0.0
C(55)=0.0, X(55)=0.0, Y(55)=0.0
C(56)=0.0, X(56)=0.0, Y(56)=0.0
C(57)=0.0, X(57)=0.0, Y(57)=0.0
C(58)=0.0, X(58)=0.0, Y(58)=0.0
C(59)=0.0, X(59)=0.0, Y(59)=0.0
C(60)=0.0, X(60)=0.0, Y(60)=0.0
C(61)=0.0, X(61)=0.0, Y(61)=0.0
C(62)=0.0, X(62)=0.0, Y(62)=0.0
C(63)=0.0, X(63)=0.0, Y(63)=0.0
C(64)=0.0, X(64)=0.0, Y(64)=0.0
C(65)=0.0, X(65)=0.0, Y(65)=0.0
C(66)=0.0, X(66)=0.0, Y(66)=0.0
C(67)=0.0, X(67)=0.0, Y(67)=0.0
C(68)=0.0, X(68)=0.0, Y(68)=0.0
C(69)=0.0, X(69)=0.0, Y(69)=0.0
C(70)=0.0, X(70)=0.0, Y(70)=0.0
C(71)=0.0, X(71)=0.0, Y(71)=0.0
C(72)=0.0, X(72)=0.0, Y(72)=0.0
C(73)=0.0, X(73)=0.0, Y(73)=0.0
C(74)=0.0, X(74)=0.0, Y(74)=0.0
C(75)=0.0, X(75)=0.0, Y(75)=0.0
C(76)=0.0, X(76)=0.0, Y(76)=0.0
C(77)=0.0, X(77)=0.0, Y(77)=0.0
C(78)=0.0, X(78)=0.0, Y(78)=0.0
C(79)=0.0, X(79)=0.0, Y(79)=0.0
C(80)=0.0, X(80)=0.0, Y(80)=0.0
C(81)=0.0, X(81)=0.0, Y(81)=0.0
C(82)=0.0, X(82)=0.0, Y(82)=0.0
C(83)=0.0, X(83)=0.0, Y(83)=0.0
C(84)=0.0, X(84)=0.0, Y(84)=0.0
C(85)=0.0, X(85)=0.0, Y(85)=0.0
C(86)=0.0, X(86)=0.0, Y(86)=0.0
C(87)=0.0, X(87)=0.0, Y(87)=0.0
C(88)=0.0, X(88)=0.0, Y(88)=0.0
C(89)=0.0, X(89)=0.0, Y(89)=0.0
C(90)=0.0, X(90)=0.0, Y(90)=0.0
C(91)=0.0, X(91)=0.0, Y(91)=0.0
C(92)=0.0, X(92)=0.0, Y(92)=0.0
C(93)=0.0, X(93)=0.0, Y(93)=0.0
C(94)=0.0, X(94)=0.0, Y(94)=0.0
C(95)=0.0, X(95)=0.0, Y(95)=0.0
C(96)=0.0, X(96)=0.0, Y(96)=0.0
C(97)=0.0, X(97)=0.0, Y(97)=0.0
C(98)=0.0, X(98)=0.0, Y(98)=0.0
C(99)=0.0, X(99)=0.0, Y(99)=0.0
C(100)=0.0, X(100)=0.0, Y(100)=0.0

```

Program for evaluating power spectral densities  
and coherence values.

```

      DIMENSION ARGG(51)
      DIMENSION IB(1024),IA(2048)
      DIMENSION S(1024),SW(1000),ACS(51),PSSC(51),PSSH(51),PSSF(51),
1ALPSSF(51),ACSN(51),W(1024),WW(1000),ACW(51),ACWN(51),PSWC(51),
1PSWH(51),PSWF(51),ALPSWF(51),CCSWP(51),CSSWC(51),CSSWH(51),
1CSSWF(51),CQSWN(51),QSSWC(51),QSSWH(51),QSSWF(51),COHN(51),
1COHD(51),CDH(51)
      DO 56656 JKJ=1,51
56656  ARGG(JKJ)=0.0
      KARGG=0
      OPEN(UNIT=1,FILE='PLOTTER.DAT',ACCESS='APPEND')
      ACCEPT 9090,IEXE
      WRITE(1,87654)IEXE
87654  FORMAT('EXERCISE NO.'//A5)
      PRINT 77,IEXE
77     FORMAT(1X,59X,'EXERCISE NO.'//A5/59X,15('-')//)
      CLOSE(UNIT=1)
      ACCEPT *,NSKIP
9090   FORMAT(A5)
      IF(NSKIP.EQ.0)GOTO 7856
      DO 5555 K1=1,NSKIP
      READ(25,202)S
5555   CONTINUE
7856   CONTINUE
202   FORMAT(12F6.0)
      READ(25,202)S
      PRINT 202,(S(LL),LL=1,10)
      CALL TREND(S)
      READ(25,202)W
C      READ(25,202)W
C      READ(25,202)W
C      READ(25,202)W
C      DO 393 LA=1,1024
C393  W(LA)=-W(LA)
      PRINT 202,(W(LL),LL=1,10)
      CALL TREND(W)
2     CONTINUE
      PRINT 15,(S(I),I=1,20)
      PRINT 74
74    FORMAT (///)
      N1=1001
      N=I-1
      NN=20
      NPN=100/NN
      M=N/NN
      M1=N+1
      DELT=32.0
      ID=1
      PI=3.1415
      DO 5 I=1,N

```





```

902   FORMAT(//,20X,'AVERAGE OF PSSH=',F13.5)
      PRINT 74
      PSSF(1)=PSSH(1)*H/((N-M)*(1.36-1.2*COS(2.*PI/(6*M))))
      PSSF(M1)=PSSH(M1)/(1.36-1.2*COS((1-(1/(6*M)))*2*PI))
      DO 13 IR=2,M
13    PSSF(IR)=PSSH(IR)/(1.36-1.2*COS((2*(IR-1)*PI)/(2*M)))
      PRINT 14, N,MMH,DELT
14    FORMAT(1H2,59X,' POWER SPECTRUM'///,' NO OF POINTS',15/' PERCENTGE'
15    ,15/,' DELT',F5.2)
      PRINT 15,(PSSF(I),I=1,M1)

15    FORMAT (1H ,10F13.5)
      PRINT 16
16    FORMAT (59X,'LOG(F) VALUES'/59X,15(' ')/)
      DO 17 IR=1,M1
      IF (PSSF(IR) .GT. 0.0) ALPSSF(IP)=ALOG10(PSSF(IR))
17    CONTINUE
      OPEN(UNIT=1,FILE='PLOTTER.DAT',ACCESS='APPEND')
      WRITE (1,28)(ALPSSF(IR),IR=1,M1)
      CLOSE(UNIT=1)
      PRINT 28,(ALPSSF(IR),IR=1,M1)
      PRINT 74
      DO 18 I=1,N
18    W(I)=W(I+ID)-0.6*W(I)
      PRINT 15,(W(I),I=1,20)
      PRINT 74
      PRINT 15,(WW(I),I=1,20)
      PRINT 74
      AVW=0.0
      DO 19 J=1,H
19    AVW=AL(I)+AVW
      AVW=AVW/H
      AVW=AVW*AVW
      PRINT 15,AVW
      PRINT 74
      ACW(1)=0.0
      DO 20 J=1,H
20    ACW(1)=ACW(1)+W(I)*WW(I)
      ACW(1)=ACW(1)/H-AVW
      PSWC(1)=0.0
      DO 21 I=2,M1
      ACW(I)=0.0
      I1=M1-I
      K=I-1
      DO 22 J=I,H
22    ACW(I)=ACW(I)+W(J)*WW(J-K)
      ACW(I)=ACW(I)/I1-AVW
21    PSWC(1)=PSWC(1)+ACW(I)*2
      DO 76 I=1,M1
76    ACWA(I)=ACW(I)/ACW(1)

```

```

      OPEN(UNIT=1,FILE='PLOTTER.DAT',ACCESS='APPEND')
      WRITE(1,15)(ACW(I),I=1,M1)
      CLOSE(UNIT=1)
      PRINT 15,(ACW(I),I=1,M1)
      PRINT 74
      PRINT 15,(ACW(I),I=1,M1)
      PRINT 74
      PSWC(1)=PSWC(1)+ACW(1)-ACW(M1)
      DO 23 I=2,M1
      PSWC(I)=0.0
      DO 24 J=2,M
24 PSWC(I)=PSWC(I)+2.0*ACW(J)*COS((J-1)*(I-1)*PI/M)
23 PSWC(I)=PSWC(I)+ACW(1)+ACW(M1)*COS((I-1)*PI)
      PRINT 15,(PSWC(I),I=1,M1)
      PRINT 74
      PSWH(1)=(PSWC(1)+PSWC(2))/2.0
      PSWH(M1)=(PSWC(M)+PSWC(M1))/2.0
      DO 25 IR=2,M
25 PSWH(IR)=PSWC(IR-1)/4.0+PSWC(IR)/2.0+PSWC(IR+1)/4.0
      PRINT 15,(PSWH(I),I=1,M1)
      AVPSWH=0.0
      DO 903 II=1,M1
903 AVPSWH=AVPSWH+PSWH(II)
      AVPSWH=AVPSWH/M1
      PRINT 904,AVPSWH
904 FORMAT(//,20X,'AVERAGE OF PSWH=',F13.5)
      PRINT 74
      PRINT 74
      PSWF(1)=PSWH(1)*N/((N-M)*(1.36-1.2*COS(2.*PI/(6*M))))
      PSWF(M1)=PSWH(M1)/(1.36-1.2*COS((1-(1./(6*M)))*2*PI))
      DO 26 IR=2,M
26 PSWF(IR)=PSWH(IR)/(1.36-1.2*COS((2.*(IR-1)*PI)/(2*M)))
      PRINT 27,N,MMN,DELT
27 FORMAT(1H2,59X,' POWER SPECTRUM'///,' NO OF POINTS',I5/,' PRCNTGE',
1 I5/,' DELT',F5.2)
      PRINT 28,(PSWF(I),I=1,M1)
28 FORMAT (1H ,10E13.5)
      PRINT 29
29 FORMAT(59X,' LOGP(F) VALUES'/59X,I5('-'//))
      DO 30 IR=1,M1
      IF (PSWF(IR) .GT. 0.0 ) ALPSWF(IR)=ALOG10(PSWF(IR))
30 CONTINUE
      PRINT 28,(ALPSWF(IR),IR=1,M1)
      OPEN(UNIT=1,FILE='PLOTTER.DAT',ACCESS='APPEND')
      WRITE(1,28)(ALPSWF(IR),IR=1,M1)
      CLOSE(UNIT=1)
      PRINT 74
      AVSC=0.0
      DO 31 I=1,N
31 AVSC=SW(I)+AVSC

```

```

      AVSC=AVSC/N
      AVWC=0.0
      DO 32 I=1,N
32  AVWC=WW(I)+AVWC
      AVWC=AVWC/N
      AVSW=AVSC*AVWC
      PRINT 15, AVSW
      PRINT 74
      CCSWP(1)=0.0
      DO 33 I=1,N
33  CCSWP(I)=CCSWP(I)+SW(I)*WW(I)+SW(1)*WW(I)
      CCSWP(1)=CCSWP(1)/N-AVSW
      CSSWC(1)=0.0
      DO 34 I=2,M1
      CCSWP(I)=0.0
      I1=M1-I
      K=I-1
      DO 35 J=I,N
35  CCSWP(I)=CCSWP(I)+SW(J)*WW(J-K)+SW(J-K)*WW(J)
      CCSWP(I)=CCSWP(I)/I1-AVSW
34  CSSWC(1)=CSSWC(1)+CCSWP(I)*2
      PRINT 15, (CCSWP(I1),I1=1,M1)
      PRINT 74
      CSSWC(1)=CSSWC(1)+CCSWP(1)-CCSWP(M1)
      DO 36 I=2,M1
      CSSWC(I)=0.0
      DO 37 J=2,M
37  CSSWC(I)=CSSWC(I)+2.0*CCSWP(J)*COS((J-1)*(I-1)*PI/M)
36  CSSWC(I)=CSSWC(I)+CCSWP(1)+CCSWP(M1)*COS((I-1)*PI)
      PRINT 15, (CSSWC(I1),I1=1,M1)
      PRINT 74
      CSSWH(1)=(CSSWC(1)+CSSWC(2))/2.0
      CSSWH(M1)=(CSSWC(M)+CSSWC(M1))/2.0
      DO 38 IR=2,M
38  CSSWH(IR)=CSSWC(IR-1)/4.0+CSSWC(IR)/2.0+CSSWC(IR+1)/4.0
      PRINT 15, (CSSWH(IR),IR=1,M1)
      PRINT 74
C      CSSWF(1)=CSSWH(1)*M/((N-M)*(1.36-1.2*COS(2.*PI/(6*M))))
C      CSSWF(M1)=CSSWH(M1)/(1.36-1.2*COS((1-(1./(6*M)))*2*PI))
C      DO 39 IP=2,M
C      39 CSSWF(IP)=CSSWH(IP)/(1.36-1.2*COS((2.*(IP-1)*PI)/(2*M)))
C      PRINT 40, (CSSWF(I),I=1,M1)
C      40 FORMAT(1H *,10E13.5)
      PRINT 74
      CCSWH(1)=0.0
      DO 43 I=1,N
43  CCSWN(1)=CCSWN(1)+SW(I)*WW(I)-SW(I)*WW(I)
      CCSWN(1)=CCSWN(1)/N-AVSW
      CCSWN(1)=0.0
      CSSWC(1)=0.0

```

```

DO 44 I=2,M1
CCSWN(I)=0.0
I1=M1-I
K=I-1
DO 45 J=I,N
45 CCSWN(I)=CCSWN(I)+S*(J)*WW(J-K)-SW(J-K)*WW(J)
CCSWN(I)=CCSWN(I)/I1*AVSW
44 QSSWC(1)=QSSWC(1)+CCSWN(I)*2
PRINT 15, (CCSWN(I),I=1,M1)
PRINT 74
QSSWC(1)=QSSWC(1)+CCSWN(1)-CCSWN(M1)
QSSWC(1)=0.0
DO 46 I=2,M1
QSSWC(I)=0.0
DO 47 J=2,M
47 QSSWC(I)=QSSWC(I)+2.0*CCSWN(J)*SIN((J-1)*(I-1)*PI/K)
46 QSSWC(I)=QSSWC(I)+CCSWN(1)+CCSWN(M1)*SIN((I-1)*PI)
PRINT 15, (QSSWC(I),I=1,M1)
PRINT 74
QSSWH(1)=(QSSWC(1)+QSSWC(2))/2.0
QSSWH(M1)=(QSSWC(M)+QSSWC(M1))/2.0
DO 48 IR=2,M
48 QSSWH(IR)=QSSWC(IR-1)/4.0+QSSWC(IR)/2.0+QSSWC(IR+1)/4.0
PRINT 15, (QSSWH(IR),IR=1,M1)
PRINT 74
QSSWF(1)=QSSWH(1)*N/((N-M)*(1.36-1.2*COS(2.*PI/(6*M))))
QSSWF(M1)=QSSWH(M1)/(1.36-1.2*COS((1-(1/(6*M)))*2*PI))
DO 49 IR=2,M
I 49 QSSWF(IR)=QSSWH(IR)/(1.36-1.2*COS((2.*(IR-1)*PI)/(2*M)))
PRINT 50, (QSSWF(I),I=1,M1)
50 FORMAT(1H,10E13.5)
PRINT 74
DO 51 I=1,M1
COHD(I)=SQRT(CSSWH(I)*CSSWH(I)+QSSWF(I)*QSSWH(I))
T=PSWH(I)*PSWH(I)
IF (T) 52,53,54
52 COHD(I)=-SQRT(-T)
GO TO 51
53 COHD(I)=1.0
GO TO 51
54 COHD(I)=SQRT(T)
51 COH(I)=COHN(I)/COHD(I)
PRINT 55, (COHN(I),I=1,M1)
PRINT 74
PRINT 55, (COH(I),I=1,M1)
OPEN(UNIT=1,FILE='PLOOR.DAT',ACCESS='APPEND')
WRITE(1,55)(COH(I),I=1,M1)
CLOSE(UNIT=1)
55 FORMAT(1H,10E13.5)
PRINT 74

```

```

      DO 56 I=1,N1
      IF (CSSWH(I)) 57,58,57
57  ARG=ATAN(QSSWH(I)/CSSWH(I))*57.29577951
      IF (QSSWH(I)) 59,59,59
58  ARG=0.0
59  ARG=-ARG
      IF (CSSWH(I)) 60,61,62
60  IF (QSSWH(I)) 63,64,65
63  ARG=ARG+180.0
      GO TO 72
64  ARG=180.0
      GO TO 72
65  ARG=ARG-180.0
      GO TO 72
66  IF (QSSWH(I)) 66,67,68
66  ARG=90.0
      GO TO 72
67  ARG=0.0
      GO TO 72
68  ARG=-90.0
      GO TO 72
69  IF (QSSWH(J)) 69,70,71
69  ARG=ARG
      GO TO 72
70  ARG=0.0
      GO TO 72
71  ARG=ARG
72  KARGG=KARGG+1
      ARGG(KARGG)=ARG
73  FORMAT (F7.2)
56  CONTINUE
      PRINT 989,(ARGG(KK),KK=1,M1)
      OPEN(UNIT=1,FILE='PLOTTER.DAT',ACCESS='APPEND')
969  WRITE(J,989)(ARGG(KK),KK=1,M1)
      FORMAT(1H ,10F7.2)
      CLOSE(UNIT=1)
      STOP
      END
      SUBROUTINE TREND(U)
      DIMENSION U(1)
      USUM=0.0
      DO 110 I=1,1001
110  USUM=USUM+(U(I)/1001.0)
      W=0.0
      DO 220 I=1,333
220  W=W+U(I)
      V=0.0
      DO 330 I=668,1001
330  V=V+U(I)
      ALPHA=(500.0/(333.0*668.0))*(V-W)

```

```
DO 440 I=1,1001
440  U(I)=U(I)-USUM*(ALPHA*(FLOAT(I)/500.0) - 1.0)
      RETURN;END
```

## APPENDIX A-4

210

Program for plotting power spectral densities  
and coherence values.

```

DIMENSION Y(53),EXNO(4)
CALL PLOTS(0,0,0)
CALL FACTOR(.8)
DO 1111 I=1,5
  READ(22,100,END=555)EXNO
100   FORMAT(4A5)
  READ(22,200,END=555)(Y(I),I=1,51)
  CALL VERT(Y,'NORMALIZED AUTOCORRELATION-STAR',31,'TIME LAG',4,
  1EXNO,0,0,1)
  READ(22,200,END=555)(Y(I),I=1,51)
200   FORMAT(1H ,10E13.5)
3     FORMAT(1H ,10F7.2)
  CALL VERT(Y,'LOGP(F)-STAR',12,'FREQUENCY',9,EXNO,0,1,0)
  READ(22,200,END=555)(Y(I),I=1,51)
  CALL VERT(Y,'NORMALIZED AUTOCORRELATION-WIND',31,'TIME LAG',8,
  1EXNO,0,0,1)
  READ(22,200,END=555)(Y(I),I=1,51)
  CALL VERT(Y,'LOGP(F)-WIND',12,'FREQUENCY',9,EXNO,0,1,0)
  READ(22,200,END=555)(Y(I),I=1,51)
  CALL VERT(Y,'COHERENCE',9,'FREQUENCY',9,EXNO,1,1,1)
  READ(22,300,END=555)(Y(I),I=1,51)
  CALL VERT(Y,'PHASE DIFFERENCE',16,'FREQUENCY',9,EXNO,1,1,0)
1111  CONTINUE
  CALL WHERE(XX,YY,FACT)
  CALL PLOT(XX,YY,999)
555   STOP
END
SUBROUTINE VERT(Y,YTEXT,NY,XTEXT,NX,EXNO,NLINE,NS,KKK)
DIMENSION Y(1),YTEXT(10),EXNO(1),X(53),XTEXT(10)
DO 1 K=1,51
  J=K-1
  X(K)=FLOAT(J)
1 CONTINUE
  X(51)=0.0
  X(52)=5.0
  CALL SCALE(Y,6.0,50,1)
  CALL HDAXIS(0.,0.,XTEXT,-NX,10.,0.,0.,5.,11.,12,1)
  GG=0.0
  DO 1000 JG=1,100
    GG=GG+.1
    CALL PLOT(GG,0.0,2)
    CALL PLOT(GG,-.06,2)
    UNN=JG-10*(JG/10)
    IF(UNN.EQ.0) CALL PLOT(GG,-.1,2)
    CALL PLOT(GG,0.0,2)
1000  CONTINUE
  SY=ABS(Y(52))
  CALL HDAXIS(0.,0.,YTEXT,NY,6.,90.,Y(51),Y(52),11,-12,1)
  IF(NS.EQ.1)X(1)=.2
  IF(NLINE.EQ.0) CALL LINE(X,Y,50,1,0,0)

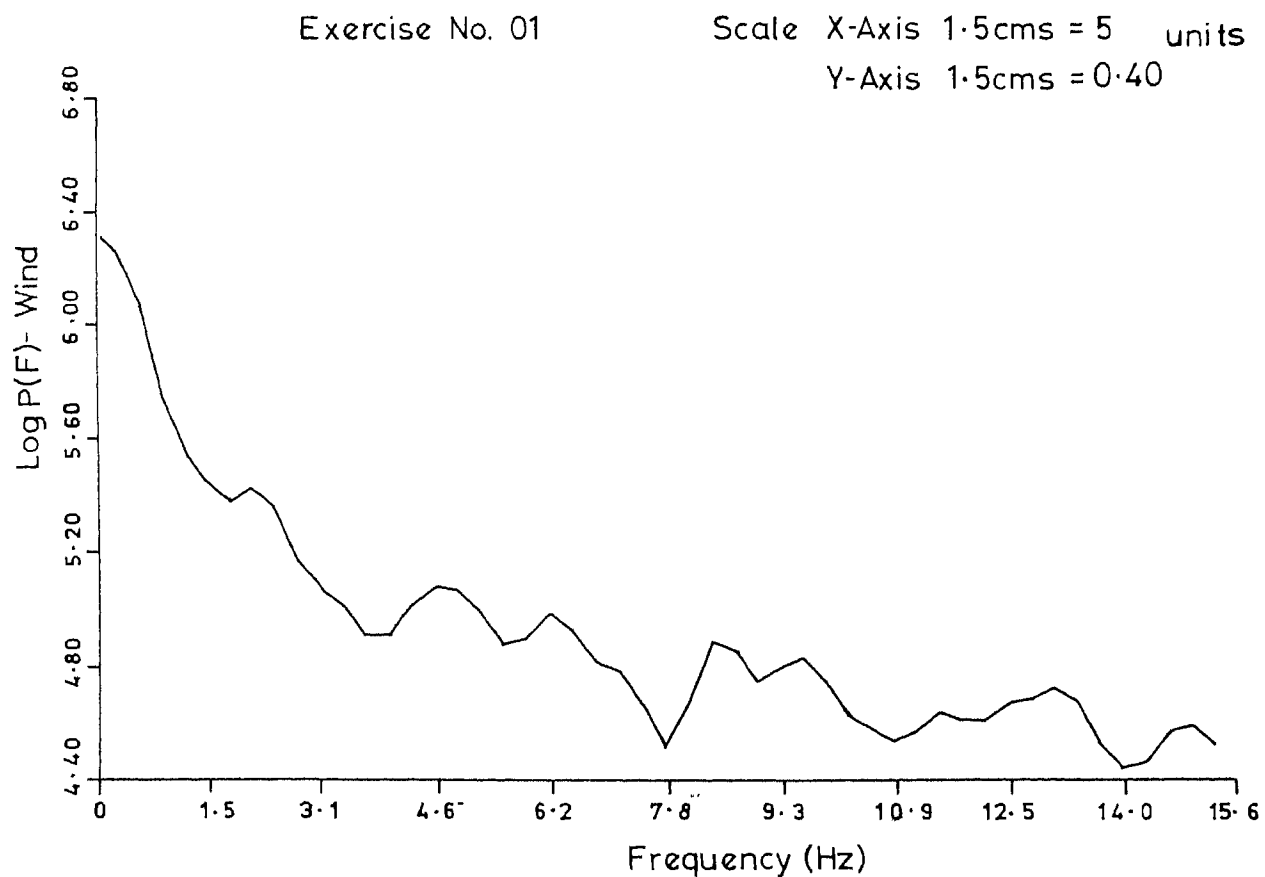
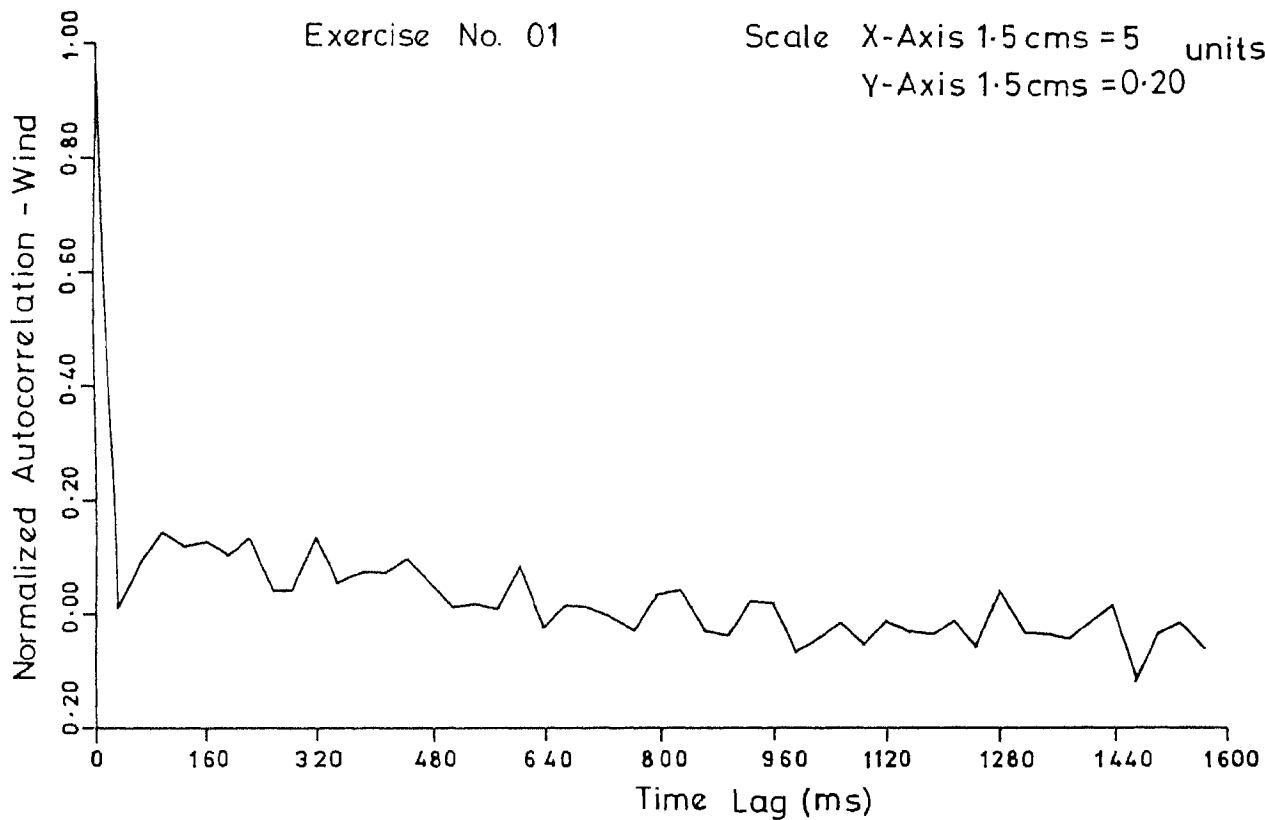
```



```
IF(OLINE.NO.1)CALL NDITLE(X,Y,50,1,-1,4,.05)
IF(KKK.NQ.0) GOTO 4545
CALL SYMBOL(0.5,6.75,.17,'POWER SPECTRUM AND COHERENCE
1 ANALYSIS OF KAVALAR SEEING',0.,55)
4545 CALL SYMBOL(1.5,6.5,.12,EXNO,0.,20)
CALL SYMBOL(5.0,6.5,.12,'SCALE: X-AXIS 1.5 CMS=5 UNITS',0.,29)
CALL SYMBOL(5.84,6.3,.12,'Y-AXIS 1.5 CMS=',0.,15)
CALL NUMBER(999.,999.,.12,SY,.0,2)
CALL SYMBOL(999.,999.,.12,' UNITS',0.,6)
CALL PLOT(0.0,-8.0,-3)
RETURN
END
```

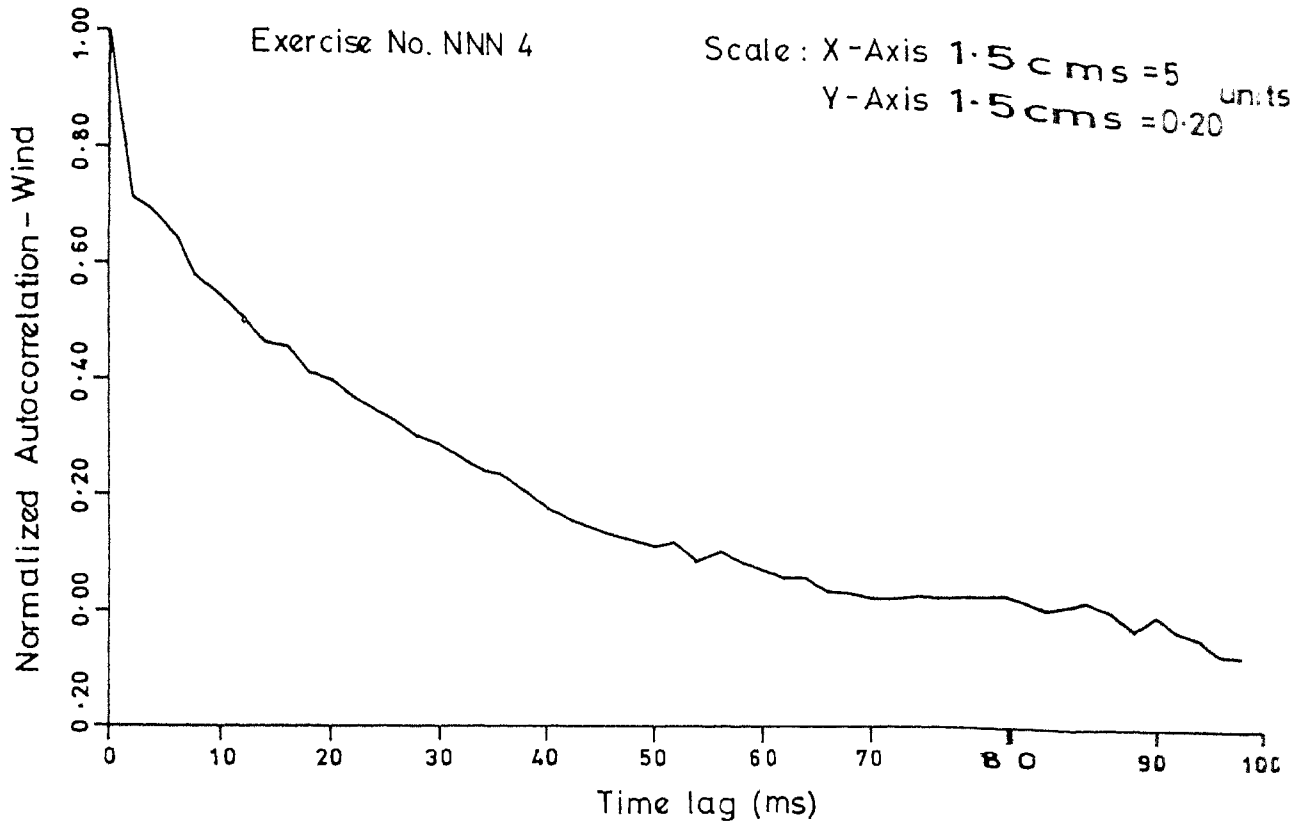
APPENDIX — B

Power spectrum and coherence analysis of Kavalur turbulence

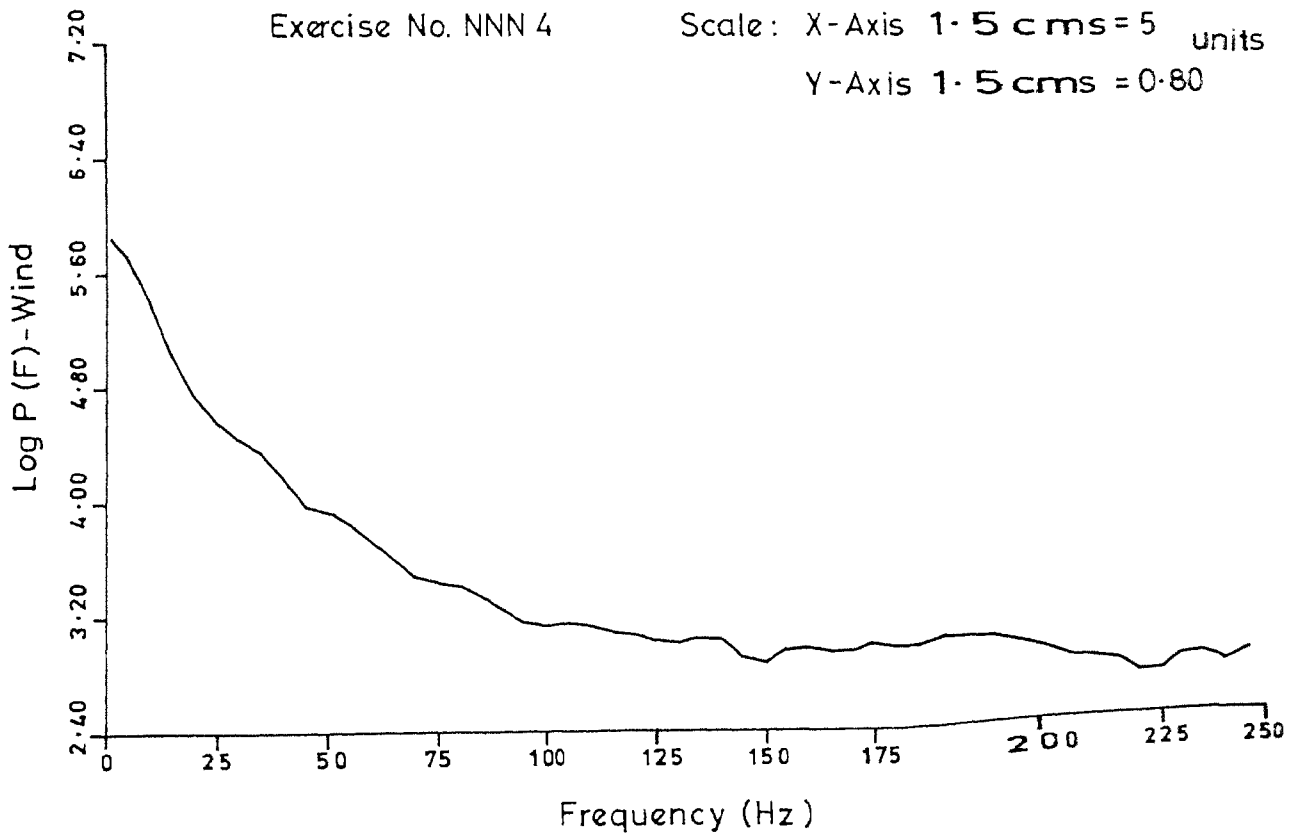


Normalized autocorrelation vs. Time lag  
Atmospheric turbulence

214



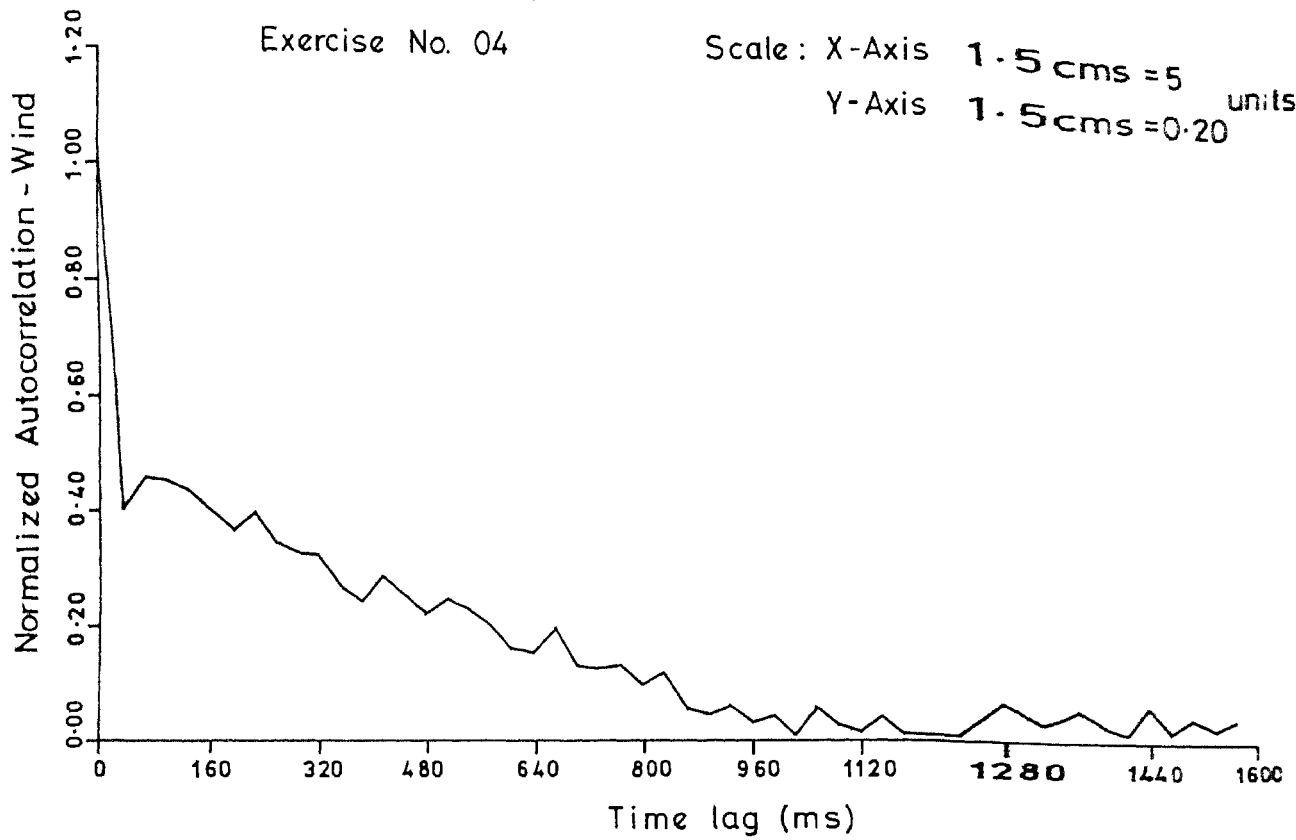
Log of power spectral density vs Frequency  
Atmospheric turbulence



Normalized autocorrelation vs. Time lag  
 Atmospheric turbulence

Exercise No. 04

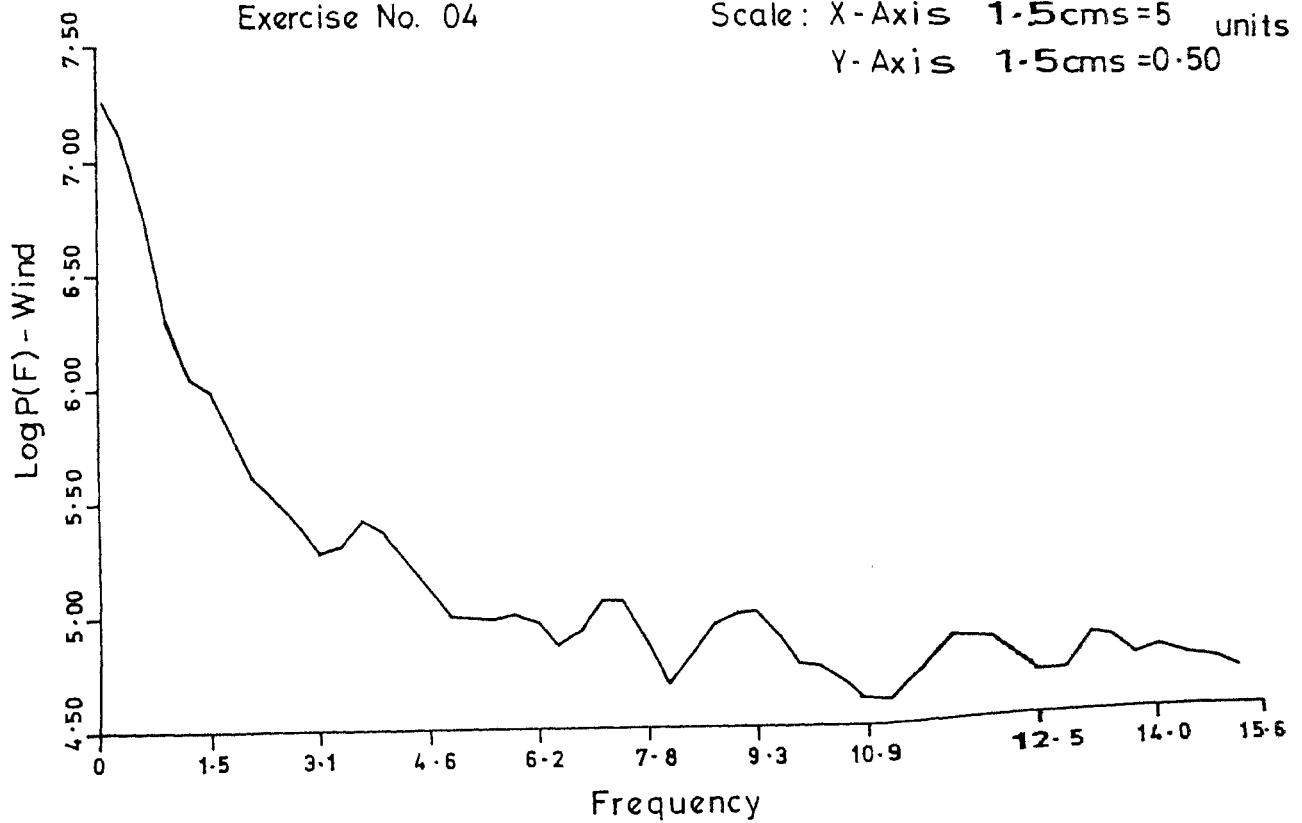
Scale: X-Axis 1.5 cms = 5 units  
 Y-Axis 1.5 cms = 0.20 units



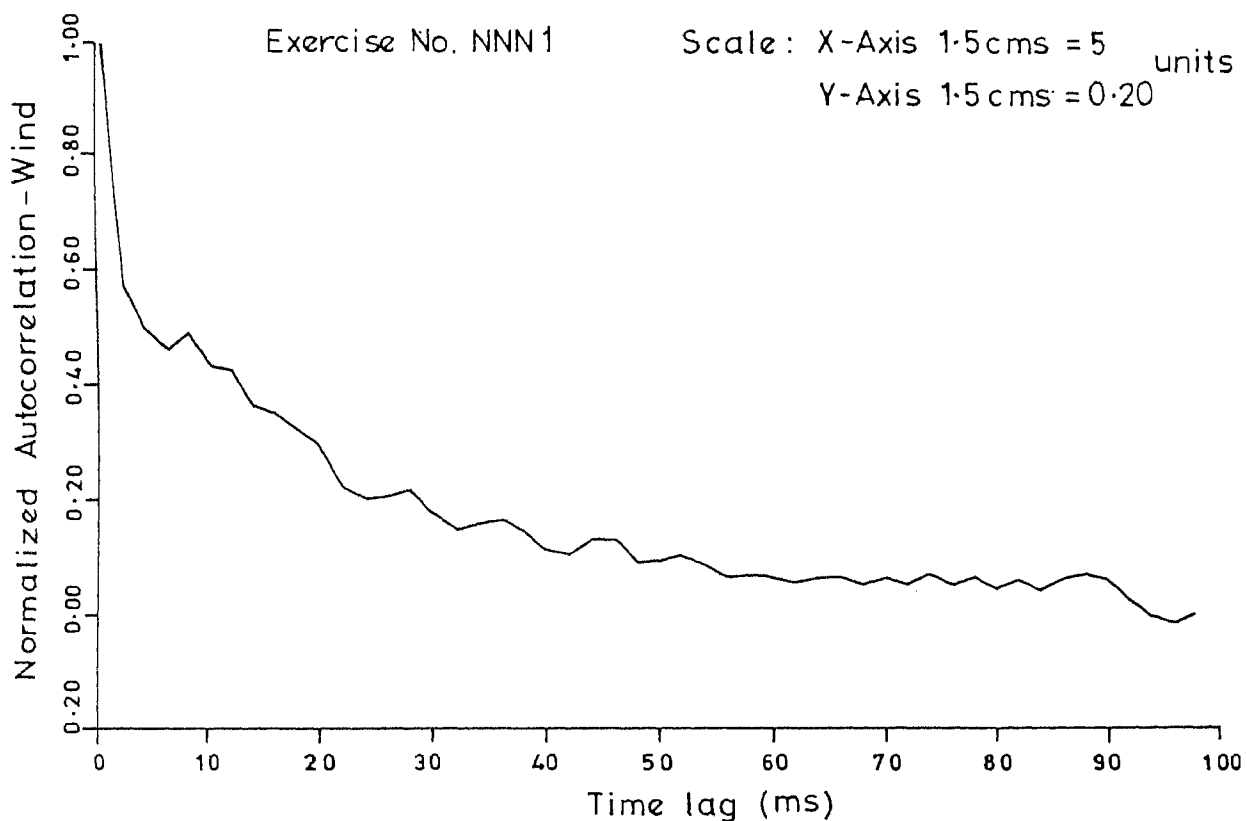
Log of power spectral density vs. Frequency  
 Atmospheric turbulence

Exercise No. 04

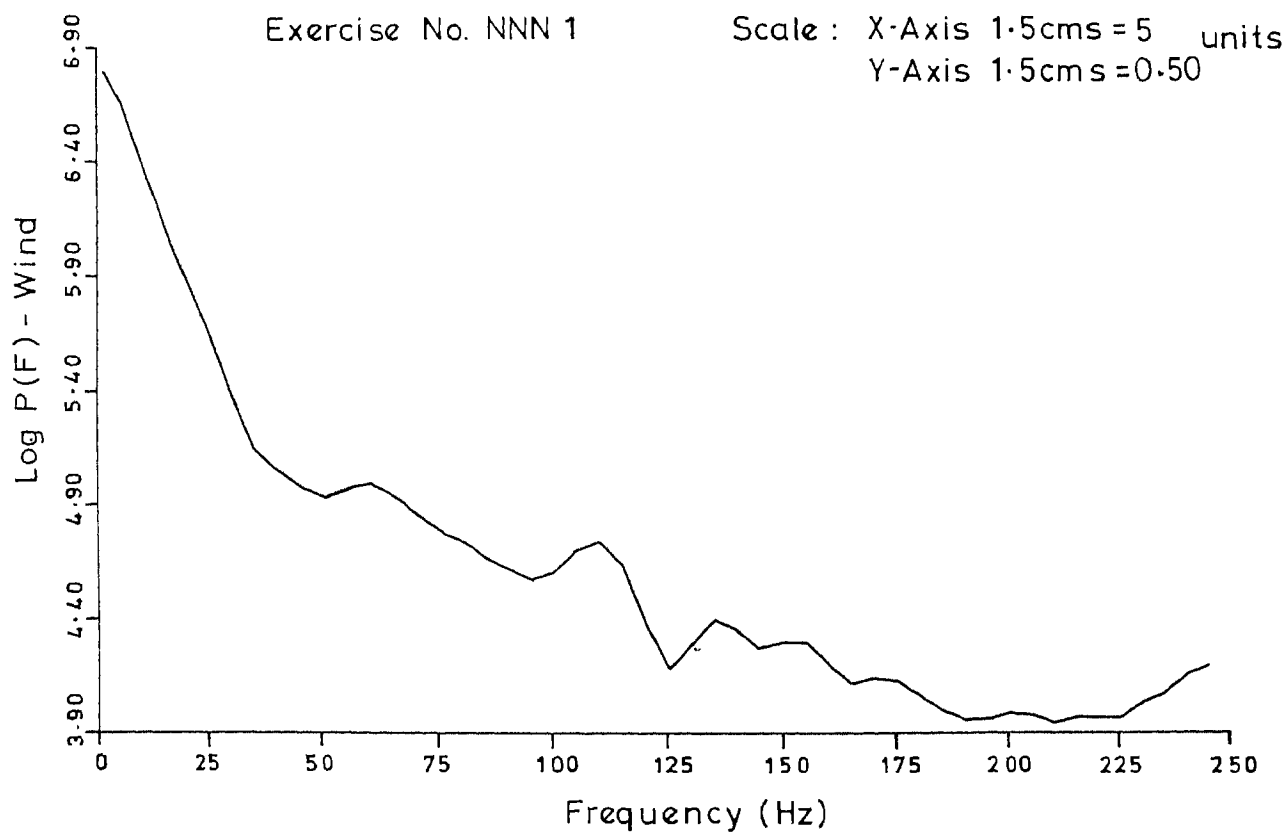
Scale: X-Axis 1.5 cms = 5 units  
 Y-Axis 1.5 cms = 0.50 units



Normalized autocorrelation vs. Time lag  
Atmospheric turbulence



Log of power spectral density vs. Frequency  
Atmospheric turbulence



REFERENCES

1. Joseph Morgan, 1953 "Introduction to Geometric Optics"  
McGraw-Hill, New York
2. V.I.Tatarski, 1961 "Wave Propagation in a Turbulent  
Medium"  
McGraw-Hill, New York
3. L.A.Chernov, 1960 "Wave Propagation in a Random  
Medium"  
McGraw-Hill, New York
4. A.H.Mikesell, A.A. Hoag, J.S.Hall, 1951 Journal of Optical Society of  
America, 41, 689
5. I.G.Kolchinski, 1952 Astron. Zh., 29, 350
6. M.Bertolitti, 1976 "Lasers and Their Applications"  
Ed. Sona  
Gordon & Breach, New York
7. J.Stock, G.Keller 1960 "Telescopes"  
Ed. Gerard P.Kuiper  
Barbara M.Middlehurst  
Chicago Press
8. Frederick, L.W. 1960 Paper read at the 105th meeting  
of the American Astronomical  
Society.
9. Danjon,A. 1926 C.R.Acad. Sci. Paris, 183, 1032
10. Little,C.G. 1951 Monthly Notices of the Royal  
Astronomical Society.,  
111, 289-302
11. Chandrasekhar,S. 1952 Monthly Notices of the Royal  
Astronomical Society.,  
112, 475-483
12. Keller,G. 1953 Astronomical Journal, 58, 113-125

13. McInel, A.B. 1960 "Telescopes"  
Ed. Gerard P. Kuiper  
Barbara M. Middlehurst
14. Kolchinski, I.G. 1957 Astron. Zh., 34, 638
15. Couder, A. 1953 Pub. Obs. Haute Provence,  
Vol. 2, No. 53.
16. Rosch, J. 1955 Ciel et terre, 71, 205
17. Sisson, G.M. 1957 Nature, 179, 937
18. Leighton, R.B. 1957 Publications of the Astronomical  
Society of Pacific, 69, 497
19. Babcock, H.W. 1953 Publications of the Astrono-  
mical Society of Pacific,  
65, 229
20. Leighton, R.B. 1956 Scientific American,  
194, 157 (No. 6).
21. Dewilt, J.H.,  
Hardie, R.H.,  
and Seyfert, C.K. 1957 Sky and Telescope, 17, 8
22. McMath, R.R. 1955 Sky and Telescope, 14, 372
23. Schwarzschild, M. 1959 Astrophysical Journal, 130, 345
24. Barnhart, P.E.,  
Keller, G., and  
Mitchell, W.E., Jr 1959 Report TR 59-291  
Air Force Cambridge  
Research Center, Bedford,  
Mass.
25. Protheroe, W.M. 1955 Contributions of the  
Perkins observatory  
(Delaware, Ohio), No. II-4
26. Mikesell, A.H. 1951 Journal of Optical Society of  
America, 41, 689
27. Gifford, F., Jr.,  
and Mikesell, A.H. 1953 Weather, 8, 195



28. Mikesell, A.H. 1955 Publications of the U.S. Naval Observatory., 2nd ser., 17, 139
29. Vernin, J. and Roddier, F. 1973 Journal of Optical Society of America, 63, no.3.
30. J.C. Bhattacharyya and A. Sundareswaran 1977 Kodaikanal Obs. Bull. Ser. A(1977), 2, 69-74.  
An analog system for fast light curve registration
31. B.G. Shivaprasad 1975 "Wind Tunnel Techniques"  
A Summary of lectures,  
A.E. Dept. IISc.
32. DISA Hot-Wire anemometer 55 M Model Manual on Scientific Research Equipment, DISA, Herlev, Denmark.
33. Official Communication August 28th, 1981 NAL Letter No. NAL/KSY/1446
34. Hinze, J.O. 1959 Turbulence-An Introduction to its mechanism and theory, McGraw-Hill, New York
35. Danilo A. Mazzarella's Letter dated January 24, 1980,  
Private Communication
36. R.M. Young Company Cup-anemometer: Manual-on sensitive Wind Instruments- Traverse City, Michigan.
37. EMI 1973 "Manual on SE Eight-Four Portable Tape Recorder, Volume 1 user guide Document Ref. CM-1001.
38. Philips 7-channel analog tape recorder Manual

39. David F. Stout  
and  
Milton Kaufman 1976 Handbook of Operational  
Amplifier Circuit Design  
McGraw-Hill, New York
40. Analog Devices Manual on Integrated Circuits.
41. Gold, B., and  
Rader, C.M., 1969 "Digital Processing of  
Signals"  
McGraw-Hill, New York
42. R.B. Blackman and  
J.W. Tukey 1958 The Measurement of Power  
Spectra From the Point of  
View of Communication  
Engineering.  
Dover Publication, INC,  
New York.
43. M.K.V. Bappu,  
S. Mohin and  
K.G. Unnikrishnan 1978 "The Astronomical Seeing at  
Kavalur" Kodaikanal Obs.  
Bull. Ser. A(1978)2, 168-179
44. Julius S. Bendat  
and  
Allan G. Piersol 1971 Random Data: Analysis and  
Measurement Procedures.  
Wiley-Interscience, New York.
45. Robert K. Otnes  
and  
Loren Enochson 1978 Applied Time Series Analysis,  
Vol. 1 Basic Techniques  
John Wiley and Sons, New York

46. Goodman, N.R., 1957 Scientific Papers No.10  
Engineering Statistics  
Laboratory, New York  
University.
47. Robert K. Otnes 1972  
and  
Loren Enochson Digital Time Series Analysis  
John Wiley and Sons,  
New York.
48. Van Isacker, J., 1961 Advances in Geophysics,  
7, 189
49. J.C. Dainty Ed., 1975 Topics in Applied Physics  
Laser Speckle and Related  
Phenomena  
Vol.9
50. E.D. Hinkley Ed., 1976 Topics in Applied Physics  
Laser Monitoring of the  
Atmosphere  
Vol.14